De biomechanische structuur van de zeepaardstaart
als inspiratiebron voor industrieel ontwerp

The Biomechanical Structure of the Seahorse Tail
as a Source of Inspiration for Industrial Design

Tomas Praet

Promotoren: prof. dr. ir. B. Verhegghe, prof. dr. D. Adriaens
Proefschrift ingediend tot het behalen van de graad van
Doctor in de Ingenieurswetenschappen: Biomedische Ingenieurstechnieken

Vakgroep Civiele Techniek
Voorzitter: prof. dr. ir. P. Troch
Faculteit Ingenieurswetenschappen en Architectuur
Academiejaar 2012 - 2013

UNIVERSITEIT
GENT

ISBN 978-90-8578-598-9
NUR 954
Wettelijk depot: D/2013/10.500/31

Supervisors:

prof. dr. ir. Benedict Verhegghe (promotor)
prof. dr. Dominique Adriaens (promotor)
dr. ir. Matthieu De Beule

Examination Committee:

prof. dr. ir. Benedict Verhegghe (promotor)
prof. dr. Dominique Adriaens (promotor)
prof. dr. ir. Hendrik Van Landeghem (chairman)
dr. ir. Matthieu De Beule (secretary)
prof. dr. Peter Aerts
dr. Anabela Maia
dr. Tom Van Hoof
prof. dr. ir. Wim Van Paepegem

Research lab:

Biofluid, Tissue and Solid Mechanics for Medical Applications (bioMMeda)
Institute Biomedical Technology (IBiTech)
Ghent University
De Pintelaan 185 - Block B
B-9000 Ghent
Belgium

This research was funded by the FWO (Fonds Wetenschappelijk Onderzoek Vlaanderen), grant number G.0137.09N.

Acknowledgements

I would like to take this opportunity to address special thanks to some people and institutes. Fruitful collaborations are vital for the successful completion of a PhD. This is especially applicable to this dissertation, as the involved research project has a distinct multidisciplinary nature. Without the advice and expertise of the people mentioned below, I would undoubtedly have been lost early on in the project.

First of all, thanks to prof. dr. ir. Benedict Verhegghe, prof. dr. Dominique Adriaens, dr. ir. Matthieu De Beule, and dr. Bert Masschaele for their successful efforts to get the research on the biomechanics of the seahorse tail on the rails. Thank you for providing me with the opportunity to work on such an unusual but fascinating topic. People's faces brightened up when I told them on what topic I was working. It seems like seahorses have a special effect on people. Their looks are considered to be cute and funny, and yet they appear to be surrounded by a veil of mystery. Being able to tell people about this catchy topic was very pleasing, and never boring. In fact I think it often even sparkled a smile on my face.

Thank you Benedict and Dominique for being my promoters. And thank you Matthieu for convincing me with your enthusiasm to start working at bioMMeda. And thank you Benedict for introducing me to the pyFormex platform. Its added value to my doctorate is undeniable.

I'd also like to express my sincere gratitude to the people of the research group *Evolutionary Morphology of Vertebrates* (department of Biology, Ghent University) for their elaborate support. Thank you for infecting me with your passion for nature and its remarkable systems. In particular, thanks to prof. dr. Dominique Adriaens, dr. Anabela Maia, and Céline Neutens. It's rare these days to find people that are this passionate about what they're doing. I know that the visions of engineers and biologists are often miles apart, but it's because of those profound differences in background that our talks were often very refreshing, hopefully for the both of us. Thanks for keeping an open mind towards my (admittedly close-minded) engineering point of view, and thanks for all the patience when trying to lead me carefully to a much needed epiphany. I hope that our joint efforts to bridge the gap between engineers and biologists will continue to produce, eh... I mean spawn, collaborate research opportunities. I also hope that this dissertation can reflect some of the benefits of combining the views of engineers and biologists.

A special word of thanks for dr. Anabela Maia for providing the kinematic data on the seahorses and for helping me out with some of the more biological parts of the dissertation. Some of the preliminary work on the project was done by dr. ir. Sofie Van Cauter and ir. Sander De Bock, who also assisted with some experiments. I would like to take this opportunity to thank them for their contributions.

Thanks to the UGCT for providing the CT-scans, and the European Synchrotron Radiation Facility in Grenoble for providing the synchrotron scans.

Special thanks to all my former and current co-workers and colleagues at bioMMeda. In alphabetical order, thanks to Abigail, Alessandra, Benjamin, Bram, Charlotte, Darya, David, Francesco, Francisco, Frederic, Joris, Koen, Liesbeth, Matthieu, Nic, Peter, Sander, and Sofie. And thanks to Patrick for coaching this inspiring team of young researchers. Thank you all for the support, companionship, and all the amusing moments that made the hard work a lot more pleasing. It honestly has been a real pleasure to be part of such a dynamic, versatile, and motivated group.

And finally, thanks to my family and friends for their continued support. Thanks for keeping up with all my complaints and other annoyances. Know that it's fully being appreciated.

Ghent, February 2013

Tomas

Table of Contents

List of Acronyms

A

ACSA	Anatomical cross-sectional area of the muscle

C

CSA	Cross-sectional area

D

DOF	Degrees of freedom

E

EAP	Electro-active polymer
EMM	Epaxial myomere muscle

F

FD	Force driven simulation
FE	Finite element
FEA	Finite element analysis
FEM	Finite element method

H

HMM	Hypaxial myomere muscle

L

LV	Left ventral dermal plate
LD	Left dorsal dermal plate

M

MVM	Median ventral muscles

P

PAM	Pneumatic artificial muscle
PCSA	Physiological cross-sectional area of the muscle

R

RV	Right ventral dermal plate
RD	Right dorsal dermal plate
RP	Simulations starting from the resting position of the tail

S

SMA	Shape memory alloys

V

VE	Vertebra of the tail segment

Nederlandse samenvatting –Summary in Dutch–

Miljoenen jaren van evolutie hebben natuurlijke organismen ertoe aangezet om oplossingen te vinden voor een resem levensechte problemen. Kleine wijzigingen in functionaliteit worden via evolutie nauwgezet gecontroleerd op hun gepastheid, efficiëntie en robuustheid. Ingenieurs worden dagdagelijks met soortgelijke problemen als deze natuurlijke organismen geconfronteerd. Aldus kan men in de ingenieurswereld inspiratie halen uit de oplossingen die men in de natuur kan vinden, zelfs binnen zeer geavanceerde toepassingsgebieden.

Een voorbeeld van een organisme dat zich op een zeer specifieke manier heeft aangepast aan haar omgeving is het zeepaard. Het overgrote deel van de vissen gebruikt undulatie (heen en weer bewegen) van het lichaam om zich voort te bewegen. Een kleiner aantal vissen, waaronder de zeepaarden, gebruikt undulatie van de vinnen als belangrijkste bron van propulsie. Veelal zijn dit vissen die nood hebben aan een hoge mate van manoeuvreerbaarheid, terwijl hoge snelheid minder van belang is. Bij het zeepaardje heeft de caudale structuur zijn functie in de voortbeweging verloren. Voor de voortbeweging vertrouwt het diertje op de rugvin en de pectorale vinnen.

Hoewel het gebruik van vinnen voor voortstuwing het rechtop zwemmend zeepaard zeer manoeuvreerbaar maakt in haar obstakelrijke omgeving, die veelal bestaat uit dichtbegroeide koralen en zeegrassen, zorgt het er tevens voor dat de zwemsnelheid van het zeepaard eerder laag is. Zeepaarden hebben dan ook nauwelijks kans om weg te zwemmen van roofvissen. Ze vertrouwen daarom voornamelijk op crypsis om te overleven. Hun kleuren zijn veelal aangepast aan de omgeving, ze bewegen traag en ze hebben een soort van beschermende, skeletale bepantsering rondom hun lichaam, wat hen allicht meer resistent maakt tegen beten van roofvissen. Ondanks dit stijf en sterk schild dat ook de staart bedekt, is de staart toch voldoende flexibel om als grijporgaan dienst te doen. Met deze grijpstaart houdt het zeepaard zich vast aan objecten en vegetatie op de zeebodem, zodat het niet wordt meegesleurd door sterke zeestromingen.

De combinatie van een in compressie stijve staart (door de bepantsering) en de buigzaamheid in ventrale richting (om als grijporgaan dienst te doen) is ook vanuit een ingenieursstandpunt interessant. Stijfheid en flexibiliteit combineren is een vaakvoorkomende vereiste in de ingenieurswereld, waaraan het bovendien vaak moeilijk te voldoen is. Zodoende bestuderen we in deze dissertatie die biomechanische structuur van de zeepaardstaart, teneinde een beter beeld te krijgen van de

principes die aan de grondslag liggen van de interessante combinatie van mechanische eigenschappen van de zeepaardstaart. Deze kennis moet de basis leggen voor ontwerpen binnen ingenieurstoepassingen waar zowel flexibiliteit als stijfheid van belang zijn.

In **Hoofdstuk 1** worden vooreerst enkele belangrijke basisprincipes besproken die van belang zijn voor de rest van de dissertatie. Vervolgens worden enkele algemeenheden over het zeepaardje uit de doeken gedaan. Het hoofdstuk wordt afgesloten met een bespreking van de doelstellingen en een overzicht van de dissertatie.

Hoofdstuk 2 focust zich op ontwerp vanuit de natuur. Dit principe wordt verduidelijkt aan de hand van enkele typische en historische voorbeelden. In het specifieke geval van vissen zijn robotten die de locomotie van vissen imiteren een hot topic in de laatste decennia. Daarom wordt er dieper ingegaan op dit toepassingsgebied via enkele interessante voorbeelden. Een zeer voor de hand liggend industrieel ontwerp geïnspireerd door de zeepaardstaart is een robot dat de grijpfunctionaliteit van de staart imiteert. Daarom worden bestaande gelijkaardige ontwerpen besproken op het einde van dit hoofdstuk.

Modelleren van een biomechanische structuur kan pas nadat de anatomie van de structuur grondig is bestudeerd. De musculoskeletale structuur van de zeepaardstaart is echter maar summier besproken in de literatuur. Daarom is **Hoofdstuk 3** gewijd aan de anatomie van de zeepaardstaart. Het skelet van de staart bestaat uit een reeks van ongeveer 30 gelijkvormige segmenten. Caudaal verkleinen de segmenten, terwijl de inclinatie van het segment vergroot. Elk segment bestaat uit een wervel omgeven door vier dermale platen (twee ventrale en twee dorsale).

Tussen de dermale platen van opeenvolgende segmenten zijn er longitudinale glijgewrichten. De caudale stekel van de meest proximale plaat past in een groef van het volgende segment van de keten. Hierdoor is de glijrichting sterk beperkt tot de longitudinale richting. Rotaties zijn door de vorm van de stekel en de groef beperkt. Tussen dermale platen binnen eenzelfde segment zijn er eveneens glijgewrichten. Deze gewrichten zijn minder strikt gedefinieerd. Twee tot drie richels op het vlakke oppervlak van de onderste plaat passen min of meer in overeenkomstige groefjes in de bovenste plaat. Dit vormt een vrij los glijgewricht met hoofdrichting volgens de verbindingslijn tussen de massacentra van beide skeletale elementen betrokken in de gewrichtsformatie.

De wervel heeft drie stekels die zich uitstrekken naar de ventrale zijde (hemaalstekel) en de laterale zijdes (transversale stekels). De tip van deze stekels vormt een gewricht met de dichtstbijzijnde dermale plaat. Deze gewrichten kunnen beschouwd worden als kogelgewrichten, aangezien de rotaties redelijk ongehinderd kunnen plaatsvinden, terwijl translaties beperkt zijn door de vorm van de skeletale elementen en het omliggend bindweefsel.

Tussen de wervels onderling is er een gewricht dat bestaat uit de restanten van het notochord en gevormd wordt door concave holtes in beide wervels met daartussen een soort vloeistofzak. Dit vormt een flexibel gewricht dat in principe zowel glijden als roteren toelaat. Incompressibiliteit van de vloeistof tussen de wervels beperkt echter het samenduwen van het gewricht.

De spierstructuur in lichaam en staart van vissen is complex. Het grootste volume aan spierweefsel wordt gevormd door myomeerspieren. Deze bestaan uit een opeenstapeling van spiervezels en collageenlagen die myosepta genoemd worden. De myosepta zijn geplooid tot vrij complexe vormen. Deze vormen bestaan meestal uit longitudinale kegels, die verondersteld zijn van bij spiercontractie energie op te slaan en de lichaamsstijfheid te verhogen. Bij de zeepaardstaart vertonen de epaxiale myomeerspieren (dorsale zijde) nog deze structuur, maar de hypaxiale myomeerspieren (ventrale zijde) vertonen een opmerkelijk afwijkende structuur. De conische structuur is grotendeels vervangen door een structuur van evenwijdige, diagonale myosepta. Hierdoor overspannen de hypaxiale myomeerspieren verschillende segmenten. De afwijkende structuur van de hypaxiale myomeerspieren is mogelijks gerelateerd aan de functie van de zeepaardstaart. Deze verschilt namelijk van de functie van de meeste visstaarten: het gros van de vissen gebruikt de staart voor de voortbeweging, terwijl het zeepaard de staart aanwendt als grijporgaan. De hypaxiale myomeerspieren bevinden zich aan beide zijden van de staart, waardoor ze zowel ventrale buiging (door bilaterale contractie) als ventro-laterale buiging (door unilaterale contractie) kunnen bewerkstelligen.

Er is nog een ander spiertype in de zeepaardstaart dat buiging van de staart kan veroorzaken: de mediaan ventrale spieren. Deze spieren bevinden zich op het midsagittaal vlak, waardoor ze enkel ventrale buiging kunnen introduceren in de staart. De oppervlakte van hun doorsnede is veel kleiner dan deze van de myomeerspieren, waardoor de krachten die ze kunnen genereren vermoedelijk veel beperkter zijn.

De passieve uitrekbaarheid van de myomeerspieren (zowel hypaxiaal als epaxiaal) werd geschat op basis van uniaxiale trektesten op spieren van een specimen van de zeepaardsoort *Hippocampus reidi*. De contralaterale spieren werden gebruikt in histologische studies. De histologische snedes lieten toe om een goede schatting te maken van de oppervlakte van de dwarsdoorsnede van de spieren. Het verschil tussen de uitrekbaarheid van de epaxiale en de hypaxiale myomeerspieren bleek zeer groot te zijn, zelfs na het verschil in dwarsdoorsnede in rekening te brengen: de epaxiale spieren bleken een stijfheid te hebben die een grootteorde kleiner is dan deze van de hypaxiale myomeerspieren. Het is mogelijk dat beschadiging van het spierweefsel een belangrijke rol speelde in de sterk verschillende opmetingen. De passieve respons van de spieren bleek goed te kunnen worden benaderd door exponentiële curves. De passieve extensibiliteit van alle myomeerspieren doorheen de staart werd geschat door op synchrotron scans de dwarsdoorsnede van de myomeerspieren op verscheidene posities in de staart op te meten, en hieruit het verloop van de dwarsdoorsnedes van de spieren doorheen de staart af te leiden. De uitrekbaarheid werd hierbij verondersteld van evenredig te zijn met de dwarsdoorsnede van de spier.

Op basis van de studie van de anatomie van de staart kunnen biomechanische modellen van de staart worden gegenereerd. Dit wordt besproken in **Hoofdstuk 4**. Het hoofdstuk begint met een bespreking van verschillende termen en simulatietechnieken die bij het modelleren van biomechanische structuren gebruikt worden. Tevens worden enkele wetenschappelijke publicaties aangehaald die zich specifiek

richten op biomechanische modellen in de biologie.

Via scripts in pyFormex worden modellen gecreëerd op basis van de gedetailleerde reconstructie van één referentiesegment van een gestrekte staart. De andere 29 segmenten van de staart worden hieruit gedistilleerd via translatie, schaling en inclinatie. Om de positie van de gewrichten en aanhechtingspunten van de spieren te bepalen worden algoritmes gebruikt in pyFormex die gebaseerd zijn op de zogenaamde *shape index* van de oppervlaktemesh van de skeletale elementen. Hierdoor kan men makkelijk het referentiesegment veranderen zonder dat een resem handmatige manipulaties hoeft uitgevoerd te worden.

Het hoofdstuk eindigt met een bespreking van het materiaalmodel dat gebruikt wordt voor de vervormbare botstructuren, en met een bespreking van de rustpositie van de zeepaardstaart. Dit is de positie van de staart wanneer geen van de spieren geactiveerd is. Metingen op geanesteseerde zeepaardjes tonen aan dat deze positie sterk afhankelijk is van het individu, en dat er kleine wijzigingen aan de positie kunnen worden aangebracht zonder dat de staart terug naar de vorige positie beweegt. Desalniettemin werd één typerende positie gedigitaliseerd en gebruikt als startpositie voor een groot deel van de simulaties.

Na de bespreking van de technieken gebruikt bij de aanmaak van de modellen in Hoofdstuk 4, handelt **Hoofdstuk 5** over de resultaten van de uitgevoerde simulaties. De opgestelde modellen werden uitgerekend met Abaqus 6.12. Dit is een weloverwogen beslissing die ons toelaat om onvervormbare en vervormbare elementen met elkaar te combineren binnen eenzelfde simulatie. Via simulaties met vervormbare skeletale elementen wordt aangetoond dat bij middelmatige staartbuigingen en bij afwezigheid van externe krachten de vervormingen verwaarloosbaar klein zijn. Zodoende focussen de meeste simulaties zich op onvervormbare skeletale elementen. Aangezien er 150 skeletale elementen in een model van de volledige staart zitten en de invloed van de vervormingen beperkt is, valt de extra computationele kost van vervormbare lichamen en contactproblemen tussen deze niet te verantwoorden.

Een selectie van de binnen het doctoraatsonderzoek uitgevoerde simulaties wordt besproken in de dissertatie. Zowel spierverkortingen als spierkrachten worden op de modellen losgelaten. De eerste zijn inverse dynamische simulaties, de tweede zijn voorwaartse dynamische simulaties. Zoals verwacht zorgt unilaterale activatie van de hypaxiale myomeerspieren voor gecombineerde ventro-laterale buiging, terwijl bilaterale activatie zorgt voor bijna puur ventrale buiging (de kleine afwijking is allicht een gevolg van kleine, natuurlijke asymmetrie in het referentiesegment).

Naast simulaties op staartbuigingen, die de flexibiliteit van de musculoskeletale structuur van de zeepaardstaart aantonen, zijn er ook simulaties uitgevoerd op de radiale sterkte van de staart. Vervormbare skeletale elementen worden tussen convergerende platen geplaatst, waarna de resulterende spanningen in het skelet worden geanalyseerd. De richels op de dermale platen blijken een belangrijke rol te spelen in het verhogen van de buigstijfheid van de vlakke delen van de dermale platen. Op zijn beurt is deze buigstijfheid van belang voor de radiale sterkte, aangezien spanningen bij de compressiesimulaties in belangrijke mate op deze richels

zijn terug te vinden.

Verschillende staartbewegingen worden geanalyseerd op basis van kinematische opmetingen. Het blijkt voorlopig echter moeilijk om algemene conclusies te trekken uit de kinematische analyses: de manier en snelheid van grijpen verschilt te sterk, zowel tussen de individuen onderling als tussen grijpbewegingen van eenzelfde exemplaar.

De toepassingsmogelijkheden van de inzichten volgend uit het bestuderen van de structuur van de zeepaardstaart worden uit de doeken gedaan in **Hoofdstuk 6**. Eerst worden twee soorten robotten besproken die gelijkaardige structuren uit de natuur imiteren: een robot geïnspireerd door de grijparmen van een octopus, en robotten die de articulatie van een reeks skeletale segmenten (van slangen en aalachtige vissen) imiteren. Deze bestaande robotten vormen een bron van inspiratie voor robotten die de staart van zeepaarden imiteren. Verschillende actuatoren die de spieren in de zeepaardstaart kunnen imiteren worden kritisch tegen het licht gehouden. De basis wordt gelegd voor enkele industriële ontwerpen geïnspireerd door de biomechanica van de zeepaardstaart, waaronder flexibele buizen met hoge radiale stijfheid en innovatieve, stuurbare katheders.

Tenslotte geeft **Hoofdstuk 7** een overzicht van de conclusies en mogelijke toekomstprojecten die kunnen verderbouwen op dit doctoraatsonderzoek.

English summary

Millions of years of evolutionary pressure have forced organisms to find suitable solutions for a whole range of real-world problems. Through evolution, small changes in functionality are tested on their fitness, efficiency, and robustness. Engineers are on a daily basis faced by the same problems. Consequently, engineers can find design inspiration in the solutions provided by nature, even for cutting-edge engineering applications.

One example of an organism that adapted to its environment in a very specific way is the seahorse. Most fish use undulatory locomotion: the body and tail perform lateral cyclic motions that propel the fish forward. A smaller amount of fish, including the seahorses, use fin undulation as main source of propulsion. These are usually fish that require high manoeuvrability at low speed. The tail of the seahorse has completely lost its function in locomotion: the animal relies on undulation of the dorsal and pectoral fins for propulsion.

The use of fin undulation conveniently renders the seahorse very manoeuvrable in its natural habitat of corals and seagrasses, but also turns it into a relatively slow swimmer. Therefore, seahorses are unlikely to escape any predatory fish. They survive by relying on crypsis: they move slowly, while their colours are often adapted to the environment. They also have an armour plating that covers the body and tail, which likely increases resilience against predatory bites. Despite the strong and stiff shielding, the seahorse tail is still sufficiently flexible to be used as a prehensile organ. With its tail the seahorse anchors itself to objects and vegetation on the seabed, as to avoid being carried away by strong currents, or to a partner during mating.

The combination of compressive stiffness and ventral bending flexibility is an interesting achievement of the seahorse tail, especially from an engineering point of view. Combining stiffness in one direction with flexibility in another is a common requirement in engineering designs, one that is often difficult to achieve. In this dissertation we therefore study the biomechanical structure of the seahorse tail. Acquiring profound insights in the mechanics involved will provide design inspiration for various engineering applications that require both flexibility and stiffness.

In **Chapter 1** some terms and principles that will be used throughout the dissertation are explained. Some attention is given to general facts about the seahorse, as to introduce the particularities of the animal. The chapter ends with the goals of the research and an overview of the dissertation.

Chapter 2 focusses on bio-inspired design. This principle is introduced by

means of some typical and historical examples. A bio-inspired design that is popular in recent decades, is the design of robotics that mimic the undulatory locomotion of fish. Some interesting examples are given to demonstrate the possible applications of such robotics. A logical application for an industrial designs inspired by the seahorse tail is a robotic that mimics the prehensile capabilities of the seahorse tail. Some robotic designs related to prehensile organs are therefore discussed at the end of the chapter.

One can only model the musculoskeletal structure of the seahorse tail after studying it. **Chapter 3** therefore focusses on the anatomy of the seahorse tail. The skeleton of the tail consists of roughly 30 segments of fairly uniform shape. The size of these segments decreases caudally, while the inclination of the segment increases. Each segment of the tail consists of a vertebra surrounded by four dermal plates (two ventral and two dorsal plates). There are longitudinally directed gliding joints between dermal plates of subsequent segments. The caudal spine of the proximal plate fits nicely into a groove in the next segment of the chain. This limits the gliding directions greatly, while also rotations are limited due to the tight fit. Gliding joints can also be found between the dermal plates of the same segment. These joints are rather flexible, with a main gliding direction along the line that connects the centres of mass of the dermal plates involved in the joint formation.

The vertebra has three spines that extend in ventral direction (hemal spine) and lateral directions (transverse spines). The tip of these spines form joints with the closest dermal plates. These joints can be considered to behave like ball-and-socket joints: rotations are rather free, while translations are limited in all directions due to the shape of the skeletal elements and the surrounding connective tissues.

Between the vertebrae is a joint consisting of the remnants of the notochord, over which the concave surfaces of the vertebrae can glide. The result is a rather flexible joint that in principle can both glide and rotate. However, the incompressibility of the fluid limits the compression of both vertebrae.

The muscle structure of the trunk and tail of fish is rather complex. The bulk of the tail muscles are myomere muscles. These muscles consist of layers of collagenous sheets, called myosepta, connected by myomere muscle fibres. This structure of alternating myosepta and muscle fibres is folded into complex shapes. Most often the shape includes longitudinally directed cones, which likely store energy and increase body stiffness during muscle contraction.The epaxial myomere muscles (on the dorsal side) of the seahorse tail still have this structure, which is typical for fish that use undulatory locomotion, but the hypaxial myomere muscles (ventral side) show a very different structure. The conical structure is replaced by a more or less parallel structure, causing the hypaxial myomere muscles to span up to eight segments. This structure could be an adaptation of the seahorse tail to its differing function (prehensile function versus locomotory function for most other fish). The hypaxial muscles can be found on both lateral sides of the fish tail, and can therefore contribute to both ventral bending (upon bilateral contraction) and combined ventro-lateral bending (upon unilateral contraction).

Another type of muscles that are involved in tail bending are the median ventral

muscles. These muscles are located on the midsagittal plane. Consequently, they can only cause pure ventral bending upon contracting. The cross-sectional area of these muscles is much lower than that of the myomere muscles, so they are less likely to generate high forces.

The passive extensibility of the myomere muscles (both hypaxial and epaxial) was estimated based on uniaxial tensile tests on the muscles of a seahorse specimen, species *Hippocampus reidi*. The contralateral counterparts of the tested muscles were used in histological studies. The histological cuts were used to get a good estimate of the cross-sectional area of the muscles. The difference between the extensibility of the epaxial and hypaxial muscles proved to be very high. Even after taking the difference in cross-sectional area into account, the extensibility of the epaxial muscles was an order of magnitude smaller than that of the hypaxial muscles. The longer myosepta of the hypaxial muscles likely play an important role in the measured difference, though damaging of the connection between fibres and myosepta of the epaxial myomere muscles currently cannot be excluded. The passive response of the muscles could nicely be approximated by exponential curves. By measuring the cross-sectional area of the muscles throughout the tail on high-resolution synchrotron scans, the extensibility of all muscles can be derived, if the extensibility is assumed to be proportional to the cross-sectional area.

Based on the anatomical study of the seahorse tail, a biomechanical model can be constructed. The details about the model construction are discussed in **Chapter 4**. The chapter commences with the introduction of some important terms and modelling techniques frequently used in biomechanics. An overview of scientific publications focussing on biomechanics in biology is provided as well.

Dedicated pyFormex scripts are used to generate models based on the detailed reconstruction of one reference segment of a stretched tail. The other 29 segments are derived by appropriate translation, scaling, and inclination. To determine the position of the joints and attachment points of the muscles, algorithms implemented in pyFormex are used. Those algorithms use the so-called *shape index* of the surface meshes of the skeletal elements to detect the position of several landmarks, so that the reference segment can easily be replaced by a simplified geometry that contains all dynamically relevant features of the realistic geometry.

The chapter ends with a discussion on the material model that is used for the deformable bony elements, as well as a discussion on the resting position of the tail. This is the position of the tail when all muscles are in rest. Measurements on anaesthetized seahorses showed large variability in resting position of the tail, both between specimens and for the same specimen. Small changes in tail position can manually be applied without the tail moving back to its previous position. One typical position of the resting position of the tail was digitized and used as starting position of several simulations.

After discussing the techniques used to generate the models in Chapter 4, the focus switches to the results of the simulations in **Chapter 5**. The models are solved using Abaqus 6.12, because this allows us to easily combine rigid and deformable bodies in the same simulations. The simulations on deformable bodies indicated that after normal amounts of bending, and in the absence of external

forces, the deformations are negligibly small. Since the full tail model consists of 150 of these skeletal elements, the additional computational cost that comes with calculating deformations cannot be justified by the minor increase in accuracy. Most simulations will therefore use only rigid elements.

A selection of the simulations that were performed during the doctoral research is discussed in the dissertation. Simulations can use both muscle shortening and muscle forces as input. In the first case, the simulations are inverse dynamics simulations, the latter are forward dynamics simulations. The unilateral muscle activation of the hypaxial myomere muscles results in combined ventro-lateral tail bending, while bilateral activation causes pure ventral bending (although small asymmetries in the reference segments can cause some insignificant lateral bending as well).

Besides tail bending simulations, which demonstrate the flexibility of the musculoskeletal structure of the seahorse tail, some simulations also included compression of the tail skeleton. Deformable skeletal elements are placed between converging plates. The resulting stresses are analysed and indicate that the ridges on the dermal plate play an important role in improving the bending stiffness of the dermal plates and by extension the compressive stiffness of the seahorse tail skeleton.

Several tail movements were analysed by kinematic analysis. These preliminary kinematic analyses did not allow us to draw general conclusions, as variability of the measurements was high, both between individuals and between measurements on the same individual.

The possible applications derived from the study of the biomechanics of the seahorse tail are discussed in **Chapter 6**. Two robotics that are closely related to the tail movement are discussed: a robot inspired by the arms of an octopus, and robots mimicking the articulation of a chain of skeletal elements (of snakes and anguilliform swimming fish). These robotics can be a starting point in the development of a robotic arm that mimics the grasping functionality of the seahorse tail. Several biomimetic actuators that can be used in such robotics are discussed. These actuators can mimic the function of the tail muscles. Robots developed in this way cannot only be used as versatile grasping robotics, but can also provide more valuable input on the biomechanics of the tail.

A conceptual for a flexible tube inspired by the seahorse tail is presented, as well as the basics for an innovative steerable catheter design. Other interesting designs that can use the biomechanics of the seahorse tail as a source of inspiration, like flexible stents and protective clothing for extreme sports, are discussed as well.

Finally, **Chapter 7** provides an overview of the conclusions and possible research opportunities that can build on the methods that were developed within the doctoral research.

1 Introduction

1.1 Background

In engineering, optimizing a design often involves finding an appropriate balance between functional requirements. For example, the chassis of a car needs to be very strong (to withstand all forces during driving), which usually means using lots of stiff and heavy materials, and yet it also needs to be very light (to minimize fuel consumption and braking distance), which requires the use of as little (and preferably light) material as possible. Finding a good trade-off between such conflicting requirements is one of the biggest challenges within the engineering field.

One particularly challenging combination of requirements is combining high flexibility in a certain direction with high stiffness in another. As an example, one can think of the steel cables of an elevator. These cables need to be very strong in the longitudinal direction, as to cope with the weight of the elevator cage and the counter weight, as well as very stiff, so that the elevator doesn't bounce up and down like a bungee cord when halting at a certain floor. At the same time, these cables need to be very flexible in bending, so that they can easily be wound around the pulley.

Another example of a device that needs to combine stiffness with flexibility, and that is more closely related to the biomedical engineering field, is the flexible stent, which is frequently used to treat vascular disease in the lower extremities. Usually, this kind of stent is placed in the superficial *femoral* and *popliteal* arteries

(these are arteries respectively located at the the medial side of the thigh and near the knee joint), which are prone to harsh loading conditions. The flexible stent needs to have a high radial stiffness, as to fulfil its main function: keeping the artery open for sufficient blood flow. On the other hand, bending flexibility needs to be high as well in these stents, as deformation of the superficial femoral and popliteal arteries can be high due to joint motion.

When looking at designing devices that need to incorporate high radial stiffness and high bending flexibility, one can first take a look at how nature managed to efficiently combine these important mechanical characteristics, instead of trying to reinvent the wheel. Doing so, our eye fell upon the specialized musculoskeletal structure of the seahorse tail. This complicated structure of articulating bony elements manages to efficiently combine high compressive stiffness (as a result of an armour plating that covers the tail) with extreme bending flexibility. This bending flexibility turns the tail into a conspicuously versatile tentacle: the tail can be used as a prehensile organ to hold on to a mate or to objects on the sea floor. In this way, the slow swimming seahorse can avoid being carried away by the strong sea currents [1–6]. Figure 1.1 demonstrates how a seahorse uses this flexibility of the tail to hold on to a horizontal dowel.

Figure 1.1: A seahorse (species Hippocampus barbouri) wraps its flexible tail around a horizontal cylinder. Courtesy of A. Dimou and D. Mitsa (Evolutionary Morphology of Vertebrates).

Given that certain applications like flexible stent design require high radial stiffness and bending flexibility, and that the seahorse tail already effectively combines both, this dissertation will study the biomechanics responsible for allowing such a usually conflicting combination of mechanical properties. Profound insights in the flexible structure of the seahorse tail can lead to design inspiration in several engineering fields, including biomedical engineering, civil engineering, and mechanical engineering.

1.2 Terminology

Throughout the dissertation, anatomical directions (Figure 1.2) and reference planes (Figure 1.3) will be used with their respective terms to indicate position and direction of anatomical features. Note that for fish, the anterior end, rostral end, and cranial end are equivalent. Likewise, the terms posterior and caudal end are interchangeable.

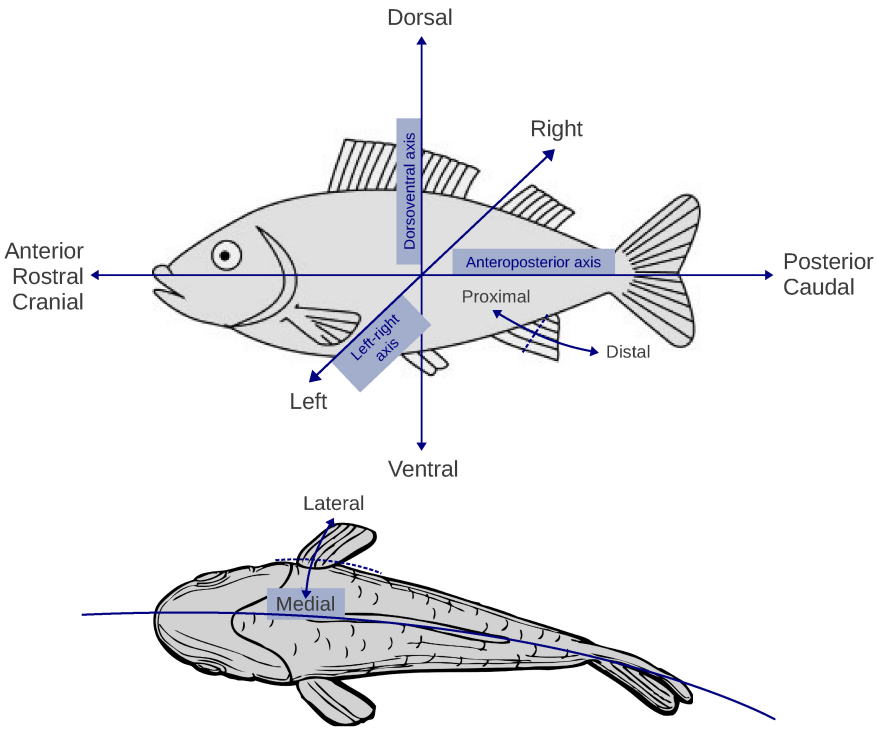

Figure 1.2: Anatomical directions in a fish.

The terms *proximal* and *distal* respectively indicate positions closer and further away from the centre of the fish or closer and further away from the base of an

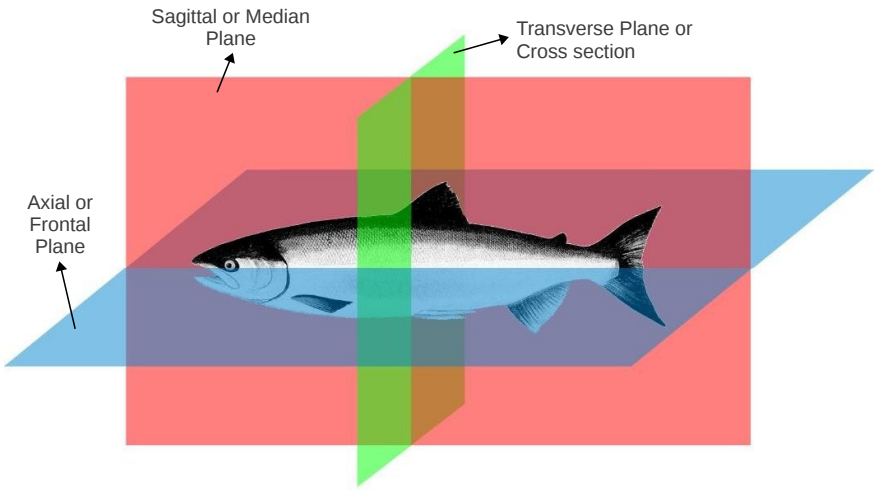

Figure 1.3: Anatomical planes in a fish (fish drawing from [7]).

appendage to the body. In Figure 1.2 this is demonstrated on the anal fin of the fish. Specifically for an entire seahorse tail, proximal should be interpreted as closer to the tail base (the part of the tail that connects to the rest of the body), while distal is closer to the tail tip. The anteroposterior axis indicated in Figure 1.2 is sometimes called the longitudinal axes, since this axis is usually the longest in fish.

When a sagittal plane (indicated in Figure 1.3) is located in the middle of the fish (and thus cuts the fish into equally sized left en right sides), it is called the *mid-sagittal* plane.

The appropriate names of the fish fins are indicated in Figure 1.4. Keep in mind that the body plans of different fish species can be profoundly different, so not all fish will have all the fins indicated in the illustration. In the seahorse for example, only the dorsal fins, pectoral fins, and sometimes anal fins are present. Especially the absence of the caudal fin is very uncommon for fish.

1.3 The remarkable seahorse

Few animals can capture human imagination like the seahorse. All seahorses are teleosts belonging to the genus *Hippocampus*. At first glance, however, it looks nothing like other teleosts (Figure1.5):

- The seahorse swims and feeds in an upright posture [1, 8–10]
- The caudal fin, pelvic fin, and adipose fin are absent

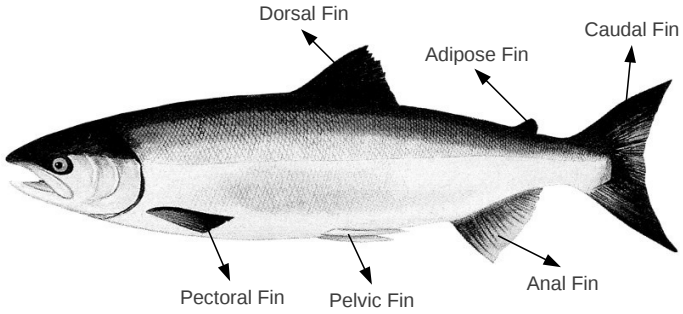

Figure 1.4: The different fins that can be found on a fish (fish drawing from [7]).

- The body is covered with rectangular bony plates (armour plating) instead of scales [2, 11]
- The head makes a 90 degree angle with the rest of the body [1]
- The tail is long and extremely flexible in a ventral direction [11]
- The snout is usually narrow and long, as the seahorse uses specialized suction feeding

The strange shape of the head and snout give the seahorse a distinct, horse-like appearance, hence its name. Seahorses belong to the Syngnathidae, a family that also includes the pipefishes, pipehorses and seadragons, and pigmy pipehorses (grouped in the subfamily Syngnathinae) [8, 12]. An overview of the taxonomy of the seahorse and some closely related branches is given in Table 1.1. Keep in mind, however, that the exact classification of the seahorse and some of its relatives is still under debate, so the presented taxonomy is by no means final.

Two genera that are very closely related to the seahorses are the *Idiotropiscis* and the *Histiogamphelus*. The first genus comprises the pygmy pipehorses, a sister taxon of the seahorses [9]. The latter genus consists of crested pipefishes. Figure 1.6a shows an example of the *Idiotropiscis* genus, namely the Sydney's pygmy pipehorse (*Idiotropiscis lumnitzeri*), whereas Figure 1.6b shows an example of the *Histiogamphelus* genus, namely the Brigg's crested pipefish (*Histiogamphelus briggsii*). Figure 1.6 also illustrates two other species of the Syngnathinae: the lesser pipefish or *Syngnathus rostellatus* (Figure1.6c), and the leafy seadragon or *Phycodurus eques* (Figure 1.6d). It can be clear that, just like seahorses themselves, the close relatives of the seahorse come in many shapes, sizes, and colours.

The genus *Hippocampus* itself comprises 47 different species, although this number changes frequently as new species are being identified. Moreover, it is often difficult to recognize seahorses of the same species, as some species change

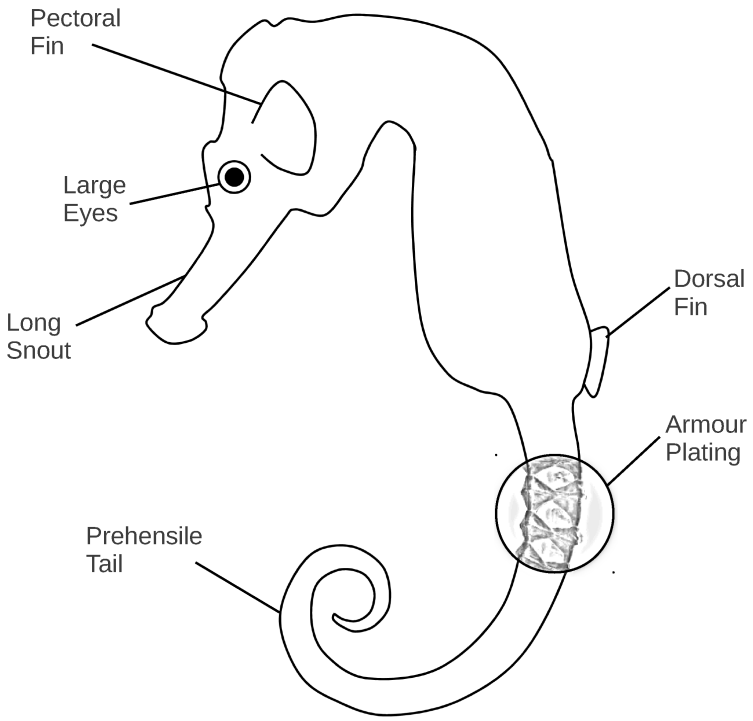

Figure 1.5: Characteristic posture of the seahorse.

colour and grow skin filaments to blend in with their specific environments [17,18], so members of the same species can sometimes look conspicuously different.

Seahorse species can be found worldwide in shallow tropical and temperate waters, mostly in coral reefs or eel grass beds. As the seahorse's habitat is close to the shore, pollution and overfishing have raged havoc under the population of many seahorse species [17,19]. In 2012, the IUCN (International Union for Conservation of Nature) Red List of Threatened Species categorized one seahorse species as *endangered*, seven as *vulnerable*, one as *least concern*, and 29 as *data deficient* [20]. All species are listed in the appendices of the Endangered species of wild fauna and flora (CITES) [17], meaning that all import and export of seahorses within the European Union is subjected to very strict regulations.

Seahorses are planktivorous[1]. They use their angled head to capture highly evasive prey like small shrimps or larval fishes. Surprisingly rapid upward rotation of the head combined with high speed suction (thanks to the long snout) allows the seahorse to rapidly position the mouth opening near the prey and suck it in, leaving it very little time to escape [1].

[1] Planktivorous animals are animals that eat or consume plankton.

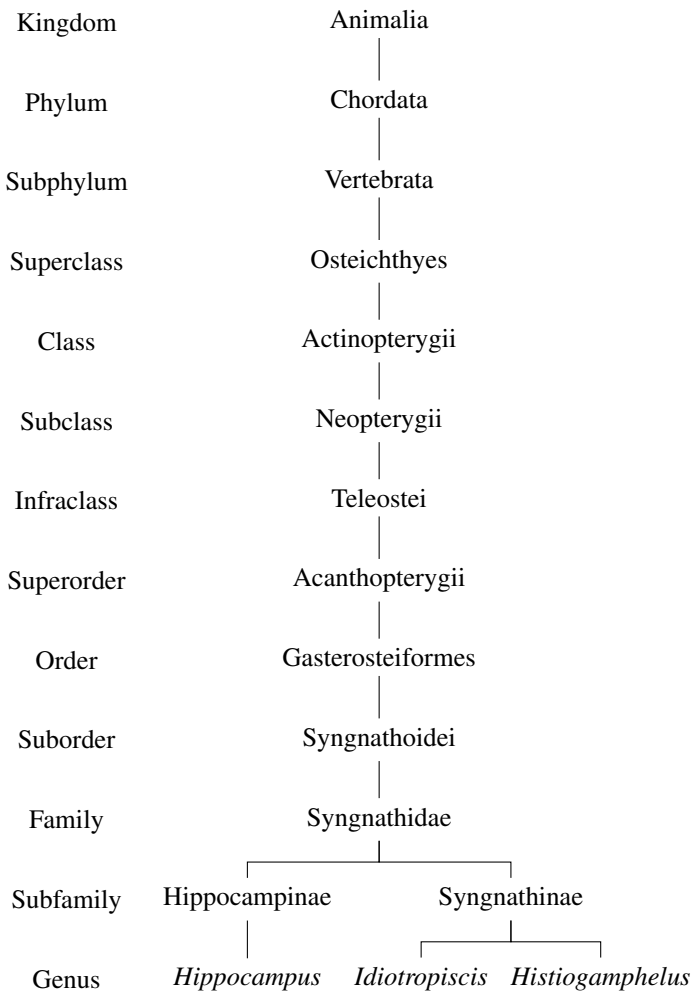

Table 1.1: Taxonomy of the seahorse and some relatives according to fishbase.org (based on the Catalog of Fishes and ITIS).

Seahorses are well-known for their remarkable parental care, as most seahorse species are socially monogamous. A truly unique feature of the seahorse is that the male will bear the unborn young [21]. During the courting, which takes place for several days, the tails of the male and female get entangled. The female seahorse places her eggs in the brood pouch on the belly of the male (Figure 1.5), after which he will fertilize them. After the eggs have hatched in the pouch, the male seahorse releases the fully developed young (up to several hundreds of them) into

(a) Sydney's pygmy pipehorse [13]

(b) Brigg's crested pipefish [14]

(c) Lesser pipefish [15]

(d) Leafy seadragon [16]

Figure 1.6: Examples of some close relatives of the seahorse, demonstrating the remarkable differences in appearance.

the open sea.

1.4 Aim of the doctoral research

The goal of the research is to provide a versatile and robust framework to perform multibody dynamics simulations on the biomechanics[2] of the complex musculoskeletal structure of the seahorse tail. This framework should allow the testing of specific biological hypotheses on the musculoskeletal system of the tail of various seahorse species (e.g. is the shape of the segments optimized to minimize energy requirements upon ventral tail bending?). Moreover, the biomechanical simulations should provide insights in how compressive stiffness can effectively be combined with bending flexibility, so that industrial designs in several engineering fields could benefit from the findings. A comprehensive figure of the doctoral

[2]Biomechanics is the study of the structure and function of biological systems by means of the methods of mechanics (definition by Hatze [22]). So basically biomechanics is mechanics applied to various systems found in nature. It addresses forces and displacements in and on biological bodies (humans, animals, plants, cells, organs, ...), as well as the resulting deformations, often by applying typical engineering techniques to the biological and medical field.

research is provided in Figure 1.7.

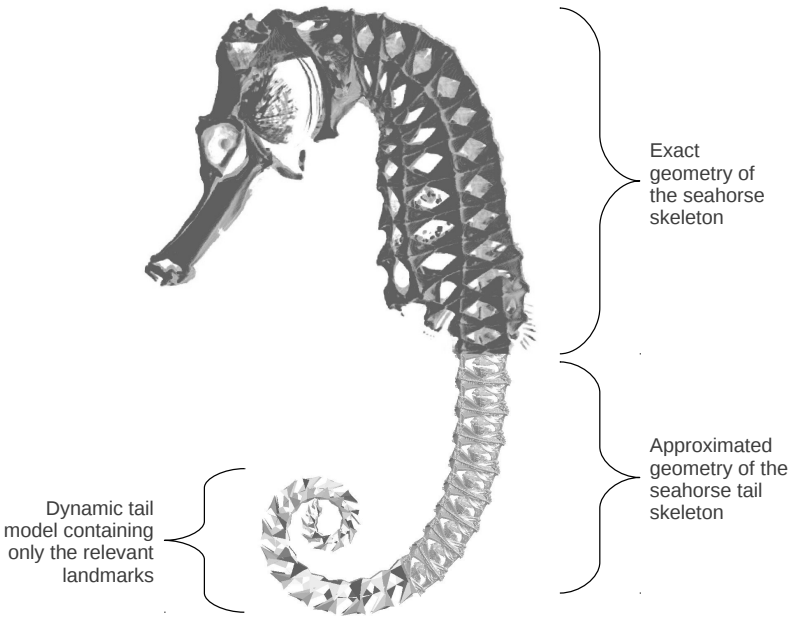

Figure 1.7: From tail anatomy to tail model. The seahorse skeleton is segmented from high resolution μCT-scans. The segmented geometry of one tail segment is then used to generate approximate geometries of the other segments, while taking into account geometric transformations. A simplified geometry that only contains the tail skeleton features that are relevant for dynamic analyses is thereafter generated from this realistic geometry.

1.5 Outline of the dissertation

The dissertation is organized as follows:

- Chapter 1: Introduction

  The first chapter is dedicated to some introducing words about this dissertation. The idea behind this dissertation is discussed, as well as its relevance. Thereafter, some important terminologies are explained. The seahorse is introduced by its taxonomy and some general facts about the species are discussed. Finally, the first chapter is concluded by explaining the aim of the research and the outline of the dissertation.

- Chapter 2: Bio-inspired design

  Nature is a widely regarded source of inspiration for a large range of designs. Such designs that are related to designs found in nature are called

bio-inspired designs. Studying nature as a source of design inspiration is often called biomimicry. Although the principle of biomimicry itself is very old, biomimicry and bio-inspired design are getting a renewed interest the past decades. Therefore a short overview of biomimicry in recent and not so recent times is given, so that the reader can get an idea of the large possibilities of applications that derive from this multidisciplinary field in science and engineering.

- Chapter 3: Seahorse tail anatomy

  To understand the biomechanics of the seahorse tail, it is vital to understand its anatomy. Given the quite unique locomotion of the seahorse, and therefore the unique function of its tail, it comes as no surprise that the anatomy of the tail is at several points profoundly different than that of most other fish. Because of this unique build-up of the seahorse tail, some important details of its musculoskeletal structure are lacking in literature. Especially the structure of the musculature of the tail is sparsely documented. Based on high resolution synchrotron scans and tensile testing of some muscles of the seahorse tail, more details on the function and structure of the seahorse tail muscles is derived. Besides the musculature, the skeletal structure is discussed, as well as the joints that link the skeletal elements together.

- Chapter 4: Modelling

  The philosophy behind the constructed models is explained in Chapter 4, as well as how the models are generated using pyFormex. The modelling techniques used are not the most common ones in biomechanics, partially because of the unique structure of the tail (with a particularly large amount of joints and muscles), partially because the model construction was deliberately kept very flexible. Where possible, comparisons are made with modelling techniques in literature. The automated landmark detection and parametric model construction are discussed elaborately.

- Chapter 5: Simulations

  Results of the simulations are discussed in Chapter 5. Simulations included rigid body analyses and finite element analyses. Both the bending flexibility and the radial stiffness are simulated and discussed. To conclude this chapter, the most important limitations of the model and the modelling techniques are discussed.

- Chapter 6: Applications inspired by the seahorse tail

  Possible applications based on the specialized musculoskeletal structure of the seahorse tail are discussed in Chapter 6. Some applications are worked out, others are merely mentioned.

- Chapter 7: Conclusions and perspectives

  Finally, in Chapter 7 conclusions that can be derived from the doctoral research and perspectives to future research that can build on this doctoral research will be discussed.

2
Bio-inspired design

2.1 Introduction

This chapter presents the basic principles of bio-inspired design, as well as some typical examples of bio-inspired design. Extra attention will be given to the examples that are somewhat related to the designs inspired by the seahorse tail. The field of bio-inspired design is extremely wide. This chapter can therefore not cover all aspects of it, and definitely not all research within the field. Hopefully this short overview can, however, provide a short introduction to the reader and tickle his or her interest in nature's designs.

2.2 Biomimicry

Biomimicry or **biomimetics** is a term derived from the ancient Greek words *bios*, meaning life, and *mimesis*, meaning to imitate. Biomimicry thus means studying nature's principles (systems, processes, models, and elements) to emulate or take inspiration from in order to solve human problems. It is therefore closely related to bio-inspired design.

Although the principle of biomimicry itself is as old as human problem solving itself, the term biomimetics and the scientific interest in it is relatively new. Biologically inspired design is rapidly gaining importance as a wide-spread movement in design for environmentally conscious sustainable development [23], as is also evident by the growing amount of websites dedicated to biomimicry and biomime-

tics (www.biomimicryinstitute.org, www.biomimicry.net, www.asknature.org, ...).

Biomimicry is a new way of viewing and valuing nature and its designs. It focuses on what we can learn from nature, rather than what we can extract from it. The latter being the approach that we used for far too long. In fact, centuries of inconsiderate extracting from nature currently limits what we can learn from it, e.g. because many interesting organisms are now extinct as a result of direct or indirect human intervention, or will be extinct before we can take a thorough look at them.

The core idea behind biomimicry is that billions of years of selective pressure have effectively forced organisms (animals, plants, and microbes) to become consummate engineers. Evolution has found what works, what is efficient, what is important, what is robust, what lasts in the specific environments imposed upon the organisms. The solutions that evolution came up with are solutions to the same real-world problems that are often faced by modern engineering. As such, one can look at nature's solutions to ones problems instead of trying to reinvent the wheel. In this way, engineers can consider nature to be the single largest database of field-tested solutions to a whole range of real-world problems.

It is important to note that the designs provided by nature are optimized, yet not necessarily optimal. In other words, the solutions provided by nature are good solutions, but not always the best possible solutions that can be imagined. This is because adaptive evolution is constrained by several processes. One constraint is that adaptive evolution works in relatively small steps, where each intermediate state of the organism during evolution must be viable and have some fitness to its environment. Resulting from this constraint is the so-called *phylogenetic*[1] *constraint*: components of the phylogenetic history of a certain species can prevent or slow down anticipated adaptations [24]. In simpler words, the way that the ancestors of a certain species developed may have led them in the (currently) wrong direction, preventing certain logical adaptations. Figure 2.1 further clarifies this principle.

Another constraint is the fact that natural selection can be slow. So if the environmental conditions change fast enough, the organism may not be perfectly adapted to it.

Other constraints are genetic constraints. For example, specific genes can have an influence on many characteristics of the organism. So optimizing such gene for a specific functionality can be detrimental for another functionality, thus preventing or slowing down this optimization. When a *heterozygote* has a higher fitness than either *homozygote*[2], another genetic constraint occurs: as homozygotes will

[1] Phylogenetics is the study of evolutionary relationships among groups of organisms which are discovered through molecular sequencing data and morphological data.

[2] An organism is a homozygote at a specific locus when it has two identical genes on the two corresponding homologous chromosomes, and heterozygote when it has two different genes on the corre-

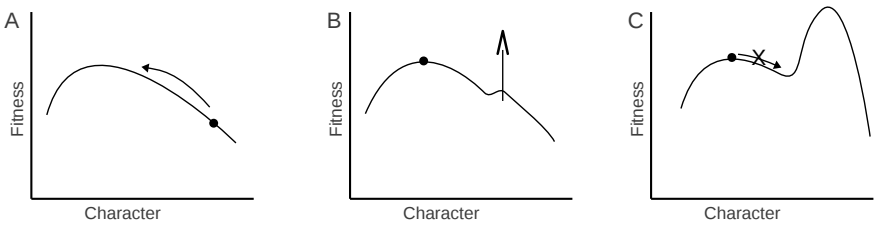

Figure 2.1: The principle of phylogenetic constraints: at a certain point in history a certain trait of a certain organism is becoming perfectly adapted (A). As the environment changes, another adaptation could gradually become more advantages (B to C), but the organism cannot achieve this adaptation because it would have to go through intermediate stages that have a poor fitness to the environment.

always exist, the population as a whole will never be completely adapted.

Whatever the exact process that guides the constraint, it should be kept in mind that the solutions provided by nature have limitations that can prevent them from being the best possible solutions.

2.3 Archetypical examples of bio-inspired design

Although biomimicry is a relatively modern term, examples of biomimicry and bio-inspired design can be found throughout the centuries of human development. Some important, ground-braking, or just eye-catching examples of biomimicry are listed in this section, so that the reader can get an idea of the extensiveness and multidisciplinarity of biomimicry in recent and not so recent times.

2.3.1 Biomimicry throughout history

One of the earliest famous examples of biomimicry is *the fall of Icarus*, a popular legend in Greek mythology (Figure 2.2). The legend tells about Icarus, who tries to escape from Crete. With the help of his father, he tries to mimic the flight of birds by binding a wing-like structure made of feathers and wax to his back. Ignoring warnings not to fly too close to the sun, the wax of the wings melts, causing Icarus to fall into the sea and towards his doom, as he drowns in the vastness of the sea. The tale is not much more than an example of failed ambition, but it does show that the ancient Greek already looked at nature and tried to learn from it, or at the very least mimic it.

The most famous pioneer of biomimicry is probably Leonardo Da Vinci (*April 15 1452, †May 2 1519). Not unlike biomimicry itself, Da Vinci was a polymath: he was a painter, musician, sculptor, scientist, engineer, inventor, and much more.

sponding chromosomes.

Figure 2.2: The fall of Icarus, painting by Peter Paul Rubens, 1636 [25].

A surprising amount of Da Vinci's sketches and designs were inspired by nature's designs. Just like the Icarus myth, Leonardo Da Vinci was obsessed by flying. Indeed, the ability to soar through the skies is one of nature's greatest accomplishments that has always caught the human imagination. Figure 2.3 shows one of Da Vinci's many designs of a flying machine. None of these machines made it to the skies in his lifetime, nonetheless flying animals have remained a major source of inspiration for advancing technologies.

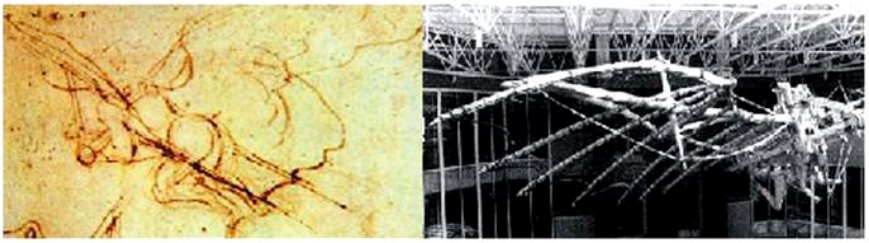

Figure 2.3: Sketch of one of Da Vinci's flying machines (left) and a model of his original drawings at the University of Limerick (right) [26].

One of the most famous and successful examples of biomimicry is the hook-and-loop fastener (more broadly known under the brand name *Velcro*). This fastener was invented by the Swiss engineer George de Mestral in the 1940s after noticing the burdock burs (sticky seeds) sticking to his clothes and his dog's fur after a hunting trip (Figure 2.4). He inspected them under a microscope and discovered that the small hooks at the ends of the burs caught onto the loops formed by textiles and fur. De Mestral mechanised the manufacturing of the hook-and-loop fastener and became a pioneer in biomimicry. To this day the hook-and-loop fastener is still a very popular system for reversibly binding two surfaces to each other.

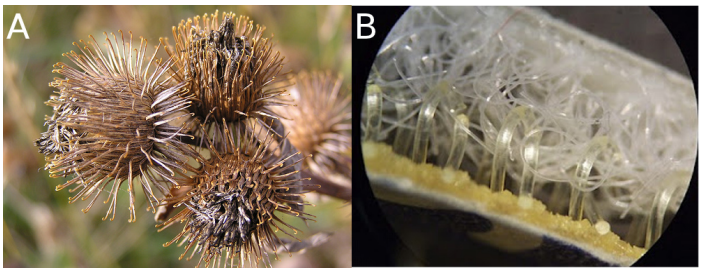

Figure 2.4: Burs (A) as a source of inspiration for the hook-and-loop fastener (B) [27].

Another famous example, more closely related to the engineering field, is the Eastgate Centre in Harare (Zimbabwe). This building uses the same passive cooling principles as a termite mound (Figure 2.5). Cold fresh air is sucked in near the ground while hot stale air is released at higher levels, using natural convection currents.

Figure 2.5: The passive cooling system of the Eastgate Centre in Harare is inspired by termite mounds [28].

2.3.2 Biomimicry in modern engineering applications

As stated in the introduction, biomimicry is gaining popularity in recent decennia, even for advanced engineering applications. Some more advanced examples of modern engineering are therefore cited in this section. This is merely a very short overview, as any attempt to list all current research and applications in the field of biomimicry is bound to fail.

Nature can sometimes come to remarkable results after long periods of trial and error. One example is how large groups of animals (swarms) behave in an efficient way. They need to move efficiently to common goals while avoiding collisions

and congestion. Studying these phenomena can for example teach us principles that can aid in better and more efficient traffic regulation [29].

Efficient power generation from natural resources like wind is currently a hot topic. As wind speeds decrease, the efficiency of wind turbines typically decreases dramatically. A common solution is to increase the angle of attack[3] of the turbine blades at low wind speeds. Sadly, stalling (turbulent flow over the blade) tends to occur at the blades when the angle of attack becomes too large. Stalling drastically reduces the power generation, causes instability, and is a major source of noise. To reduce stalling of the blades, engineers looked at geometry of the flippers of humpback whales and other marine mammals, which are equipped with tubercles (small round shapes, Figure 2.6 A) to reduce stalling at low speeds (Figure 2.6 C) [30]. The humpback whales are very aerodynamic, despite their enormous size (12 to 16 meters in length), partially thanks to the specialized design of their flippers. The principle of tubercles is currently used on some advanced turbine blades to increase power generation efficiency at low wind speeds and to reduce noise pollution (Figure 2.6 B) [26].

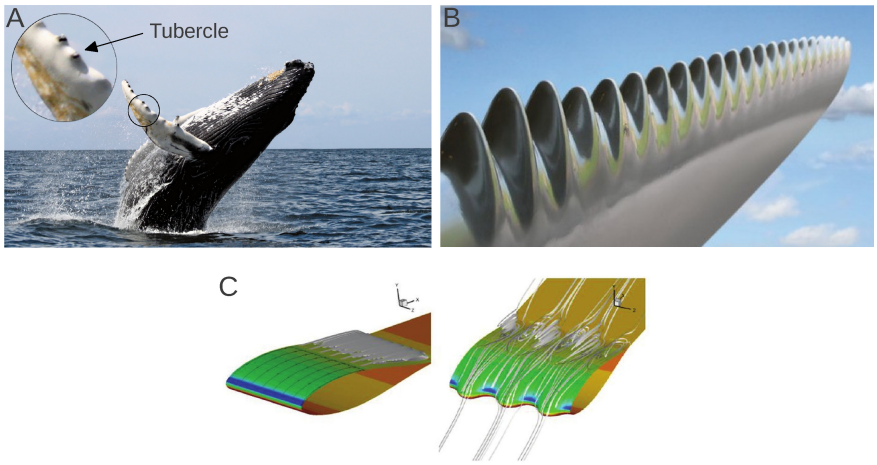

Figure 2.6: The geometry of the flippers of the humpback whale (A) [31] inspired the design of efficient wind turbine blades (B) [32]. The improvement in efficiency at low speeds is illustrated by simulated surface pressure contours and streamlines at a 10° *angle of attack, without and with tubercles (C) [30].*

Changing the properties of surfaces is another major challenge that is often countered by applying principles from nature. Nature-inspired surfaces range from adhesive surfaces inspired by the sticky gecko feet [33], to water repellent, self-cleaning surfaces inspired by the lotus plant [34].

[3]The of attack of the windmill's blades is the angle between the blades and the flow direction of the wind.

In Japan, very fast, so-called bullet trains have been around for several decennia. These trains can easily obtain speeds over 300 km/h, so fast that the bullet shape of the nose of the train was starting to be an issue. As the train was going through the numerous Japanese tunnels, a cushion of air builds up in front of the train. When exiting the tunnels, these air cushions suddenly expanded, causing a loud booming noise that quickly became a nuisance to local residents. One of the engineers working on solving this problem was a bird watcher. He noticed that the kingfisher (a brightly coloured bird in the order Coraciiformes) dove into water at high speeds while creating very little splash. In the late nineties, he therefore designed the tip of the bullet train like the sharp beak of the kingfisher (Figure 2.7), effectively solving the problem of the sound pollution at tunnel exits, and significantly reducing power consumption of the train.

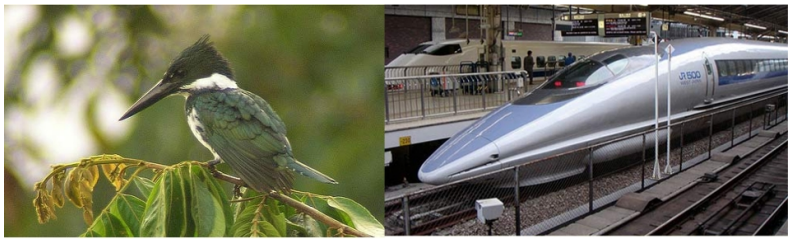

Figure 2.7: The shape of the kingfisher's head was used to design the nosecone of Japanese bullet trains [35].

Creating robotics that mimic flying animals is currently very popular. Flying robots have a lot of possible applications, as they reach places that humans can't (because of difficult position or hazardous environment). Flying robots can be inspired by flying insects [36–38], birds, and other flying animals. These robotics have the advantage that they can be small, efficient, and manoeuvrable.

Sometimes biomimicry can be found in less obvious areas of engineering. Efficient algorithms have been developed for continuous optimization problems of engineering design [39], and principles of certain enzymes are mimicked for improved catalysis [40].

2.4 Robotic designs inspired by animal locomotion

Some of the most obvious bio-inspired designs are robotic designs that mimic animal locomotion. Therefore, this section and the next will focus on such bio-inspired robots. This dissertation focusses on the musculoskeletal system of the seahorse tail, and possible industrial designs (including robotics) that can benefit from it. The seahorse tail is a prehensile appendage, yet robotic designs inspired by prehensile appendages are scarce. Robotic designs inspired by animal locomo-

tion are much more abundant. Moreover, actuators and control systems used in robotics that mimic animal locomotion are not so different than those that mimic prehensile appendages of animals. Consequently, this section will focus on the robotic designs inspired by animal locomotion, with special attention to robotics inspired by fish locomotion, because the seahorse essentially uses the same tail muscles as fish that use undulatory locomotion. The next section will then focus on the group of robotics inspired by prehensile organs.

Locomotion is the ability of a system to produce net displacement through internal shape changes and through interactions with the external world. *Animal locomotion* is therefore the ability of an animal to change its three-dimensional position in space from point A to point B. Animal locomotion can consist of walking, running, creeping, flying, swimming, burrowing, etcetera. In each of these cases the locomotion occurs through some sort of contact with the surrounding medium, be it air, soil, water, ice, or other. The animal uses muscle forces to obtain geometric changes of (parts of) the body, which in turn exert forces on the surroundings. Given Newton's third law of motion (the action-reaction principle), the surroundings exert opposite reaction forces on the animal, propelling it in a certain direction.

The wide range of locomotion mechanisms used by animals is stunning. Many animal species have developed strikingly different ways to interact with their physical environment, even if that physical environment itself is not so different. For example, both a camel and a snake move through the sandy desert, but each in a very different way. The camel walks on the sand with large cushions on its feet that impact the sand at each stride, while the snake uses lateral waves that propel the animal forward.

These very different and yet efficient ways of locomotion are an enormous source of inspiration for robot designers. In the early days, locomotion robots were equipped with conventional industrial manipulators, which are essentially discrete multibody systems. But as robots became more complex, and efficiency and flexibility became more important, engineers and designers turned to nature for design inspiration. Consequently, robot designs shifted from conventional discrete mechanisms to hyper-redundant continuous mechanisms[4]. This caused a dramatic increase in bodies, actuators, and internal degrees of freedom, necessitating novel modelling techniques and advanced control mechanisms. These control mechanisms require small controllers with relatively high computing power. The popularity in the last decades of robotics that mimic the locomotion of animals is therefore closely related to the availability of such cost-effective high-speed controllers.

[4]Hyper-redundant systems can obtain certain motions with more than just one activation pattern of the actuators, meaning that the system has more actuators than strictly required for the motion.

2.4.1 Bio-inspired fish robots

The last decade, several research groups have been focussing specifically on the locomotion of fish to develop swimming robots [41–51]. Through evolutionary pressure, fish have developed very efficient ways of swimming. Therefore, swimming robots that mimic the way that fish swim have the potential for very high efficiency. Also, mimicking the motion of fish for propulsion has the potential of propelling water vehicles in a way that is less noisy and less lethal for fish than the use of regular propellers.

The robot fish come in a variety of shapes and sizes, and mimic several swimming modes. The swimming modes of fish are explained in more detail in Chapter 3.1.1.1. There are fish robots that mimic thunniform swimming [43,44,47,50], e.g. the fish robot demonstrated in Figure 2.8. This kind of robot only uses lateral swinging of the caudal fin for propulsion.

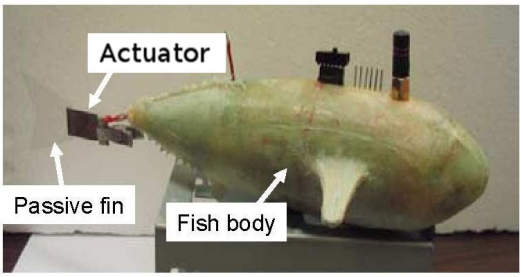

Figure 2.8: Tunniform fish robot, developed by Chen et al. [47].

Other fish robots mimic carangiform swimming [41, 48]. One example is demonstrated in Figure 2.9. Notice that the part of the tail that can move is much larger. Propulsion of the fish is achieved by lateral movement of the caudal fin, as well as some undulating movement of the rest of the tail.

Figure 2.9: Carangiform fish robots swimming in an aquarium, developed by Yu et al. [41].

The last swimming form is the anguilliform swimming. Since the whole fish body is undulating in this swimming form, a lot of actuators are needed to mimic this swimming mode with robotics. Moreover, controlling and steering these kind of robotics requires complex controllers that use complex algorithms. Because of that, few anguilliform swimming robots are described in literature [42, 46]. One such anguilliform swimming robot is demonstrated in Figure 2.10. The full-body undulation of the anguilliform robots has an additional advantage: with some minor adjustments these robotics can be used for locomotion on land as well.

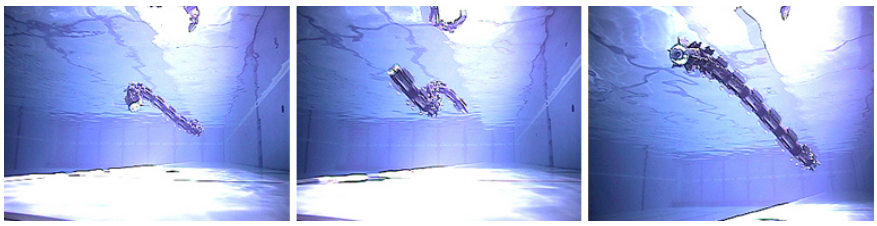

Figure 2.10: Anguilliform fish robot that propels itself through the water, developed by Yamada et al. [42].

One fish robot described in literature is able to perform all three major swimming modes of fish: anguilliform, carangiform, and thunniform [51]. This is interesting, because the effect of the different swimming modes on the flow can be quantified, as well as the swimming speeds and swimming efficiency. A picture of the fish robot built by Wen et al. is provided in Figure 2.11.

Figure 2.11: Fish robot that can swim in all three modes, developed by Wen et al. [51].

A less common source of propulsion during swimming is the use of fin undulation. Some fish use pectoral fin, dorsal fin, or anal fin undulation as their main source of propulsion. Robot fish can mimic this motion as well, but the amount of actuators and their control is a limiting factor [49, 52]. An example of such a robotic device is given in Figure 2.12. This robot mimics the locomotion of the manta ray. It is called RoMan-II, as it is the second version of the robotic manta.

The RoMan-II has three fin rays on each side. The fin rays are made of elastic materials to improve the compliance. Six independent brushless servo motors

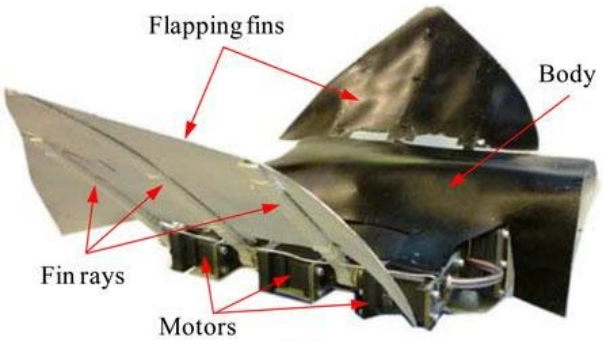

Figure 2.12: Fish robot inspired on the locomotion of the manta ray, developed by Zhou and Low [52].

generate waves in the large pectoral fins. The motors are controlled by an optimized motion controller, so that the different motion patterns of the manta ray can be mimicked. Consistently generating forward thrust by large fins can be very energy-efficient, so mimicking the locomotion of the manta ray can be interesting for future underwater vehicles that need to cover large distances.

2.4.2 Bio-inspired snake-like robots

Apart from the robotics inspired by fish locomotion, there is another topic in robotics that uses undulation: robots inspired by the serpentine locomotion of snakes [42, 45, 46, 53–57]. The way that is coped with the high number of degrees of freedom in serpentine locomotion can be inspiring for constructing robotics based on the seahorse tail.

Robots inspired by serpentine locomotion will generally only use lateral bending, as bending in the other directions is not strictly required for the locomotion. The seahorse tail on the other hand can bend in all four directions (ventral, left, right, and dorsal). This makes it easier to find appropriate actuators for the snake robot, as motorized hinges with only one degree of freedom can be used. If the robotic inspired by the seahorse tail uses only ventral bending (the most common bending mode of seahorses), the actuators used to introduce bending in the robot can be similar, as there is no fundamental difference in generating lateral or ventral bending in a robot, aside from actuator orientation.

When designing a snake-like robot, there is an important issue to consider: in order for the undulating motion to cause an axial displacement of the body, the ground friction has to be anisotropic. More in particular, the ground friction in lateral direction needs to be significantly smaller than the ground friction in axial direction [58, 59]. The snake creates an anisotropic friction by orienting the edges of the ventral scutes (Figure 2.13) perpendicular to the axial axis. In most

snake-like robots, the axial friction is reduced by axially directed wheels on the articulating segments [42, 45, 56].

Figure 2.13: Frictional anisotropy of snakeskin that arises from the orientation of the ventral scutes [58].

An example of a robot that uses serpentine locomotion is given in Figure 2.14. Contact with the floor is made with passive, axially directed wheels. The snake-like robotic system that use passive wheels show good results on flat surfaces. When moving through rough terrain, few wheels can make contact with the soil. In those cases, wheel-less snake-like robots show better results [53, 57]. The forward thrust is then mainly generated by contact of the lateral sides of the body with surrounding obstacles.

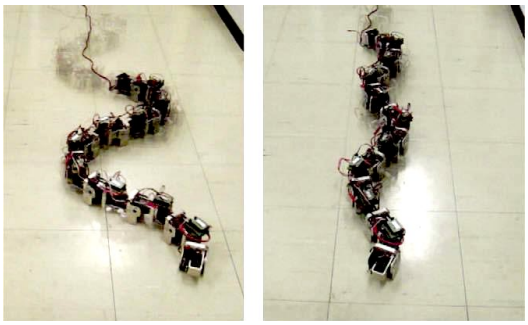

Figure 2.14: Snake-like robot developed by Wu and Ma [56] at different undulation wavelengths and amplitudes.

2.5 Bio-inspired robotics of prehensile organs

In this section, an overview of some recent research and designs inspired by *prehensile* (i.e. grasping and holding) organs is given, since our research focusses on applying the biomechanical principles of the seahorse tail (which is also a prehensile organ) to industrial applications.

Within the animal kingdom, several appendages have developed into prehensile organs, including:

- Feet - e.g. most primates
- Tails - e.g. some lizards
- Tongues - e.g. giraffes
- Lips - e.g. rhinos
- Noses - e.g. elephants (although the elephant trunk is also partially lip)
- Tentacles - e.g. octopuses

The first two prehensile organs usually have an articulating rigid skeleton that aids in the prehension, while the latter four have to rely solely on muscle contractions and hydrostatic pressures (so-called *muscular-hydrostats* [60]).

Prehensile organs are an interesting topic in biomimicry and robotics, since robots that mimic long prehensile organs can be very versatile: they can grasp objects of fairly variable geometry and size of which the exact position and orientation in space are not necessarily known beforehand. This principle is demonstrated in Figure 6.1.2.1: if the object that needs to be grasped is slightly moved or rotated, there is a good chance that the more regular robotic arm (Figure 6.1.2.1 A) will fail to grasp the object, while the robot inspired by the prehensile organ (Figure 6.1.2.1 B) has a better chance of still catching the object, as it can bend around the object even it is (slightly) out of place. Because of the improved robustness in grasping, robotics that mimic prehensile organs can be used in a large variety of applications. An important disadvantage of the prehensile organ robot over the more common grasping robots is that the grasping and releasing will generally (but not necessarily) require more time.

Most traditional robot manipulators will use (a series of) actuated joints between connected links to create motion, as indicated in Figure 6.1.2.1 A. These robots are so-called *discrete manipulators*. The robotics inspired by prehensile organs will, however, often show a different characteristic: they can bend (parts of) the prehensile organ continuously over its length, as demonstrated in Figure 6.1.2.1 B. Hence these robotics are called *continuum style robots*. As another example, Figure 2.16 shows a continuum style robot inspired by the trunk of an elephant. The grasping robot can adapt its curvature (almost) continuously over a large area, thus ensuring a firm grip on irregularly shaped object.

This robot of Figure 2.16 is not the only one that is inspired by the versatility of the elephant trunk. The *Bionic Handling Assistant* from Festo also mimics the elephant trunk, but doesn't use wires and springs like the previous example. Instead, this device is pneumatically driven, while mimicking the trunk of an elephant to obtain a high degree of freedom (Figure 2.17 A). The robotic arm consists of chambers that expand longitudinally when filled with pressurized air (Figure 2.17 B).

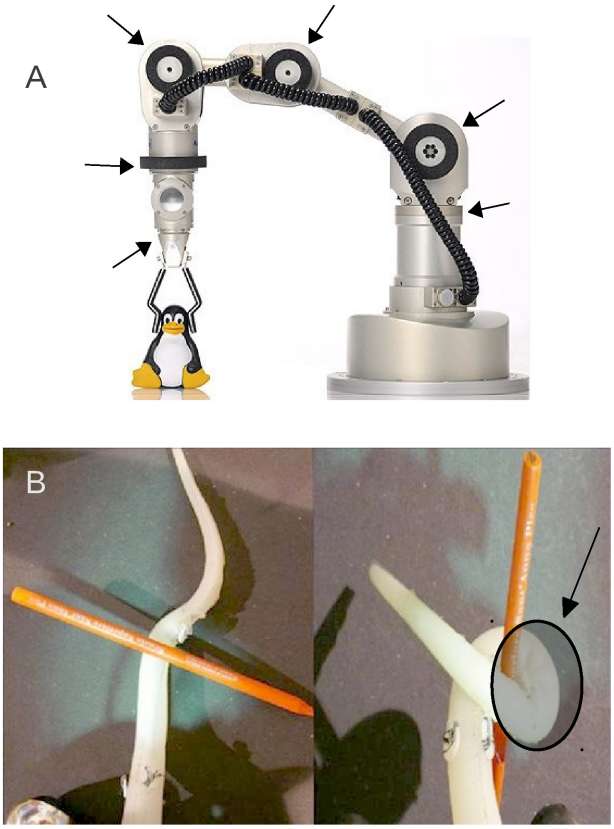

Figure 2.15: Example of the improved versatility and the actuation of a robotic prototype inspired by prehensile organs (B) [61] compared to more common robotics (A) [62], with indicated regions of actuation (localised in A and continuous in B).

By combining three such chambers next to each other, the distal end can be manoeuvred into almost any angle by pressurizing one or two chambers. Pressurizing all three chambers allows for a longitudinal displacement of the distal end. Three large sections, each consisting of three chambers, are placed after each other to allow a higher positional flexibility of the gripping fingers.

The function of robots inspired by tentacles of animals can go beyond mere grasping of an object. For example, robots inspired on animal tentacles are sometimes used to assist in minimally invasive surgery [65, 66]. One example of a robot specifically designed to assist in minimally invasive surgery is the so-called *CardioArm* robot, which is shown in Figure 2.18. The high bending flexibility of this kind of robots is not used to wrap around objects, but to manoeuvre through regions of high geometric complexity, like regions of the human body. In this particular example, the robot can be used to manoeuvre an ablation catheter within

Figure 2.16: Manipulator inspired by the elephant trunk [63].

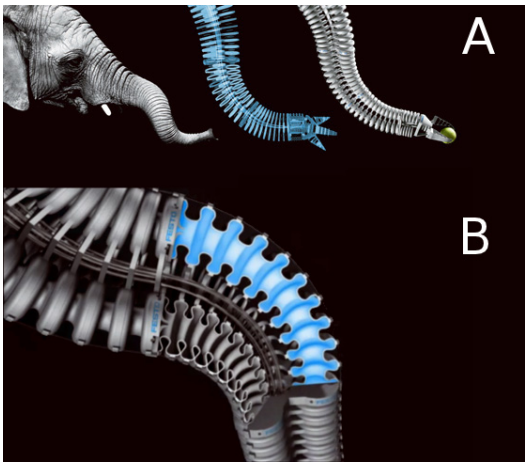

Figure 2.17: The trunk of an elephant as inspiration for a versatile robotic arm [64].

the pericardium[5] in order to perform epicardial[6] ablation.

The previously discussed robots still require a structure of rigid bodies to support the movement. Recently, some bio-inspired robots have been developed that mimic the hydrostatic, skeleton-less motion of some animal tentacles. For example, the biomechanics of the octopus arm was studied and mimicked in a specialized robotic arm [61, 67], as demonstrated in Figure 2.19. The robotic device

[5]The pericardium is a membranous sac filled with fluids that encloses the heart and the roots of some large blood vessels.

[6]The epicardium is a layer of connective tissue that encompasses the heart. It is the inner layer of the pericardium.

Figure 2.18: Bio-inspired robot designed to assist in minimally invasive cardiac surgery [65].

consists of a silicon arm with a centric steel cable (for longitudinal contraction of the limb) and an eccentric fibre (for bending of the limb). This robot arm is developed for underwater manipulation and can elongate, shorten, and bend in any direction.

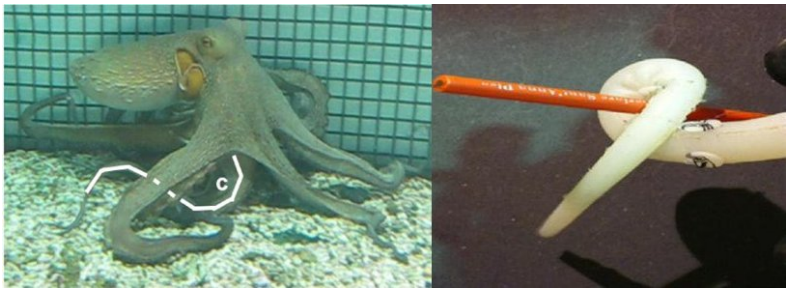

Figure 2.19: The tentacles of the octopus inspired the design of a robotic arm [61].

Both the trunk robot and the octopus tentacle robot show a high level of flexibility, similarly to that of the seahorse tail. However, these robotics use a limited amount of actuators, so very localized bending is not possible. The seahorse has a remarkable control over the tail, enabling it to bend very locally. It would be beneficial to keep this aspect of the tail in robotics inspired by the seahorse tail.

These nature-inspired robotics demonstrate how the biomechanics of prehensile organs can be applied to robotics, and are thus an important reference for the development of engineering applications in the presented dissertation. A more elaborate study of some of these existing robotics will hence be conducted in section 6.1.2.

2.6 Conclusions

Several bio-inspired designs have been presented in this chapter. Except for some general examples meant to demonstrate the broad applicability of bio-inspired designs, the focus lay on robotics inspired by nature. To the best of our knowledge, not a single robotic inspired by the seahorse tail has been designed. Therefore, this chapter focused on robotics inspired by the movement of structures that are somewhat comparable to the seahorse tail, either by structure (the tails of other fish and snakes) or by function (prehensile organs other than the seahorse tail).

Most fish-inspired robotics can only bend their tails very locally, thus limiting the amount of bending that can be achieved. This is logical, since the amount of tail flexibility required for undulatory locomotion is much less than the amount required for grasping. Only for the few fish robots that mimic anguilliform swimming, is the amount of flexibility sufficient to be relevant for a grasping robotic arm based on the seahorse tail. These anguilliform swimming robots have many similarities to snake-like robots. Bot types of robotics suffer from a major drawback: a large amount of actuators is required. Usually, the robotic design consists of a long chain of segments connected by actuators. Consequently, the robotic designs are very complex and expensive. Moreover, controlling the different actuators is difficult and requires sophisticated (and therefore expensive) motion controllers. Using the same approach for robotics inspired on the seahorse tail is therefore expensive (as the seahorse tail would also require at least one actuator per segment of the chain). The design can be simplified by having fewer actuators that actuate several joints at once.

Bending a robotic over a longer area along its length is achieved in the robotics inspired on prehensile organs. This limits the amount of control that can be achieved locally (i.e. the local curvature is dependent on the curvature in nearby areas), but it reduces the amount of actuators and the complexity of actuator controllers drastically.

3

Seahorse tail anatomy

3.1 Introduction

In order to understand the biomechanics of the seahorse tail, one must first study the anatomy. Despite the fact that the musculoskeletal structure of the seahorse tail has some peculiar differences compared to that of other fish, published studies on the seahorse tail anatomy are rather scarce [2, 11, 68]. To get a better idea of the musculoskeletal structure of the tail, high resolution μCT-scans and synchrotron scans of the tails of some *Hippocampus reidi* specimens were acquired. The μCT-scans are segmented to obtain the geometry of the skeletal elements, whereas the synchrotron scans are used to study the muscle structure of the tail. Additionally, some muscles were dissected and used for tensile testing, which gives an indication on the passive extensibility that can be expected from the passive muscles in the tail.

3.1.1 Fish and seahorse locomotion

Most fish use their tail for underwater propulsion. In contrast, seahorses use undulations of the dorsal fins as main source of propulsion. The general principles of both general modes of underwater locomotion are explained in the following paragraphs.

3.1.1.1 Undulatory locomotion

Most fish use undulatory (wavelike) locomotion to propel themselves through the water: by periodically contracting muscles on both lateral sides of the strong yet flexible central axis (formed by the backbone), they generate waves that travel through their bodies towards the caudal fin (Figure 3.1). In this way the fish generate forces with their body on the surrounding water. During normal forward swimming, the lateral components of those forces cancel each other out, leaving only a longitudinal net force that propels the fish forward. Simultaneously with this forward propulsion, most fish will use their pectoral fins to steer or to create lift [69].

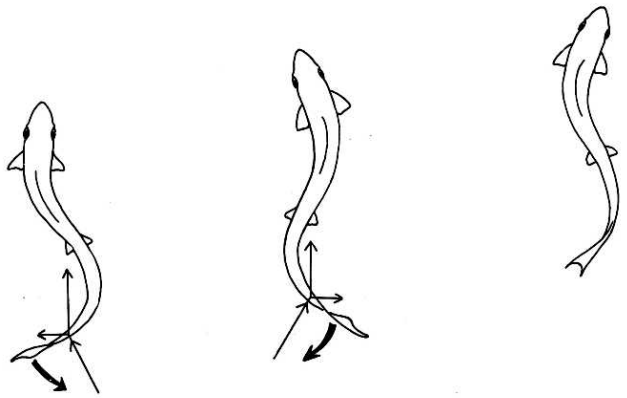

Figure 3.1: Undulatory motion of fish [70]. The thin arrows indicate the reaction forces of the water on the fish, while the bold arrows indicate the movement of the caudal fin.

Although the internal structure of the body of a fish is very heterogeneous in nature (as it is composed from bone, muscles, tendons, connective tissue, etcetera), during undulatory locomotion the fish body can be considered to behave as if it were a simple beam [71]. This means that the body behaves as if it were one single monolithic block of homogeneous, isotropic, and linearly elastic material, with one axis (the anteroposterior axis) being at least an order of magnitude larger than the other two axes. During the undulatory locomotion, a specialized system of myosepta, tendons, skeletal elements, and skin redistributes the internal forces to allow the beam-like behaviour of the body [71].

The undulatory locomotion of fish can be divided into three main categories: *anguilliform*, *carangiform*, and *thunniform* motion [51, 69, 72]. These swimming forms are called after fish that typically show this motion form: the eel (*Anguilla*), the jack (*Caranx*), and the tuna (*Thunnus*), respectively. The division into cate-

gories is slightly arbitrary and is based upon the portion of the wavelength of the motion that can be distinguished in the body curvature during normal swimming: more than one wavelength for the anguilliform, less than one wavelength for the carangiform, and almost pure caudal fin movement for the thunniform. This corresponds to an increasing body stiffness of the fish and an increasing swimming efficiency, as well as on average an increasing swimming speed. This higher swimming speed was also observed by Wen et al. on a robot that could swim in all three swimming modes [51].

Some authors will define a swimming mode between the anguilliform and the carangiform: the subcarangiform motion [73]. All four types are visualised in Figure 3.2. Not all fish use these swimming forms for propulsion: some rely on fins other than the caudal fin for powering the locomotion. Some fish use dorsal fin undulation (e.g. seahorses and Amiiformes), anal fin undulation (e.g. Gymnotiformes), or pectoral fin undulation (e.g. Rajiformes, Diodontidae, and Labridae) [73].

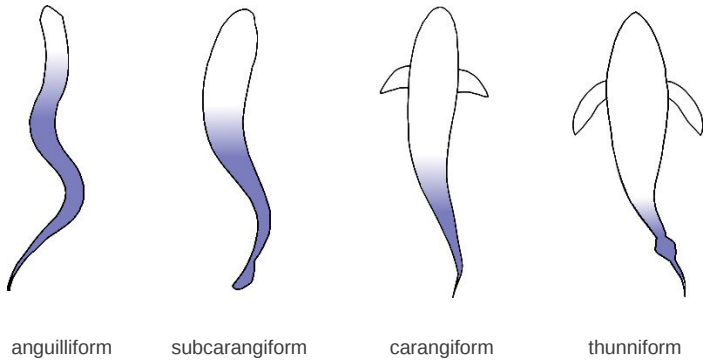

Figure 3.2: Swimming modes of the caudal or trunk swimming fish species. The coloured areas are the undulating parts of the body.

3.1.1.2 Dorsal fin propulsion of the seahorse

The seahorse is one example of a fish that doesn't use one of these common swimming modes for propulsion. The caudal fin is completely absent in seahorses, and the whole caudal regions has lost its role in locomotion [2]. Instead, seahorses use high velocity vibratory fins to propel themselves [2, 74–76]. The main propulsion is generated by the dorsal fin, while the pectoral fins are predominantly used for steering (Figure 1.5). Locomotion by fin undulation is common among fish that need high manoeuvrability at low swimming speeds [75]. Seahorses typically live in corals and seagrasses. In such environments that are abundant in obstacles, the locomotion by dorsal fin undulations of the seahorse may be an advantage.

In fin undulations, the fins are not simply moved from left to right in a flapping motion (i.e. oscillatory locomotion), but instead, the rays of the fin generate high velocity waves that propagate from the anterior side towards the posterior side of the fin (i.e. undulatory locomotion) [75, 77], as indicated in Figure 3.3b. This figure was drawn based on a high speed video from a camera taking 300 pictures per second. As can be deduced from Figure 3.3b, it takes roughly 30 frames to complete one full cycle (one wave travelling through the entire fin), which corresponds to 0.1 seconds [74].

(a) Undulating dorsal fin (courtesy of A. Dimou and D. Mitsa).

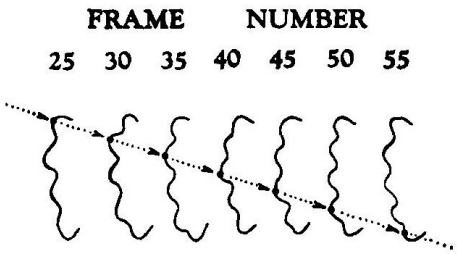

(b) Wave travelling through dorsal fin [74].

Figure 3.3: Undulation in the dorsal fin of the seahorse.

At normal swimming speeds, each individual ray of the dorsal fin moves from side to side roughly 70 times a second [74]. The oscillatory movement of the individual rays is generated by a complex system of small muscles, tendons, and elastic cartilage [75]. Even with the high velocity oscillations, the seahorse can still only obtain relatively low swimming speeds [2, 76].

3.1.2 The unique function of the seahorse tail

The seahorse has to rely on dorsal fin undulation as its main source of propulsion, whereas most fish use body undulation ending in a strong caudal fin for propulsion. This essentially turns the seahorse into a slow swimming fish, which is unlikely to outswim any predatory fish. The seahorse thus has to rely on crypsis (avoiding detection by other organisms) to avoid predation. This means that it uses a combination of defence mechanisms to stay unnoticed by predators. These defence mechanisms include:

- Camouflage according to its specific environment
- Slow, unsuspicious movements (except when reaching for its prey)

- Hiding in the vegetation

The ventral bending ability of the seahorse tail is quite unique among fish. The seahorse tail shares its prehensile tail ability only with some closely related pipehorses [11]. The ventral curling of the tail is only possible due to a specialized mechanical system of muscles, tendons, and bones that evolved from the fishes complex musculoskeletal system used for lateral bending during undulatory locomotion. Although the function of the seahorse tail is profoundly different than that of most other fish species, the basic morphology of the seahorse tail has, perhaps surprisingly, quite some similarities with the tail morphology of fish that use undulatory locomotion [11]. The most important differences appear to lay in the fact that the seahorse tail has dermal plates, as well as in the myoseptal organisation of the hypaxial myomere muscles, as will be evident from the discussion section of this chapter.

3.1.3 General muscle structure of fish

The structure and mechanics of the fishes' muscular system is not yet fully understood [78]. On both lateral sides of the fish body, there are myomere muscles that power the undulatory propulsion of the fish. These short muscle fibres are separated by collagenous sheets, called myosepta [79, 80]. This structure of longitudinally alternating myomeres and myosepta is folded into often very complex shapes [78, 81] that can greatly differ between fish species [82].

In most species the myoseptal structure shows distinct longitudinally directed cones [78–82], resulting in a typical W-shaped pattern in sagittal slices of the trunk muscles, which you can for example clearly distinguish in common slices of smoked salmon (Figure 3.4). Conversely, transverse slices of the fish trunk muscles will show a distinct pattern of concentric ellipses. The muscle cells are oriented longitudinally, but the angle of the fibres with the longitudinal axis varies with its position in the tail [80].

Most fish have a *horizontal septum* (a horizontal layer of collagen fibres) that divides the muscles into *hypaxial muscles* (lower half of the body) and *epaxial muscles* (upper half of the body). The myosepta act as sheets that transmit the forces generated by the myomeres to the skin and the horizontal septum. In turn, the horizontal septum is an important transmitter of muscle forces to the axial skeleton [83].

Fish also use their myomere muscles to modulate the body stiffness, and therefore the natural oscillatory frequency of the body. Tuning the natural frequency of the body to the tailbeat frequency likely minimizes the mechanical cost of bending the body during undulatory swimming [84].

Muscle fibres are usually split in two categories: *red* and *white muscle fibres*. In general, the red fibres are predominantly used in slower, more prolonged muscle

Figure 3.4: Lateral view of the myomeres and myosepta on smoked salmon, clearly showing the anterior cone near the top.

contraction, as they are slow to fatigue. The red colour of these fibres is caused by the presence of the oxygen binding protein myoglobin and the relatively large amount of capillaries. The white muscle fibres are predominantly used for faster, more forceful contraction bursts, like in the fast-start of fish. These fibres are more prone to fatigue. The absence of myoglobin gives them a white colour and forces the white fibres to rely on glycolytic enzymes.

Numerous studies on dynamic myomere muscle function in swimming fish have revealed that red muscle strain consistently increases along much of the body [85]. A summery of the results of several of these studies is illustrated in Figure 3.5. The indicated strain is the ratio of the maximum elongation of the muscle fibres during a swim cycle to the initial length of the fibres (so the muscle fibre length in a straight tail).

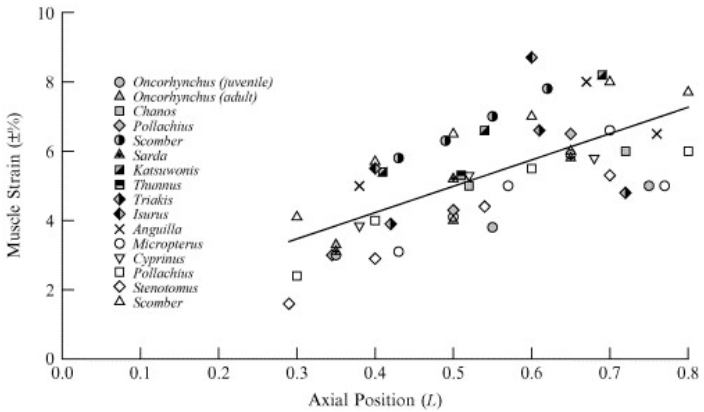

Figure 3.5: Red muscle strain in several fish species [85].

Equation 3.1 is the equation of the trend line in Figure 3.5, with l being the

axial position (0 is the rostral tip and 1 is the caudal tip). Generally, the red fibre strain is roughly four times larger than that of white fibres [86].

$$\varepsilon_{muscle} = 7.554\, l + 1.197, \quad l = 0..1 \tag{3.1}$$

3.2 Materials and methods

3.2.1 Scanning of the seahorse tail geometry

To study the poorly documented structure of the seahorse tail, several scans were acquired. Five different μCT-scans were acquired from a specimen of an adult seahorse, species *Hippocampus reidi* (also known as longsnout seahorse or slender seahorse). The tail was manually fixed in three different positions: (ventrally) curled, stretched, and (dorsally) over-stretched. For all scans, a tube voltage of 70 kV was used together with a detector with a 127 μm pixel pitch. The individual details for each of the five scans are summarized in Table 3.1.

Scan	Tail position	Voxel size	Region of interest
1	Curled	13 μm	Full tail
2	Stretched	37 μm	Full tail
3	Stretched	7 μm	Four segments
4	Over-stretched	50 μm	Full tail
5	Over-stretched	11 μm	Four segments

Table 3.1: Details of the five different μCT-scans of the seahorse tail.

The μCT-scans were made by the Centre for X-ray Tomography (UGCT) of Ghent University (`http://www.ugct.ugent.be/`). The results of segmenting the bony elements of each of the three full tail scans are shown in Figure 3.6. All the scans were segmented using the open source software 3D Slicer 3.6. The focus on using open-source software whenever possible was kept throughout the project.

The μCT-scans showed nice contrast on the bony elements. However, muscles and connective tissues had insufficient contrast to allow investigation of their structure. Therefore, two other adult specimens of the *Hippocampus reidi* species were additionally scanned simultaneously by dr. Renaud Boistel (Université de Poitiers) using a high-resolution phase contrast synchrotron X-ray scanner at the European Synchrotron Radiation Facility in Grenoble. A resolution of 2048 by 2048 pixels and voxel size of 7.46 μm were obtained using a FreLoN CCD camera.

As could be suspected, the structures of the muscles and connective tissues were a lot easier to identify on the synchrotron scans. For one tail the more anterior segments of the tail were scanned. For the other tail, mostly the posterior

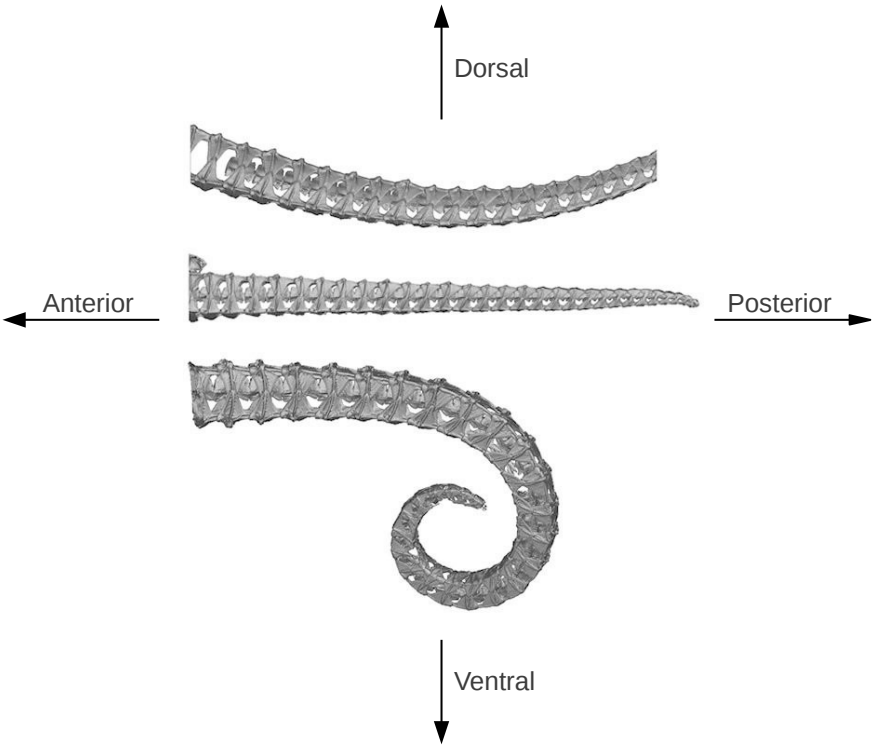

Figure 3.6: Three different tail positions of an adult Hippocampus reidi specimen (over-stretched, stretched, and curled, respectively), scanned using a μCT-scanner.

segments were scanned. Both tails scanned by the synchrotron scanner were fixed in a ventrally bended position.

3.2.2 Tensile testing of the seahorse tail muscles

An adult male specimen of the *Hippocampus reidi* species was subjected to an overdose of anaesthetics (MS222, according to Belgian law for the use of lab animals). Since the seahorse tail muscles are very small, the largest available adult male specimen was chosen. From one side of the body the hypaxial and epaxial myomere muscle bundles were dissected to be used in tensile tests, while the other side was kept intact to be used in histological studies. These histological studies were conveniently used to get an accurate estimate of the cross-sectional area of the muscles. The dissected muscles were contained in a saline solution for roughly one hour before being tested. After being removed from the liquid, the tests were conducted as soon as possible, to avoid excessive drying of the muscle tissue. Time between removal from the saline solution and the tensile tests shown in the results

was roughly ten minutes (time needed to properly position the samples in the grips, enter the parameters in the computer, and conduct the preconditioning steps).

The muscle bundles were subjected to uniaxial tensile tests. The tensile testing equipment used was an INSTRON® 5942 electromechanical tensile test system (Instron, Norwood, MA, USA). The experimental setup is shown in Figure 3.7. A load cell of 10 N with pneumatic grips was used. The pneumatic pressure exerted on the grips measured 4 bar. The axial strain rate was kept fixed at 0.1 % per second during the tests, which is lower than the strain rates that can be expected during tail bending of seahorses. However, we opted to measure the quasi-static response of the muscles, with limited effect of inertia and visco-elasticity. This is the passive response that can be suspected during very slow tail bending, or during prolonged periods of bending.

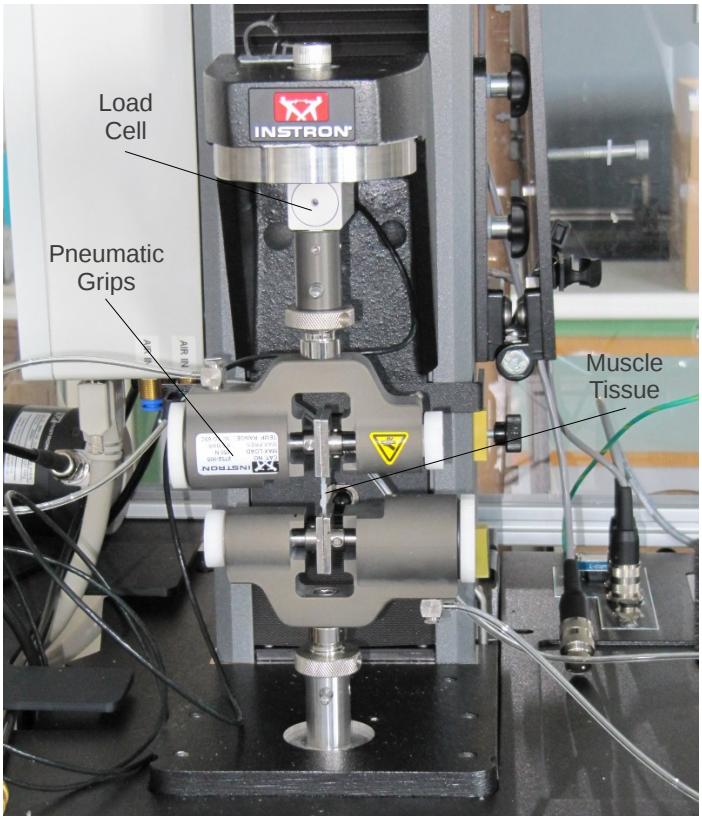

Figure 3.7: Tensile testing of a seahorse myomere muscle.

Immediately after dissection, the muscles showed considerable shortening. It would appear that the myomere muscles are still slightly prestressed in an almost

stretched tail, even after sedation. The exact shortening was too difficult to quantify and will therefore be estimated based on the results. The muscles were vertically suspended between the grips, with a sufficient amount of tissue between the grips.

Biomaterials typically require proper preconditioning when conducting tensile tests, since the tissue will show a large, variable initial period of excessive hysteresis after being stretched from a completely stress free condition [87]. No appropriate preconditioning procedure for fish myomere muscles was found in literature. We therefore chose to precondition the HMM and EMM by stretching the muscle to 5% at a first cycle, 20% at a second cycle, and 30% at the third cycle. The fourth cycle was then taken as being representable for the normal passive response (the fourth cycle also included stretching to 30% of the initial muscle length). Yoo et al. reported a steady state after three to five cycles for extraocular bovine muscles [87]. Whether the three precycles we used is appropriate for the myomere muscles is debatable, but given the fragile state of the muscles, we did not want to risk accumulating too much damage to the tissue before measuring the passive extensibility. Moreover, we wanted to avoid excessive drying of the tissue. If in the future more tests were to be conducted on fish muscle tissue, a proper preconditioning procedure should be developed. Our current data is insufficient to determine whether the steady-state muscle response was achieved in the presented data.

Both myomere tissue samples were dissected from the same side of the body. Their contralateral equivalents were also dissected, but not used in the tensile testing. Instead, they were used for histological cuts, meant for studying the structure on a microscopic level. At the same time, these cuts provide a convenient vehicle to measure the area of the muscles rather accurately. Using callipers to measure the cross-sectional area is inaccurate due to the irregular shape of the cross-section that cannot accurately be approximated by a regular geometry, and high resolution synchrotron scanning was deemed to be too expensive and time consuming for merely this purpose. Figure 3.8 shows the slices of the HMM and the EMM that were used to measure the cross-sectional area. The measurement was done using the LabelStatistics module of Slicer 3.6. Small inaccuracies in cross-sectional area are possible due to improper dissection of connective tissues and due to distortion of the slices.

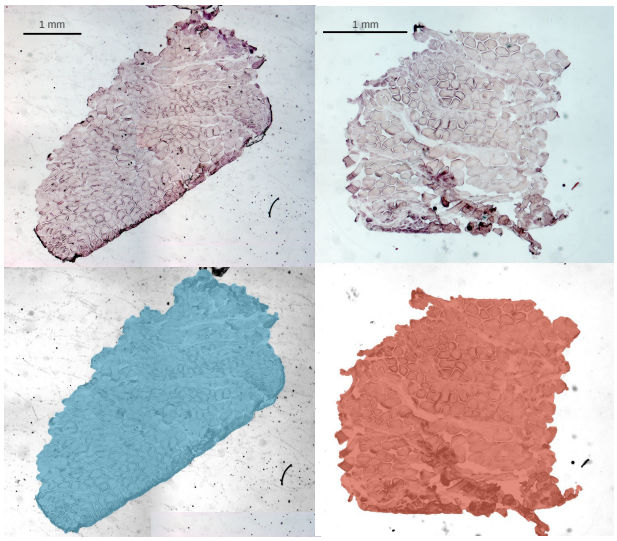

Figure 3.8: Histological cut of the contralateral HMM (left) and EMM (right) and their coloured cross-sectional areas (bottom). Courtesy of Céline Neutens.

3.3 Results and discussion

3.3.1 Seahorse tail skeletal structure

In order to act as a prehensile organ, the tail as a whole needs to be extremely flexible. Since the body of the seahorse is covered in a protective armour, the skeletal structure of the tail is adapted to maintain its flexibility. The tail consists of a chain of approximately 30 skeletal segments of caudally diminishing size (Figure 3.9). Each of these segments consists of five basic skeletal elements:

- A central vertebra (VE)
- A left dorsal dermal plate (LD)
- A right dorsal dermal plate (RD)
- A left ventral dermal plate (LV)
- A right ventral dermal plate (RV)

The backbone of the seahorse tail consists of a series of *amphicoelous* vertebrae located at the centre of each segment. The term amphicoelous means that the central part of the anterior and posterior surface of the vertebra is concave, as is the case for most teleost vertebrae. Each vertebra of the tail is surrounded by the four

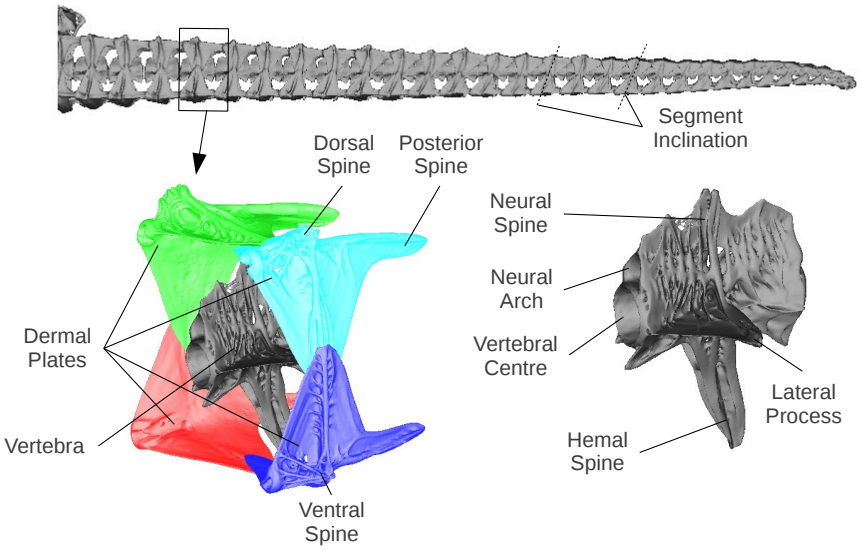

Figure 3.9: Uniform skeletal segments of the seahorse tail, skeletal elements of the segments, and the processes of the vertebrae.

dermal plates, in each corner of the cross-section, as indicated in Figure 3.9. The plates are positioned left and right dorsolaterally and ventrolaterally. Each dermal plate forms a corner by stretching medially on one side and towards the lateral midline on the other side. The specialized articulation of the skeletal elements is crucial to the flexibility of the seahorse tail, as the bending of the tail needs to be distributed between the many segments.

Figure 3.9 also shows the processes[1] that can be found on the bones of the seahorse tail. The vertebra has four processes or spines that stretch out towards the dermal plates: a lateral process on both lateral sides (also called transversal spines), a hemal spine at the ventral side, and a neural spine at the dorsal side. The shape of the caudal vertebrae is fairly uniform [2].

The dermal plates each have a posterior spine that fits into a groove on the anterior side of the consecutive dermal plate in the chain. There are also dorsal and ventral spines on respectively the dorsal and ventral dermal plates, which are usually more pronounced on the rostral segments than on the more caudal segments, and more pronounced on the dorsal than on the ventral side.

The size (width, height, and length) of each segment of the tail was measured on the segmented stretched *Hippocampus reidi* tail using pyFormex. As an illustration, the measured distances of a single segment are demonstrated in Figure 3.10. The width of a segment was determined as the distance along the left-right axis

[1] Processes are natural outgrowths or prolongations of tissues.

between the left-most and the right-most point of the segment. The height was defined as the distance along the dorsoventral axis between the most dorsal and the most ventral point of the segment. The most dorsal point is usually located on the dorsal spine. Since the ventral spine is generally much smaller than the dorsal spine, the most ventral point of the segment is not always on the ventral spine. Instead, it can mostly be found on the ridges of the ventral surface of the ventral dermal plates. Finally, the length of the segment was determined as the longitudinal distance between the points in between the consecutive vertebrae. Except for the most rostral tail segments, the distance between the vertebrae is so small compared to the scanning resolution that the vertebrae cannot be separated by regular segmentation algorithms. The points in between the vertebrae are therefore determined manually.

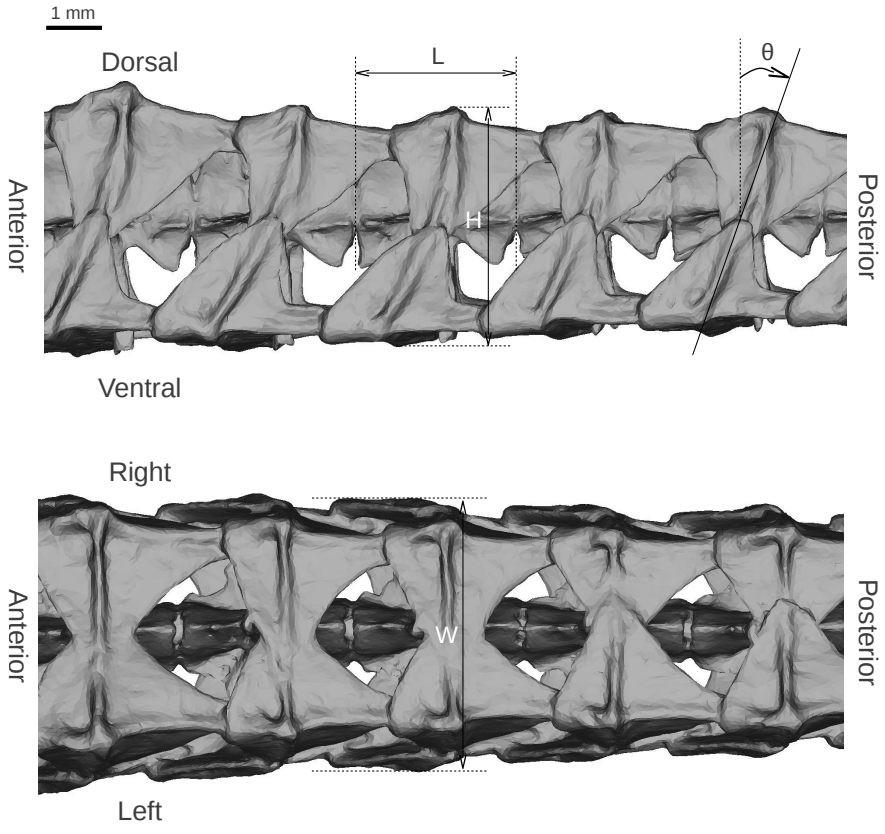

Figure 3.10: Measuring the width (W), height (H), length (L), and inclination (θ) of a seahorse tail segment.

The results of the measurements are summarized in Figure 3.11. The heights and widths of the segments are closely related. Consequently, the cross-section of

the segments is shaped like a square. The length of the segments on the other hand is smaller. The difference between the length and the width and height of the segments becomes smaller towards the tail tip. As a result, segments close to the tail tip are nearly shaped like cubes, whereas the anterior segments are longitudinally compressed.

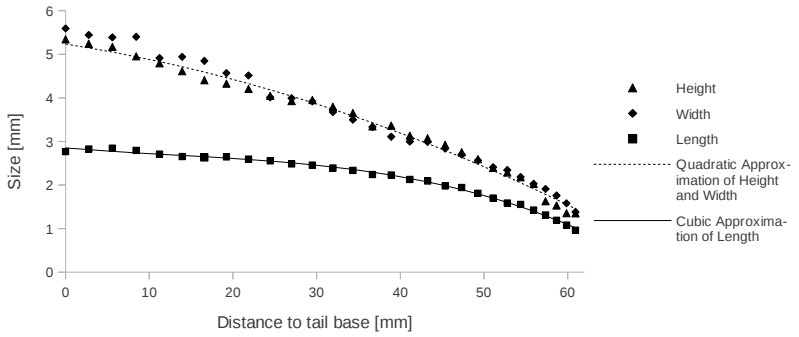

Figure 3.11: Size of the segments of the seahorse tail in function of distance to the tail base, with best fitting quadratic (for the width and height) and cubic (for the length) polynomial approximations.

The height, width, and length of the segments throughout the tail can be approximated by polynomials in function of the relative position in the tail (lines in Figure 3.11). Since the height and width are similar, they are approximated by the same second degree polynomial. For the length, the fit of second degree polynomials was rather poor. A third degree polynomial was found to be a lot more appropriate. We found no evident reason as to why the height and width were better approximated by a quadratic curve, while the length was better approximated by a cubic curve.

To obtain the relative position, the length along the tail is made dimensionless by dividing it with the total length of the tail (63.080 mm). In this way the tail model can be scaled to account for longer or shorter seahorse tails. The resulting approximations are given in equation 3.2 for the segment height ($H(l)$) and width ($W(l)$) and in equation 3.3 for the segment length ($L(l)$). The Pearson product-moment correlation coefficients for the approximations are respectively 0.991, 0.988, and 0.996.

$$H(l) = W(l) = -2.086\, l^2 - 1.896\, l + 5.233, \quad l = 0..1 \tag{3.2}$$

$$L(l) = -2.619\, l^3 + 1.613\, l^2 - 1.13\, l + 2.851, \quad l = 0..1 \tag{3.3}$$

The segments in the seahorse tail vary also in another way than just size. As indicated in Figure 3.9 and Figure 3.10, the segments show a certain inclination

towards the tip of the tail [2]. The more distal the segment, the more the ventral side gets tilted anteriorly and the more the dorsal side gets tilted posteriorly. To assess the inclination, the direction of the lateral ridges of the dermal plates was used. The measured inclination for the adult *Hippocampus reidi* specimen is given in Figure 3.12.

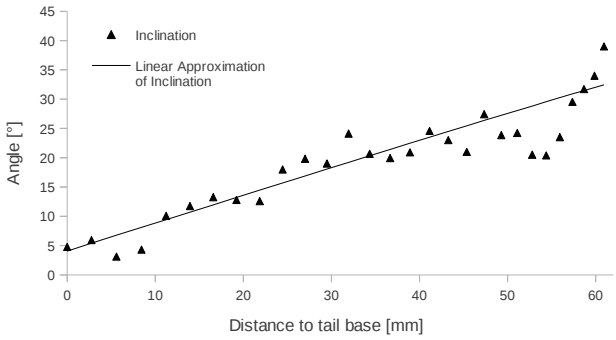

Figure 3.12: Skewing or inclination of the segments of the seahorse tail in function of distance to the tail base.

A linear approximation for the inclination in function of distance to the tail base is used. The Pearson product-moment correlation coefficient is 0.845. Using quadratic and cubic polynomial approximations did not offer much improvement in the fit (Pearson product-moment correlation coefficients of respectively 0.848 and 0.868), so for the sake of simplicity, the linear approach was used. The inclination measurements in the most posterior segments is not very reliable, since the ridges on the dermal plates are almost invisible in the posterior region. The poor fit of the linear approximation in the final segments was therefore deemed acceptable. It is possible that there is a pattern in the inclination of the most distal segments that is ignored by the linear approximation. After rescaling to dimensionless length, equation 3.4 was obtained for the inclination $\theta(l)$ in degrees. The presented approximation equations will later on be used to automatically generate the segments of the tail starting from a single segment.

$$\theta(l) = 28.396\, l + 4.048, \quad l = 0..1 \tag{3.4}$$

3.3.2 The joints in the seahorse tail

The seahorse tail contains twelve joints for each segment, eight of which act like gliding joints, two behave like ball-and-socket joints and two behave in a more complex way. The position of the joints is indicated in in Figure 3.13. The anatomy of the joints is discussed below, whereas the function of the joints is discussed more elaborately in Chapter 4.2.2.

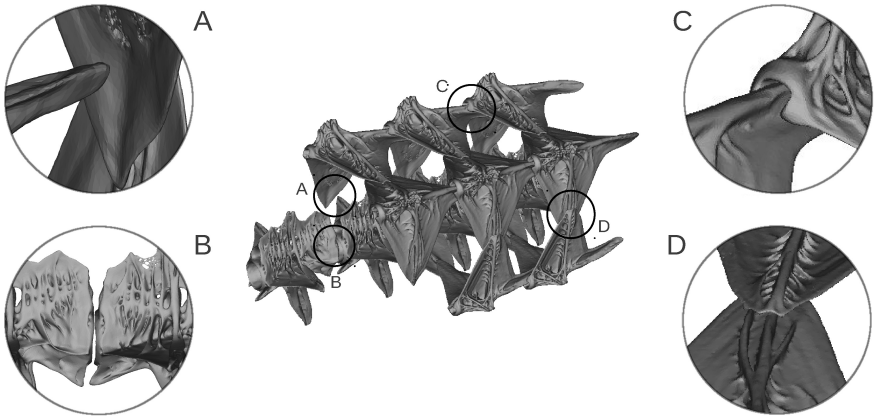

Figure 3.13: The different joints of the seahorse tail: ball-and-socket joints between vertebrae and dermal plates (A), intervertebral joints (B), intersegmental gliding joints (C), and intrasegmental gliding joints (D).

The distal ends of the lateral processes of the central vertebra are connected to the dorsal dermal plates by a joint in which all three rotational degrees of freedom are free, while translations are rather limited by connected tissues (Figure 3.13A). This means that the joint basically behaves like a ball-and-socket joint, although the socket of the joints between the lateral processes of the vertebra and the dorsal dermal plates is not always clearly visible on the medial surface of the dermal plates, and sometimes even completely absent. Presumably, the socket is predominantly formed by connective tissues, like a *syndesmosis*[2].

The hemal spine of the vertebra connects to the ventral dermal plates, although the distal end of the hemal spine is located at some distance of the ventral plates. The joint, however, is established through thick subdermal collagen layers that connect the tip of the hemal spine to the dermal plates [11], which results in a rather flexible joint. The joint therefore has some translational freedom, and a lot of rotational freedom.

The joints between the amphicoelous vertebrae allow for quite some rotation around all three axes (Figure 3.13B). In between the vertebrae and the connective tissues interconnecting the vertebrae are the remnants of the larval spinal column (i.e. the notochord). Some limited gliding of the joint is therefore possible.

Subsequent dermal plates are connected by gliding joints. The posterior spine of the anterior dermal plate fits into a rostral groove in the posterior dermal plate (Figure 3.13C). The posterior spine is shaped like a rail, which limits the movement of both bony elements in relation to each other substantially: only linear

[2] A syndesmosis is a form of joint in which opposing bone surfaces that are relatively far apart are united by fibrous connective tissues forming an interosseous membrane or ligament.

motion in the longitudinal direction shows low resistance. The tight fit of the joint even limits the rotation around the anteroposterior axis. The surface of the posterior spine is slightly curved in the longitudinal direction, which will make the bony elements rotate slightly when the joint is compressed or elongated. The groove in the dermal plates ends rather abruptly, so at a certain penetration of the posterior spine, resistance against further penetration of the plates rises quickly. This is the position where the gliding joint is compressed to its maximum.

The dermal plates have bony 'ridges' on the otherwise flat outer surfaces near the joints between dermal plates of the same segment (Figure 3.13D). These ridges provide a small rail over which the other plate can slide. The rounded shape with relatively low curvature creates a gliding joint that is much less tight than the gliding joints between subsequent dermal plates. Both rotation and sliding along a varying direction is still possible up to a certain degree. We believe that the ridges on the dermal plates actually play a more important role in increasing the bending stiffness of the dermal plates, rather than providing a strong supporting rail for the joint. At the lateral gliding joints, the plates are stacked with the ventral on top of dorsal dermal plate (the dorsal plate needs to be on the medial side because it connects to the transverse spines of the vertebra). The stacking at other gliding joints within a segment (these are the ventral and dorsal gliding joints) seems to vary without a clear pattern. It's possible that the stacking of the gliding joints on the ventral and dorsal side occurs randomly when both plates grow towards each other.

3.3.3 Seahorse tail muscles

The seahorse tail has two types of muscles: myomere muscles (MM) and median ventral muscles (MVM). Looking at a transverse section of the seahorse tail (Figure 3.14), one can see that the seahorse tail has a horizontal septum that separates the hypaxial myomere muscles (HMM) and epaxial myomere muscles (EMM). The myomere muscles clearly encompass the biggest area in the cross-sections.

3.3.3.1 Median ventral muscles

The median ventral muscles (MVM) are segmental muscles that lie near the midsagittal plane. In fact, the MVM consists of a pair of muscles, one on each side of the vertical septum [11], but for the sake of simplicity, the MVM will be considered to be one single bundle of muscle fibres for the remainder of the dissertation. The MVM connect the distal ends of the hemal spines of subsequent segments, as illustrated in Figure 3.15.

The size of the MVM was measured by Hale for eight individuals of the *Hippocampus kuda* species [11]. These results are summarized in Figure 3.16A. As indicated in Figure 3.16A, Hale fitted the lengths of the MVM throughout the tail

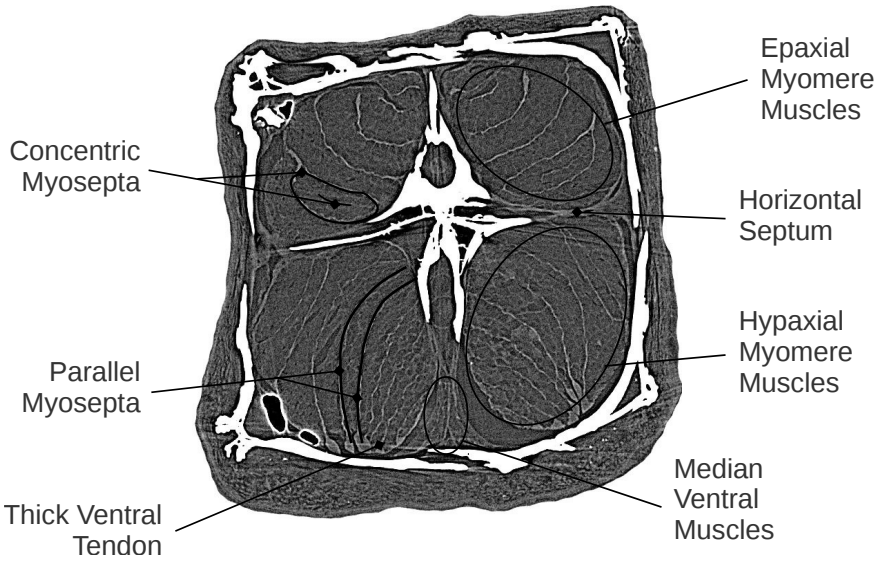

Figure 3.14: Muscle structure in the seahorse tail on a transverse synchrotron scan slice.

with a linear approximation ($R^2 = 0.74$), although a second order polynomial would result in a slightly better fit ($R^2 = 0.79$). The MVM connect adjacent hemal spines, and the hemal spines themselves are, compared to the segments, small in the anterior-posterior direction, as can clearly be seen in Figure 3.15. So the length of the MVM should roughly follow the length changes of the segments themselves. Given the fact that the length of the segments can hardly be considered to be a linear function of the distance to the tail base, as was previously shown in Figure 3.11, the better fit of the polynomial does not really come as a surprise.

The position of the MVM on the midsagittal plane allows only for purely ventral tail bending. Since the MVM are paired muscles lying on the ventral midline of the fish, they were likely derived from the *infracarinalis posterior* muscles [11], which are muscles that usually protract the anal fin. Based on the histochemistry of the muscles, the MVM are likely used for slower, more sustained tail bending [11], as in holding on to an object.

3.3.3.2 Hypaxial and epaxial myomere muscles

Looking at the myomere muscles in a transverse synchrotron scan slice (Figure 3.14), the layout of the myosepta in the epaxial and hypaxial muscles is strikingly different. The epaxial myosepta have the concentric structure that is commonly found in other teleosts. They form the typical 'cones' that are hypothesized to be important for energy storage and body stiffness during myomere muscle contraction [80]. During the muscle contraction, the longitudinally directed myomere

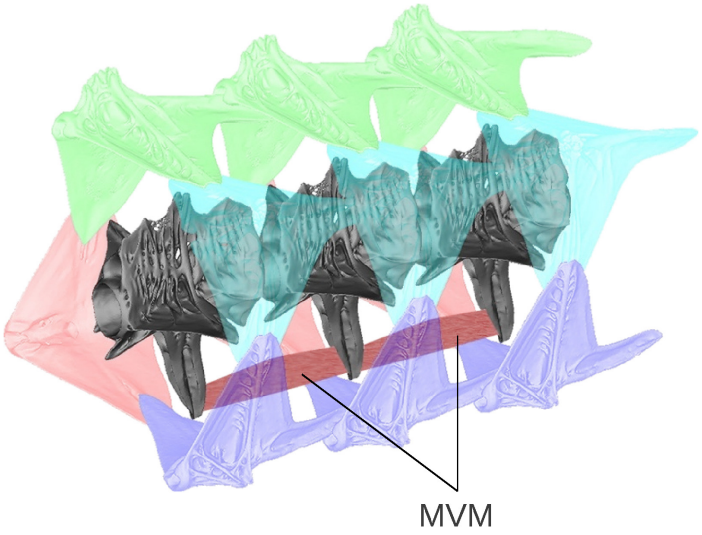

Figure 3.15: Position of the MVM in the seahorse tail.

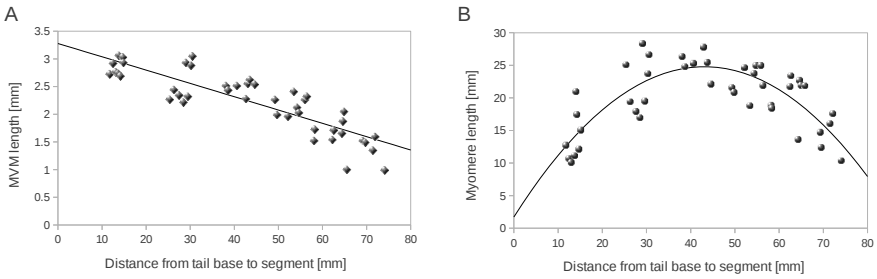

Figure 3.16: Length of the median ventral muscles (A) and hypaxial myomere muscles (B) throughout the tail of the Hippocampus kuda, as measured by Hale [11].

muscle fibres cause the cones to contract in the longitudinal direction and expand in the radial direction. This radial swelling causes an increase in hydrostatic pressure, as the backbone, septa, and skin of the fish counteract the expansion [80].

The conic structure is absent in the biggest part of the hypaxial muscles, except for a small anteriorly directed cone on the lateral-most side. Instead of the common concentric configuration, the myosepta are arranged in a more or less parallel configuration. This could indicate that the radial expansion of the hypaxial myomere muscles upon muscle fibre contraction is less constrained by the myosepta. As the muscle fibres contract, the longitudinal length of the muscle diminishes, while the muscle extends in the radial direction. In this situation conic myosepta get stretched more (since they fully span the radial direction) than parallel myosepta (that only span part of the radial direction).

The absence of clear conic structures could indicate that the hypaxial myomere muscles store less (elastic) energy upon contraction, possibly allowing the seahorse to keep the tail ventrally bended for prolonged periods of time with less effort. Since we didn't observe a locking mechanism that could keep the tail fixed in a curved position, it would seem logical that the structure of the seahorse tail somehow minimizes elastic strain energy during the long periods of tail curling. It could be worthwhile to investigate this hypothesis in a follow-up study. As for the increased body stiffness upon contraction of conical myomeres, it is possible that the absence of a clear conical structure on the ventral side of the body partially avoids this stiffening mechanism, thus insuring the flexibility of the tail is not affected too much when the tail is in a ventrally (or ventral-laterally) bended position. This is an important hypothesis that deserves further investigation. The modelling that is used in this dissertation does, however, not allow us to verify this hypothesis.

The lengths of the HMM throughout the tail, as measured by Hale, are displayed in Figure 3.16B, as well as the best fitting second order polynomial ($R^2 = 0.63$). The lengths of the HMM are much higher than the lengths of the MVM. As a consequence of the parallel configuration, the hypaxial myosepta can span several segments (Figure 3.17): up to eight segments near the middle of the tail, while the myosepta near the tail base and tail tip are much shorter. The actual muscle fibres that connect the the myosepta are a lot smaller: $0.40\ mm \pm 0.04\ mm$ for *Hippocampus reidi* [68].

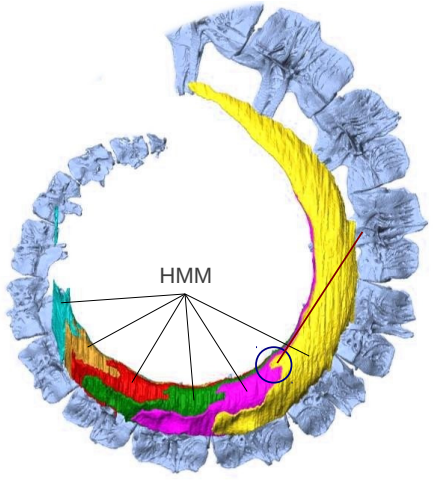

Figure 3.17: Position of the HMM in the seahorse tail (courtesy of Céline Neutens [68]) and the connection that will model the HMM.

The structure of the myosepta varies somewhat throughout the tail, but the

basic idea remains the same: conic structures on the dorsal side and predominantly parallel structures on the ventral side.

Finding the attachment points of the myomere muscles proved to be challenging. Contrary to mammals, the tendons of muscles in fish tend to be difficult to distinguish from the muscle tissue, if present at all. The tendons that connect the myomere muscles in seahorse tail to the different skeletal elements do not show a clear attachment location. Instead, they appear to be running over relatively long distances, likely transmitting forces over quite a large area. The exact attachment points of the HMM and EMM are therefore debatable. Nevertheless, we chose exact attachments in the modelling based on visual observations on the synchrotron scans, histological cuts and dissections.

Figure 3.17 shows how the HMM is modelled (red line). On the ventral side, the HMM shows a relatively thick ventral tendon (blue circle in Figure 3.17, also shown on the synchrotron scan in Figure 3.14) that connects to the medial surface of the ventral dermal plates. These ventral tendons transmit the myomere-generated muscle forces to the ventral plates [11]. On their turn the ventral plates transmit the forces to the backbone via the hemal spine and the lateral processes.

On the anterior side, the HMM connection is less obvious. The most anterior point of the HMM is located in the corner near the hemal spine of the vertebra and the ventral gliding joint between the two ventral plates. In that area, however, no clear tendons are visible near the vertebra, suggesting that force transmission to the spine is minimal in that area. We therefore chose to take the anterior HMM connection at the most anterior point where a tendon is clearly distinguishable, being in the corner between the dermal plate and the lateral spine of the vertebra (anterior end of the red line in Figure 3.17). The number of segments that get spanned in this way is less than the total amount of segments spanned by the full length of the muscle (which is up to eight segments), and varies throughout the tail.

Since in the modelling of the muscles only one element (a beam) will be used between the attachment points to the skeleton, we need to severely simplify the HMM structure in the model. The beams do not have contact definitions, so they cannot transmit forces to each other (or skeletal elements that they come into contact with). As a result, taking many segments between the connection to the vertebra and the connection to the ventral dermal plate will induce unrealistic situations: the beam will go outside of the tail when a certain level of bending is achieved, leaving a high angle at the attachment points to the skeleton. This means that the direction in which the muscle pulls on the skeletal element, which is a very important parameter in the analyses, is too far away from the anteroposterior axis. Because of these issues, we will always model the HMM as a connection between a ventral plate and the vertebra which is located two segments more proximally. Especially for the muscles near the middle of the tail (which span many segments),

this is not such a good approximation. The modelling of the HMM therefore leaves some room for improvement, but for the current simplified modelling technique, the choice for the two segment spanning showed the most promising results. The number of segments that are spanned by the connectors representing the HMM is left as a parameter that can easily be changed.

One way to enable the connectors to span more segments without affecting the pulling direction of the HMM during high bendings is to add an intermediate point in the connector, effectively splitting the initial connector into two new connectors. This point can then be connected to the vertebra and a ventral plate by means of springs. These springs will prevent the intermediate point from moving too far in the lateral and ventral direction, and therefore make sure that both connectors remain inside the cross-sectional area of the tail during high levels of bending. The basic principle of this solution is demonstrated in Figure 3.18. Implementing this principle would increase the complexity of the model (the contraction of the HMM would have to be translated to more connectors, and the stiffnesses of the springs would have to be optimized).

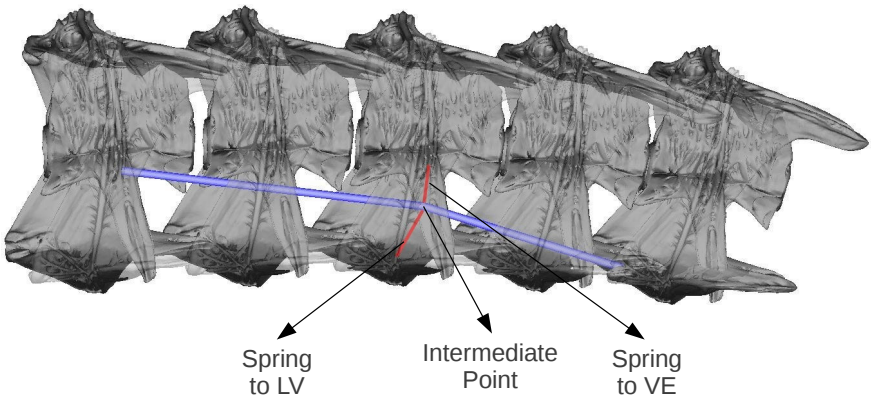

Figure 3.18: Basic principle of adding an intermediate point on the HMM to avoid the muscle leaving the cross-section of the tail during high bending. The intermediate point is connected by springs to the vertebra and the left ventral dermal plate. Deflection of the intermediate point is exaggerated for clarity.

On the dorsal side, the connection of the EMM to the skeleton is even less clear than the connection of the HMM. For the sake of both simplicity and symmetry, we will model the EMM just like the HMM, until more information becomes available on the precise attachment of the EMM to the tail skeleton. It should be noted that since the EMM do show the conic structure, they span less segments than the HMM, so the applied approximation should be better for the EMM than for the HMM.

The ventro-lateral position of the HMM allows for both ventral and combined

ventro-lateral tail bending. To achieve pure ventral bending, both left and right HMM need to produce equal forces, while combined ventro-lateral bending can be achieved by unilateral contraction of the HMM. Pure lateral bending of the tail would require the epaxial and hypaxial myomere muscles on one side to contract simultaneously with equivalent force, but this has never been observed for a full tail [11].

To demonstrate the modelling of the myomere muscles and median ventral muscles, Figure 3.19 shows the position of the modelled muscles in a section of the tail.

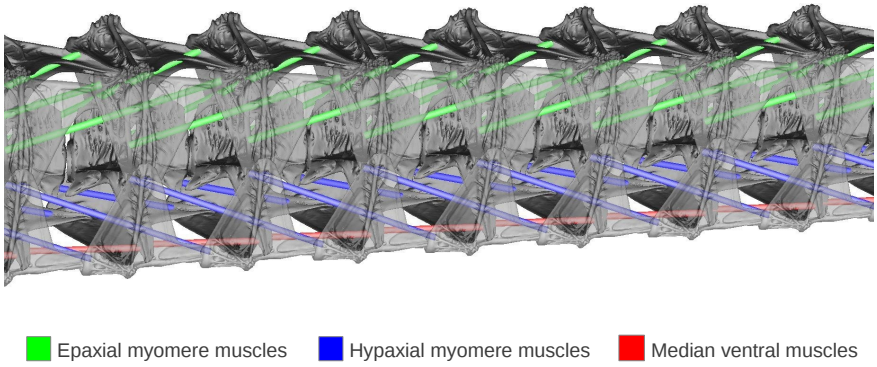

Figure 3.19: Modelled muscles in the seahorse tail.

3.3.4 Estimated muscle performance

Measuring muscle forces on the seahorse tail is challenging. The size of the muscles is very small and the generated forces are not so high. Luckily, the muscle performance can be estimated from a few parameters.

Muscle performance is largely determined by the timing of the muscle activity relative to its movement: maximum power production during cyclical movements requires fully active muscles during shortening and full relaxation during lengthening [86]. However, neither muscle activation nor deactivation are instantaneous events. To study the muscle movement, work-loop techniques are typically used: isolated fibres are subjected to cyclical length changes while measuring the force production. This method was used by Altringham and Johnston on muscles of the teleost fish *Myoxocephalus scorpius* [88]. Figure 3.20 shows some of the results on slow and fast muscle fibres. Muscle length of 0 is the resting fibre length as measured in a fish. The work required for the cycle of the fast muscle fibres (Figure 3.20A) was 6.43 μJ at 6 Hz cycles, whereas the work required for the slow fibres (Figure 3.20B) was 2.14 μJ at 0.5 Hz cycles.

Mean muscle-mass-specific power outputs of fish have been reported in ranges

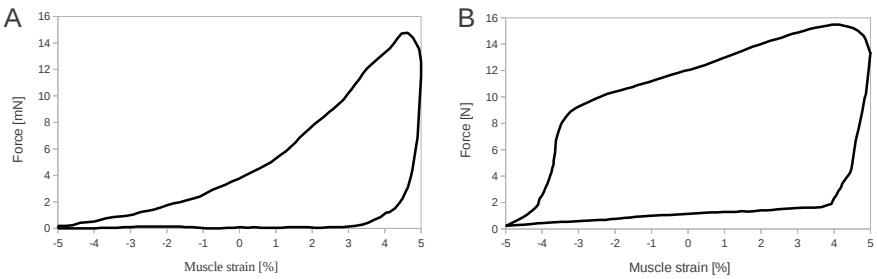

Figure 3.20: Example of fish muscle oscillatory work output of a fast muscle fibre bundle (A) and a slow muscle fibre bundle (B) [88].

from 18.1 $W\ kg^{-1}$ to 75.7 $W\ kg^{-1}$ [86]. Wakeling and Johnston also reported data on the fast fibre contractile properties in the rostral part of the fish tail: maximum fibre stress of $163.62 \pm 17.67\ kN\ m^{-2}$ in twitch, maximum fibre stress of $239.18 \pm 16.72\ kN\ m^{-2}$ in tetanus, and mean power output of $142.73 \pm 12.30\ W\ kg^{-1}$ [86]. The muscle fibre stresses for fish are lower than those for most skeletal muscles of land animals, e.g. Curtis et al. used a muscle stress of $300\ kN\ m^{-2}$ in their multibody simulations of the biting force of a lizard [89].

3.3.4.1 Cross-sectional muscle areas

Based on the estimated maximum muscle stresses we can make a conservative estimate of the maximum force that the different seahorse muscles can generate. For this, we need to know the cross-sectional area of each muscle. Since the tail becomes smaller towards the tail tip, the cross-sectional muscle area will also decrease.

The cross-sectional muscle area has been measured on the synchrotron scans, while the skeletal segments used in the simulation are based on μCT-scans of a different specimen of roughly the same size. Therefore, the cross-sectional areas of the muscles are measured as fractions of the total cross-section of the tail at that position (relative to the total length of the tail). This fits in the general philosophy of this dissertation to develop models that can easily be adapted to include other seahorse specimens and species (and possibly other species that are related to seahorses).

The cross-sectional areas were measured using the LabelStatistics module of Slicer 3.6, after manually selecting the muscles on transverse slices (the contrast of muscle tissue is, even in the synchrotron scans, too low for fully automatic segmentation). The slices were chosen as perpendicular as possible to the local anteroposterior axis of the tail. However, small divergence from this transverse plane cannot be excluded. Yet, since the relative and not the absolute cross-sectional areas are used, the effect of small errors in the direction of the plane should be

minimal. Figure 3.21 demonstrates how the different muscles were determined on a transverse slice of the synchrotron scan.

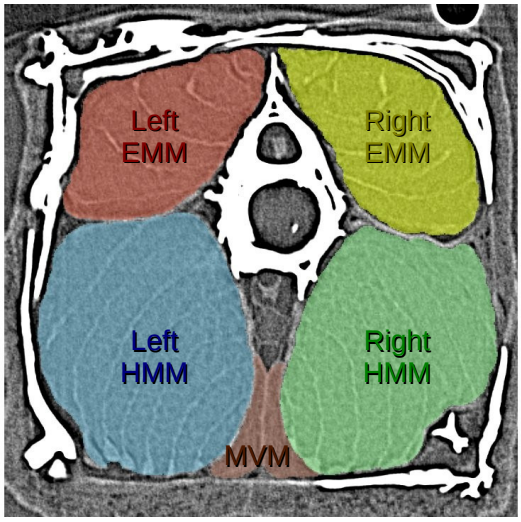

Figure 3.21: Determining the muscle areas on a transverse synchrotron slice of the 13^{th} *segment. The measured areas are* $1.280\ mm^2$ *for the left EMM,* $1.319\ mm^2$ *for the right EMM,* $2.518\ mm^2$ *for the left HMM,* $2.210\ mm^2$ *for the right EMM, and* $0.297\ mm^2$ *for the MVM.*

The seahorse tail counts roughly 30 segments. The relative muscle areas were determined within five segments of the tail (like in the rest of this dissertation, the first segment is the most anterior segment): segment 1, segment 5, segment 13, segment 21, and segment 25. The most posterior segments were not considered, since the cross-sectional area becomes rather small towards the tail tip, making it difficult to distinguish between the different tissues. The position within the segments was near the distal end of the segment, where the cross-sectional area of the muscles is the largest. The results of the measurements are summarized in Figure 3.22.

The relative size of the MVM clearly increases caudally. This means that the absolute cross-sectional area of the MVM posteriorly diminishes less than the total cross-sectional area of the segments. On the other hand, the relative cross-sectional area of the myomere muscles remains more or less constant. The average relative area of the HMM is 16.79%, with standard deviation 1.33%. For the EMM, the average is 9.01%, with standard deviation 1.27%. The seahorse tail is relatively symmetric around the midsagittal plane. This also holds for the myomere muscle: the difference in relative area between the left and right myomere muscles is not statistically significant, or at least not based on the limited amount of measurements that we used. Using one-way ANOVA, the significance level for the

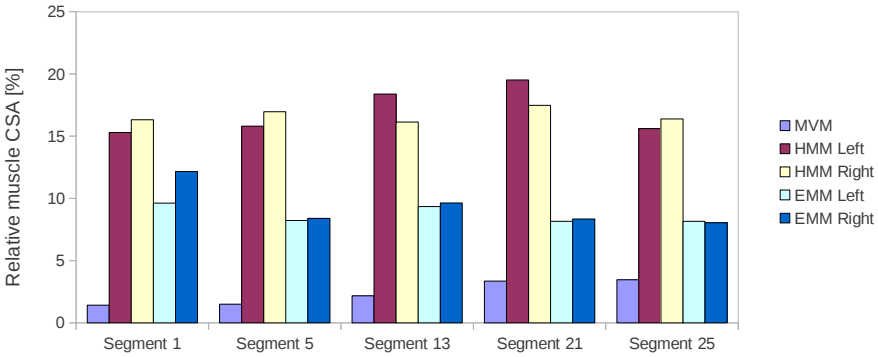

Figure 3.22: Relative cross-sectional area (in %) of the tail muscles at different tail positions.

average size difference between the left and right myomere muscles is 0.772 for the HMM and 0.327 for the EMM, where a significance level of less than 0.05 would be required to accept a significant difference between the average relative cross-sectional areas between the left and right muscles.

The synchrotron scans were taken with the tails in a ventrally bended position. This likely creates a shift in the relative areas of the hypaxial and epaxial muscles: the hypaxial muscles get slightly compressed (and thus their cross-sectional area increases), while the epaxial muscles get elongated (causing a decreased cross-sectional area). In any case, the cross-sectional area of the EMM is significantly lower than that of the HMM, even in a fully stretched tail. Since no synchrotron data is available on a stretched tail, this data will be considered to be sufficient as an approximation of the muscle cross-sectional areas. We do not pretend to get an precise estimate of the muscle forces, since there currently are too many unknowns for the seahorse tail muscles. Nevertheless, these calculations should suffice to get a rough estimation of possible muscle forces, so that the magnitude of the simulated muscle forces can be judged to be realistic or not.

3.3.4.2 Correcting for the muscle fibre angle

The cross-sectional muscle areas are measured in the transverse planes. However, the myomere muscle fibres do not run exactly in the direction of the anteroposterior axis (which is perpendicular to the transverse plane). To get an accurate estimate of the muscle force, an additional factor is required that accounts for the angle between the muscle fibres and the anteroposterior axis. To the best of out knowledge no data currently exists on the direction of the muscle fibres in the seahorse tail. To get a rough estimate of the required angle, the angle of some hypaxial muscle fibres was measured in the sagittal and the axial plane at a few locations in the most proximal segments of the tail, as demonstrated in Figure 3.23. Determining

the angles for the more caudal segments proved to be too challenging, as the tail curvature makes it difficult to determine the local anteroposterior axis.

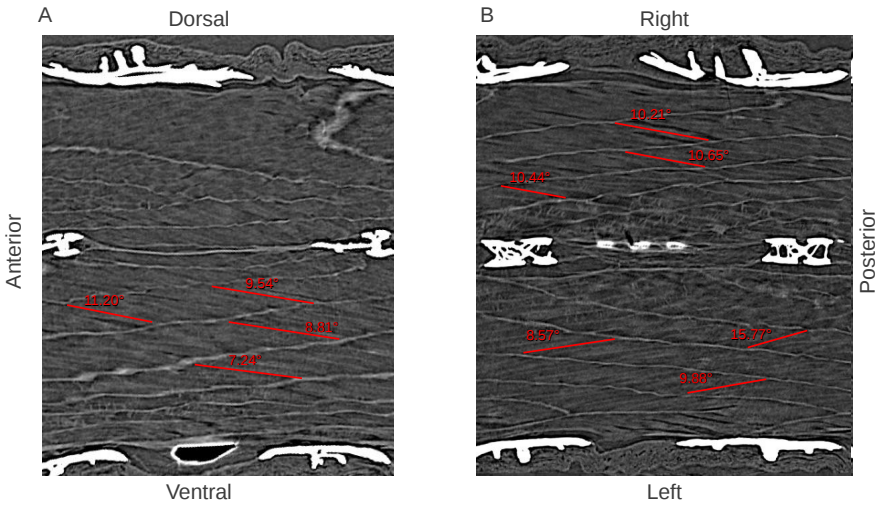

Figure 3.23: Angle between some hypaxial muscle fibres and the anteroposterior axis in a sagittal (A) and axial (B) slice of the synchrotron scan.

On average, both in the axial and sagittal plane the angle between the longitudinal axis and the muscle fibre was close to ten degrees. This results in a total angle of roughly 14 degrees. A more rigorous analysis on a preferably stretched tail would be required to confirm this estimate, and to study whether the pennation angle varies throughout the tail.

3.3.4.3 Estimated maximum muscle force

An estimation of the maximum muscle forces throughout the tail can be derived using Equation 3.5, in which S is the estimated maximum fibre stress, and PCSA is the physiological cross-sectional area of the muscle.

$$F_{max} = PCSA \times S \tag{3.5}$$

Since the fibres of the hypaxial myomere muscles are more or less parallel, the PCSA can be approximated by the maximum cross-sectional area of the muscle multiplied with a correction factor for the direction of the muscles fibres. This factor is the inverse of the cosine of the angle determined in the previous section (14 degrees).

For the tail scanned in stretched position this results in the maximum forces that are shown in the graph of Figure 3.24. The maximum fibres stress was taken at 239.18 $kN\ m^{-2}$, which is an estimation for the maximum stress in tetanus for

myomere muscles [86]. The fibres of the MVM are assumed to be directed parallel to the contraction direction (i.e. the anteroposterior axis), so no correction factor is used for these muscles. The cross-sectional area of the left and right myomere muscles is assumed to be equal.

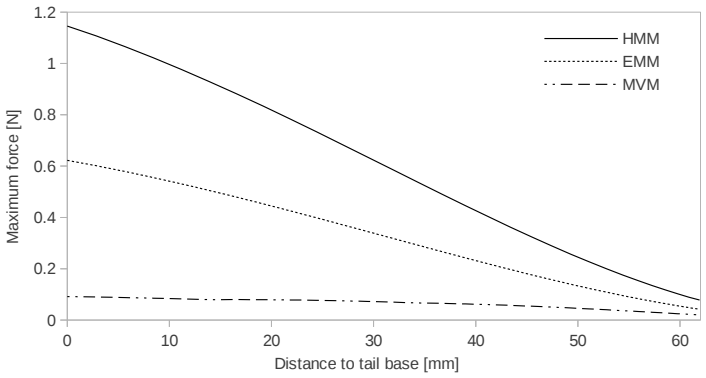

Figure 3.24: Estimated maximum contraction force of the muscles throughout the seahorse tail.

The maximum force of both HMM and EMM decreases drastically throughout the tail. The estimated maximum MVM force is more constant, but still shows an important decrease. The HMM seem to be able to generate much higher forces than the MVM upon ventral contraction. It is possible that the larger HMM forces are needed to account for the inertial and drag forces during relatively fast tail bending, while the MVM could be primarily used in situations where less force is required, like holding the tail bent around a support.

It should be noted that the presented maximum forces are only very rude estimates. Nevertheless, they do give an indication of the order of magnitude of forces that can be expected and/or allowed during the simulations. Another remark that should be made is that we will mostly simulate tail motion. It is very unlikely that the tail muscles would generate maximum forces during motion when no external forces are present, so the forces in the simulations should be considerably lower at all times. The presented maximum forces could be generated for example when the tail wraps very tightly to a support during very strong currents.

3.3.4.4 Characterisation of the passive muscle response

The passive muscle response of the myomere muscles will be considered in this section. The passive response of the median ventral muscles will not be covered, since the cross-sectional area of the MVM is low (so the elasticity of the muscle will be rather low), and because the ventral position of these muscles makes them unlikely to be significantly stretched when the tail is ventrally or ventral-laterally

bended (which are the situations on which we primarily focus in this research).

Upon ventral bending, the EMM plays the role of the *antagonist* muscle (or extensor muscle), whereas the HMM plays the role of *agonist* (or flexor muscle). Most fish use undulatory locomotion, in which case the antagonistic muscles during swimming are the muscles on the opposite side of the midsagittal plane. Passive and active muscles cyclicly alternate during undulatory swimming. The passive muscle function of the myomere muscles of the seahorse tail does not appear to be cyclic (the tail can remain bended for a prolonged period of time). This could be a possible explanation as to why the structure of the epaxial and hypaxial myomere muscles differs in seahorses: since the muscles do not operate in a undulatory way, and the tail is bended ventrally more often than dorsally, the passive extensibility is a less important parameter for the HMM than for the EMM.

Data on the passive muscle response of myomere muscles is rare in literature. For skeletal muscles of mammals, on the other hand, more data is available [90]. The muscle tissue's behaviour is known to be *viscoelastic*, which means that the muscles will appear to be stiffer when they are stretched faster. Moreover, viscoelastic energy in muscles is lost during stretching cycles, which manifests itself as a *hysteresis loop*. The passive response itself is typically exponential. The typical exponential response and hysteresis are demonstrated in Figure 3.25. The grey area shows the energy lost by hysteresis during one cycle.

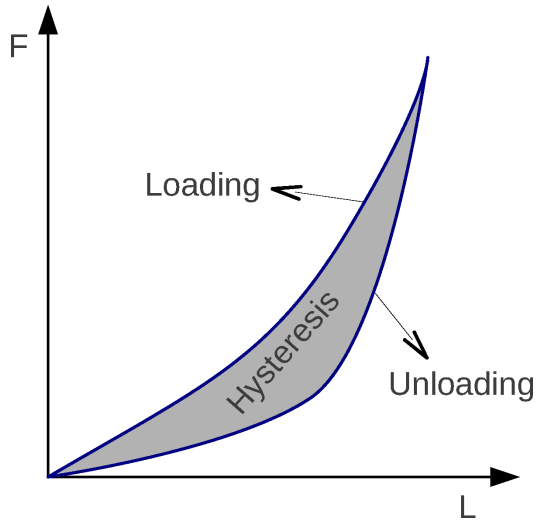

Figure 3.25: Force needed to passively stretch and relax a typical skeletal muscle.

Passive muscles will be modelled with a non-linear elastic (i.e. hyperelastic) response. The hysteresis (and thus viscoelasticity) will not be modelled: in contrast to other fish, the seahorse tail muscles are not used in long lasting cycles (no

undulatory locomotion), so the total energy loss due to hysteresis will be minimal and therefore neglected.

To get an accurate estimate of the passive response of the seahorse tail muscles, tensile tests were conducted on a sample of the HMM and EMM. The HMM and EMM on the opposite side of the body were used for histological cuts and thus allowed detailed analysis of the cross-section.

Figure 3.26 shows the result of the uniaxial tensile test on the HMM (Figure 3.26A) and the EMM (Figure 3.26B) samples. As mentioned above, passive muscles typically show an exponential response. The measured curve is therefore approximated by an exponential curve with general Equation 3.6. The exact values found for Equation 3.6 applied to both curves are summarized in Table 3.2. The fit of the exponential curves is remarkably accurate, as can be deduced from the presented graphs and the squared correlation coefficient in Table 3.2.

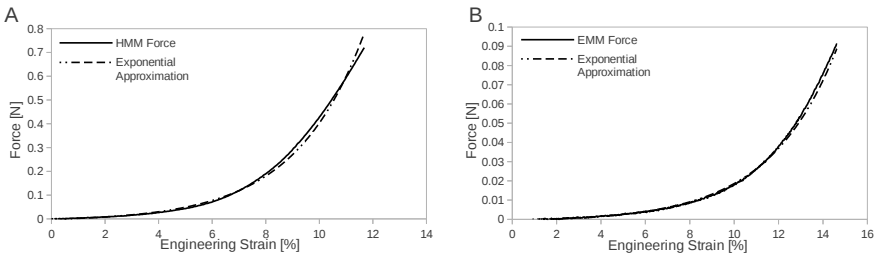

Figure 3.26: Passive response of the HMM and EMM muscles.

$$F(\epsilon) = e^{a\ \epsilon + b} + c \tag{3.6}$$

Muscle	a	b	c	R^2
HMM	0.388	-4.76	-0.0104	0.997
EMM	0.327	-7.19	-0.00126	0.996

Table 3.2: Parameters of the best fitting exponential curves.

The measured cross-sectional muscle area was 9.651 mm^2 for the HMM and 5.169 mm^2 for the EMM. In the scan of the seahorse tail in straight position (on which the models will be based), the areas of the muscle at the same tail position are 4.331 mm^2 for the HMM and 2.353 mm^2 for the EMM (obtained by using the cross-sectional size from Equation 3.2 and the relative areas from Chapter 3.3.4). Evidently, the seahorse specimen used in the µCT-scans was smaller than the one used for the tensile tests (or at least the tail was smaller). The ratio of the cross-sectional HMM area over the cross-sectional EMM area, however, is

similar: 1.87 on the histological slices, while the measurements on the synchrotron scans showed a ratio of 1.84. The measurements on the synchrotron scans are assumed to be more accurate (because of the distortion of the slices is assumed to be lower), so the latter ratio will be used in the modelling.

The passive extensibility of the muscles in the model will be approximated using Equation 3.6 with the parameters from Table 3.2, and scaled according to their local cross-sectional area divided by the cross-sectional muscle area in the histological cuts. We will assume that the muscle forces (both active and passive) vary proportionally with the cross-sectional area of the muscle.

When comparing the passive response of the HMM and EMM, the higher stiffness of the HMM is striking, even when factoring in the difference in cross-sectional area the HMM is still roughly ten times stiffer in extension than the EMM. The profoundly different myoseptal structure presumably plays a key role in this: in the HMM, the myosepta are more or less in the direction of the tension applied during the measurements. The resulting stiffness will therefore be determined for a large part by the myoseptal stiffness, and much less by the stiffness of the muscle fibres themselves. On the other hand, the myosepta of the EMM are folded into cones, so that they expand over a longitudinal distance smaller than the distance between the grips used in the tensile tests. Therefore, the stiffness of the myosepta will contribute less to the overall stiffness of the muscle, while the contribution of the fibre stiffness, the alignment of these fibres with the direction of the forces, and the volumetric changes of the cones will be more pronounced.

Another possible explanation for the large difference in passive extensibility is that, since the myosepta did not span the distance between the grips, damage accumulation of muscle fibres detaching from the myosepta during the tension resulted in a bad measurement. This damage would have been occurring during the first preconditioning cycle, since the difference in stiffness was already a factor ten during the very first loading cycle. More tensile tests on the muscle tissue would be required to determine whether the passive extensibility of epaxial and hypaxial really is that much different, or whether damaged tissue caused us to obtain bad measurements. We opted not to do this for the current research, as we did not want to sacrifice more seahorse specimens just for this purpose.

3.3.5 Mass density and bone volume fraction of the seahorse tail

When modelling the dynamics of the seahorse tail, the inertial properties of the tail could play a role. Therefore, the mass and volume of a tail of an adult seahorse specimen of the *Hippocampus reidi* were determined. The tail was cut at the most proximal caudal vertebra. The measured mass was 1.252 g and the volume 1.20 cm^3, resulting in an average mass density of 1.04 g/cm^3 for the entire tail. This

mass density is close to that of seawater ($\rho_{seawater} \approx 1.030\ g/cm^3$ [91]), which could be expected from the fact that the seahorse can easily float in seawater.

The tail consists of bone and soft tissues (muscle fibres, connective tissues, tendons, skin, ...). The density of bone is typically significantly higher than that of soft tissue. We therefore split the inertia of the tail into inertia caused by bone and inertia caused by soft tissue. Since the geometry of the bony segments varies somewhat throughout the tail, the bone volume fraction (ratio of bone tissue volume of a segment over the total volume of the segment) will differ between segments. Therefore, the bone volume fraction was determined for each tail segment using pyFormex. The measurement was done on a 3D surface model segmented from a CT-scan of a stretched tail of a specimen of the *Hippocampus reidi* species. The results are shown in Figure 3.27. The total length of the tail was 63.080 mm.

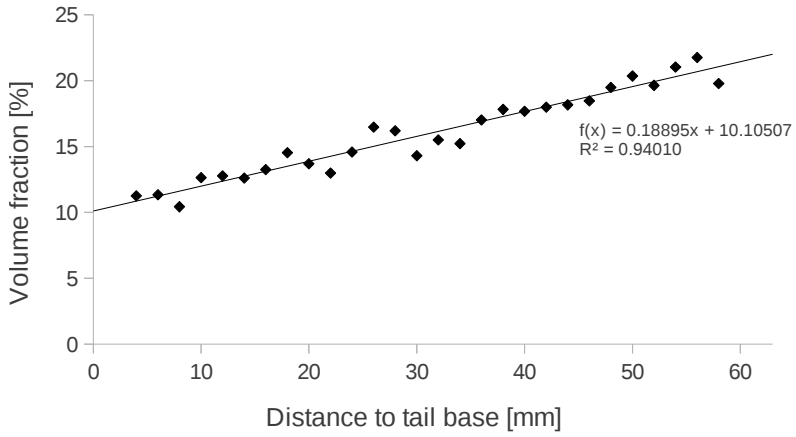

Figure 3.27: Bone volume fraction throughout the tail of a Hippocampus reidi specimen.

It appears that the bone volume fraction varies more or less linearly in function of length along the tail. The volume fraction of the bone (ϕ_{bone}) recalculated to the dimensionless length (l) along the seahorse tail is given in Equation 3.7. The Pearson product-moment correlation coefficient for the linear approximation is 0.940, as indicated in Figure 3.27.

$$\phi_{bone} = 0.115\, l + 0.10105, \quad l = 0..1 \tag{3.7}$$

For the most proximal segments, roughly 10% of the volume is bony tissue, whereas for the most distal segments, roughly 20% of the volume is bony tissue. So the volume fraction of the bone approximately doubles throughout the tail. This will have an important impact on mass distribution and therefore inertia throughout the tail.

The total bone volume fraction of a tail cannot be derived from Equation 3.7

alone, since the cross-section of the tail is not constant. In equation 3.2 the height and width throughout the tail was determined, so the cross-sectional area can be determined at all positions in the tail. With this cross-sectional area and the bone fraction equation 3.7, the volume of the tail bone (V_{bone}) can be determined, using Equation 3.8. In this equation, L stands for the total length of the tail under consideration (63.080 mm).

$$V_{bone} = \int_0^1 \phi_{bone}(l)\ H(l)\ W(l)\ L\,\mathrm{d}l \tag{3.8}$$

$$= \int_0^1 \phi_{bone}(l)\ H(l)^2\ L\,\mathrm{d}l \tag{3.9}$$

$$= 125.712\ mm^3 \tag{3.10}$$

Similarly, we can determine the total volume of soft tissues of the tail (V_{soft}).

$$V_{soft} = \int_0^1 (1 - \phi_{bone}(l))\ H(l)\ W(l)\ L\,\mathrm{d}l \tag{3.11}$$

$$= 771.988\ mm^3 \tag{3.12}$$

We can now determine the average bone fraction of the entire tail (ϕ_{av}).

$$\phi_{av} = \frac{V_{bone}}{V_{bone} + V_{soft}} = 0.140 \tag{3.13}$$

The average mass density of the soft tissue (ρ_{soft}) can be determined based on the mass and volume measured on the tail specimen (Equation 3.16). The differences in density between the different types of soft tissues (muscle fibres, myosepta, connective tissue, skin, ...) are neglected for the sake of simplicity. The mass density of the bone (ρ_{bone}) is assumed to be $1.80\ g/cm^3$ and constant. This value for fish bone density was taken from literature [92] and will be further discussed in Chapter 4.3.3.

$$m = 1.252\ g = V_{bone}\ \rho_{bone} + V_{soft}\ \rho_{soft} \tag{3.14}$$

$$= \phi_{av}\ V\ \rho_{bone} + (1 - \phi_{av})\ V\ \rho_{soft} \tag{3.15}$$

$$\Rightarrow \rho_{soft} = \frac{m - \phi_{av}\ V\ \rho_{bone}}{(1 - \phi_{av})\ V} = 0.920\ g/cm^3 \tag{3.16}$$

The specific mass density of fish myomeres is reported in literature as $1.06\ g/cm^3$ [71, 86], which is significantly more than the $0.920\ g/cm^3$ for the soft tissues found here. The largest volume fraction of the soft tissues is taken by the muscles, so the difference between the muscle mass density and the soft tissue mass density

should be lower. It is possible that the assumed bone mass density is a bit too high, or (though less likely) that the mass density of seahorse tail muscles is lower than that of other fish.

Finally, the local mass density in function of the relative position in the tail can easily be approximated with Equation 3.17.

$$\rho(l) = \phi(l)\ \rho_{bone} + (1 - \phi(l))\ \rho_{soft} \tag{3.17}$$

$$= 0.101\ l + 1.009, \quad l = 0..1 \tag{3.18}$$

Equation 3.18 gives a linear approximation for the local mass density throughout the tail and is represented as a graph in Figure 3.28. This approximation takes into account the density changes *between* tail segments, but it does not take into account the density changes *within* a segment (e.g. at transverse cross-sections near the posterior spines, the mass density would be considerably lower, since the dermal plates will have a smaller cross-sectional area in those regions). Since the masses of the segments will usually be modelled as concentrated in the centre of mass of the bony skeletal elements, this is not a real limitation for most simulations. In those cases that deformable bodies are used, the distribution of the bone mass is automatically taken into account by the finite element solver.

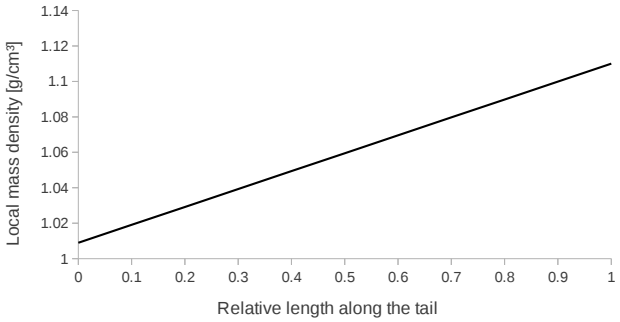

Figure 3.28: Local mass density of the tail.

It may seem contradictory that towards the tail tip, the relative volume fraction of the bones becomes larger, while the relative cross-sectional area of the myomeres stays roughly the same (and the relative cross-sectional area of the MVM increases, though slightly). The increase of the relative amount of bone, however, is mostly compensated by less soft tissues other than muscle tissue. The surface of the dermal plates becomes relatively larger for the more posterior segments (because the segments become more longitudinally stretched, and because of the inclination), and the thickness of the spines (of both the vertebrae and dermal plates) diminishes less quickly than the total size of the segments. For example, this will cause the more posterior MVM to be slightly shorter relative to the segment length.

It's not entirely clear whether there is a benefit to the larger bone fraction in the posterior part of the tail. As the segments become smaller and more longitudinally compressed, the number of articulations per unit of volume becomes higher. Perhaps this large number of joints partially accounts for the larger bone volume fraction. Also, the anterior segments are more longitudinally compressed, causing the triangular shapes of the flat surfaces of the dermal plates to be more sharply angled.

3.4 Conclusions

3.4.1 Skeletal structure of the seahorse tail

Based on μCT-scans, the skeletal structure of the seahorse tail was analysed. The tail consists of a chain of uniformly shaped segments that caudally diminish in size. The width and height of the segments are almost equal (so the cross-section is shaped like a square). The length of the segments is slightly smaller than the width and height for the most posterior segments, and almost half of the the width and height for the most anterior segments. The height, width, length, and inclination of each segment in the tail was measured and approximated by polynomials, so that the basic geometry of the tail skeleton can automatically be generated from the geometry of only one segment.

Each of the segments of the chain consists of one vertebra surrounded by four dermal plates. The dermal plates are connected by gliding joints, while the connections between the plates and the vertebrae behave like ball-and-socket joints. The joints between the vertebrae show a lot of rotational freedom and some gliding capability.

3.4.2 Muscle structure of the seahorse tail

Based on high-resolution synchrotron scans the muscle structure of the seahorse tail was studied. The tail has median ventral muscles on the ventral side of the mid-sagittal plane. The bulk of the muscle volume consists of myomere muscle fibres that are separated by large sheets, called myosepta. Based on whether these muscles are located ventrally or dorsally of the horizontal septum, they are respectively called hypaxial or epaxial myomere muscles. The epaxial muscle are structured in a cone-like configuration, which is typical for fish myomere muscles. The hypaxial myomere muscles show a more parallel configuration, which is uncommon. The seahorse tail can be bent ventrally (or ventro-laterally) for long periods of time, so the differing structure of the hypaxial myomere muscles could be an adaptation to minimize energy consumption during ventral bending, or an adaptation to reduce tail stiffness during ventral bending. Based on the observations, a simplified

model of the tail muscles, which can be used in the biomechanical modelling, was proposed.

A rough estimate of the maximum contraction forces of the muscles throughout the tail was derived based on the cross-sectional area of the muscles and the maximum fibre stresses. The estimated forces diminish caudally. The decline is more pronounced for the myomere muscles than for the median ventral muscles.

3.4.3 Passive muscle extensibility

The passive extensibility of the myomere muscles of an adult male seahorse specimen was measured by tensile testing and approximated by exponential curves. To find the passive response of the muscles in the tail models, the local cross-sectional area of the muscles is compared to the cross-sectional area of the tested muscles and scaled accordingly. The measured passive response of both the hypaxial and epaxial myomere muscles could closely be approximated by exponential curves.

The difference between the passive response of the HMM and EMM was large (almost a factor ten). It is possible that the passive response of both muscle bundles is indeed profoundly different, since the myoseptal structure is very different, but a bad measurement of the EMM muscle due to excessive damage to the connection of the muscle fibres to the epaxial myosepta cannot be ruled out. Since only one sample of each muscle type was tested, some reservation towards the quantitative results should be kept at all time. For the current study, sacrificing more seahorse specimens to confirm the results was considered less than ideal.

3.4.4 Mass density

Based on the measured average density of a tail and the bone volume fraction throughout the tail (measured on a segmented stretched tail), the local mass density throughout the tail was estimated. Neglecting the density differences within the segments themselves, the estimated local mass density rises linearly towards the tail tip.

4 Seahorse tail modelling

4.1 Introduction

Several models were constructed of (parts of) the seahorse tail. The details about the construction of the models will be discussed here, while the results of the simulations will be discussed later on in Chapter 5.

As part of the introduction, some modelling terms and techniques will first be discussed, as well as some relevant examples from literature.

4.1.1 Kinematics and dynamics

The terms *kinematics* and *dynamics* are frequently used in this and other chapters. In classical mechanics, kinematics is the study of motion (position, velocity, acceleration, rotation, angular velocity, etc.) without any consideration for what causes this motion (in essence, these causes of motion are forces). On the other hand, dynamics studies both motion and the causes of motion.

Kinematic analyses can be used to study and compare swim patterns of fish. For example, Herrel et al. used kinematic analyses to determine whether burrowing specialisation of anguilliform fishes affects the swimming kinematics [93]. They reported important differences in kinematics during backwards swimming, while kinematics during forward swimming appeared to be similar.

Specifically for the seahorse tail, looking purely at the motion of the tail, without consideration for the (inertial, drag, and reaction) forces that govern the motion, will require the use of kinematic techniques. For example, we can track the

motion of the tip of the tail while the seahorse grasps onto a support. Obviously, the amount of information that can be derived from kinematic analyses is limited. For example, kinematic analyses contain no information on the muscle forces involved in the tail motion. Most simulations on the seahorse tail will therefore be dynamic simulations that take into account the forces generated by the muscles (both active and passive), as well as inertial forces involved in the motion. Some other forces, like the drag forces, will be neglected in the current models. For a complex geometry like the seahorse tail, drag forces are not easy to determine. The movement of the tail is rather slow, but still the drag forces could be significant. Neglecting them is therefore an important limitation of the presented models when it comes to quantifying forces. The drag forces will, however, have little effect on the joint movements and tail kinematics.

Another neglected force is gravity. The effect of gravity on the simulation results should be minimal though. Firstly, the small size and mass density of the seahorse tail will keep the gravitational forces low. Secondly, the buoyancy will neutralize most of the gravitational effects, as the mass density of the tail was shown to be only slightly higher than seawater in Chapter 3.3.5. The modelling technique does allow for easy implementation of gravitational forces in future models.

4.1.2 Rigid body dynamics

In classical mechanics, a *rigid body* is essentially a solid object of finite size in which all deformation is neglected. This means that the distance between any two given points of the object remains exactly the same, regardless of its motion and regardless of the forces acting upon it. As such, the position in space of a rigid body (and all of its particles) is fully defined by the coordinates of one single point of the object (from here on called the *reference point*), and the angular position around this point (demonstrated in Figure 4.1).

Usually the centre of mass of the rigid body is chosen as its reference point, since in free space the motion of the centre of mass is generally the simplest motion of any of the points of the body. The three coordinates of the centre of mass and the three parameters of the angular position (rotations around the X, Y, and Z-axis) around it are thus the only six parameters required to fully define the spatial position of the rigid body (and all of its points) at a certain moment in time.

Rigid body dynamics is the study of the motion of rigid bodies and the causes of that motion, as can be derived from the aforementioned definitions. Rigid body dynamics is typically used in analyses and computer simulations of physical systems and machinery where rotations are important, while deformations have an insignificant effect on the motion of the total system. For example, a typical simulation that might use rigid body dynamics is the simulation of a four stroke engine, where the motion of shafts, pistons, and valves will be monitored. For all the ob-

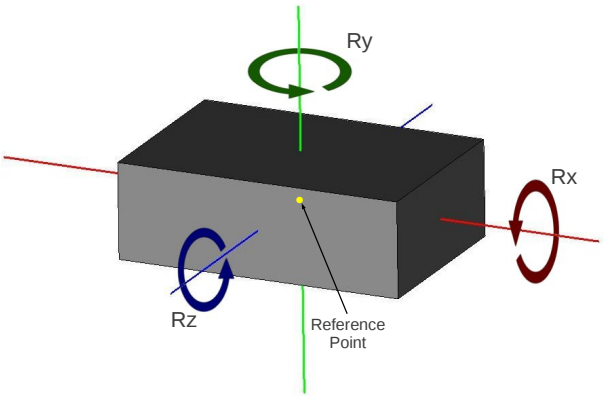

Figure 4.1: The position of a rigid body is fully defined by a reference point and the angular position (Rx, Ry, and Rz) around this reference point.

jects in the rigid body dynamic analyses, mass, centre of mass, and moment of inertia are primordial, as these parameters will determine the motion of the object when forces are applied.

4.1.3 Multibody dynamics

Multibody dynamics studies the dynamics of interconnected rigid or flexible bodies. In that sense, it is closely related to rigid body dynamics, but it goes a bit broader, since not all parts need to be rigid. As a result, multibody dynamics will focus even more on computer simulations (finding analytical solutions to deformable bodies is only reasonably feasible on a limited subset of rather simple loading conditions and geometries).

A multibody system consists of a collection of subsystems called *bodies*, *components*, or *substructures*. Different types of joints and contacts impose kinematic constraints on the motion of the subsystems, and each subsystem may undergo large translations and rotations [94]. Because of these large body rotations, the mathematical models underlying the multibody dynamics will generally be highly non-linear. Combined with deformable bodies the underlying mathematics of the multibody dynamic analyses becomes very complex.

Multibody dynamics is typically used for automotive applications, aerospace applications, robotics, and more recently biomechanics. Some examples of multibody dynamics in the biomechanical area can be found in the references [95, 96].

The models of the seahorse tail will include pure rigid body dynamics and multibody dynamics. The number of bodies in the simulations will often be extensive. Therefore, we will leave the solving of the seahorse tail models to the advanced solving capabilities of Abaqus, which is a software package dedicated to

solving complex finite element problems and commonly used in diverse engineering fields. The readers that wants more information on the mathematics involved in multibody dynamics are urged to consult specialist literature on the subject [94].

4.1.4 Forward and inverse dynamics

Multibody dynamic simulations on rigid bodies can be divided into two groups: *forward* and *inverse dynamics*. Simply put, forward dynamics computes the motion of rigid bodies based on the applied forces, whereas inverse dynamics uses body motions and measured external forces to calculate forces [96, 97]. This difference between forward and inverse dynamics is demonstrated more clearly in Figure 4.2. The components that are known at the start of the simulations are given with a black background, the unknown components are given with a white background.

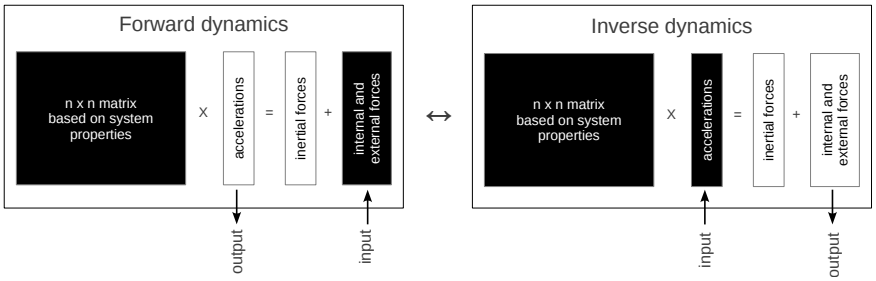

Figure 4.2: General principle of forward and inverse dynamic simulations.

Inverse dynamic simulations on musculoskeletal systems (like the seahorse tail) are often faced with an inherent problem: the number of unknowns (like muscle forces and joint forces) exceeds the number of equilibrium equations [96]. This means that there are many combinations of muscle recruitment that satisfy the observed motion of the musculoskeletal system. Such a system is called *hyper-redundant*. To solve this problem, researchers will often try to minimize some additional biological or neurological condition, like the forces acting upon a certain joint or the sum of all muscle forces [96, 98].

4.1.5 Multibody simulations in biology

Most publications on multibody dynamic simulations in biomechanics focus on human motion. Specialized software packages are available that specifically target multibody dynamic analyses in humans, e.g. the Simtk package[1]. However,

[1] Simtk is an open access software framework initiated and developed by Simbios, the National NIH Center for Biomedical Computing focusing on Physics-based Simulation of Biological Structures. More information can be found on `http://simtk.org`.

using these packages for simulating the motion of the musculoskeletal system of animals is not always so trivial, since anatomic features in animals can be very different than those in humans. Some packages that specifically target multibody simulations on animals do exist, like the GaitSym package (although these packages usually only target mammals). In this section, we will focus on literature of multibody simulations on the musculoskeletal system of animals.

Curtis et al. did extensive multibody modelling on the skull of the rhynchocephalian *Sphenodon* [89, 99, 100]. The geometry and modelled muscles are demonstrated in Figure 4.3A. Another reptile skull multibody model was published by Moazen et al. [101]. In both studies, the goal was to investigate the biomechanics behind the strong bite forces that these lizards can generate.

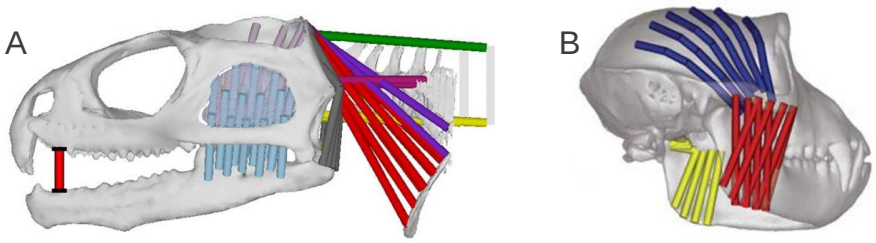

Figure 4.3: Multibody dynamic model of a reptile skull (A) [99] and a macaque skull (B) [102].

Besides reptile skulls, Curtis et al. also modelled the macaque skull [102]. This model is presented in Figure 4.3B. Again the focus lay on bite forces. The focus on bite forces of these simulations is logical. Firstly, bite performance is an important parameter in biology, as it can be a determining factor in the diet of the animal. Secondly, compared to many other forces, biting force is relatively easy to measure in a consistent way, for example by letting the animal bite on a force gauge.

Multibody analyses are not only an important tool for simulations on bite performance of extant (i.e. living) animals, but also for simulations on bite performance of extinct animals. Multibody dynamics have for example been used by Bates and Falkingham to estimate the bite forces of the *Tyrannosaurus rex* [103]. These simulations showed an important increase in bite performance during ontogeny of the *T. rex*, indicating that the prey range of these dinosaurs may have expanded to include the largest contemporaneous animals. Multibody analyses may thus prove to be an important tool in studying the behaviour of extinct animals.

4.1.6 Rationale behind the simulations

The general approach of the current study consists of five major steps, as demonstrated in Figure 4.4. In a first step, the geometry of the tail of a *Hippocampus reidi* was digitized using μCT-scanning. Using Slicer 3D (version 3.6), one detailed segment of the stretched tail was segmented into a surface model consisting of five skeletal elements (four dermal plates and one vertebra). From this reference segment, several models are generated using dedicated scripts in pyFormex (version 0.8.7). These dedicated scripts allow for the specification of parameters to easily adapt the models to different geometries, muscle contraction, speeds, etcetera. The result of the model generation are Abaqus input files.

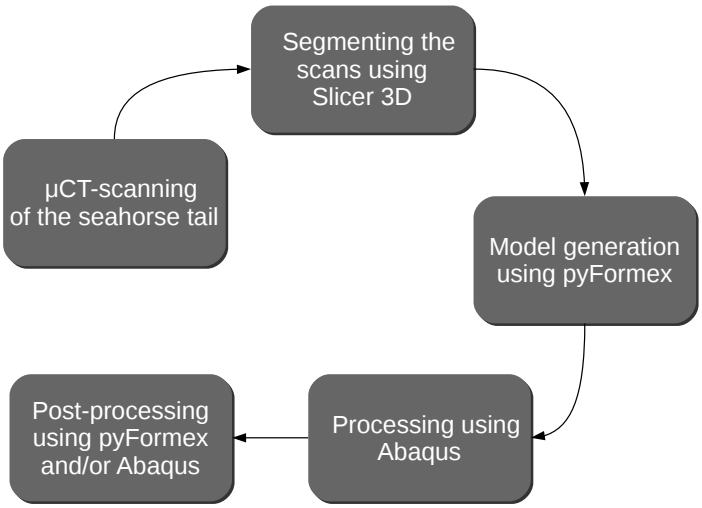

Figure 4.4: General approach that was used for the modelling.

The generated input files are afterwards solved using Abaqus (version 6.12), which is a finite element solver from the SIMULIA package (Dassault Systmes, Vlizy-Villacoublay, France). Using a finite element solver allows us to easily integrate deformable and rigid bodies in the same model.

The results are processed partially in the visualisation module of Abaqus, and partially within pyFormex (e.g. to make comparisons with measured data, generate graphs, or calculate volume changes). Dedicated Abaqus scripts are sometimes required to extract information from the output files that cannot be determined from within the visualization module of Abaqus, e.g. the bending and torsion angles of the segments of the tail.

Just in sheer numbers the complexity of the seahorse tail is already quite substantial: the total tail of the seahorse consists of 150 skeletal elements connected by 360 joints. Figure 4.5 shows a few anterior segments of a generated model with

the muscles, joints, and appropriate local axes systems. These are just a few segments; a total tail model has 30 segments. Clearly, the model complexity becomes very high when all segments are included. This makes the use of some regular simulation software impractical. Manually creating all connections and local axes of the joints on several models is laborious and to a certain degree user dependent. By using pyFormex, a lot of the work can be done automatically. Moreover, many parameters needed for the modelling of the seahorse tail are currently unknown or roughly estimated, and determining all of them accurately would vastly exceed the time available for this project. By using the parametric capabilities of pyFormex, we can generate the models with some first approximations for these parameters, that can later on easily be improved. Some parameters that are currently approximated by educated guesses are the Young's modulus of the bony elements, stiffness of the joints, exact muscle contractions, and so on.

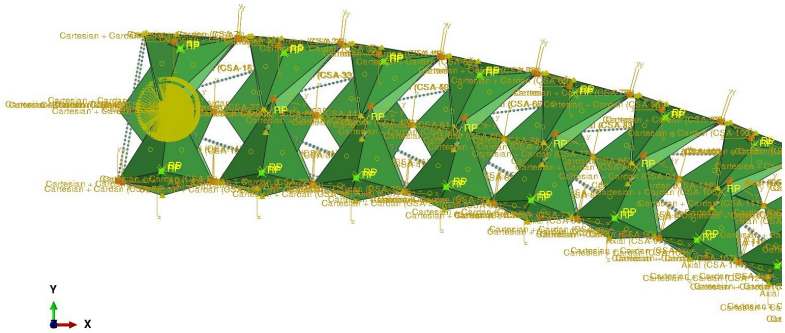

Figure 4.5: Example of the large amount of connectors and local axes in the anterior region of the tail model.

Forward and inverse dynamics input

The models constructed from within pyFormex can use forward or inverse dynamics. For the inverse dynamics, the motion of (some of) the skeletal elements can be used as input, or the motion of the muscles (changes in distance between the attachment points of the muscles). The latter has the advantage that the forces that are used to obtain the muscle shortening can be monitored (and for example be used in a subsequent forward dynamics simulation). A certain percentage of muscle shortening can be given for each muscle group (for example when the strain of certain muscles is known or can be estimated), or a list of shortening percentages of each individual muscle can be used as input. This list has to be provided in a csv file, which is a text file that can be generated form any regular spreadsheet software.

The forward dynamics need muscle forces as input. Not all muscles need to

be accompanied by a force for all simulations (for example, muscles on one side of the body can be activated while the muscles on the other side remain inactive). Again, the forces can be provided for muscle groups (either a force value for all muscles, or a value of force stress that needs to be multiplied by the cross-sectional area of the muscle), or for each individual muscle, starting from a list. Just like for the inverse dynamics, this list has to be in a csv file that can be accessed by pyFormex. The muscles that are not activated can either be neglected or given a certain passive extensibility. This passive extensibility will usually be calculated based on the expected cross-sectional area of the muscle.

Output that can be extracted from the models

Some outputs of the model can easily be visualised and extracted from the visualization module of Abaqus. This includes the displacements and rotations (and their time derivatives), stresses and strains of deformable bodies, etcetera. However, some other outputs require dedicated scripts to extract the data, and sometimes pyFormex scripts to visualize the results. For example, the torsion throughout the seahorse tail can be an important parameter, so a python script was written to calculate the local torsion of each segment based on the coordinates of the central vertebra of the segment.

Some outputs need to be specified before running the simulations. For example, the output files of Abaqus do not by default include the forces and moments generated by (or imposed upon) the connectors (these are the muscle forces and joint forces). The user needs to create separate sets of connectors and specifically request force output for these sets. In the current Abaqus version, the muscle and joint forces can only be shown in graphs, not colour coded in the visualization module.

A frequently used output that requires Abaqus scripts to extract is the joint compression or extension. Since the tail is very flexible and has several gliding joints, the movement of the joints can become extensive. To track this movement, scripts were written that extract the coordinates of the points that make up the joint (one point on each of the articulating bony elements).

Input parameters of the model

The parameters that are used as input for the model generation in pyFormex are listed below. Some parameters need to be provided by filling them in into the input menu that pops up upon starting the model generating scripts, other more extensive parameters need to be read in from csv files. In those cases the location of the csv file is used in the input menu, so that switching between files can be very fast. Some input parameters are numbers or text, others or just on/off switches for certain model features.

The exact input parameters are:

- Name of the input file that will be created.
- The number of tail segments that need to be generated.
- Path to the files that contain the geometry of the skeletal elements, both as a surface (for the simplified model) and as a volume (for the deformable segments), as well as the number of the reference segment from which the skeletal elements were segmented.
- Whether to include inclination of the segments.
- Whether to allow joint motion in the tip (most caudal tail segment).
- Whether to fixate the vertebra of the most anterior segment (this accounts for the constraint that the rest of the body imposes on the tail). Without fixation of the first vertebra, the tail will bend around a point that is near its centre of mass. Since inertial forces are typically very low, this will not significantly influence the results. Moreover, the kinematic analyses on grasping seahorses (discussed in Chapter 5.3.5) showed little movement of the tail base. Most simulations will therefore use the fixation of the first vertebra. In case that the reaction forces in the fixed point are needed, a connector should manually be created at this point and connected to the ground. Next, a set containing this connector needs to be created and the force and moment output needs to be requested for this point.
- Whether to use display elements (if not, the skeletal elements will just be represented by their centre of mass, muscle attachment points and joint locations).
- Total simulated time period (smaller values will augment the inertial effects).
- Time increment (only when no deformable bodies are present, as Abaqus will not be able to compute a stable time increment in that case). Lower time increments may improve stability of some simulations (especially when inertia becomes important), but will also augment computing time. The effect on the result is minimal as long as this value is sufficiently small (at least 1000 times smaller than the time period, but preferably much smaller).
- List of segments that should be deformable (all other will be rigid bodies).
- Which muscles should be included.

- Which muscle are active or passive, and if active, which are guided by contraction force or by shortening. Links to files can be included if the force or shortening differs between individual muscles of the same group.
- Parameters that determine the exponential curve of the passive response of the muscles (i.e. the parameters from equation 3.6).
- Elasticity of the joints (both translational and rotational, with link to a csv file if non-linear).
- Whether to start from a stretched tail position or a resting tail position.

The large amount of input parameters allows for en enormous amount of different simulations (though most will not be very relevant).

4.2 Materials and methods

4.2.1 Automated landmark detection using the shape index

In many simulations the geometry of the skeleton of the seahorse tail will be simplified. Some geometrical features have an important function when it comes to kinematics and dynamics. Therefore, these geometrical features need to be determined, preferably in a fast, user-independent way. Luckily, pyFormex offers a range of tools that help in automatically detecting landmark positions, most of which have been developed and optimized by Van Cauter [104].

To determine the location of the joints in the tail, the average is taken between two landmarks, one on each bony element involved in the articulation of the joint. To do the landmark detection in a general and user-independent way, we use the *shape index* [105]. The shape index is a parameter in the range [-1,+1] that indicates the local shape of the surface, as indicated in Figure 4.6. In this figure, the grey areas are the inner surfaces, while white areas are the outer surfaces. The shape index is calculated from the local principal curvatures k_1 and k_2 (with $k_1 > k_2$) using equation 4.1.

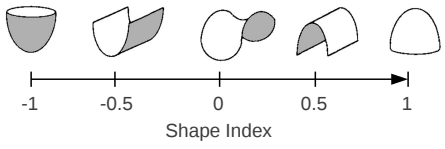

Figure 4.6: Shapes corresponding to different shape indices [106].

$$shape\ index = \frac{2}{\pi}\ arctan\left(\frac{k_1 + k_2}{k_1 - k_2}\right) \tag{4.1}$$

To be able to use the shape index for landmark detection, the surface model of the bony element must be very smooth, otherwise local fluctuations can cause incorrect results. Consequently, some smoothing operations need to be conducted on the segmented surface models. Laplacian smoothing is the most common procedure for surface smoothing. Sadly, Laplacian smoothing steps tend to 'shrink' the model, as the meshpoints on a convex surface slowly converge to their geometric centre during Laplacian smoothing. Since the landmarks we are looking for are often on the tip of a process, even small shrinkage effects can significantly affect the modelling results. To solve the shrinkage problem, a special algorithm, based on the HC-algorithm (Humphrey's Classes algorithm) [107], has been implemented in pyFormex and counteracts the shrinkage of Laplacian smoothing. After a few smoothing steps with this algorithm, the landmark detection based on the curvature shape factor can be used robustly.

4.2.2 Joint modelling

The anatomical details of the joints of the seahorse tail were discussed in Chapter 3.3.2. This section will focus on the modelling of these joints, while referring to the previously discussed joint anatomy wherever necessary.

The joints will be modelled using *connectors* in Abaqus. Such a connector is a connection between two points that can be given certain properties (stiffness, plasticity, damage, damping, failure, ...). Each connector has an axis system associated to it, so that the properties can be direction dependent. The property can depend on three translational directions (X, Y, and Z direction), and three rotational directions (rotations around the X, Y, and Z axis). Not all directions need to have properties, and directions can be kept fixed as well. In this way, the connectors can mimic joints. For example, a hinge can be defined by a connector in which all three translational degrees of freedom and two rotational degrees of freedom are fixed, while one rotational degree of freedom is left free (or given a certain stiffness). This situation is demonstrated in Figure 4.7. The figure on the right demonstrates how a hinge connector can be created in Abaqus: the available degree of freedom is UR1 (rotation around the first axis, i.e. the X axis), while the constrained DOF are U1, U2, U3, UR2, and UR3.

The elastic properties can be linear, in which case a single stiffness parameter needs to be provided per direction, or non-linear, in which case a list of displacements (or rotations) and corresponding forces (or moments) needs to be provided. In case of non-linear stiffness, the stiffness can be different for compression and extension of the joint.

When modelling the joints of the tail, we will avoid fully constraining a degree of freedom. Instead, we will use high linear stiffness in direction in which the joint is not supposed to move. This approach is chosen for three reasons:

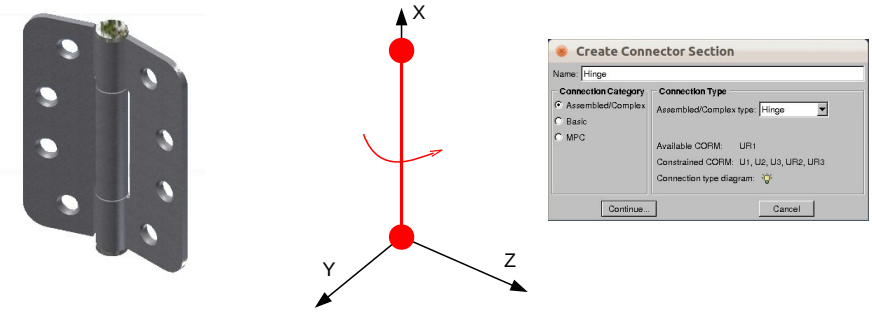

Figure 4.7: A hinge modelled by an Abaqus connector.

- In certain situations, a system that contains strictly constrained joints can become locked, as any displacement or rotation is countered by one or more of the constraints.

- Stability of the simulations will benefit from avoiding strict constraints. Should a joint be stretched in a direction of high stiffness, the potential energy of the total model will rise drastically, allowing detection of this unwanted situation.

- Joints in nature are never completely rigid. Small displacements in all directions are always possible up to a certain degree. So by using high stiffness in the models instead of rigid constraints, we can somewhat mimic this natural joint behaviour.

Similarly, joint directions in which the stiffness can be assumed to be zero, will sometimes still be given a very small linear elasticity to improve the stability of the simulations.

4.2.3 Muscle modelling

Similarly to the joints, the muscles were also modelled by connectors. These connectors are axial elements: the behaviour is only defined in the axial direction. This means that the connector representing the muscle is free to rotate, but the length is subjected to a certain behaviour. For an active muscle, time dependent length changes of the muscle or muscle force need to be provided. If the muscle is passive, then a non-linear extensibility needs to be provided for the connector that models the muscle. This extensibility is estimated based on tensile testing of the muscle tissue (Chapter 3.3.4.4). The response is scaled based on the maximum cross-sectional area of the muscle. The stiffness of the epaxial myomere muscles is much lower than that of the hypaxial myomere muscles.

An important parameter that is currently unknown is how much the muscles are stretched in the resting tail position. In this position, all passive forces are in equilibrium, but that does not necessarily imply that all muscles are at their unstretched position. Usually, the muscles will be somewhat prestretched, as to maximize the initial force they can generate (this force is the sum of the passive force caused by the stretching of the muscle, and the active force generated by contracting the muscle fibres). Visual inspection during muscle dissection showed significant shortening of the myomere muscles when the restrictions imposed by the neighbouring tissues were removed. The exact shortening, however, was not measured. Some of the shortening was counteracted by the prestretching steps used during the tensile tests. Also, the data given in Chapter 3.3.4.4 is already shifted so that the (0,0) coordinate is located at a small force of 0.01 N, which explains why the strain does not go up to 30%. This initial strain will be assumed to be equal to the prestretching. It is currently unclear whether this is a good approximation for the strain of the muscles in a resting tail.

The eventual passive response of the HMM and EMM that was used in the simulation is demonstrated in Figure 4.8. The force is scaled for a muscle with a cross-sectional area of 1 mm^2. The passive response of an individual muscle will be scaled according to its specific cross-sectional area.

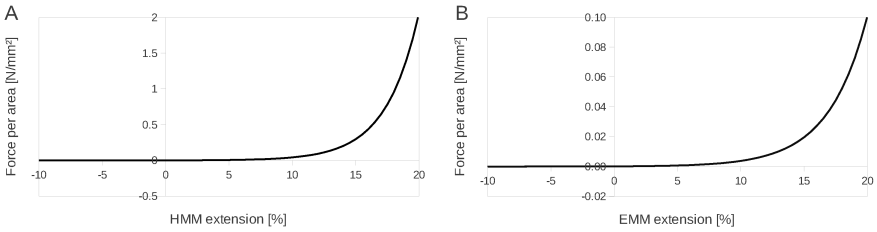

Figure 4.8: Modelled passive response of the HMM (A) and EMM (B) muscles.

4.2.4 Modelling of the seahorse bone

The bone of seahorses and most other teleosts is *acellular* and therefore somewhat different than the *cellular* bone of for example mammals and birds. Both cellular and acellular fish bone has a much lower Young's modulus than that of mammals and birds [108]. Research by Biltz and Pellegrino on the bone properties of adult vertebrates showed that acellular fish bone has the lowest density of all 16 considered species [92], namely $1.80\ g/cm^3$. It also has the highest water content and, apart from turtles, the lowest mineral content. The acellular bone of specimens of the *Lutjanus purpureus* fish species was taken as representable for all fish bone.

Bone has the known ability to adapt to changing mechanical loading conditions and damage accumulation by alterations in architecture (termed *modelling*)

and self-repair (termed *remoddeling*) [108–110], causing alterations in shape and material properties throughout time. Both bone modelling and remodelling are governed by local changes in strain or strain energy density levels. The detection of these local mechanical changes is widely attributed to *osteocytes* [108]. These cells reside within small holes in the extracellular matrix of the bone, called *lacunae*. However, the acellular bone of teleosts does not contain osteocytes. Moreover, basal teleost bone is cellular, so the lack of osteocytes in the acellular bones is a derived property. Consequently the acellular bone should have some mechanical advantage to the skeleton [108].

The lack of osteocytes should severely hinder the modelling and remodelling capabilities of acellular bone, but interestingly this does not seem to be the case. For example, sustained swimming will severely affect the mineralization and mechanical properties of the acellular bone of a fish [111]. How acellular bone is able to respond to changing loading conditions without the strain sensing capability of the osteocytes is currently unknown [108].

Detailed information on acellular bone properties of teleosts is very scarce in literature [108, 112]. This is probably because teleosts' bone is mostly small and full of long cavities, making the production of normal-sized test specimens cumbersome [112]. However, we do need exact values of the material properties of acellular bone, since some simulation in Chapter 5 will include deformable bodies.

Horton and Summers conducted a series of three-point bending tests on the ribs of the great sculpin (*Myoxocephalus polyacanthocephalus*) [109]. An average Young's modulus of $6.48\ GPa$ was found, while the standard error of the mean was $0.31\ GPa$. Cohen et al. tried to compare the material properties of cellular and acellular teleost bone [108]. The acellular bone was taken from specimens of the tilapia (*Oreochromis aureus*), while the cellular bone was collected from specimens of the carp (*Cyprinus carpio*). Bone samples were obtained from the ribs and from the operculum[2]. The samples of the operculum were taken in two directions: axial and dorso-ventral. The mean values for the Young's modulus were $8.6\ GPa$ (range from $3.5\ GPa$ to $10.87\ GPa$) for the acellular bone of the rib of the tilapia, $7.7\ GPa$ ($5.3\ GPa$ to $10.9\ GPa$) for the operculum bone in axial direction, and finally $5.8\ GPa$ ($5.1\ GPa$ to $6.0\ GPa$) for the operculum bone in dorso-ventral direction. Surprisingly, the Young's modulus of the cellular fish bones was not significantly different than that of the acellular fish bones. So although the structure and mineral content of the bone is very different, the (macroscopic) mechanical properties seem to be quite similar.

[2]The operculum is a bony flap that covers the gills of teleost fish

4.2.5 Resting tail position

The neutral position or resting position of the seahorse tail is the position in which the tail will be when all tail muscles are relaxed (i.e. the position of minimal potential energy). The tail bending at resting tail position will be taken as the initial position for many simulations. It should be noted that the resting position of the tail is not well defined: small changes can be applied by manual manipulations with minimal effort, and without the tail going back to the previous position. Also, the neutral position appeared to be dependent on the individual. The approximate resting tail position of several individuals was photographed by dr. Anabela Maia. In the end, a typical neutral tail position of an adult seahorse (*Hippocampus reidi*) was chosen (Figure 4.9) and digitized. The divergence from the midsagittal plane (i.e. the lateral displacement) is very small and therefore neglected.

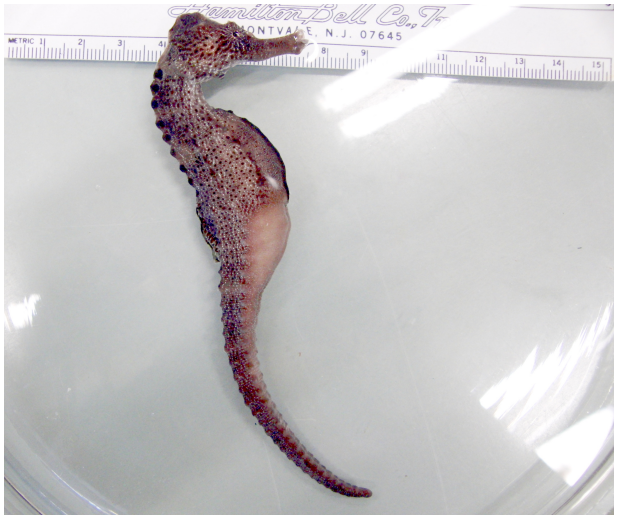

Figure 4.9: Neutral position of the tail. Courtesy of dr. Anabela Maia.

4.3 Results and discussion

4.3.1 Results of the landmark detection

4.3.1.1 Spine detection

The tip of the lateral spines of the vertebrae is detected using the shape index introduced in Chapter 4.2.1. Figure 4.10 demonstrates the shape index applied on the region of the left lateral spine (the colour coding is generated using pyFormex). The landmark that corresponds with the left lateral joint is chosen as the meshpoint

that has the highest shape index (black dot in Figure 4.10), since a shape index of 1 corresponds to a point where the local shape is perfectly elliptical.

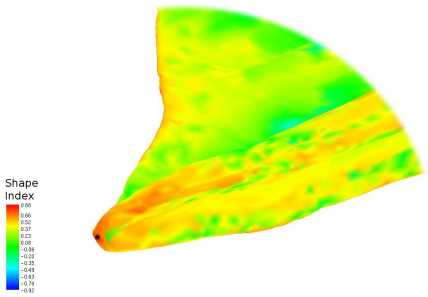

Figure 4.10: Landmark detection at the lateral spine of the caudal vertebra.

Similarly, the shape index method is used for detection of the tips of the neural spine, the hemal spine, and the tip of the ridges of the dermal plates (Figure 4.11).

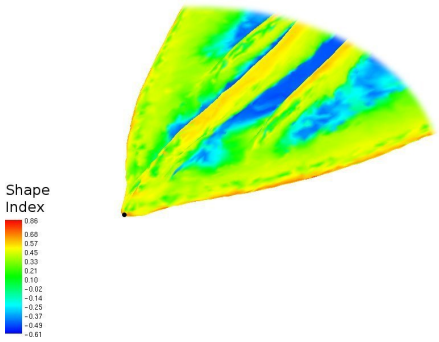

Figure 4.11: Landmark detection at the ventral tip of left dorsal dermal plate (lateral gliding joint).

4.3.1.2 Hemal spine and MVM attachment detection

The hemal spine is not only involved in the formation of a joint, it's also the anchoring point for the MVM. Based on visual observations on the synchrotron scans, an attachment at 90% of the total length of the hemal spine was deemed a good approximation for the position of muscle attachment (Figure 4.12A). To separate the hemal spine from the vertebrae, the main axes of inertia of the vertebra is used. After separating the spine from the rest of the vertebra, the main axis of the spine itself is calculated to obtain the direction in which the spine length should be measured (the hemal spine is usually tilted with its distal end at a more distal position within the segment compared to its base). At 90% distance, the attachment of the

proximal and distal MVM is taken as the intersection points with a line on the midsagittal plane perpendicular to the main direction of the spine.

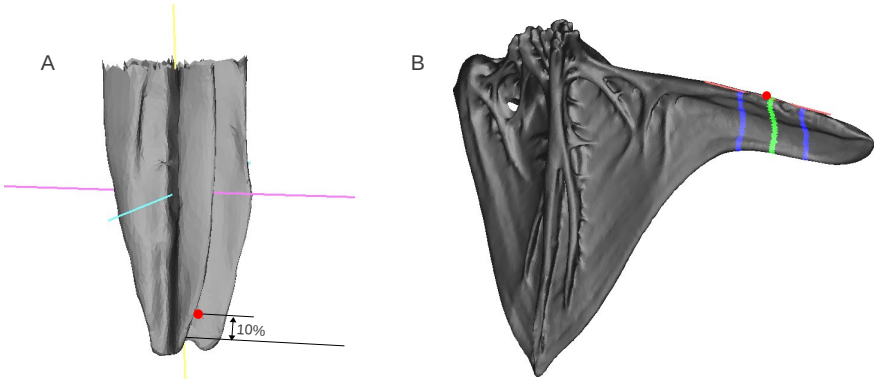

Figure 4.12: Position of the MVM attachment points (A) and the longitudinal gliding joints and their direction (B).

Figure 4.13 illustrates the connection between the two attachment points of the MVM between two subsequent segments (dark red line).

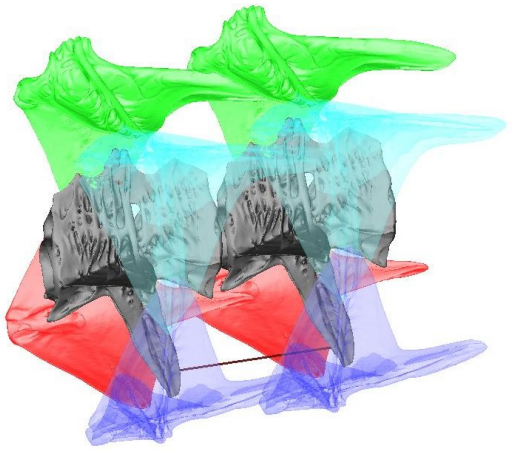

Figure 4.13: Position of the MVM muscle as a line between the attachment points.

4.3.1.3 Gliding joint detection

The gliding joint between subsequent dermal plates needs both a position and a direction (since the gliding direction is very specific for this kind of rail joint). In Figure 4.12B the red dot is the point of joint position, while the red line is the

direction of the gliding joint (i.e. the direction in which movement has minimal resistance). The joint position is at 23% of the length of the dermal plate, closest to the corner of the plate, while the direction is determined by the line that connects points at a 6% more proximal and distal position. These parameters can easily be adapted, but were set to these values based on expected compression and extension of the joint during common bending modes of the tail. If necessary, the direction can be further fine-tuned based on other expected intrusions of the distal spine into the proximal groove.

4.3.1.4 Vertebral joint detection

The joint between the vertebrae is the most important joint in the tail, as it determines the centre of rotation for each segment of the tail. It is a complex joint, consisting of two vertebrae that move around a sort of fluid sack (remnants of the notochord). The net result is that the two vertebrae can rotate around a certain centre of rotation located in between both, while maintaining some manoeuvrability in the translational direction (the fluid sack creates a gliding joint with rotational freedom). This joint will therefore be modelled as a translational and rotational spring. Translational stiffness is high in all three directions, but not as high as with the ball-and-socket joints. Rotational stiffness is low and equal around all axes. Using torsional springs for the intervertebral joint is common practice in dynamic analyses [71].

To calculate the centre of rotation for modelling purposes, the intersection of the vertebrae with a transverse plane at 20% of the length is taken, as demonstrated by the green points in Figure 4.14. From this intersection, the second largest intersection line is taken (since the largest will be the outer surface line and the smallest will be the surface of the neural canal). This line closely resembles a circle (pink points in Figure 4.14). The centre of this circle (red point in Figure 4.14) is then calculated by averaging the coordinates of the points of this circle. An algorithm was devised that calculates the centre of the best fitting circle, but the result was not significantly different from the average of the points on the circumference. The additional computing time needed to run such an algorithm was therefore considered unjustifiable. Finally, the centre of rotation is taken at the position of the average of the calculated distal point of the anterior vertebra and the calculated proximal point of the posterior vertebra.

4.3.1.5 Myomere muscle attachment to the vertebrae

The connection of the myomere muscles to the skeleton was discussed in Chapter 3.3.3.2. There it was argued that the myomere muscles attach to the vertebrae somewhere in the corner region created by the transversal and hemal spines. The connection points between the HMM, EMM, and vertebrae were approximated by

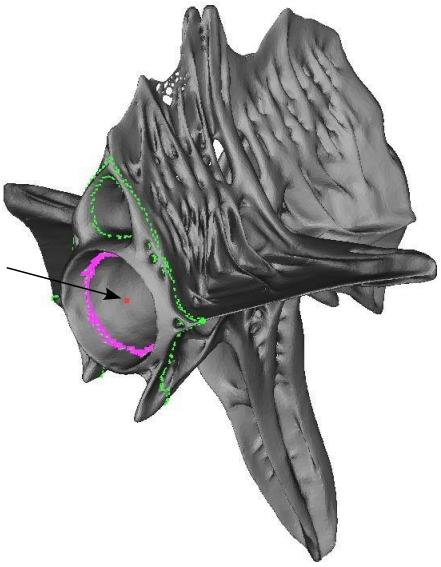

Figure 4.14: Centre of rotation between two vertebrae.

cutting the vertebra with two planes containing the X axis which are diagonal in the Z-plane (blue section in Figure 4.15), calculating the four extreme points and projecting those on the cross-section going through the centre of mass of the vertebra. The four connection points (two for the EMM and two for the HMM) which are calculated in this way are demonstrated by red dots in Figure 4.15.

4.3.1.6 Myomere muscle attachment to the dermal plates

On the caudal side, the HMM attach to the ventral dermal plates. Similarly, the EMM connect to the dorsal dermal plates. To find the landmark of the attachment to the dermal plates, the plate was cut with a plane perpendicular to the longitudinal axis at 8% of the total longitudinal length of the plate. This section was then again cut with a diagonal plane parallel to the longitudinal axis (blue area in Figure 4.16), so that only the ventral part remains for the ventral plates, and the dorsal part for the dorsal plates. From this area, the most proximal point (red dot in Figure 4.16) is now taken as the attachment point of the myomere muscle. This point approximates the position of the thick ventral tendons that are assumed to transmit the myomere forces to the ventral dermal plates.

4.3.1.7 Other landmarks

In addition to the aforementioned landmarks, there is one more point that is crucial for the dynamic simulations: the centre of mass of each skeletal element of the sea-

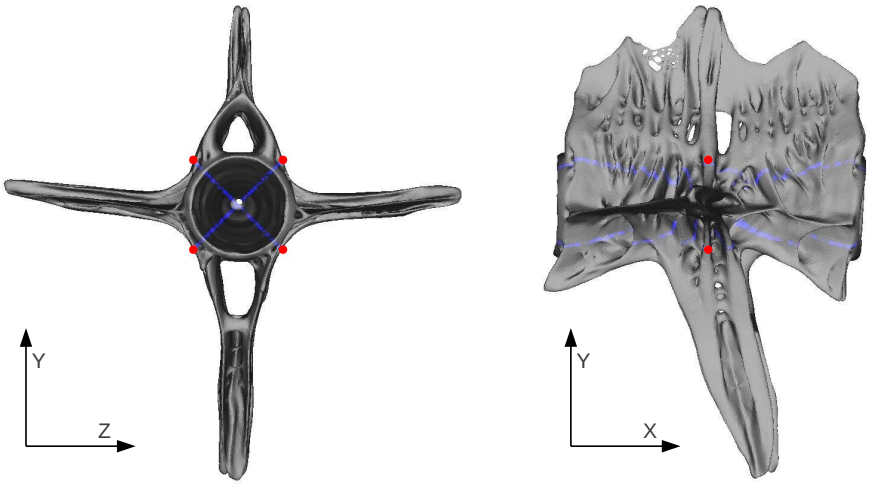

Figure 4.15: Connection points of the myomere muscles on the central vertebrae.

horse tail. This point is calculated for each skeletal element using the TriSurface plugin of pyFormex. At the same time, the rotational inertia around the main axes is calculated.

The segmented geometries are now substituted with a simplified representation that possesses the same important landmarks, as well as the properties that are important for dynamic analyses (masses and inertia). Figure 4.17 gives an example of a simplified model (the lines) and the segmented geometry that it corresponds to.

4.3.2 Joint modelling

The exact directional stiffness values that were used in the simulations are summarized in Table 4.1, and will be explained separately in the following paragraphs, as well as the exact non-linear behaviour. The given values are parameters used as input by the model generation script in pyFormex, and can therefore easily be changed, for example when more information about the behaviour of the joints in the seahorse tail becomes available. Open cells indicate that those degrees of freedom (DOF) are kept completely free (so no stiffness at all is associated with those directions).

Each joint can be given a damping factor as well, which can be useful when the simulations give unstable results. None of the presented simulations, however, will use damping in any of the joints.

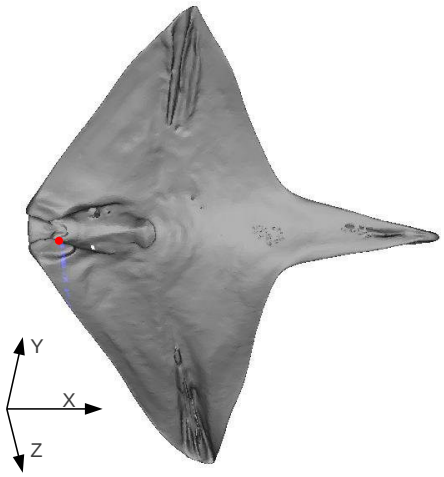

Figure 4.16: Connection point of the hypaxial myomere muscles on the right ventral dermal plate.

	X transl	Y transl	Z transl	X rot	Y rot	Z rot
Intersegmental gliding joint	non-linear	1e-6	1e-6	0.01	0.1	0.1
Intrasegmental gliding joint	1e-6	0.1	0.1	0.1	0.1	0.1
Vertebral joint	10	1	1	1e-6	1e-6	1e-6
Lateral joint	1	1	1	1e-6	1e-6	1e-6
Hemal joint	0.1	0.1	0.1			

Table 4.1: Assigned joint stiffnesses (in N/mm for displacement and N mm/rad for rotation).

4.3.2.1 Gliding joints between subsequent dermal plates (intersegmental gliding joints)

The gliding joints between subsequent dermal plates (Figure 3.13C) were modelled as connectors with a non-linear elastic response in compression along the direction of the groove of the joint, and a very small linear elastic response in extension. The other two translational directions were given a high linear elastic stiffness. Rotation around the local longitudinal axis (so around the distal spine) has a medium stiffness, the other two rotational directions have a high linear stiffness. The exact values are given in Table 4.1.

To get an estimate of the non-linear stiffness behaviour in compression, a displacement driven FE simulation was performed. In this simulation, two subsequent right dorsal dermal plates are pushed along the axis of the gliding joint in between both (Figure 4.18). Within the joint, frictionless contact between the surfaces of

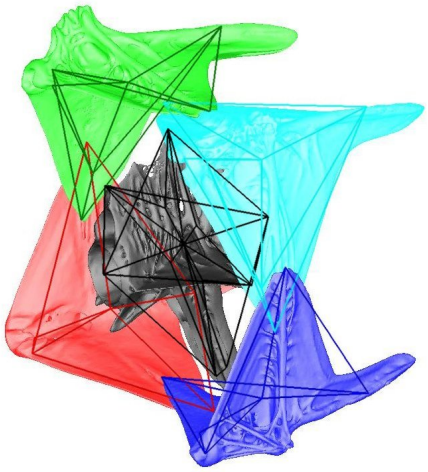

Figure 4.17: Simplified geometry of a segment of the seahorse tail.

both skeletal elements was assumed. Both skeletal elements were deformable, with a linear elastic material model that is discussed in Chapter 4.3.3.

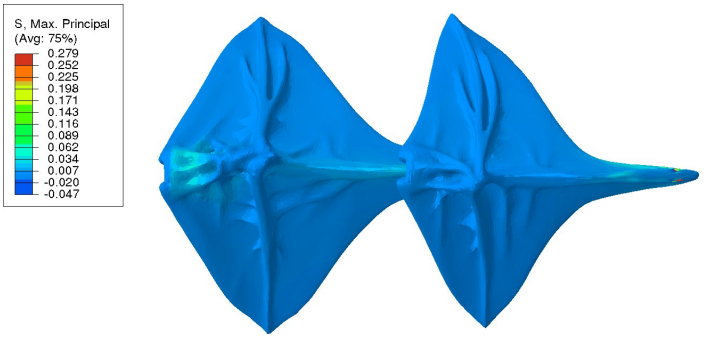

Figure 4.18: Principal stresses in MPa during compression of the joint between two subsequent right dorsal plates.

The exact force-displacement curve is given in Figure 4.19B. Compression and compressive force are given by negative values. From the graph it is clear that the force amplitude rises quickly in the grey area. This is caused by the limited size of the proximal groove in the posterior dermal plate that ends rather abruptly (Figure 4.19A). Once the joint is compressed to that point, additional compression requires high forces, since deformation of the bony elements will be large.

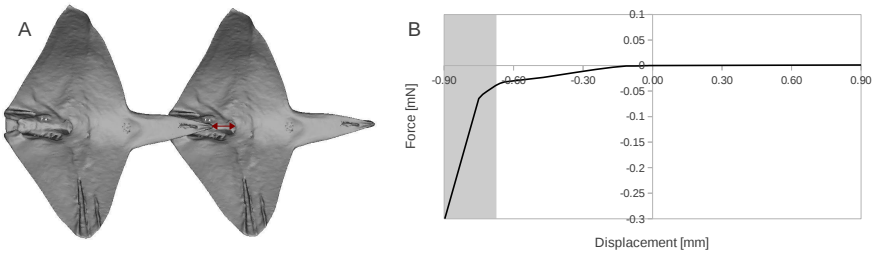

Figure 4.19: Gliding joint compression that reaches a maximum penetration after which the required force rises quickly.

4.3.2.2 Gliding joints between intrasegmental dermal plates (intrasegmental gliding joints)

Although the different gliding joints within the same segments (Figure 3.13D) differ slightly, they will be modelled as similar elastic joints. In the main gliding direction of the gliding joints (the local X axis), resistance against compression and elongation can be considered to be minimal. A very small linear elasticity is given to this joint in the X direction. The other translational DOF are given medium elasticity values, while the rotational directions have high values.

4.3.2.3 Joints between subsequent vertebrae (vertebral joint)

The behaviour of the joint between the amphicoelous vertebrae (Figure 3.13A) can be rather complex. The fluid sack in between could create a combination of a gliding joint (some translation in the directions perpendicular to the longitudinal axis could be possible) and a ball-and-socket joint (during large tail bending the spine behaves like a hinge). The presented model will focus on large tail bendings, in which case the hinge-like properties will be more important to the joint behaviour. Moreover, while a certain side of the tail gets contracted during bending, the other side gets stretched, with passive muscles storing the potential energy. This causes relatively large reaction forces within the joints between the vertebrae. These forces are presumably counteracted predominantly by the connective tissues around the joint, as well as by the incompressibility of the intervertebral fluid and contact between both vertebrae (as the reaction forces will mostly compress the joint in longitudinal direction). Given the large forces that will be imposed on this joint, we chose to severely limit the translations that the two vertebrae can undergo compared to each other, thus neglecting the gliding joint capability that is typical for the joints between amphicoelous vertebrae. Limiting translations in the backbone appeared to be vital for a robust functioning of the musculoskeletal model on a larger scale.

The rotational DOF will be given a very low stiffness, as rotations can become

high during bending of the tail. In the translational X direction, stiffness will be assumed to be high, since compressive forces will compress the (almost incompressible) fluids between the vertebrae, causing the vertebrae even to make contact during high tail bending. As discussed above, the stiffness in the Y and Z direction (so in the cross-sectional plane) will be rather high, neglecting the gliding capabilities of the joint.

In conclusion, the joints between subsequent vertebrae will be modelled as flexible ball-and-socket joints with linear elastic parameters that are summarized in Table 4.1.

4.3.2.4 Ball-and-socket joint on the lateral sides (lateral joint)

The joints between the lateral spines of the vertebra and the dorsal dermal plates (Figure 3.13B) will be modelled as ball-and-socket joints. This means that all translational DOF are limited, while the rotational DOF are kept free. Again, the exact numbers that were used are given in Table 4.1.

4.3.2.5 Joint at tip of the hemal spine (hemal joint)

At the distal tip of the hemal spine, connective tissues create a flexible joint with the ventral dermal plates. The joint was modelled as a ball-and-socket joint, with small linear elastic stiffness equal in all directions.

4.3.3 Material model of the acellular bone

Finding an appropriate material model for bone is always tricky: bone material properties show large variations and are usually not constant in time, nor in space, nor in direction [113]. Performing elaborate material testing on the seahorse bone fell outside of the scope of our research, since the bones of the seahorse are very small and irregularly shaped, especially in the tail, which would make the production of regularly shaped test samples and the quantifying of the material properties very time consuming. Because information on acellular bone is very scarce in literature, a simple material model was used for the deformable bodies in the finite element simulations. A linear elastic isotropic material model with a Young's modulus of $\mathbf{6.48\ GPa}$ (based on the average Young's modulus reported by Horton and Summers for fish ribs [109]) and a Poisson's ratio of 0.3 were used for those simulations.

For the acellular bone, significant difference in stiffness between axial and dorsoventral samples of the operculum was reported by Cohen et al. [108], indicating that acellular bone is not always isotropic (this means that the mechanical properties will depend upon the direction in which they were measured). Cohen et al. is the first to report on the anisotropic behaviour of acellular bone, and only in

bone samples from the operculum of tilapia specimens. Until more information is available on the actual mechanics of acellular bone, the seahorse bone will still be modelled to be isotropic.

For the majority of simulations performed, deformations were small to insignificant, so the effect of a more appropriate material model is supposed to be fairly limited (unless the Young's modulus of the seahorse bone is very different from the values found in literature for similar bony elements, which is unlikely).

Measurements on the microhardness of dermal plates of *Hippocampus kuda* specimens showed significant differences based on position on the plate, but not between dermal plates on different positions in the tail [10]. These hardness measurement on the dermal plates are an important indicator (but no proof) that the elasticity of the acellular bone in the dermal plates is non-uniform, while the elasticity modulus does not change significantly throughout the tail itself.

Other research on other fish did show important changes of bone stiffness throughout the tail. At least for herring (*Clupea harengus*) bones, mineralization and indentation modulus decreases caudally [114]. Also for the *Myoxocephalus polyacanthocephalus* studied by Horton and Summers, the most caudal ribs had significantly lower stiffnesses [109]. The bone of the fifth rib had the highest stiffness, though the considerable variability might mask the real change in stiffness throughout the body. One explanation for the higher proximal stiffness could be that the bones with higher stiffness are located in regions with higher muscle forces. Similarly, the possibility of higher bone stiffness in regions of the seahorse tail of high muscle forces could somewhat be expected, but the research from Porter et al. showed no such indications [10]. In any case, all bony elements were given the same material properties in the performed simulations.

4.3.4 Digitized resting tail position

From the digitized tail position, an appropriate strain for the MVM was determined, so that a simulation could be performed to move the segments from the stretched position to the resting position. This is needed because initial position of the skeletal elements is determined from CT-scans with the tail in a stretched (so not resting) position. A separate simulation was therefore used to assess the position of the skeletal elements after bending the tail to the resting position. This means that the skeletal elements of the tail are not just rotated to resemble a tail in resting position, but their precise position is determined from a simulation to account for small changes in angles or position, e.g. because certain joints move the bony elements closer to each other (or further away). The appropriate strains for the scanned tail that were derived from the digitized resting tail position are shown in Figure 4.20.

Figure 4.21 shows what the tail model looks like after bending it to the resting

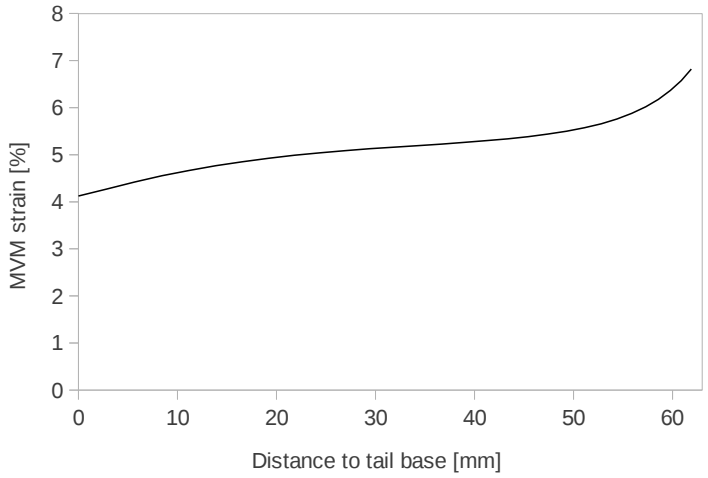

Figure 4.20: MVM strains needed to bring the stretched tail to the resting position.

position measured from Figure 4.9. This position will be used for simulations where the potential energy stored in the muscles is important, since in the resting position, the forces created by the passive muscles are balanced.

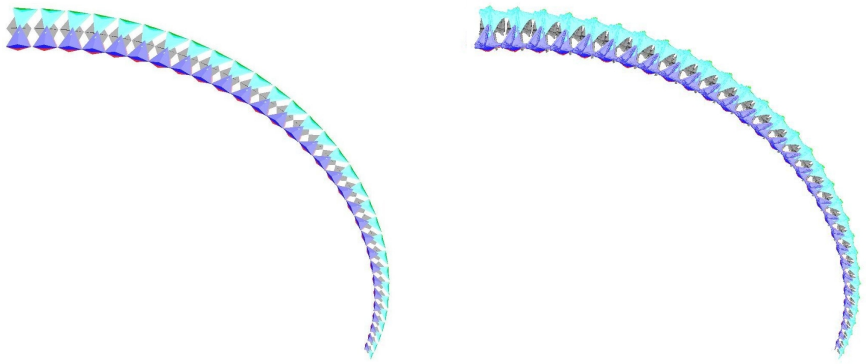

Figure 4.21: Neutral position of the tail imposed on the simplified model (left) and on the realistic geometry (right).

4.4 Conclusions

The model of an entire seahorse tail consists of such a large amount of skeletal elements, joints, and muscles that it becomes impractical to generate all models manually. Moreover, generating models of other seahorse specimens or species would each time require going through the entire model generating procedure. The models of the seahorse tail are therefore generated by dedicated pyFormex scripts. Many features of the models are parametric, so that many models can be generated in a short amount of time, and the models can be adapted as more information on some of the parameters becomes available.

The location of the joints and muscle attachment points is automatically determined based mostly on the shape factor at different locations of a segmented reference segment of a seahorse tail.

When the skeletal elements are modelled as being deformable, a simplified linear elastic material model is used for the bony structures of the tail, because detailed information on the material properties of acellular bone is scarce, and specifically for seahorse bone, currently non-existent.

The resting tail position (i.e. the position of the tail when there is no muscle contraction) of seahorses is not well defined, and is different for each specimen. A general resting position of one specimen was assumed to be a good approximation and representable for all specimens. The shape was digitized so that it can be used as a starting position for a variety of simulations.

5 Simulations

5.1 Introduction

This chapter will include the actual simulations on the musculoskeletal structure of the seahorse tail. Simulations can include rigid bodies, deformable bodies, or a combination of both. Throughout the development of the model, many simulations were performed on many versions of the model. Moreover, there is a large amount of parameters that can be chosen as input for the model. For some of these values, it is difficult to make a good estimate of the actual value in a real seahorse tail, so the used values of those parameters should be considered to be first approximations. This chapter will only include a very small portion of the total amount of simulations that were run. Hopefully the presented simulations will at the very least provide an insight in the range of possibilities provided by the developed biomechanical model.

Before going to the actual simulations and their result, some important principles will be discussed as part of the introduction.

5.1.1 Maximum principal stress

When visualizing results of finite element simulations on deformable bones, the colour coding will, unless specifically stated otherwise, include the maximum principal stresses, rather than the more often used von Mises stresses. Von Mises is in essence a yield criterion for metals, or by extension typical **ductile materials**. These are materials that show considerable plastic deformation upon failure, in

contrast to **brittle materials**, that show very little plastic deformation before failing. In brittle materials, the maximum tensile stress within the material is often a good parameter to asses the risk of failure, as failure in brittle materials usually initiates from small cracks. So generally speaking, using von Mises stresses is more relevant for ductile materials and maximum principal stress is more relevant for brittle materials.

Both the von Mises stress and the maximum principal stress are a scalar values at each point inside a material. So how do these values relate to the real stresses in that point? To fully describe the stress conditions at a certain position in an object, a stress tensor (equation 5.1) is needed, containing nine components: three normal stresses (σ) and six shear stresses (τ). These stress components are indicated on the left in Figure 5.1.

$$\boldsymbol{\sigma} = \begin{bmatrix} \sigma_x & \tau_{xy} & \tau_{xz} \\ \tau_{yx} & \sigma_y & \tau_{yz} \\ \tau_{zx} & \tau_{zy} & \sigma_z \end{bmatrix} \tag{5.1}$$

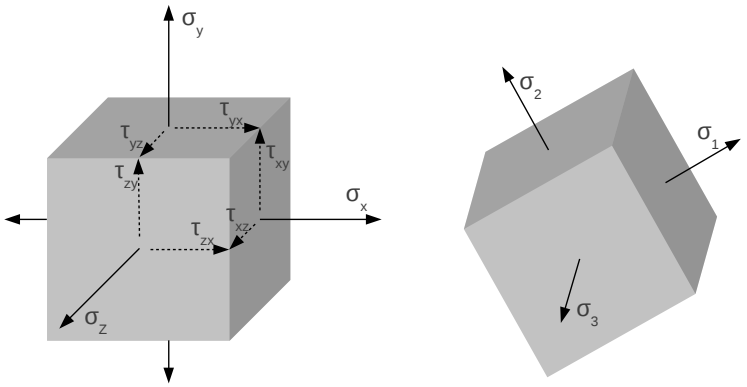

Figure 5.1: Components of the stress tensor (left) and principal stresses (right) on a small cube.

Creating colour plots with nine components is not feasible, and generating nine plots for every simulation is not very practical. So most of the time we have to limit ourselves to a scalar value that somewhat represents the state of the stresses residing within the material. The von Mises stress came into common use because it

provides an easily computable scalar value that is representable for the stress at a particular position inside typical ductile materials. For less ductile materials the von Mises stress is sometimes also used, although its physical relevance is debatable in those cases. The formula for the von Mises stress is given in Equation 5.2.

$$\sigma_v = \sqrt{\frac{1}{2}\left[(\sigma_x - \sigma_y)^2 + (\sigma_y - \sigma_z)^2 + (\sigma_x - \sigma_z)^2 + 6\left(\tau_{xy}^2 + \tau_{yz}^2 + \tau_{xz}^2\right)\right]} \tag{5.2}$$

From Equation 5.2, an important disadvantage of the von Mises stress can be derived: the von Mises stress is independent of external pressure. External pressure will increase the normal stresses (σ_x, σ_y, and σ_z) by the same amount, while the shear stresses remain unchanged. Since the normal stresses are subtracted in the von Mises stress formula, the von Mises stress is not influenced by external pressure. Depending on the goals of the simulation, this may or may not be a desirable effect.

The cube in Figure 5.1 can be rotated so that all shear stresses become zero. Only the normal stresses will then remain. In this special case the normal stresses will be called *principal stresses*. Obviously, the maximum principal stress is the maximum of those three principal stresses. To distinguish the principal stresses from the normal stresses, the principal stresses will be called σ_1, σ_2, and σ_3. These principal stresses are demonstrated on the right in Figure 5.1. There is no simple formula to quickly calculate the maximum principal stress from the stress tensor. The three principal stresses are the three real roots for S from equation 5.3.

$$\begin{aligned} &S^3 - (\sigma_{xx} + \sigma_{yy} + \sigma_{zz})\, S^2 \\ &+ (\sigma_{xx}\,\sigma_{yy} + \sigma_{yy}\,\sigma_{zz} + \sigma_{zz}\,\sigma_{xx} - \tau_{yz}^2 - \tau_{zx}^2 - \tau_{xy}^2)\, S \\ &- (\sigma_{xx}\,\sigma_{yy}\,\sigma_{zz} + 2\tau_{yz}\,\tau_{zx}\,\tau_{xy} - \sigma_{xx}\,\tau_{yz}^2 - \sigma_{yy}\,\tau_{zx}^2 - \sigma_{zz}\,\tau_{xy}^2) = 0 \end{aligned} \tag{5.3}$$

It can be proven that the maximum principal stress is the highest stress of all possible directions at that place. Since brittle materials will typically fail when the tensile stress becomes so high that (quickly expanding) cracks occur at a certain location within the material, the maximum principal stress is considered to be a good indicator for brittle failure.

In general, bone is not a typical ductile material, nor is it a typical brittle material. Its behaviour during failure depends on the loading conditions and mostly shows both ductile and brittle components (i.e. there is some plastic deformation upon failure, but usually not much). Human bone is more ductile at young age and more brittle at old age [115]. It is also more brittle at higher strain rates.

A very recent study by Porter et al. suggests that the bones in the seahorse tail can withstand rather large amounts of deformation [10]. The tail can be compressed by roughly 50% before permanent deformation becomes apparent. At

higher compressions, there is some plastic deformation of the bone, while parts of the tail skeleton buckle. Before this information was published, we chose to use principal component stresses when showing results of finite element simulations that include deformable bodies, assuming that acellular bone would show only small amounts of plastic deformation before failing. The new information suggests that the use of von Mises stresses instead would be more appropriate in this particular case. It currently cannot be excluded that the material properties of the skeleton observed by Porter et al. were influenced by the preservation method (immersed in 70% isopropanol). In any case, given the new information it would be prudent to compare the maximum principal component stresses that are provided in this dissertation to the von Mises stresses. It is likely that there are some quantitative differences between both, while the stress distributions are relatively similar.

5.1.2 Smooth amplitude

In order to avoid sudden peaks in forces, accelerations should be continuous throughout the simulations. Therefore, a smooth step amplitude will be used for all shortening of the connectors that represent the muscles, as well as for most of the forces. This means that the amplitude will change with time according to equation 5.4. The resulting graph is shown in Figure 5.2. The time step is chosen to be one second, but can be scaled to any other time step.

$$A(t) = -2\,t^3 + 3\,t^2, \quad t = 0..1 \tag{5.4}$$

$$\frac{dA}{dt} = -6\,t^2 + 6\,t, \quad t = 0..1 \tag{5.5}$$

$$\frac{d^2A}{dt^2} = -12\,t + 6, \quad t = 0..1 \tag{5.6}$$

The first derivative of the amplitude equation (equation 5.4), which is basically the speed of the connector shortening, yields equation 5.5. Both at the beginning of the step (t = 0 seconds) and the end of the step (t = 1 s), the derivative of the amplitude is zero, so that the connector shortenings are no longer causing any additional kinetic energy by the end of the step. And finally, the acceleration (equation 5.6) is continuous and varies linearly with time. During the first half of the simulation (t = 0 s to 0.5 s), the acceleration is positive (contraction speeds are rising), while during the second half of the simulation (t = 0.5 s to 1 s) acceleration is negative, so the muscle shortening is slowing down.

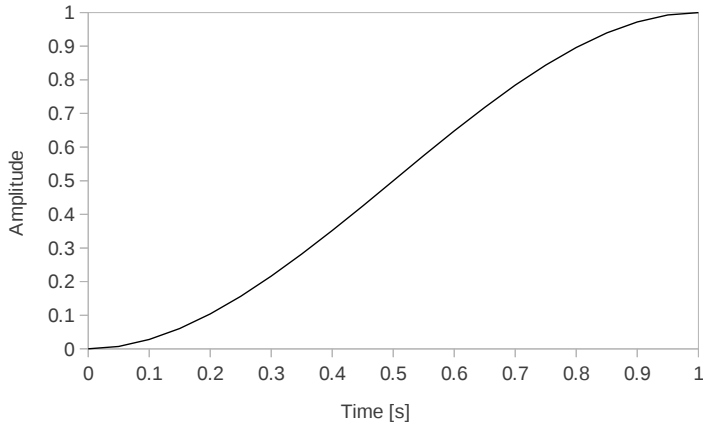

Figure 5.2: Amplitude that will be used for muscle shortening.

5.2 Materials and methods

5.2.1 Multibody dynamics models

Much of the materials and methods used to generate the models were discussed in the previous chapter. Using dedicated pyFormex scripts, the input files of the simulations are generated starting from a reference segment of the *Hippocampus reidi* tail skeleton, taking into account scaling and inclination measured on a μCT-scan of the stretched tail of the same individual. The passive extensibility of the myomere muscles was determined using uniaxial tensile testing equipment. The generated input files are solved using the finite element solver Abaqus 6.12. Results are analysed using the visualization module of Abaqus, dedicated Abaqus scripts, and dedicated pyFormex scripts.

Most of the simulations include only rigid bodies and thus rely on the assumption that the deformation of the skeletal elements during tail bendings is low enough to be neglected. This is a common assumption in biomechanical model, as the Young's modulus of bone is typically much higher than that of the surrounding soft tissues. Moreover, skeletal elements typically show low deformations under normal loading condition (otherwise the risk of bone fracture under slightly higher forces would be too high). However, the fish bone is less stiff than the bone of humans and other mammals that are the subject of the bulk of the biomechanical models. Some simulations will therefore be performed on bending tails that include some deformable skeletal elements, while checking whether the strains inside these skeletal elements remain negligible under the loading condition imposed by the tail bending.

Additionally, using deformable bodies opens a whole range of new simulation opportunities. But it also creates some new issues. For example, the use of con-

tacting surfaces helps to make the joint movement more realistic, but without any additional constraints to the joints, the simulation will fail as the slightest force on one of the deformable bodies can pull the joint apart (both deformable bodies will start to float freely through space). So, additional constraints are needed to keep the joints together. In reality, these constraints are created by ligaments, connective tissues, and other surrounding soft tissues. Like for rigid bodies, connectors can be used to model the necessary constraints in the joint regions. These connectors will again cause some issues though, as the nodes of the deformable body, in contrast to those of rigid bodies, can rotate freely, which makes the locally defined axes (that determine the direction of the joint or connector) useless. This is not a general principle, but a result of how Abaqus handles the finite elements of deformable bodies.

The issue of the freely revolving meshpoints can be solved by using a small trick: an additional meshpoint is added to the deformable body near the position of the joint. This point is then *kinematically coupled* with some points of the deformable body in the joints region (preferably at the surface that will be part of the joint). This means that this point will translate according to the coupled points, as well as rotate (the added point cannot rotate independently from the points it is coupled to). Figure 5.3 shows an example of a kinematically connected point on the posterior spine of a dermal plate.

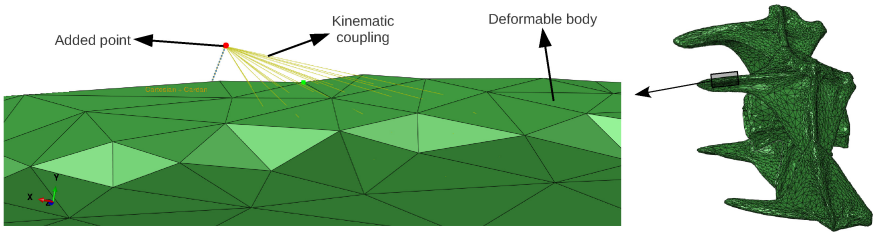

Figure 5.3: Close-up of the kinematic coupling of the joint at the posterior spine of a right dorsal dermal plate.

By adding kinematically coupled points to both deformable bodies involved in the joint formation, and adding a connector beam (with directional stiffnesses) between both points, the joint can be constrained in a proper way. The use of the kinematically coupled points will make the results in the joint region less reliable, as the elements that contain the coupled points can not freely deform (the strains are locally incorrect). So if the contact pressure in the joint region needs to be assessed, separate simulations will need to be performed, using only the deformable bodies involved for the specific joint, and with external (reaction) forces applied that mimic the effect of the other bones of the tail during the motion. The applied forces can for example be determined from the simulations with the kinematic coupling. As long as the focus is not on the strains in the joint, *Saint-Venant's*

principle[1] assures that the deformation in the rest of the deformable body (so away from the joints) is reliable.

5.2.2 Compressive model

Apart from the high bending flexibility, this study also focusses on the high radial stiffness of the seahorse tail. To get an idea of how the tail copes with the radial forces, finite element simulation using Abaqus 6.12 are carried out on the tail skeleton. In structures that are composed of materials with significantly different stiffnesses, the substructures made from the highest stiffness material will be most important for the overall stiffness of the structure. We therefore model only the skeletal structure (which has a relatively high stiffness), and not the soft tissues (which have relatively low stiffnesses). Stress concentration in the soft tissues are unlikely under radial compression, as the skeleton will be the supporting structure, except for the soft tissues located in direct proximity of the joints between the skeletal elements. The incompressibility of these soft tissues, however, may have a significant influence on the results. The amount of compression is therefore kept low.

Four adjacent segments of the stretched seahorse tail were segmented. The resulting surface models were preprocessed in pyFormex into volumetric models. The elements are linear tetrahedral elements. One important limitation of the current model is that the gliding joints (both intersegmental and intrasegmental) are not modelled. So during the radial compression, the dermal plates can not slide over each other. For small compressions this is not a large issue, but for larger compressions the influence will be high. Large compressions will not be modelled since the influence of the compressed soft tissues would become important. The joints between the backbone and the dermal plates are modelled, so forces that are imposed on the dermal plates can be transmitted via the vertebral spines to the backbone. In this way, the vertebrae support the dermal plates during the radial compression.

To compress the model, pyFormex is used to determine four planes that nicely fit onto the most protruding dorsal and ventral spines of the dermal plates. So the planes almost make contact with the skeleton, and shortly after the start of the simulation the planes will contact three points of that side of the skeleton (the irregular shape of the dermal plates makes it impossible to have a better initial contact). The four planes are illustrated in Figure 5.4 with their initial position. The planes consist of quadrilateral undeformable shell elements.

During the simulations, two of the four planes (left and right, or dorsal and ventral) start moving towards each other at a constant pace. This means that these

[1] Saint-Venant's principle states that the difference between the effects of two different but statically equivalent loads becomes insignificant at sufficiently large distances from the load.

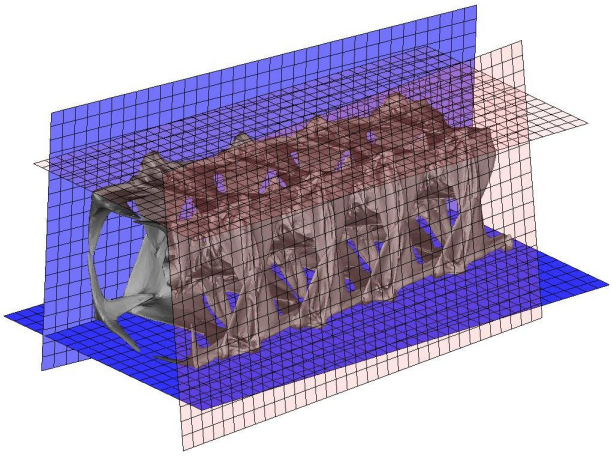

Figure 5.4: Planes used to compress the tail skeleton (the plates closest to the viewpoint are translucent for clarity).

simulations are displacement driven, which in turn means that contact forces can possibly rise very suddenly, with the risk of failure of convergence of the simulation (i.e. the simulation stops because too many increments are needed to obtain equilibrium), though this is only an issue during large compressions.

5.2.3 Measured tail kinematics

In order to relate the results of the multibody dynamics models to realistic tail motions, the grasping of live seahorses was quantified. The three-dimensional kinematics of the seahorse tail was recorded using high speed video (240 frames per second) by dr. Anabela Maia. Six live seahorse specimens of the *Hippocampus reidi* species were manually manoeuvred into the vicinity of a horizontal cylinder with a diameter of 8 mm, so they would grasp onto it. During the grasping, five more or less equidistant points along the tail were tracked. X and Y coordinate were respectively measured as horizontal and vertical pixels on the video. To obtain the Z-coordinate (i.e. the lateral movement of the tail), a mirror under an angle of 45 degrees was placed beneath the horizontal support, and again the vertical pixels were measured.

In total 15 kinematic recordings of grasping seahorse tails were obtained with five equidistant points, and one more detailed recording where 15 points were tracked, so that the curvature of the tail could be monitored more closely. For all 16 trials, the average recorded time of tail bending movement was 772 ms, with a standard deviation of 286 ms. This time frame (0.5 to 1 second) was therefore used for the bending time of the multibody dynamics models. As an example, one

frame of the detailed point tracking is demonstrated in Figure 5.5.

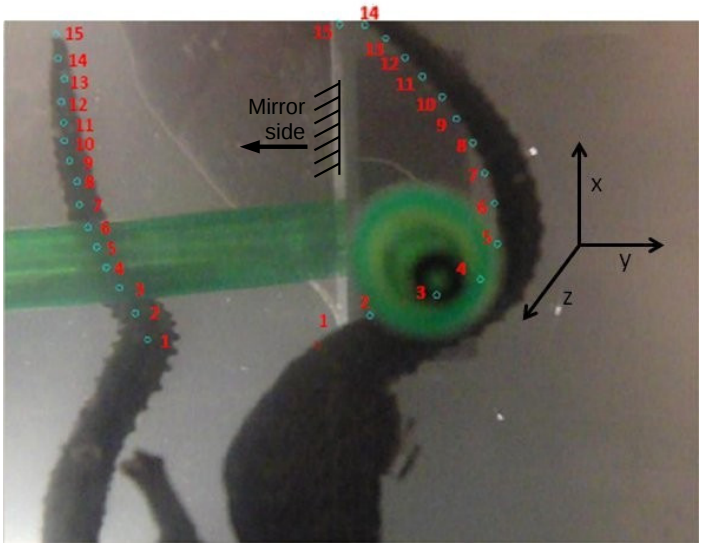

Figure 5.5: Point tracking on a grasping seahorse tail. Courtesy of dr. Anabela Maia.

5.3 Results and discussion

5.3.1 Rigid body dynamics simulations on the seahorse tail

The seahorse tail shows a very large flexibility in ventral direction, and a considerable flexibility in lateral and dorsal direction. The remarkable biomechanics of the seahorse tail depends largely on joint articulation, rather than local deformations. The macroscopic behaviour of the tail can therefore be modelled accurately by rigid body simulations, in which the skeletal elements are assumed to be rigid, and the movement is obtained by articulation of joints between the rigid bodies.

The musculoskeletal structure of the seahorse tail is most probably a *hyper-redundant system*. This means that a certain movement of the tail can be achieved by more than just one sequence of muscle activation. For example, a pure ventral tail bending can be achieved by a bilateral contraction of the hypaxial myomere muscles (HMM), but equally well by contraction of solely the median ventral muscles (MVM), where the contraction of each MVM is tuned to deliver the same tail movement. Combining activation patterns for the MVM, HMM, and EMM can result in a whole range of tail movements, much more than we can discuss here, and much more than can be observed in live seahorses as well. Some movements and muscle activations will be discussed in this chapter. This list of movements is by

no means exhaustive, nor does it pretend to be representative for all observed tail movements. The discussed tail movements should however demonstrate the flexibility of the rigid-body tail model to simulate a large amount of tail movements.

For simplicity, the rigid skeletal elements of the tail were substituted with objects of just a few elements that contain the important landmarks of the realistic geometry, as well as the parameters that are important for the dynamics. This was discussed in detail in Chapter 4. To make the generated figures below easier to interpret and more visually attractive, the realistic geometry is mostly superimposed on the movement of the simplified skeletal elements, which can easily be achieved by using the *display body* functionality of Abaqus. The superimposed geometries also provide a convenient way to visually check the joint movements, and to check whether intrusion of skeletal elements is acceptable. This is necessary since the contacting surfaces within the realistic geometries are not modelled within these simulations. Their effect is, however, modelled in the behaviour of the connectors that represent the joints by attributing large stiffnesses in the directions in which the bones would come into contact.

Since the model generation is parametric, many combinations of parameters and features are possible. For the convenience of the reader, Table 5.1 gives an overview of the most important parameters of the simulations of the following sections. Simulations that are force driven are forward dynamics simulations, whereas simulations that are not force driven are inverse dynamics simulations.

5.3.1.1 Natural ventral tail bending

Starting from the resting position of the tail (discussed in detail in Chapter 4.3.4), the tail model is bended ventrally by shortening the HMM and MVM simultaneously during one second (a realistic bending speed for the seahorse tail, as will be discussed in Chapter 5.3.5). The length changes of the connectors that represent the HMM are determined based on equation 3.1: the estimated regular muscle strains of the myomere muscles throughout the body of a fish. Given the different structure of the hypaxial myosepta of the seahorses, compared to the myosepta of other fish species, it is possible that the naturally occurring strains in the seahorse's muscle fibres is very different. Measuring the strain or activation patterns of the myomere muscles of the seahorse tail is very difficult due to the small size of the seahorse tail, the large amount of muscles, and the dermal plates that largely cover the myomere muscles. Connector shortenings that are derived from equation 3.1 will hereafter be called *natural muscle shortening*, and tail bendings that result from such shortenings will be called natural tail bendings. A total of 30 caudal segments in a tail at full length will be assumed here and for the remainder of the chapter. This parameter can easily be changed, but this has little qualitative influence on the results.

The data on the muscle strains does not state clearly where the strains were

Section	RP	FD	MVM contr	HMM contr	Remarks
5.3.1.1	yes	no	natural	natural bilateral	Tail bending when using natural muscle strains
5.3.1.2	yes	no	uniform	no	Maximum ventral bending based on geometrical considerations
5.3.1.3	yes	no	linear	no	Matching the MVM shortening to measured maximum bending
5.3.1.4	yes	no	linear	no	Matching the MVM shortening to observed tail bendings
5.3.1.5	yes	yes	no	uniform bilateral	Bending when all HMM forces are equal
5.3.1.6	yes	yes	based on CSA	based on CSA	Bending when all muscle forces are proportional to their CSA
5.3.1.7	yes	no	no	natural ipsilateral	Bending when using ipsilateral natural muscle strains
5.3.1.8	yes	no	no	uniform ipsilateral	Bending when using ipsilateral uniform muscle shortening
5.3.1.9	yes	yes	based on CSA	ipsilateral based on CSA	Bending when ipsilateral forces are proportional to their CSA
5.3.1.10	no	no	natural	natural bilateral	Testing the effect of segment inclination

Table 5.1: Overview of the various features used in the simulations (RP = starting from the rest position, FD = force driven simulation, contr = contraction, CSA = cross-sectional area).

measured. Since the fish body curves along the midsagittal plane during swimming, the muscle strain will be higher for muscles that are further away from the midsagittal plane, and smaller for the muscles closer to the midsagittal plane. The strain could have been measured near the skin, in which case the strain is the highest strain for any muscle fibre in that region. But it could also be interpreted as the cross-sectionally averaged muscle strain in that position (which would roughly be the strain in the center of the muscle). We will assume the latter.

The connectors used in the muscle modelling only allow for a single strain that is applied along the entire length of the connector. The connectors that represent the HMM run from the dorsal side to the ventral side of the myomere muscle bundle, and thus comprise equal parts of regions of both high and low strains during ventral bending. The muscle also runs from a medial position anteriorly to a lateral position posteriorly. Consequently, during lateral bending the connector will also go through an equal amount of regions of lower (medial) and higher (lateral) strains. Therefore, the average strain throughout the connector will be taken directly from equation 3.1.

The shortening of the MVM connectors is determined so that it is compatible with that of the HMM. If not, high reaction forces can occur within the model, resulting in unrealistic displacement of certain segments. Since the MVM are located almost at the ventral edge of the midsagittal plane, the strain in the MVM will be almost double the average strain in the HMM when the tail bends ventrally. The resulting tail position after the normal ventral bending is shown in Figure 5.6.

The curvature clearly becomes progressively larger towards the posterior end of the tail, caused by a combination of higher muscle shortening (equation 3.1) and smaller segment lengths (equation 3.11) towards the tail tip.

Energy considerations during natural ventral bending

The external work, potential energy, and kinetic energy throughout the simulation are given in Figure 5.7. Except for the first few time steps of the simulation, when all energy levels are very small, the kinetic energy remains less than 1% of the potential energy. In the second half of the simulation, kinetic energy really becomes negligible (less than 0.05% of the potential energy). Decreasing the total time of bending (and thus increasing the speed of muscle shortening) will increase the relative importance of the kinetic energy, though significant amounts of kinetic energy only occur during contraction speeds that are much higher than observed on live seahorses.

The kinetic energy is very small throughout the simulation, and no energy is lost during the simulation (no friction or damping), so almost all energy delivered to the model is stored as potential energy. This potential energy is stored in the passive muscles and in the springs that represent the joints. The difference between the potential energy and external work is so small that both graphs are almost

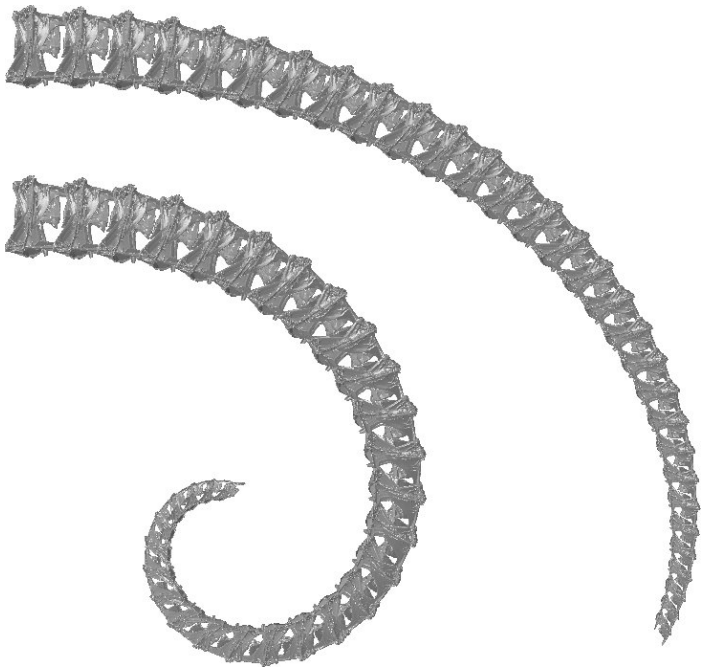

Figure 5.6: Resulting tail shape before (top) and after (bottom) muscle shortening based on normal hypaxial myomere strains.

indistinguishable from each other in Figure 5.7.

Since the kinetic energy is low, the impact of the dynamics is rather low. The shape of the tail during bending will therefore not differ significantly when the total time of contraction is augmented, or shortened moderately. Only when the bending becomes much faster than what was observed on living seahorses, will the dynamic effects become visible. Besides the rather slow movement of the seahorse tail, the cause of the negligible dynamics lies in the small dimensions, and hence masses, of the seahorse tails. Since the kinematic energy is low, the tail will not continue to move when the muscle length is held constant at the end of the simulation.

If the muscle length limitation is removed after the simulation, the potential energy in the model will be converted into kinetic energy: powered by the elastic strain energy stored in the passive muscles and the elastic joints, the tail starts moving back towards the resting position. However, since no energy dissipation is used in the modelling, the tail will keep moving indefinitely, constantly distributing the available energy between movement (kinetic energy) and elastically stored energy (potential energy). The tail basically starts resonating at certain (high) natural frequencies, resulting in rather complex cyclic movement that depends on the applied

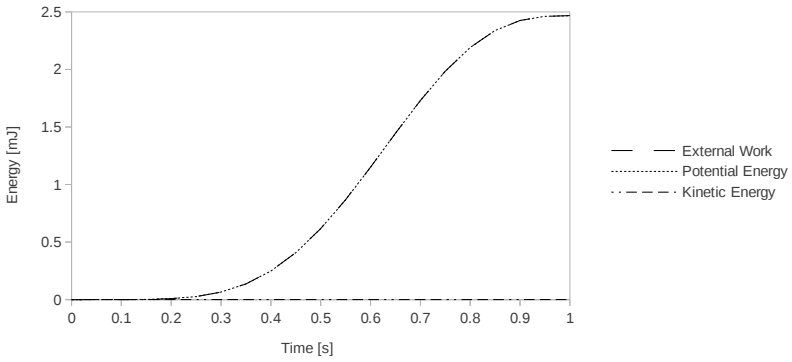

Figure 5.7: Energy graphs for the ventral bending simulation.

contractions and the inertial properties of the skeletal elements. Obviously, this movement is of no relevance to the movement observed in nature, and will therefore not be discussed any further (here or in any of the following simulations). Studying such cyclic movements is difficult anyway, because the sampling rate of the output can potentially mask the real frequencies of the movement.

It can be noted that the work needed to bend the tail becomes almost exponentially larger when the tail gets more and more bended (keep in mind that the muscle length shortening follows a smooth step amplitude). This will be the case for most of the following simulations as well. The reason behind this is the exponential response of the passive muscles, as well as the more or less exponential elasticity of the joints between the subsequent dermal plates (i.e. the intersegmental joints). So as the tail becomes bended to a certain curvature, additional increase in curvature will require progressively more energy. The total energy remains low though: for the natural ventral bending demonstrated here, the required energy for all muscles combined is merely 2.5 mJ.

Only the lateral view of the tail is given in Figure 5.6, since the displacements in lateral direction (so along the global Z-axis) are minimal. The small lateral displacements that do take place can be contributed to the natural asymmetry of the reference segment that was chosen as a building block of the model. This lateral displacement accumulates over the total length of approximately 63 mm. The largest lateral displacement for any vertebra can be found at the posterior tip of the tail: 1.28 mm. This is only a fraction of the width of the tail (which is almost 6 mm). The largest torsion was found for the third vertebra counting from the posterior tip and was 9.53 degrees. This is a small angle that again results from the accumulation of small asymmetries in the reference segment. The two most distal segments show no additional torsion, which is probably because there are no myomere muscles connected to the vertebrae (which is the skeletal element on which the torsion is measured) of these segments, since the myomere muscles are

chosen to span two segments.

Golden spiral

The curvature of the tail in Figure 5.6 looks rather familiar. It approximates the shape of a *golden spiral*, which is an often encountered shape in nature, for example in the shape of a nautilus shell. The golden spiral is a specific case of a logarithmic spiral. More in particular, it is a logarithmic spiral whose growth factor is the golden ratio (again something that is often found in nature's designs). This means that each quarter turn, the spiral widens by a factor that is equal to the golden ratio. The formula for the golden spiral in polar coordinates is given in equation 5.7 [116]. The parameter a is the scale factor for the spiral.

$$r = a\, e^{\frac{2}{\pi}\, ln\left(\frac{1+\sqrt{5}}{2}\right)\theta} \tag{5.7}$$

Figure 5.8 shows how a golden spiral can be fitted to the tail bending. The fit is close, but not perfect, especially in the anterior region, but there the tail bending is usually very small [11]. Exactly why the tail seems to bend like a golden spiral is unclear. All we can say is that this shape can be found in many of nature's designs.

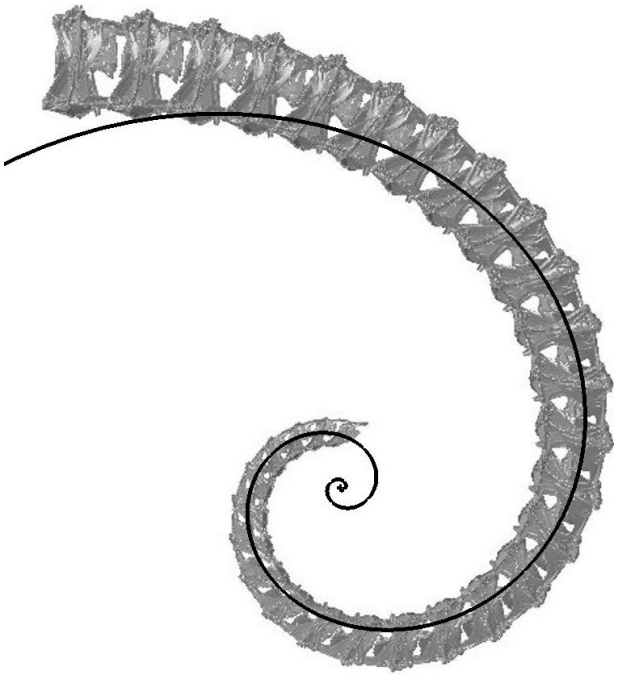

Figure 5.8: Golden spiral fitted to the simulated natural tail bending.

Curvature of the tail

To determine the (three-dimensional) curvature of the tail, a Bézier spline is constructed through the centres of mass of the vertebrae. The curvature of the spline is calculated using the curve plugin of pyFormex. The result is shown in Figure 5.9. In the distal part of the tail, the curvature rapidly rises to a maximum value of 0.314 mm^{-1}. The curvature of a point of a curve is the inverse of the radius of curvature in that point, which is the radius of a circle that best approximates the curve near that point. This means that the tail tip would fit nicely around a dowel with a diameter of 3.18 mm.

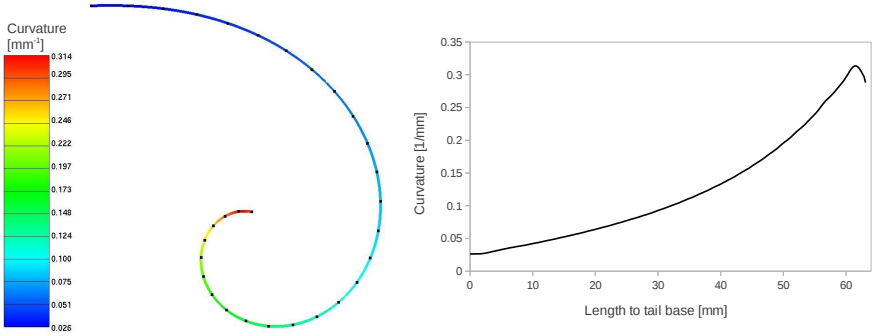

Figure 5.9: Curvature of the tail after ventral bending.

It should be noted, however, that for the last segment the curvature value is not nicely defined, since boundary conditions imposed on the dermal plates of the final segment can introduce unrealistic values. This could account for the sudden drop of curvature in the last segment. Moreover, the modelling of the myomere muscles may be incorrect in the most distal segments of the tail tip: it is currently not known how the myosepta are organised in the tip, but it is unlikely that the cross-section near the tip contains many parallel myosepta like the rest of the tail. The very small size of the segments in the tail tip made it impossible to distinguish the myosepta and myomeres on the provided synchrotron scans. Higher resolution scans of solely the tip would be required to study the muscle structure in this area.

Joint behaviour

As the tail bends, each of the joints behaves in its own particular way. Some gliding joints get compressed (i.e. the connector representing the joint becomes shorter), while others get stretched. Figure 5.10 shows the compression of the four intrasegmental gliding joints throughout the length of the tail: the ventral gliding joint (between the left and right ventral dermal plates), the dorsal gliding joint (between the left and right dorsal dermal plates), the left lateral gliding joint

(between the left ventral and left dorsal dermal plates), and the right lateral gliding joint (between the right ventral and right dorsal dermal plates). The boundary conditions on the anterior and posterior ends of the tail model cause some sudden and unexpected changes in joint extension and will therefore be excluded from the following discussion. The current boundary conditions on both ends of the tail may be a bit too restrictive, at least during ventral bending.

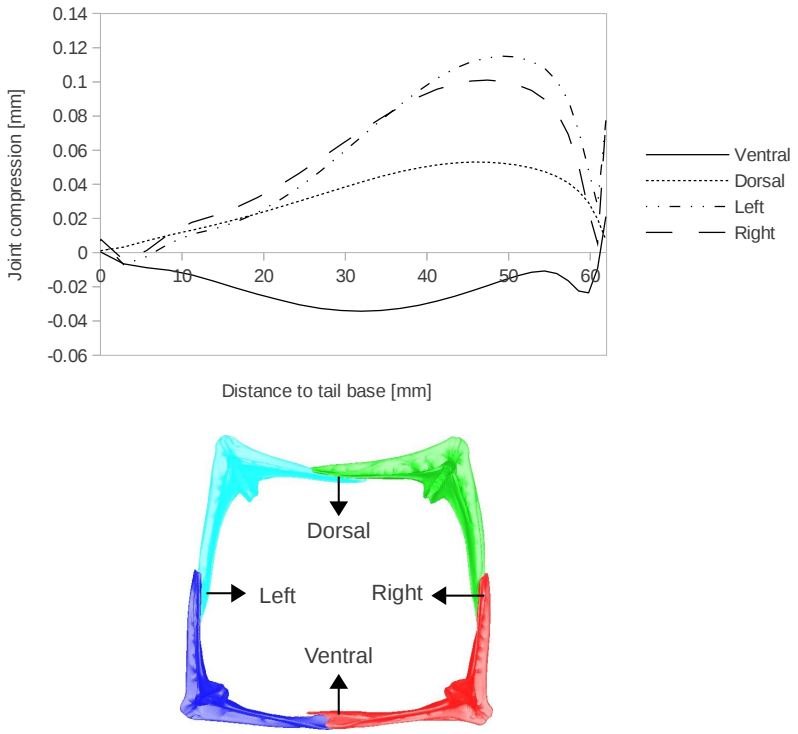

Figure 5.10: Movement of the different intrasegmental joints throughout the tail after ventral tail bending (top) and their location within the segment (bottom).

The left and right lateral gliding joints show a similar compression along the tail (though not exactly the same, since the asymmetry of the reference segment is extrapolated to the other segments). Both show a maximum compression at roughly 50 mm from the tail base, which is around the twentieth segment, counting from the most anterior caudal vertebra. The maximum compression of the left and right lateral gliding joints is 0.115 mm and 0.101 mm, respectively.

The intrasegmental ventral and dorsal gliding joints show an opposite behaviour: the ventral joint extends (meaning that the left and right ventral dermal plates move apart), while the dorsal joint compresses (meaning that the left and right dorsal dermal plate move away from each other). The ventral gliding joint

extends most (in absolute values) near the middle segments of the tail, while the compression of the dorsal joints reaches its maximum in more posterior segments. Since the cross-sectional shape of the tail is close to a rectangle, the net result of the gliding joint motions during ventral tail bending is a diminishing of the cross-sectional area of the segments, which is more pronounced in the posterior segments.

The extension of the ventral joint may be necessary to account for the bulging of the HMM during ventral tail bending. Likewise, the cross-sectional area of the EMM diminishes when they get stretched, which could explain why the dorsal joints compress slightly. The forces that the bulging muscles exert on the surrounding skeletal elements are not directly taken into account by the simulations, but it could be the configuration of the joints is somewhat adapted to this radial extension of the muscles during contraction.

Preliminary validation of the joint behaviour

To check whether the compression of the lateral gliding joints is realistic, the compression of the lateral gliding joints on the scanned ventrally bended tail was quantified. This tail was bended by manual manipulations (passive bending), while the simulations use active bending. Moreover, the total amount of bending is not equal in the scan and in the simulation: the scanned tail has a higher bending in the distal regions, and almost no bending in the proximal regions. The measurement was purely conducted to check qualitatively whether it is realistic that the lateral joint compresses rather than extends.

To measure the compression, the distance was measured between the most dorsal point of the ventral plate and the most ventral point of the dorsal plate, both for the tail scanned in stretched and in bended position. The difference between both distances was then taken as the joint compression. The results are summarized in Figure 5.11.

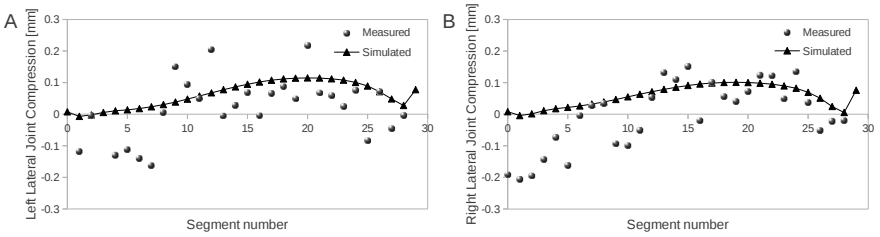

Figure 5.11: Comparison between the simulated compression of the left (A) and right (B) lateral joint and the measured compression on a manually bended tail (the amount of bending is not equal).

The measured compression shows a lot of variance. In the bended region of

the tail, there is on average more compression than extension of both the left and right lateral gliding joint, which confirms that on average the joint does indeed compress during passive ventral bending. It is currently unclear whether active bending of the tail would show the same result. Reliably measuring such small relative movements of skeletal elements on live seahorses is difficult, since the required resolution would be very high. It is noteworthy that for the anterior lateral joints we measured an extension of the gliding joints, while the bending is minimal in that region of the tail. A possible explanation could lay in the hypaxial myosepta that span many segments, redistributing strains from the bended middle region of the tail to the unbended anterior region of the tail.

Volume change

As the soft tissues in between the skeletal elements can be considered to be almost incompressible, the change in volume of the tail should remain small throughout the entire tail bending sequence. Yet the cross-sectional area becomes smaller during ventral bending simulations. If the seahorse tail were a simple beam with rectangular cross-section, the neutral axis[2] would be at half of the height of the cross-section. The real neutral axis in the tail will go through the centres of rotation in between the vertebrae, which is not exactly at half the height of the segments. In the modelled tail, this centre of rotation was assumed to be at the centre of the best fitting circle on the articular surfaces of the vertebrae (Chapter 4.3.1.4). This is true as long as the bending does not become too high: at very high bending, the vertebrae can come into contact on their ventral side, causing the centre of rotation to shift to a more ventral position. Figure 5.12 shows the approximate measurement of the centres of rotation (and thus neutral axis of the modelled tail) in a stretched tail, as a percentage of the total height of the segment. The neutral axis is more or less in the middle in the anterior segments, but becomes progressively more dorsal in the posterior segments. This means that for the posterior segments, the volume will decrease upon ventral bending if the intrasegmental gliding joints are kept fixed. In other words, in the posterior region the rostro-caudal compression on the ventral side is more pronounced than the rostro-caudal extension on the dorsal side. Consequently, both the movement of the joints and the position of the neutral axis reinforce the decrease in volume.

As the tail starts to bend, the simulations suggest that the ventral dermal plates get compressed into the dorsal dermal plates (compression of the lateral joints). As the vertebrae are connected to the dorsal plates by ball-and-socket joints with limited translational freedom, the centres of rotation will shift to a position closer to the half of the height of the segments, though not enough to fully compensate

[2]The neutral axis is an axis in the cross-section of a beam along which the longitudinal stresses or strains are zero during bending. In case of a symmetric and isotropic beam, the neutral axis is at the geometric centroid.

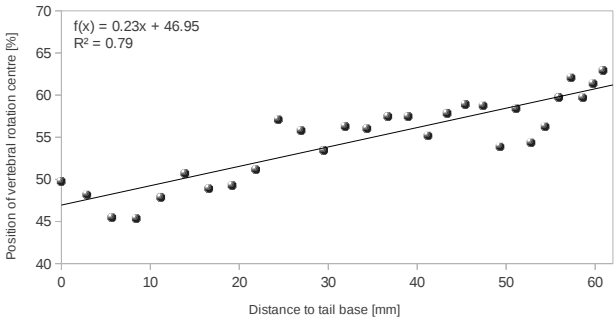

Figure 5.12: Position of the vertebral rotation points as measured throughout a scanned stretched tail, relative to the height of the segment, and a linear approximation of the measurements.

the initial divergence from the neutral axis of a simple beam. Consequently, the model predicts a continuous volume decrease during ventral bending. To check if the volume changes are acceptable, the volume change of the total tail model is calculated. To accurately determine the internal volume, the convex hull of each segment is calculated using pyFormex, as demonstrated in Figure 5.13.

For the natural ventral tail bending, the initial tail volume (at resting position) was 663.762 mm^3, while after bending the volume diminished to 653.094 mm^3, or a relative compression of 1.61%, which is not dramatic. Yet keeping in mind that the majority of the volume change can be found in the posterior segments, this is still a cause of concern. The volume change of each segment after tail bending is given in Figure 5.14. The highest compression is 5.86% and can be found in segment 21.

The rigid body simulation does not take the effect of incompressibility of the soft tissues of the segments into account. Especially for the more posterior tail segments, this appears to be an oversimplification. Modelling the effects of the soft tissues on the tail bending is not so trivial: it would require simulations of higher complexity and higher computation time. The incompressibility of the soft tissues would likely limit the lateral joint compression.

Muscle forces

Besides the displacements and rotations, the model output can also contain the forces and moments of the different connectors: the force and moment output of active and passive muscles can be requested, as well as those of the joints. Figure 5.15 shows the forces of the muscles between the 14^{th} and 15^{th} segment of the tail, counting from the tail base. These muscles were randomly chosen because they are near the middle of the tail. The output force is likely to represent the forces at play in the same muscles in nearby segments.

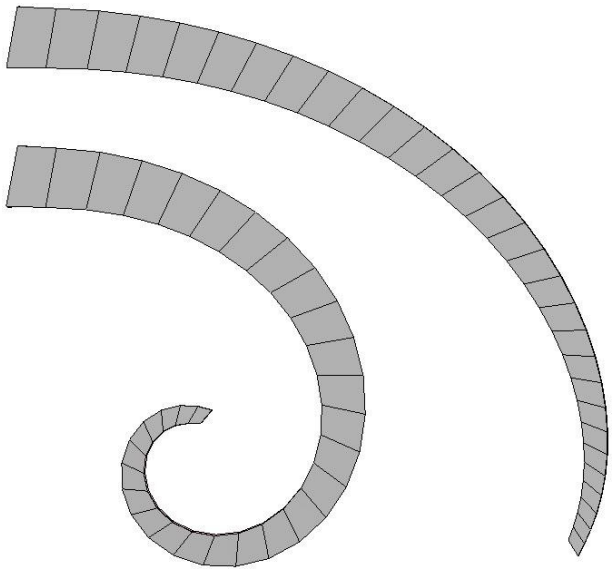

Figure 5.13: Using the convex hull of each segment to find the change in volume after bending simulation.

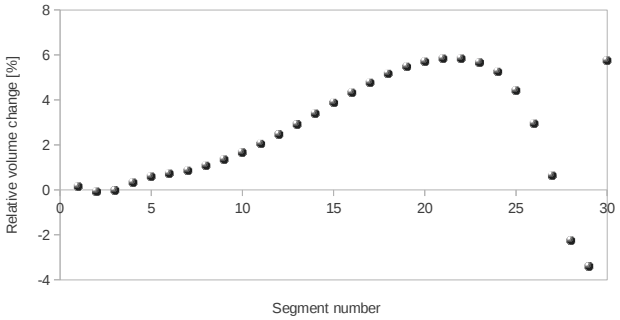

Figure 5.14: Ratio of the volume after tail bending over the volume before the tail bending for each segment in the seahorse tail.

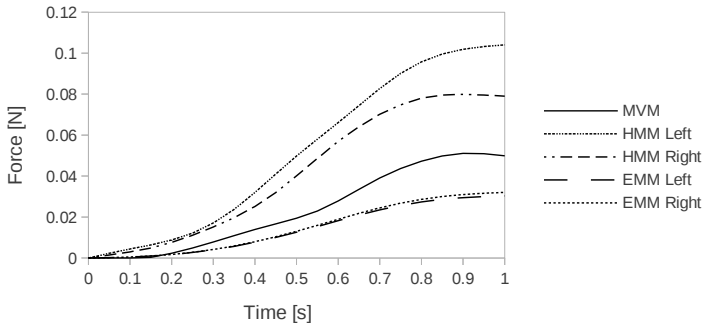

Figure 5.15: Caudal muscle forces estimated by the model.

The sum of the EMM forces is still significantly lower than the sum of the HMM and MVM forces. This is normal, since forces will not only be distributed among the passive muscles, but also among the joints. Changing the stiffness parameters of the joints can optimize this balance, but too low of a stiffness of the joints tends to destabilize the simulations, as some joints break apart, thus allowing unrealistic motions of the skeletal elements. In reality, significant elastic energy is known to be stored in the skin and joints, though most probably not as much as predicted here. It is clear that the model could use some more tweaking to cope with this inconsistency.

Conclusions on natural tail bending

The final curvature in Figure 5.6 is the curvature when the tail muscle lengths are activated with strains that are typical for fish. It is obvious though that this level of muscle shortening is insufficient to be able to use the tail efficiently as a prehensile organ: the seahorse needs to be able to grasp onto vegetation which often has very small diameters. Therefore, the strains need to be significantly higher than assumed here based on observations on fish that use undulatory locomotion, especially near the tail tip. Indeed, observations on grasping seahorses show much larger curvatures in the tail tip than estimated here based on bending of other fish. Some seahorses can even bend their tails into a closed spiral where the dorsal tail surface is in full contact with the ventral tail surface.

5.3.1.2 Maximum ventral tail bending based on geometrical considerations

The previous section illustrated how the usual strain levels found in undulating swimmers is insufficient to fully explain the grasping capabilities of the seahorse tail. So what then are the anticipated strains in the seahorse tail while grasping onto an object? To answer this question, we first take a look at what happens when we assume maximum strains in the muscles. We will first limit ourselves to MVM contraction, since it is easier to link MVM contraction to a certain degree of bending than it is to link HMM contraction to a certain degree of bending. Hale did some calculations based on measuring the maximum degree of bending between adjacent vertebrae on live seahorses (species *Hippocampus kuda*) that grasped onto a support with a small diameter of 6.5 mm [11]. The calculated MVM contraction in the region in which tail bending was observed was 26.7% of the initial muscle length, with a standard deviation of 4.5%. Exactly which region of the tail is considered to be bending was not mentioned. It stands to reason that the most distal region of the tail was taken, since this is the region that makes contact with the support, but exactly up to which segment the bending should be considered is subjective. Hale also mentioned that high levels of muscle contraction of the most anterior MVM are not observed in living seahorses. A picture of such a seahorse

grasping on to the support is shown in Figure 5.16.

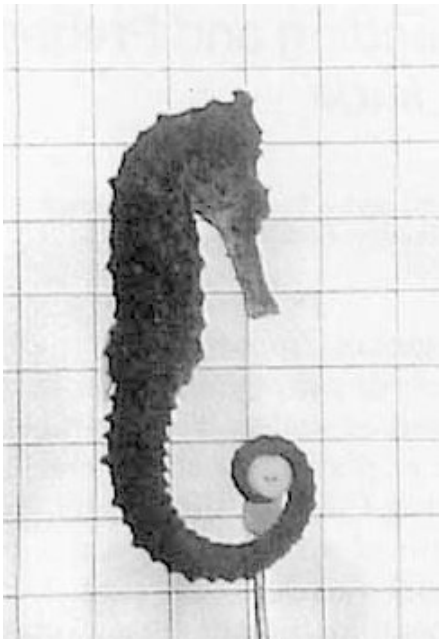

Figure 5.16: Hippocampus kuda grasping a support [11].

Bending until segment collision occurs

Inspired by Hale's estimates, MVM shortenings that range from 20% to 30%, equal for each MVM in the tail, are imposed on the simulations. Figure 5.17 A to C shows the resulting tail curling for some of these contractions. Since no contact definitions were defined, the segments will just move through each other instead of colliding when the bending becomes so large that the ventral tail surface near the anterior end comes into contact with the dorsal surface of more posterior segments. The first collision of the segments occurs around an MVM shortening of 24% of the initial length. But even with a MVM shortening of 30%, the most posterior segments still show some possibility for additional bending (i.e., the tail is not yet bended into a full spiral).

To get an estimate of the diameter around which the simulated tail bending would wrap nicely, the diameter of curvature is taken at a spiral angle of 180° (half a winding) from the tail tip. For the 23%, 25%, and 30% MVM shortening, this diameter is 8.27 mm, 7.86 mm, and 7.28 mm respectively.

The diameters derived from our model are larger than the cylinder diameter of 6.5 mm that was used by Hale. However, Hale used the *Hippocampus kuda*

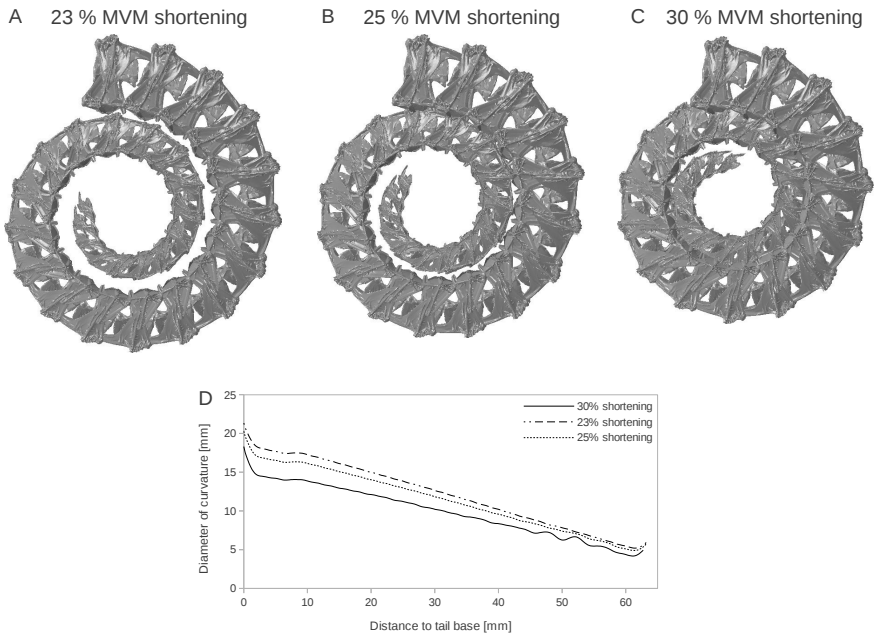

Figure 5.17: Tail position at different large MVM shortenings (A-C) and their diameter of curvature throughout the tail (D).

species for his experiments, while our simulations are based on the *Hippocampus reidi* species. There could be a difference in tail geometry between both species, as well as important differences in size between the specimens that were used. The seahorse specimens used by Hale had a length range of 102 to 122 mm. The seahorse specimen that was used in our CT-scans was not measured before cutting the tail. The tail had a length of 63 mm, and the length of the tail can, as a first approximation, be considered to be half of the total length. This would put our seahorse's length just above the range of those used by Hale, which could partially explain why the fitted cylinder in our simulations has a larger diameter at higher MVM shortenings (7.28 mm at 30% contraction) compared to Hale's observations (6.5 mm at 26.7% $\pm$ 4.5%). It is, however, more likely that the muscle contractions are not equal throughout the tail during grasping. Visual observations indeed suggest that the bending is particularly high in the most distal segments during grasping. Also for the measurements of Hale the MVM contractions can be assumed to be highest near the tail tip (the reported range is 19.7-32.5%), but information on the distribution of the MVM contraction was not provided.

Maximum intrusion of the distal spines

Another geometric restraint on the ventral tail bending is the maximum intrusion of the distal spines of the dermal plates in the anterior grooves of the dermal plates in the next segment of the chain. This constraint is already taken into account in the tail model by the exponentially increasing hyper-elasticity of the gliding joint between subsequent plates. However, it is reasonable to assume that the compression of these joints will rarely be high enough to be in the exponential region (grey area in Figure 4.19B), which is the region where the distal spine is completely pressed into the posterior groove, and all further compression requires deformation of the plates.

To get an estimate of maximum intrusion of the distal spines, the distance was measured between the tip of the distal spines and the end of the groove of the subsequent dermal plates. Since large curvature only happens in ventral bending, only the distances of the ventral distal spines is taken into account. Figure 5.18A shows the relative measured distances for the left and right ventral plates throughout the reconstructed stretched tail.

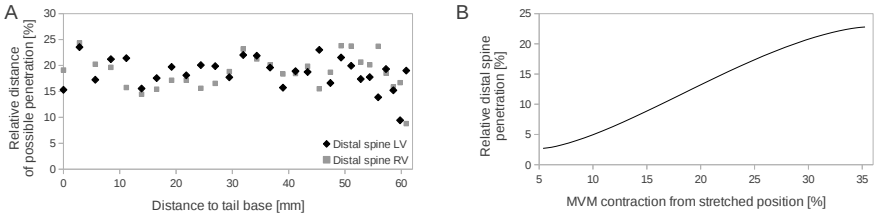

Figure 5.18: Measured maximum relative penetration distance (A) and simulated average relative penetration distance at different MVM shortenings (B).

The average relative compression is 18.60% of the segment length, with a standard deviation of 3.19%. There is no statistically relevant difference between the left and right relative penetration: a T-test on the means results in a t value of 0.18, where the critical value for t to reject the hypothesis of equal mean values is 2.01 for $\alpha = 0.05$ (and 0.68 for $\alpha = 0.50$).

To obtain a relative penetration of 18.60% of the segment length, the model predicts that the MVM needs to shorten by 26.66% of its initial length. This is based on Figure 5.18B, where the simulated average relative compression of the ventro-lateral joint is given for a range of MVM shortenings. The standard deviation of 3.19% on the compression results in a standard deviation of 5.35% on the MVM's length change. The graph of the simulated compressions does not start at (0,0), since the simulations start from the neutral tail position, whereas the measurements are done on the tail in stretched position. The average MVM compression needed to get to the neutral tail position is 5.31%, at which point the average ventral intersegmental joint compression is 2.71% of the segment length.

So a MVM shortening of 26.66% would bring the ventro-lateral gliding joints to their maximum compression. Hale's model predicted a maximum MVM contraction of 26.7% of the initial length (standard deviation 4.5%) in the posterior segments [11], which is in the same range. It therefore seems like the maximum compression of the gliding joints could be the limiting factor in the amount of curvature that the seahorse tail can obtain in a certain region of the tail. This is in agreement with the assumption of rigid skeletal bodies in these simulations: if the bones would deform considerably during bending, the geometric maximum compression of the intersegmental gliding joints would be much less of a limitation.

5.3.1.3 Maximum ventral tail bending compared to measurements on manually curled tail

The tail of an adult *Hippocampus capensis* specimen was manually (so passively) bent in ventral direction to its maximum by Neutens [68]. In Figure 5.19 this measured ventral bending is compared to some simulated maximum bendings.

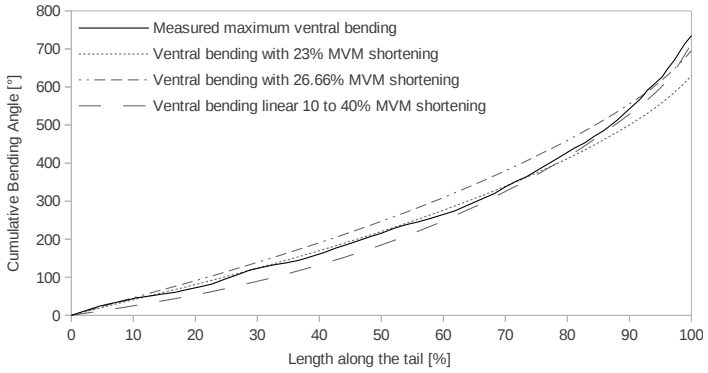

Figure 5.19: Comparison between simulated and measured maximum tail bending.

The bending after MVM shortening based on the geometrical considerations (discussed in the previous section) shows a relatively good agreement with the measured maximum tail bending in the anterior segments. However, the measured bending in the distal part of the tail is higher than predicted by this simulation. The bending after MVM shortening based on maximum intrusion of the posterior spines shows a better approximation of the maximum bending in the distal regions, but overestimates the ventral bending in the other tail regions. None of these two situations can thus fully explain the shape of the seahorse tail at maximum bending.

Clearly, the maximum ventral bending requires a more complex pattern of muscle contraction. As an example, a linearly rising relative MVM shortening of 10% anteriorly to 40% posteriorly is shown as well in Figure 5.19. This simulation shows a better agreement in the distal tail region, indicating that the rela-

tive MVM contraction required to obtain maximum tail bending becomes progressively higher in the most distal segments.

The fact that the measured maximum bending is higher than the maximum bending estimated based on posterior spine intrusion is interesting. However, the standard deviation on the MVM shortening calculated based on the maximum posterior spine intrusion is over 5%, which could explain the difference. Moreover, the measurements were done on a different seahorse species. It's possible that different species have different tail flexibilities.

Another simple explanation could be that during the manual manipulation of the tail to its maximum bending, some deformation of the bony elements near the tail tip was introduced. These skeletal elements are the smallest and therefore the easiest to deform. Moreover, there could be a difference in maximum passive tail bending and maximum active tail bending.

There is also a possibility that the tail tip, in order to allow even more flexibility than the other segments, has some additional adaptations that the model failed to take into account. The reference segment used in the simulations is taken from the anterior region of the tail. Using this reference segment as an approximation (after scaling and inclining) for the most posterior segments could possibly be too much of an approximation, or the inclination of the segments in the tail tip is incorrectly approximated by a linear curve. Indeed, the fit of the linear curve on the measured inclination in Figure 3.12 is rather poor.

5.3.1.4 Linearly rising MVM shortening

The tail curvatures which are shown in Figure 5.17 are never observed in living seahorses. More in particular, the proximal segments never show such a large bendings, or even moderate bendings for that matter [11]. So in following simulations we assume that the most proximal MVM doesn't change at all, while the most posterior MVM has the largest shortening. This corresponds more or less to many observed tail bendings in living seahorses, and results in a more natural looking tail curvature. The previous paragraph showed that MVM shortenings up to almost 30% (taking into account the standard deviations of the previous paragraph and the 5% shortening required to get to the resting tail position) are possible in the seahorse tail. So, let us assume a length change of 30% for the utter most posterior MVM and no length change for the most anterior MVM. The MVM in between are now given a relative change in length that rises proportionally to the distance to the tail base. The tail position at the start of the simulation is again the resting position. The resulting tail bending is shown in Figure 5.20A.

This bending of the tail looks more like the bending that can be seen when a seahorse holds on to a horizontal dowel. Augmenting the maximum muscle contraction even more will lead to a tighter grip of the tail (Figure 5.20B). It is unclear whether such high length changes are possible for these kind of muscles, and, as

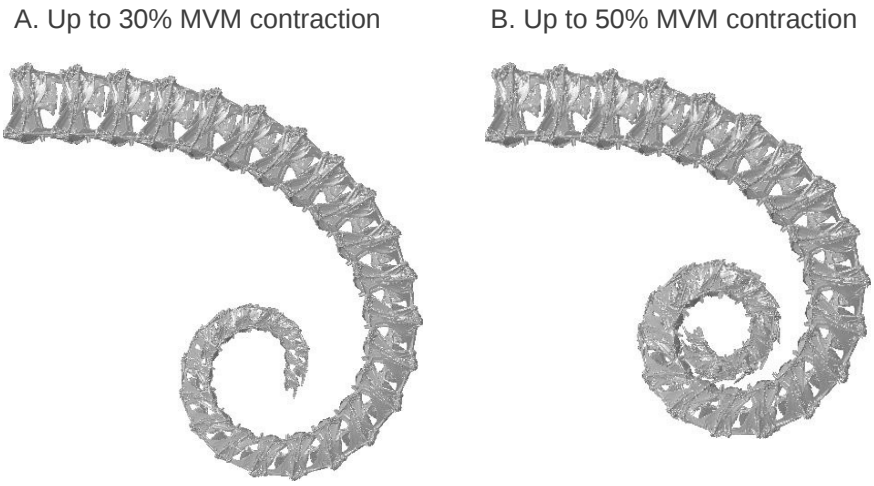

Figure 5.20: Resulting tail bending with a posteriorly rising MVM shortening of maximum 30% (A) and 50% (B).

discussed before, it is doubtful that the lateral-ventral gliding joints would allow such a motion. Generating large forces at such high levels of muscle contraction is unlikely for most muscle types (though it is not impossible). However, since the seahorse uses the MVM to keep the tail in a certain curved position (wrapped around an object), the MVM muscles will usually not have to produce large forces (large forces are most probably generated by the myomere muscles instead). It seems plausible in general that the seahorse tail muscles may have sacrificed large force generation for increased bending capabilities [11].

5.3.1.5 Forward dynamics: uniform HMM force

Instead of using the shortening of connectors, the muscle forces can also be used as input for the rigid body simulations. In this example, a contraction force of 0.1 N is applied to all the HMM muscles. This will force the tail to bend ventrally. The resulting position of the tail is shown in Figure 5.21A.

The curvature does not increase a lot throughout the tail (Figure 5.21B), which is not what we expected. Since the tail usually has a much higher curvature in the posterior regions, it would be expected that for the same contraction forces, the tail would bend substantially more near the tail tip. Even more so since the cross-sectional area of the HMM is much smaller in the posterior regions, which limits the maximum contraction forces of these muscles even more. The relative cross-sectional area of the MVM does become larger towards the tail tip, so it could be that the forces generated by the MVM, which are assumed to be zero in this simulation, are more important in the distal area of the tail.

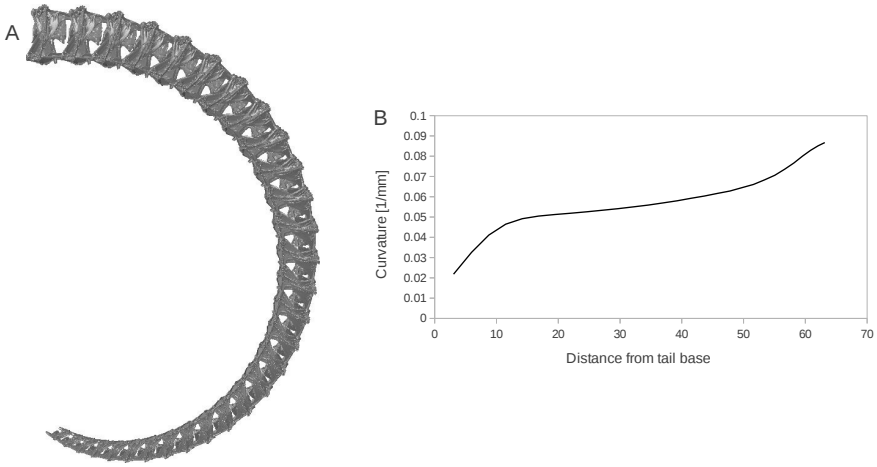

Figure 5.21: Tail bending after a uniform force applied to all HMM (A) and the corresponding curvature (B).

Another possibility is that the estimated joint elasticity is far too high for the distal segments of the seahorse tail. In the current model, the elasticity of the joints is kept equal throughout the segments. Since the absolute joint motion caudally becomes smaller when the curvature is equal throughout the tail, the joint forces within the distal segments were assumed to scale accordingly. This may very well be an oversimplification.

It should be noted that for pure ventral tail bending, the forward dynamic simulations often showed poor stability. As the forces generated by the HMM become high (and conversely the passive forces of the EMM), the compressive forces within the segments reach a point where *buckling*[3] issues start occurring: the vertebrae begin to rotate around their local dorsoventral axis, alternating in direction between subsequent segments (i.e. the forces no longer generate ventral bending, but rather tail shortening). As these rotations become larger, the tail can reach a situation where some segments simply collapse, as the vertebra flips 180 degrees. Adapting certain parameters can alter the maximum obtainable forces before buckling, but we have been unable to develop a robust solution to the issue.

5.3.1.6 Forward dynamics: forces proportional to cross-sectional area

The force that a certain muscle can generate is usually proportional to the physiological cross-sectional area (PCSA) of that muscle. Assuming that the fibre stress is more or less equal throughout the tail during a ventral bending motion of the

[3]Buckling is a mathematical instability, where increasing loads can be sustained in one of two states of equilibrium: an undeformed state or a laterally-deformed state.

seahorse tail, each ventral muscle in the model can be given a contraction force proportional to its maximum cross-sectional area. As a result, the posterior HMM generate less force than the anterior HMM. For the current example, the fibre stress is taken as a quarter of the estimated maximum fibre stress (muscle forces will be calculated as discussed in Chapter 3.3.4.3). The MVM are given the same fibre stress, though compared to the HMM forces, the MVM forces only become significant in the posterior tail regions, where their relative cross-sectional area is larger. The resulting position of the tail model is demonstrated in Figure 5.22A.

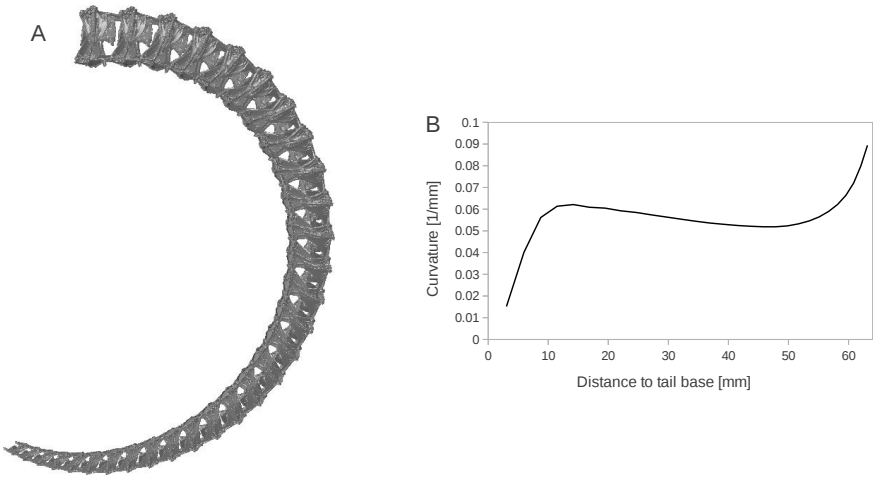

Figure 5.22: Tail bending after applying forces that are proportional to the PCSA of the muscles, with a fibre stress at 15% of the assumed maximum (A) and the corresponding curvature (B).

Compared to the curvature after uniform HMM contraction forces (Figure 5.21B), the distribution of the curvature after applying forces proportional to the cross-sectional area (Figure 5.22B) is different: the curvature no longer shows a continuously rising trend throughout the tail. In the first few segments the curvature rises quickly. As the cross-sectional area of the HMM becomes smaller, the generated forces diminish, which in turn produces less curvature in the tail. Only near the tail tip (where the segments are short and curvature therefore is easier to produce) will the curvature rise again. The increasing relative importance of the MVM forces towards the tail tip may partially offer an explanation of the observed curvature. In the most anterior and the most posterior segments the curvature may also be affected by the fact that there are less connectors in the cross-sections of these segments (as the connectors that model the myomere muscles span several segments). The provided results suggest that while grasping, muscle activation should be much higher near the middle and distal end of the tail.

The buckling issue can also occur in this type of simulation, but the MVM

forces have some moderating influence, meaning that the HMM forces can be higher before the buckling becomes evident.

5.3.1.7 Natural ventro-lateral tail bending

Starting from the resting tail position, an ipsilateral shortening of the left HMM is introduced, while the EMM act as passive muscles. The shortening of each connector that represents the left HMM muscles is calculated based on the strains found in fish myomere muscles during undulatory swimming (Equation 3.1). This is therefore again an inverse dynamics simulation. Because of the left-ventral location of the left HMM, the tail will undergo a combined ventro-lateral bending. At the same time, significant torsion will be introduced throughout the tail.

Upon ipsilateral HMM contraction, the seahorse tail starts to bend in both ventral and lateral direction. The bending results in a helical shape of the tail. More in particular, since the segments posteriorly become smaller, the shape of the tail is approximately a tapered helix (the diameter of the helix becomes smaller towards the tail tip, like a cone). This helical shape can be seen in Figure 5.23 from the lateral view (A) and from the transverse view (B).

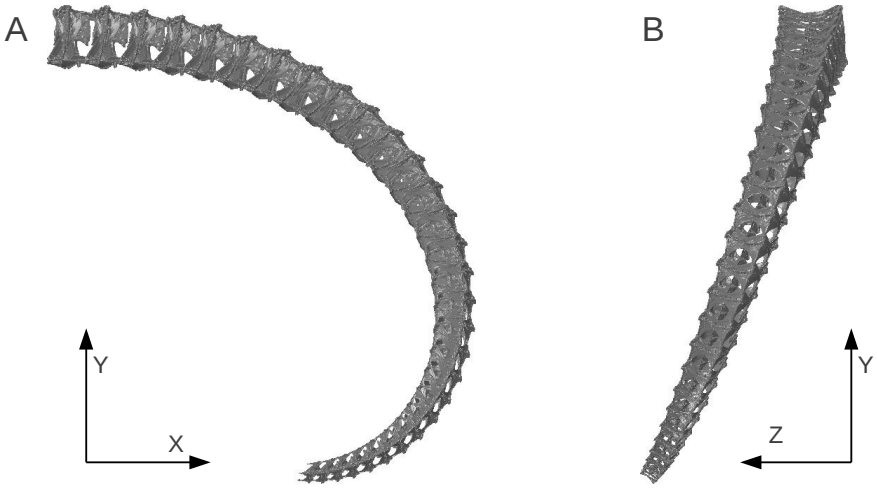

Figure 5.23: Resulting tail position after natural left HMM shortening.

The amount of bending in ventral direction is slightly higher than the amount of bending in lateral direction. This can be seen from the graph in Figure 5.24B. The more pronounced ventral bending of the tail near the tip is actually caused by the rather large torsion of those segments, as can be derived from Figure 5.24C. Similarly, the less pronounced lateral displacement of the more posterior segments (Figure 5.24A) can also be attributed to the torsion.

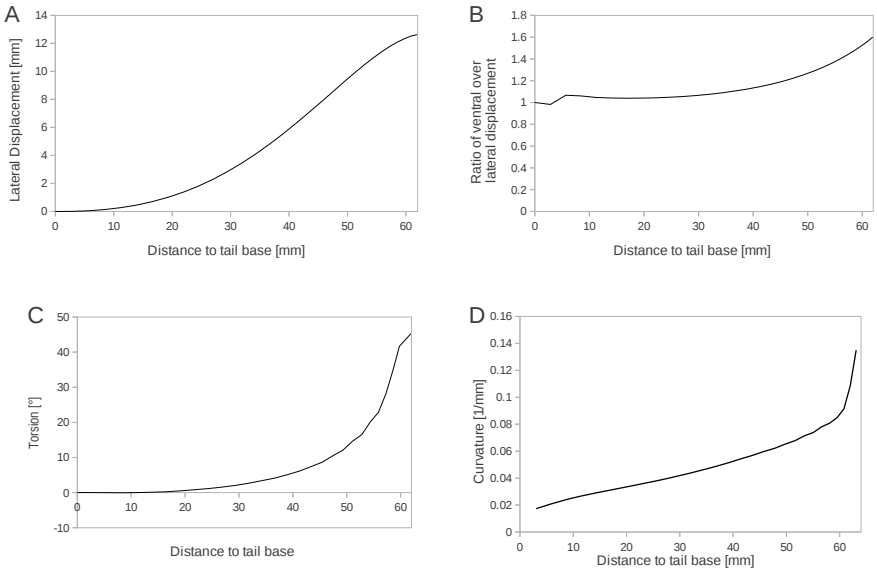

Figure 5.24: Lateral displacement (A), ratio of ventral over lateral displacement (B), torsion (C), and curvature (D) throughout the tail after natural unilateral HMM bending.

The torsion of the tail is defined as the rotation of the segments around the local anteroposterior (or longitudinal) axis. The rotation of the segments is assumed to be equal to the rotation of the central vertebra of that segment (the dermal plates often show some small additional rotations). To calculate the local torsion angle θ, we rotate the local axes system of the vertebrae (defined by the vector connecting the tips of the lateral spines and the local anteroposterior axis) so that the anteroposterior axis coincides with the initial local anteroposterior axis, and the dorsoventral axis is located in the original transverse plane. The torsion is now defined as the angle between both dorsoventral axes (or both left-right axes).

The curve of the torsion (Figure 5.24C) shows some irregularities near the tail tip, indicating that the torsion twists a bit near the tail tip (at least at rather large changes in muscle length). This can be contributed to the boundary conditions imposed on the final segment of the chain. The dermal plates of the final segment are connected to the vertebrae by stiff springs. This imposed boundary condition is not very compatible with the large torsion induced by ipsilateral contraction of the HMM.

Joint behaviour

During combined ventro-lateral tail bending, powered by ipsilateral HMM shortening, the compression and extension of the intrasegmental joints is different than

during pure ventral bending. Figure 5.25 depicts the graphs of the gliding joints between the dermal plates of the same segment throughout the tail model.

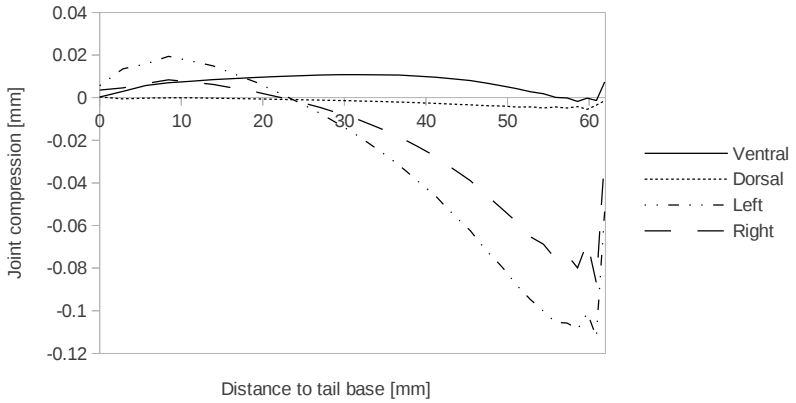

Figure 5.25: Movement of the different intrasegmental joints throughout the tail after natural ipsilateral HMM shortening.

The ventral gliding joint gets compressed, while the dorsal gliding joint is slightly elongated. This is the opposite situation of what we found during purely ventral bending (Figure 5.10). The amount of compression and extension of the ventral and dorsal gliding joints is small though, so the effect on the volume change will be low. Just like in the simulations that included ventral bending, the ventral gliding joints that show the most length changes are near the middle of the tail, while the largest dorsal joint movements can be found more posteriorly.

For the lateral intrasegmental gliding joints, the amount of joint extension becomes large towards the tail tip (where the relative muscle shortenings are larger). On the left side, the amplitude of the joint movement is consistently higher than that on the right side. Given that the left HMM were the only active muscles in the simulation, this comes as no surprise.

Figure 5.26 shows how the volume of the tail was calculated before and after tail bending. Before bending the volume was 663.534 mm^3, after bending it was 663.954 mm^3. This is an increase in volume of 0.06%, which is insignificant, keeping in mind the numerous simplification of the model.

Looking at the relative volume changes of individual segments, however, shows a different result. Figure 5.27 shows the compression of each segment. Until segment number twelve, the joint movements cause a decrease in segment volume. From segment number thirteen on, the internal volume of the segments increases. The relative compression of the proximal segments is smaller than the expansion of the distal segments, but since their absolute volume is much higher, both effects more or less cancel each other out when the total volume change is calculated.

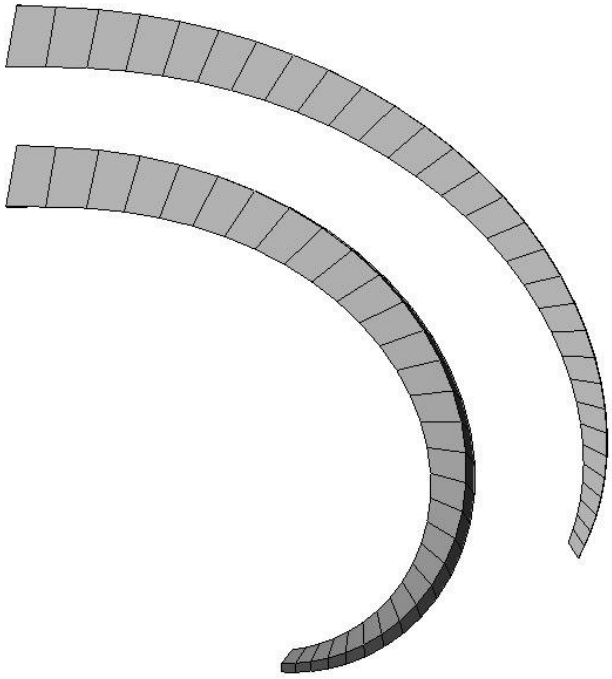

Figure 5.26: The volume of the tail model before (top) and after (bottom) lateral-ventral bending simulation, determined as the sum of the convex hull of each segment of the tail.

Only for the ten most distal segments is the volume change significant. Increasing the joint stiffnesses in the distal segments reduces the effect, but a rigorous solution again requires augmenting the model complexity significantly to account for the effect of the incompressible soft tissues.

Muscle forces

As the tail bends in left lateral-ventral direction, the active muscle forces are expected to be highest on the left side of the tail, while the passive forces are expected to be highest on the right side. Figure 5.28 demonstrates the simulated muscle forces near the 22nd segment of the tail, counting from the tail base. A segment in the distal part of the tail was chosen, since the muscle shortenings in the anterior segments are low. Moreover, Figure 5.25 showed some boundary issues near the tail tip, so the predicted forces of the most distal muscles may be less reliable, hence the avoidance of using the force outputs of the most distal segments. The forces of the MVM and right HMM are not shown in the graph since their predicted forces are nearly zero throughout the simulation: these muscles are passively compressed, which generates very little force, as can be deduced from

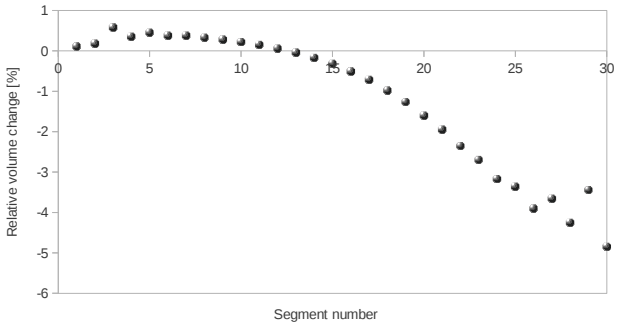

Figure 5.27: Relative volumetric compression of each segment after ipsilateral HMM contraction.

Figure 4.8.

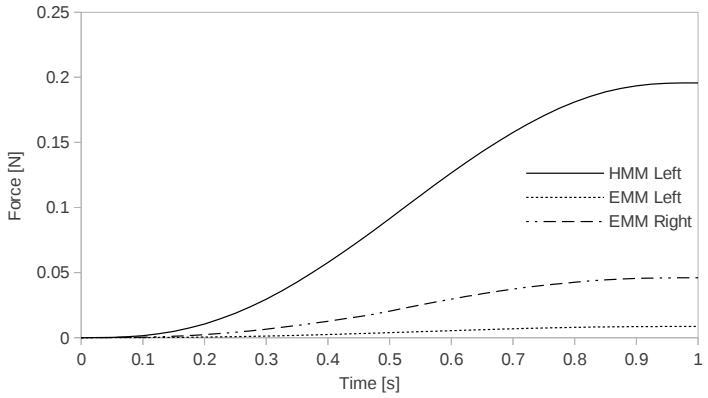

Figure 5.28: Muscle forces between segment 22 and 23 during lateral-ventral bending.

As suspected, the largest force can be seen for the left HMM muscle, which is the only actively shortening muscle in the simulation. The right EMM has the highest passive force, though the passive force generated by the left EMM is still significant. Both the active and passive forces are positive, since in both cases the force vectors are directed towards the centre of the muscle.

The sum of the EMM forces is still significantly lower than the left HMM force. As discussed in Chapter 5.3.1.1, the amount of potential energy stored in the joints may be too high.

5.3.1.8 Uniform ventro-lateral bending

Using a uniform ipsilateral HMM shortening gives a slightly different result. The tail shape will no longer be resembling a tapered helix. In the presented example,

a shortening of 10% was applied uniformly to each left HMM muscle, since this is roughly the maximum muscle shortening that can be observed in the natural bending (Chapter 5.3.1.7). The resulting tail bending is illustrated in Figure 5.29.

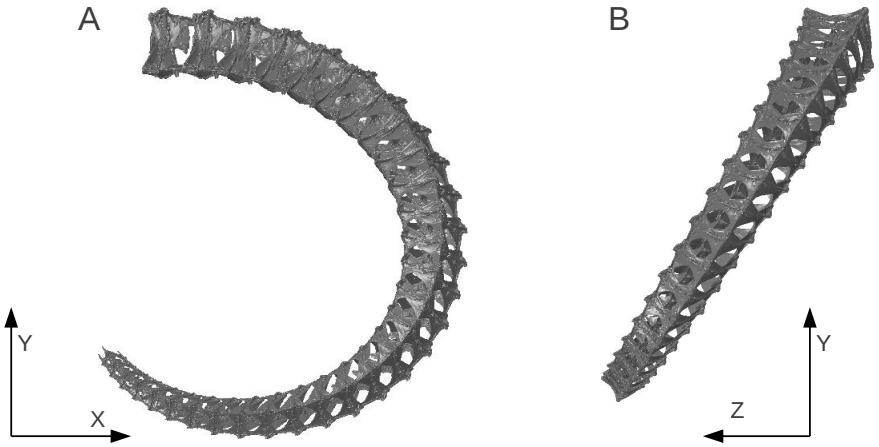

Figure 5.29: Resulting tail position after continuous left HMM contraction (left and dorsal view).

As can be expected, the bending is more continuous throughout the tail (i.e. the shape of the tail from a lateral point of view is more like a circle). The bending is also more pronounced, since the average HMM contraction is higher. Figure 5.30 shows the lateral displacement, torsion, and curvature graphs derived from the continuous lateral displacement.

In the most posterior segments, the torsion becomes very high. Consequently, the increase of lateral displacement is smaller, since it was calculated as the distance travelled by the segment along the global Z-axis. Another consequence of the large torsion is that the shape is not helical. In tail regions with significant torsion, combined ventro-lateral tail bending will result in complex shapes.

The final segment aside, the tail curvature is rather constant throughout the tail (Figure 5.30C). Looking at Figure 5.29A, this may not be so obvious (the curvature seems larger in the middle section of the tail), but the calculated curvature is the three-dimensional curvature of the tail, so the lateral view gives a distorted view of the curvature. Given that the HMM span many segments, and that the MVM are probably of minor importance during large lateral bending, the resulting curvature of the tail could be fairly realistic, although this would have to be verified based on kinematic data of ventro-laterally bending seahorse tails, which are currently not available.

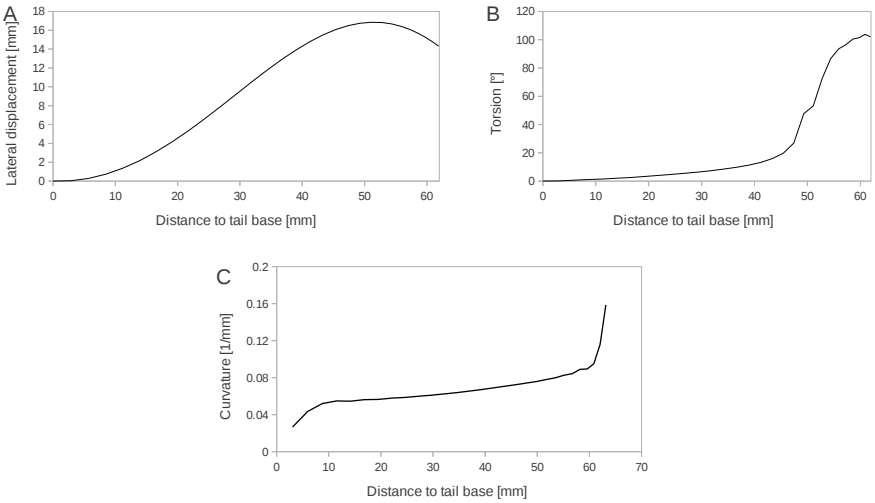

Figure 5.30: Lateral displacement (A), torsion (B), and curvature (C) after uniform ipsilateral HMM contraction of 10%.

5.3.1.9 Forward dynamics: unilateral HMM force

For this simulation, the left HMM and the MVM were given a force based on fibre stresses at 25% of the estimated maximum. The force of each HMM is proportional to its cross-sectional area. The resulting tail bending is shown in Figure 5.31, while the tail curvature is shown in Figure 5.32.

Compared to the previous simulation that used uniform HMM shortening, the bending in the proximal tail region is higher, while the bending near the tail tip is lower. Whether the fibres stresses throughout the tail are fairly uniform during ventro-lateral bending is debatable, but the fact that the HMM span many segments should provide some redistribution of the generated forces that makes high differences in forces over a small area unlikely.

5.3.1.10 With and without inclination

One of the on/off parameters in the model is the segment inclination. This parameters skews the reference segment based on equation 3.4. Figure 5.33 shows how the modelled stretched tail looks like with and without this segment inclination, compared to the real geometry. It is unclear why the seahorse tail has this segments inclination. The inclination becomes progressively larger towards the more posterior segments. A possible explanation for the higher inclination of the posterior segments could be that those segments are more optimized for higher ventral bending, since these segments will be more often in a bended position and with a higher curvature.

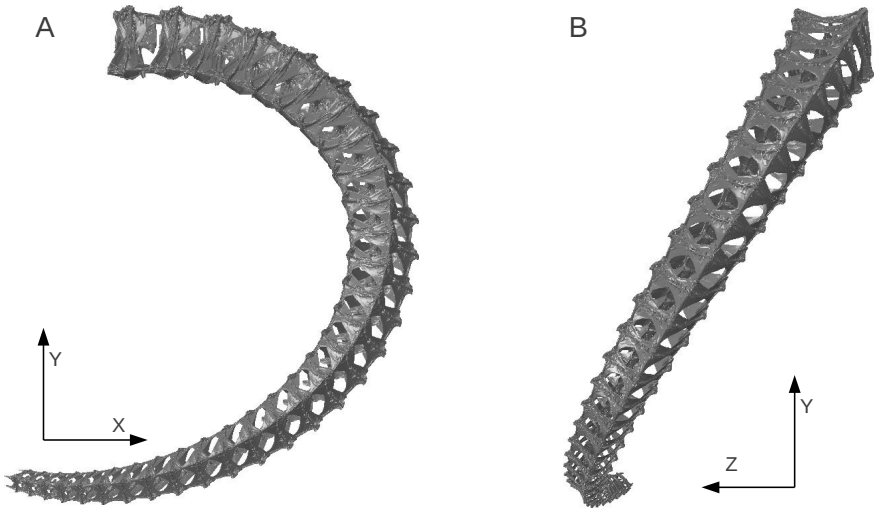

Figure 5.31: Tail bending after applying forces to the left HMM based on fibre stresses at 25% of the estimated maximum.

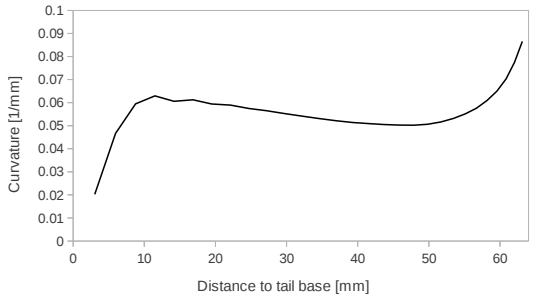

Figure 5.32: Tail curvature after applying unilateral HMM forces.

So does the inclination of the segment have energetic advantages upon ventral tail bending? To answer this question, two separate simulations were run: one of the ventral bending of a tail with an inclination equal to the inclination measured on the scanned stretched tail, and one of the ventral bending of a tail with a constant inclination equal to the inclination of the proximal segments. The ventral bending is powered by shortening the HMM and MVM according to the natural muscle shortening that was discussed earlier. In the first simulation the total energy required to bend the tail was 0.606 mJ, while for the latter the total energy was 0.652 mJ. Contracting only the left HMM requires 0.350 mJ if segment inclination is applied, and 0.412 mJ without segment inclination.

It seems like the inclination is indeed providing some advantages when it comes to energy usage while bending the tail, both in ventral and combined ventro-

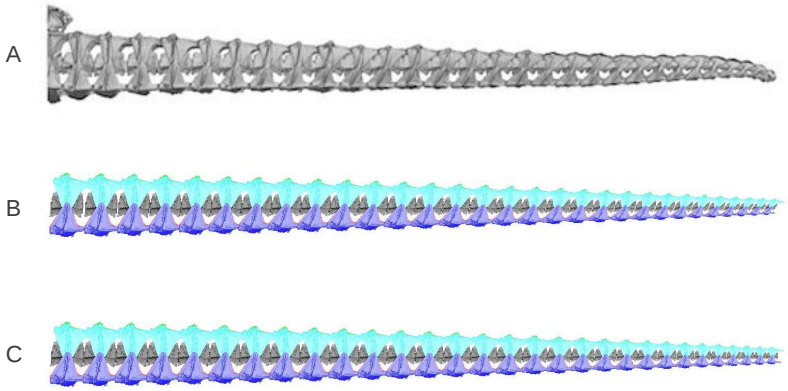

Figure 5.33: Lateral view of the segmented stretched tail (A) and stretched tail model with (B) and without (C) segment inclination.

lateral tail bending. The most important difference appears to be in the compression of the gliding joints between the subsequent ventral dermal plates. These longitudinal joints get significantly more compressed when no inclination is available. The extension of the ventral joints that get compressed are shown in Figure 5.34.

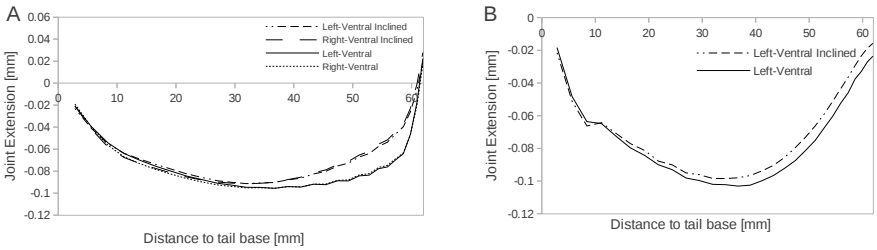

Figure 5.34: Movement of the compressed longitudinal gliding joints upon ventral (A) and ventro-lateral (B) tail bending.

Whether this energetic advantage is the driving force behind the inclination of the segments is questionable. There may be more important reasons for the segment inclination. All we can say from the provided simulations is that the simulations that include the segment inclination have a significant, though not very large, energetic advantage.

5.3.1.11 With another reference segment

The model geometry is generated from one single skeletal segment called the reference segment. Which segment is chosen as the reference segment is arbitrary, as long as the shape is representable for the rest of the tail (i.e. the chosen segment

should not contain obvious deformities or scanning artefacts). Since the reference segment is arbitrary, the results can depend on the chosen segment. The results presented in this chapter use the fourth segment of the tail, counting from the tail base, as the reference segment (Figure 5.35A). To determine the effect of choosing a different segment, the next segment of the chain is also segmented (Figure 5.35B). The model requires the position of the reference segment as input, but besides this position no other parameters in the model were changed. For segment number five, the automated landmark detection worked flawlessly. It is possible that in case the shape of the reference segment differs more (e.g. because a segment of the distal part of the tail is taken, another specimen is taken, or a different species was taken), some fine-tuning of the algorithms may be needed.

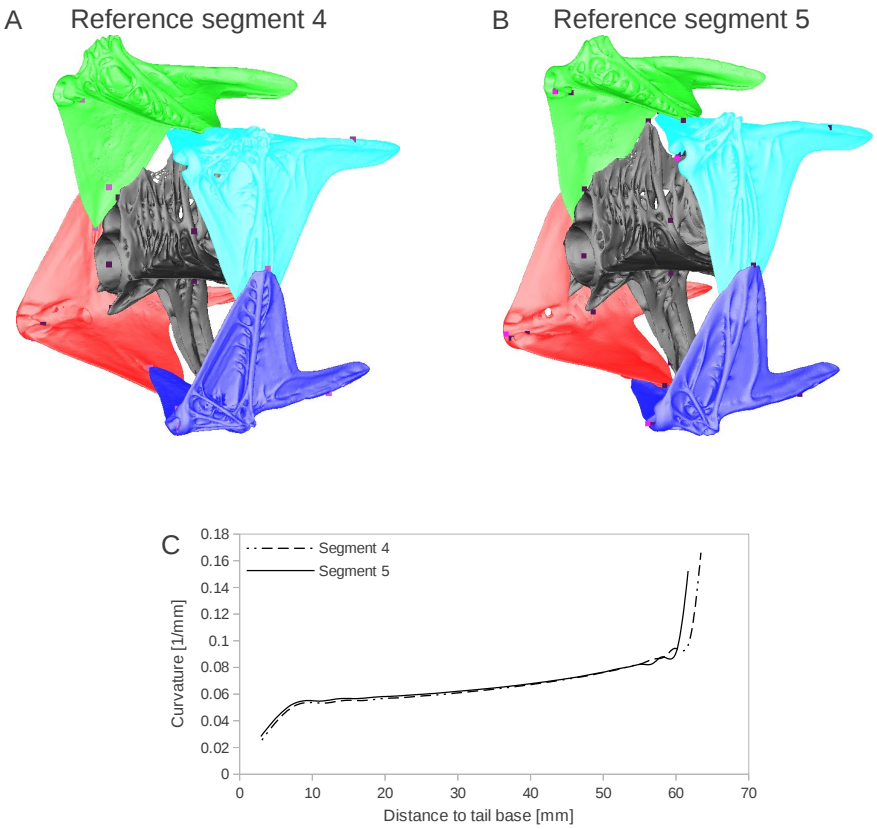

Figure 5.35: Geometry of segment 4 (A) and segment 5 (B) of the stretched seahorse tail, with the automatically detected landmarks (purple squares) and the resulting curvature difference upon unilateral HMM shortening (C).

Figure 5.35C shows the effect of changing the reference segment on the curvature after a uniform ipsilateral shortening of the HMM over 10%. The required

energy is 1.10 mJ for the first simulation and 1.01 mJ for the second simulation. The displacement of the tail tip is 47.7 mm for the first simulation and 47.0 mm for the second simulation.

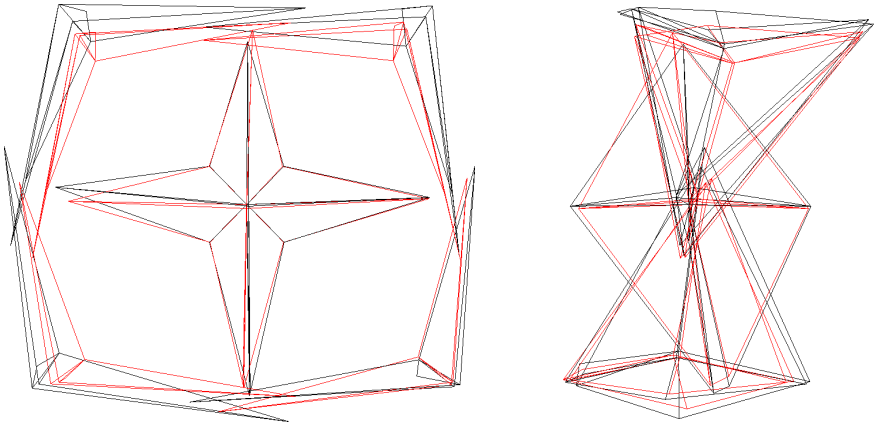

Figure 5.36: Frontal (on the left) and left lateral (on the right) view of the reconstructed most proximal segment based on reference segment number 4 (black lines) and reference segment number 5 (red lines).

Figure 5.36 visually shows the difference of the reconstructed landmarks of the first segment of the tail based on both reference segments. On average, the distance between all these landmarks is 0.221 mm (standard deviation 0.135 mm).

There are clear differences in model geometry and simulation results when a different segment is chosen as the reference segment. Most obvious is the slightly shortened tail when segment number five was used. This can be contributed to the slight difference in real reference segment size and assumed reference segment size (Figure 3.11). Since this segment is copied and scaled based on the original size, this small error accumulates when looking at the total length of the tail.

The natural variance in geometry of the skeletal elements of the seahorse tail has some significant effects on the simulation results, because this variance is copied to all segments of the tail. One possible solution could be to calculate the anatomical landmarks for all segments of the tail. However, deriving 3D models from the scans is cumbersome and time-consuming due to the large contacting surfaces in the gliding joints that render automated segmentation algorithms useless.

5.3.2 Deformable bodies

The previous simulations included rigid bodies and thus relied on the assumption that the deformation of the skeletal elements during tail bendings is low enough to be neglected. The following simulations include deformable bodies as well in order to study the stresses and strains in the skeletal elements.

5.3.2.1 Ventral bending with deformable bodies

Simulations on ventral bending with deformable bodies are performed to check whether the assumption of rigid bodies is valid: some segments of rigid bodies are substituted with deformable bodies to check if the deformations are small enough to be neglected. The segments with rigid elements are used at the proximal and distal side to make sure that the constraints on the elements are the same in the deformable and rigid case. The joints are still modelled as elastic elements (springs), but with the added kinematically coupled points that are described in the material and methods section. Within the gliding joints, contact is defined between the surfaces of both skeletal elements that are involved, so that the deformable bodies can not penetrate each other.

In contrast with most other simulations, we start from a completely stretched part of the tail (so not from the resting position). The geometry of the deformable bodies is segmented from a proximal part of a stretched tail segment (with the appropriate scaling and skewing for the position of the segment in the tail). Even in the resting position, bending is small in the proximal part of the tail.

Figure 5.37 shows the logarithmic (or natural) strain ε upon a ventral bending of the tail. The MVM are shortened by 16% in this simulation, which is a moderate amount of muscle shortening. The deformation is insignificant in most parts of the deformable bodies. Only in the distal spines and the grooves in which they reside, the strains are somewhat higher. The peak strains are almost 2%, but those are localised on the contact surfaces in the gliding joints. Peak strains aside, the highest strains are roughly 1%. These high strains can be found in the distal spines of the dermal plates. The deformation is more or less equal in all four distal spines of a segment.

As suspected, the deformations of the skeletal elements are small when the tail is moderately bended in the absence of external forces (other then the reaction forces that keep the most proximal segment in place). Higher amounts of bending will induce higher strains, especially in the more distal skeletal elements. Yet as long as no external forces are applied, the deformations remain acceptable.

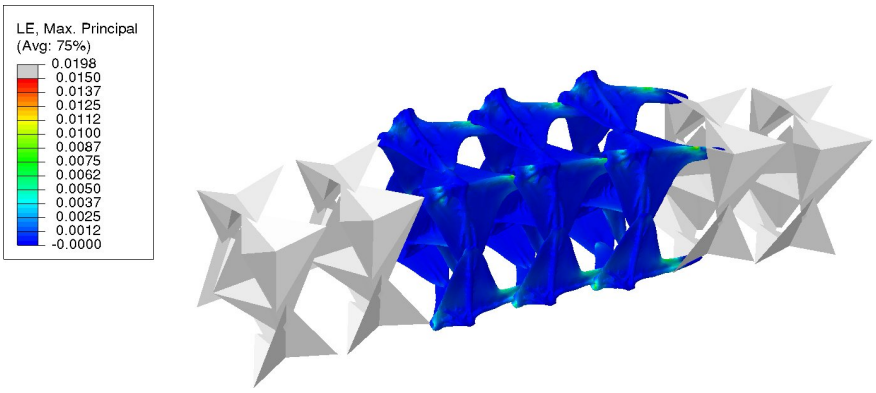

Figure 5.37: Maximum principal strain in deformable segmentss after moderate ventral bending.

5.3.3 Compressive models

This section focusses on the high compressive stiffness of the seahorse tail. Through finite element simulations, the stress and strain distribution in the tail skeleton during compression is studied.

5.3.3.1 Straight configuration

Dorsoventral compression

When the dorsal and ventral plane move towards each other, the dorsal side of the dorsal dermal plates and the ventral sides of the ventral dermal plates will come into contact with the converging surfaces. To avoid computational instabilities caused by too sudden rises of contact stresses, the contact is modelled with a linear penalty function, meaning that a normal force arises at the contacting surfaces with an amplitude which is linear with the penetration depth of the surfaces. The resulting maximum principal component stresses in the bone after a dorsoventral compression of 0.1 mm are illustrated in Figure 5.38.

From the results it can be seen that, as can be suspected, the highest stresses occur at the contacting surface between the skeleton and the planes (i.e. the contact pressure). Interestingly, some lateral ridges on the dermal plates show maximum principal stresses which are almost as high as the the contacting stresses. Evidently, the ridges play a role in coping with the compression forces. As the tail gets compressed, the flat surfaces of the dermal plates start to bend. This bending is contained by the ridges on the plates.

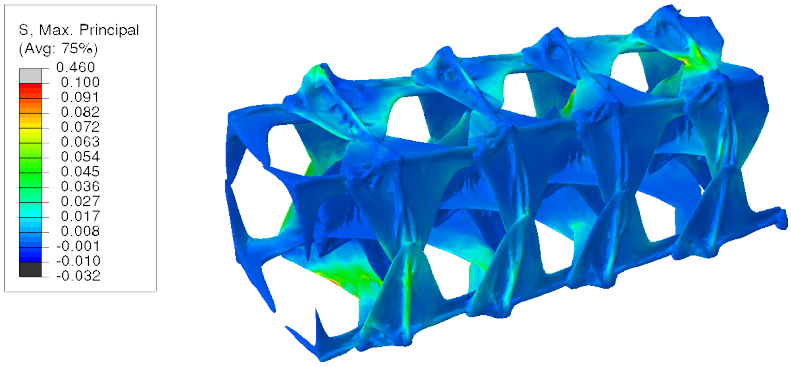

Figure 5.38: Principal stress distribution in MPa in the tail skeleton under dorsoventral compression.

Lateral compression

Instead of dorsoventral compression, we can also model lateral compression by converging the left and right planes. This corresponds for example with a predator biting the seahorse tail from in front or behind of the animal with a relatively low force. Qualitatively the results are comparable to the dorsoventral compression: high contact stresses on the side where the planes converge (in this case the lateral sides) and high stresses on the ridges of the other sides (dorsal and ventral side) caused by bending of 'wings' of the dermal plates.

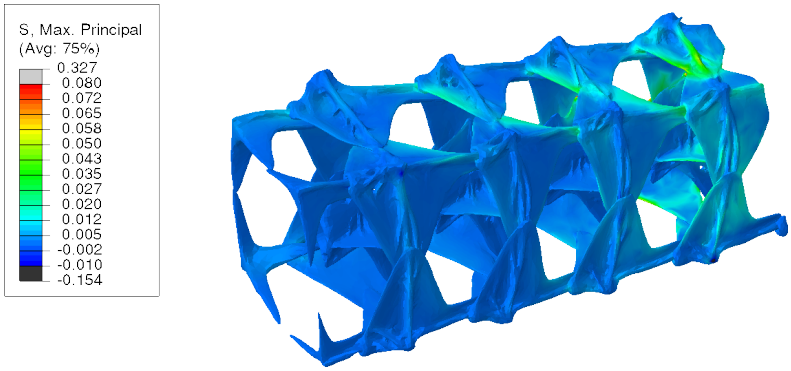

Figure 5.39: Principal stress distribution in MPa in the tail skeleton under lateral compression.

The compressive stiffness again seems to be created by the vertebrae that support the outer structure of dermal plates, combined with the bending restriction imposed by the ridges on the flat surfaces of the dermal plates on the ventral and dorsal sides. The most posterior segment shows the highest principal stresses,

probably because this is the smallest segment.

5.3.3.2 Function of the ridges on the plates

When describing the joints of the seahorse tail (Chapter 3.3.2), it was already mentioned that the function of the ridges of the dermal plates is unlikely to be providing a rigid supporting rail for the gliding joint. Since the compressive simulations show stress concentrations on these ridges, we believe that they are involved in distributing stresses in the tail. More in detail, we believe that the main function of the ridges is coping with bending forces on the otherwise flat surfaces of the dermal plates. Simulations were done on the bending stiffness of the flat sides of the dermal plates with and without the ridges to study the effect that these ridges have on the bending stiffness of the dermal plates. Using pyFormex, the ridges were somewhat flattened out on a left ventral dermal plate, while keeping the same cross-sectional area. In this way we can study the influence on the bending stiffness of a more flat shape with the same volume. The normal and flattened geometries are shown in Figure 5.40.

Figure 5.40: Cross-section of the ridges on a ventral dermal plate, before (left) and after (right) flattening using pyFormex.

Simulations were done on the normal and the generated geometry. Linear tetrahedral elements were used. A single force normal to the flat plane of the dermal plate was applied to the most distal tip of the plate (which is located on the central ridge). Care was given to the corresponding position of the force, so that the moment arm in both simulations is exactly the same. The result of the simulation in demonstrated in Figure 5.41.

Even when the ridges are only partially removed, the stiffness of the flat side of the dermal plate already goes down by 20%: the vertical displacement of the tip of the lateral part of the ventral dermal plate is 0.256 mm without flattening the ridges and 0.317 after flattening the ridges. The reason is that even though the cross-sectional area remains the same, the second moment of inertia (or area moment of inertia) of the cross-section decreases when the ridges become smaller, much like an I-beam has a higher bending stiffness than a beam with a squared cross-section if the cross-sectional area is equal for both.

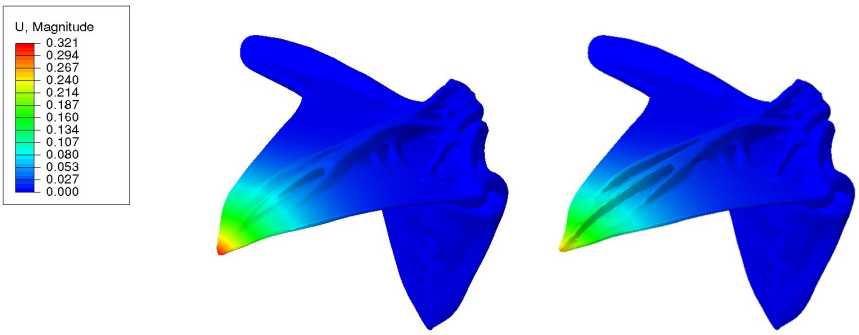

Figure 5.41: Deflection (in mm) of the flat part of a dermal plate with (left) and without (right) smoothing of the distal part of the ridges.

5.3.4 Lateral spine of the vertebrae

The shape of the vertebrae of the seahorse tail is somewhat peculiar. The lateral spines have a shape that somewhat resembles the wings of a plane. In proximal direction, there is a plate-like structure supporting the lateral spine. This forms a right triangle with the spine, as demonstrated in Figure 5.42.

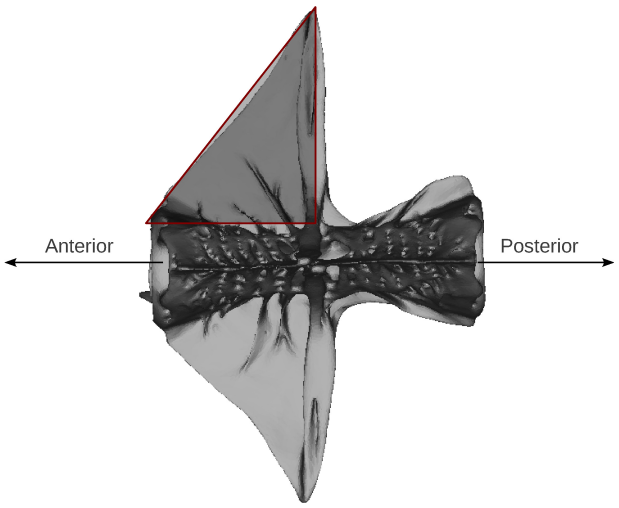

Figure 5.42: Triangular shape on a dorsal view of a caudal vertebra.

The triangular shape of the supporting structure of the lateral spine should make the lateral spine significantly stiffer in the longitudinal direction of the tail, which should make it easier to cope with longitudinally directed forces. To check this hypothesis, a sagittal rotating force vector is applied to the most distal point of

the lateral spine, while tracking the deflection of the spine. The resulting deflection at force magnitudes 0.0001 N, 0.0005 N, and 0.00025 N are given in Figure 5.43.

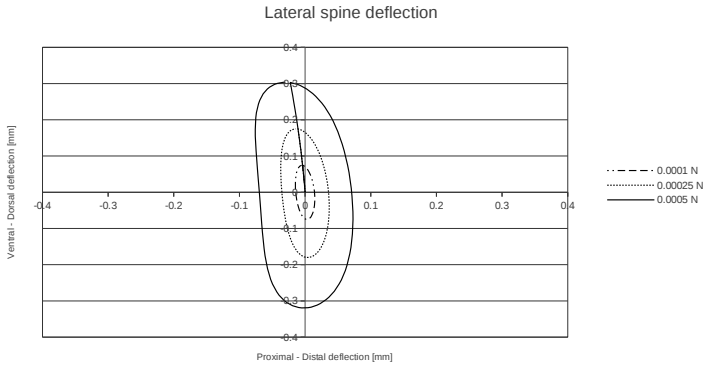

Figure 5.43: Directional deflection of the tip of the left lateral spine of the third caudal vertebra in the seahorse tail at three different load amplitudes.

The force vector $\vec{F}$ consists of an $\vec{F}_X$ component along the X-axis (the longitudinal axis) and a $\vec{F}_Y$ component along the Y-axis (the dorsoventral axis). To obtain a rotating vector the amplitude of both components follows a sinusoid with a phase difference of one quarter of the wavelength, as demonstrated in Figure 5.44. The simulation is static, so the displayed stresses are independent of the chosen time period (in this case one second). Figure 5.43 clearly shows that the deflection in the dorsoventral direction is a lot higher than the deflection in anterior-posterior direction. So the lateral process is much stiffer in the longitudinal direction. The amount in which the stiffness is higher is indicated in Table 5.2. For small deflections, the ratio is over five, while for the larger deflections the ratio becomes smaller.

Force	0.0001 N	0.00025 N	0.0005 N
Dorsal displacement (Fig. 5.44A)	0.0740 mm	0.175 mm	0.304 mm
Posterior displacement (Fig. 5.44B)	0.0146 mm	0.0364 mm	0.0723 mm
Ventral displacement (Fig. 5.44C)	0.0750 mm	0.180 mm	0.319 mm
Anterior displacement (Fig. 5.44D)	0.0142 mm	0.0354 mm	0.0700 mm
Ratio dorso-ventral over longitudinal	5.18	4.95	4.38

Table 5.2: Deflection amplitude at the different moments indicated in Figure 5.44. The last row shows the average ratio of the dorso-ventral deflection over the anterior-posterior deflection.

The higher stiffness along the anteroposterior axis could be an adaptation to the forces imposed on the vertebrae by the myomere muscles. As discussed earlier, the

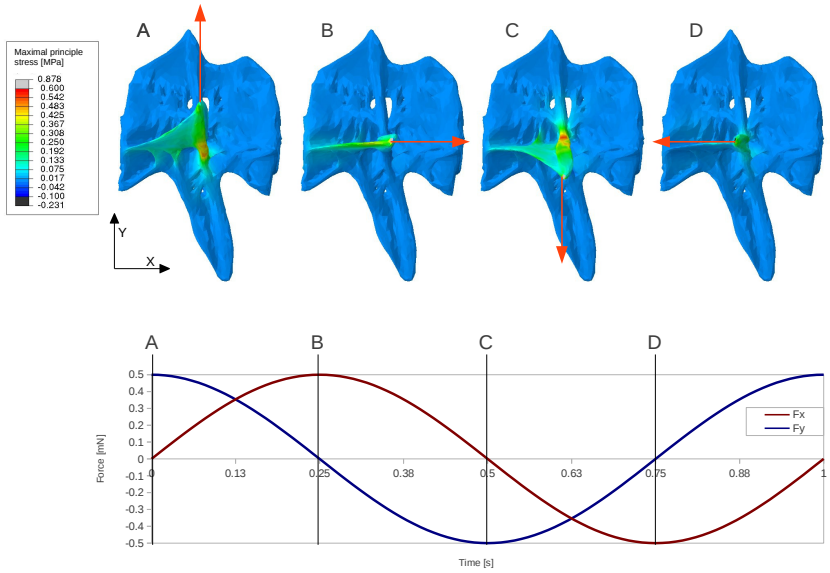

Figure 5.44: Finite element simulation of the lateral spine deflection at a rotating force vector with amplitude 0.0005 N.

exact attachment of the HMM to the vertebrae is not yet fully understood, but the synchrotron scans of the seahorse tail show some tendons near the lateral spines of the vertebrae. The main force component in the myomere muscles is along the anteroposterior axis. A portion of this force is likely transmitted to the lateral spines of the caudal backbone.

5.3.5 Preliminary results of the measured tail kinematics

The kinematics of the seahorse tail were measured by dr. Anabela Maia for five points along the tail of seahorses grasping on to a horizontal dowel. As an example, the digitized points at three different time steps (starting position, halfway the bending, and final position) of the tail bending are shown in Figure 5.45 from two perpendicular viewpoints. The blue point is the most anterior point (i.e. the tail base), while the red point is the most posterior point (i.e. the tail tip). The lines of the grid in the back are spaced 10 mm apart. The axis system is oriented as indicated in Figure 5.5, with the Y-axis being the vertical axis. In this particular case, the seahorse grabs the support with its body directed more or less downward.

The red line that represents the seahorse tail is calculated as a Bézier spline running through the measured points. The total length of the Bézier spline (and thus the tail of this particular seahorse specimen) was 42.5 mm. The total time of tail bending for the illustrated trial was 483 ms.

In the lateral view of Figure 5.5 the increasing curvature of the tail is visible. The tail makes its first contact with the horizontal cylinder near the middle of the tail. Afterwards, the tail part distal of the initial contacts winds around the support. This behaviour, where the tail makes an initial contact somewhere near the middle of the tail and the distal end winding up from this position, can be seen on multiple kinematic recordings. Detailed analyses of the kinematic data was performed by dr. Anabela Maia, who will be publish the results later on. Details about the analyses fall outside of the scope of this dissertation.

In the ventral view, it is obvious that in this particular case there was a significant lateral displacement of the more posterior segments of the tail. This helical winding can be found in other occasions as well, but again the detailed analyses will not be discussed here.

Dedicated pyFormex scripts were developed to analyse the kinematic data and to apply similar movements on the tail model. Figure 5.46 gives an example of how both the shape of the tail and the path of the tracked points can be visualized at the same time. The smaller lines with a colour scale from blue to red are the shapes of the tail at different time steps (10 time steps in this example). Blue colours indicate anterior regions of the tail, whereas red colours indicate posterior regions of the tail. The colour range from dark to bright indicate the time progression. So the black line is the tail position at the start of the recording, and the bright line is the tail position when the seahorse is attached to the support. The 15 lines that go from black to bright throughout their length are the paths of the tracked points throughout time.

Except for the aforementioned initial contact and subsequent winding, there seems to be no obvious pattern in how the seahorse tail approaches and grasps the support. Future analyses could benefit from the developed pyFormex applications to investigate the grasping patterns more elaborately.

The measured tail motions can be applied to the multibody dynamics model of the tail. The motion of each of the tracked points can be imposed on corresponding vertebrae. From this imposed motion, the length changes of the connectors that represent the muscles can be monitored. In a subsequent step, these length changes can be imposed on the muscles in the model, which should lead to the same tail motion as measured in the kinematic analysis. In this way, estimates can be made on the required forces for each of the muscles in the model.

Several scripts were created to facilitate such analyses of the muscle forces based on kinematic measurements of the tail motion. However, the obtained resolution of the motion tracking proved to be insufficient to yield reliable results in the multibody simulations. Small changes in distance between the tracked points (due to resolution limitations) have a relatively large impact on the tail curvature during the simulations where this motion is imposed on the corresponding vertebrae. As the distance between two subsequent points increases by only a minor fraction,

the tail segments in between the measured points are stretched, causing very local bending of the tail near the measured points. Vice versa, small decreases in distance tend to buckle the tail between the measured points, introducing large and unrealistic bending in those segments. Smoothing of the kinematic data improves the quality of the results, but insufficiently to yield reliable results. Improved kinematic measurements (mainly in spatial resolution, as the time resolution is more than sufficient) would be required to generate good results with the simulations based on the tracked motions.

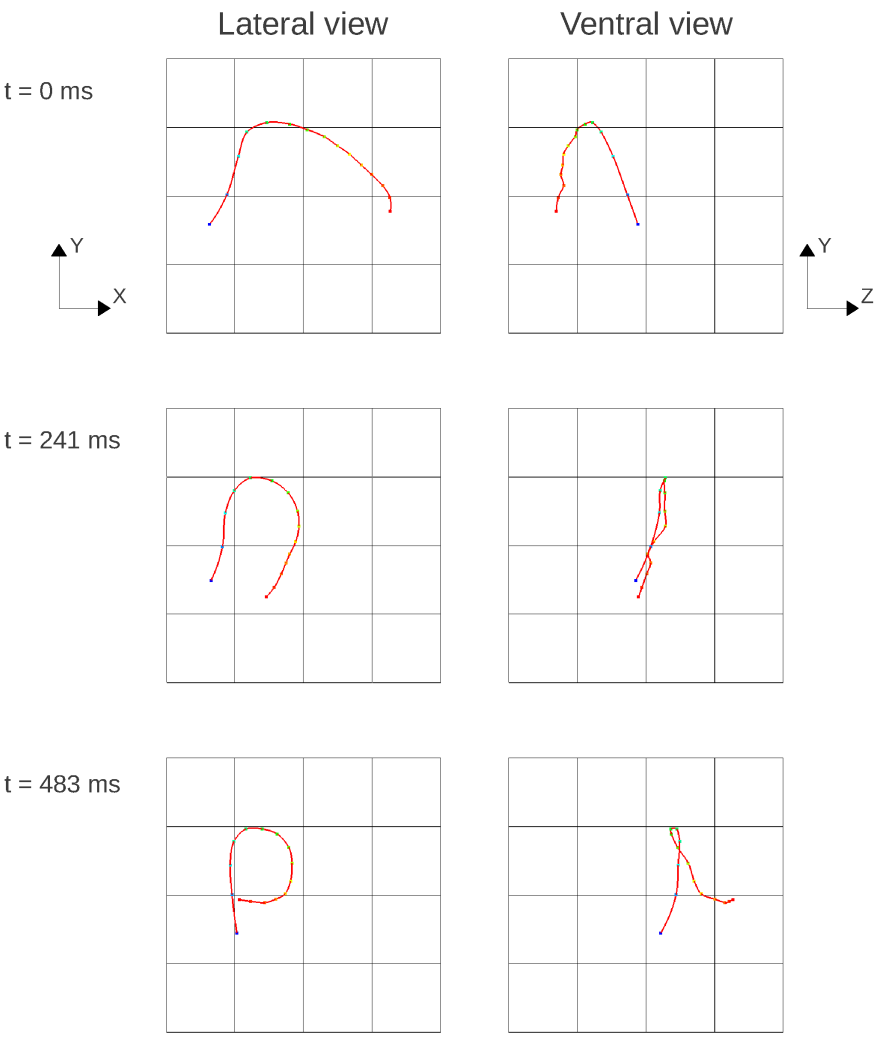

Figure 5.45: Measured tail position at different time steps of a seahorse grasping on to a horizontal support. The blue point is the most proximal segment, red the most distal.

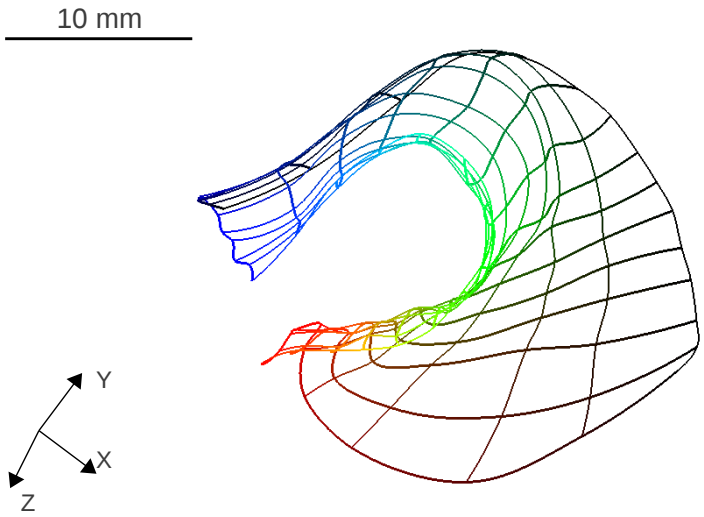

Figure 5.46: Example of the measured movement lines of the tracked points of a grasping tail. Blue is proximal, red is distal; dark colours are near the beginning of the movement, bright colours are near the end of the movement.

5.4 Conclusions and limitations

In this chapter a whole range of simulations were discussed. Some included only rigid bodies, while others included deformable bodies for the skeletal elements. It was shown that without large external forces the deformation of the skeletal elements of the seahorse tail remain insignificant. This confirms the hypothesis that flexibility of the tail can accurately be modelled by using articulating rigid bodies.

5.4.1 Conclusions and limitations of the rigid body simulations

Many rigid body simulations were performed on the model of the musculoskeletal structure of the seahorse tail, of which the most important ones were discussed in this chapter. Since the model generation is parametric, many more simulations can easily be performed, especially as new data become available.

The myomere strains that can usually be found in fish that use undulatory locomotion are too low for the myomere muscles in the seahorse tail during grasping and holding. Higher strains need to be assumed if the distal part of the tail is to be wound around a support with a small diameter. In the distal region, muscle shortenings need to become as large as 40% or 50% of the resting length to be able to wrap the tail around a small support. Such high curvatures compress the ventral intersegmental gliding joints to their maximum. This maximum compression of the ventral joints may be an important factor in the bending flexibility of the seahorse tail.

Unilateral contraction of the HMM introduces ventro-lateral bending of the tail, combined with relatively high amounts of torsion. This torsion could be used by the seahorse to adapt its orientation while holding on to an object.

Attributing forces to the muscles based on constant fibre stresses and proportional to the maximum cross-sectional area of each muscle yields tail bendings that are rather small in the middle region of the tail. Moreover, introducing high fibre stresses causes unrealistic buckling effects in the tail, rendering such simulations useless. The presented model behaves in an unreliable way when forces are used as input, unless the maximum force is kept relatively low.

Versatility and flexibility are the strong points of the modelling strategy that was used. In contrast, the Achilles heel of the current modelling is the limited validation capability. Consequently, the presented results have a limited quantitative value. Currently, there is simply insufficient information available about the structure and operation of several key features of the seahorse tail. We tried to derive the details about several features ourselves, like the passive muscle response or the myomere muscle structure. However, a thorough investigation of all modelling parameters was not possible within the available time frame. Some technical challenges await to improve the model validation. For example, the input of some

measured muscle contraction of several muscle groups during grasping of a seahorse tail would be very welcome, but measuring electric signals in such small muscles is challenging and expensive.

An inherent limitation of the modelling procedure that was used comes from the uncertainty on the geometry. The geometry of the tail skeleton is generated from a single segment of a single scanned seahorse tail. Simulations starting from a different reference segment indicate that the geometry of the reference segment is not fully representable for the geometry of the other segments (taking into account the geometric transformations applied to the reference segment) and probably not fully representable for other specimens of the same species. Visual inspection of the generated and segmented segments show good agreement, but some geometrical differences certainly remain. For example, the ventral and dorsal spines of the (anterior) reference dermal plates are more pronounced than those found in the posterior dermal plates. Although this does not change the position of the landmarks used for the joints and muscle attachments, the size of the ventral and dermal plates do influence the position of the centre of mass. In short, not all geometric changes are not taken into account when generating the geometry of all tail segments from the reference tail segment, only the most pronounced geometric changes are modelled (being scaling and inclination).

Another important limitation are the assumed values for the joints stiffnesses. These stiffnesses were not measured, but estimated based on the geometry of the joints, on finite element simulations on joint compression (that assume that all elasticity comes from bone deformation) and some limited information of joint flexibility [11]. The uncertainty of these values is a major limitation on the quantitative results of the multi-body simulations. Within the model generation, all joints stiffness values are parametric, so that these values can easily be adapted as more information on the joints becomes available.

The passive response of the myomere muscles is estimated based on a single measurement of the hypaxial and epaxial myomere muscles of a single specimen, and can thus only be considered to be a first approximation. Moreover, it was assumed that the passive response is proportional to the cross-sectional area of the muscles. The cross-sectional area of the tested muscles was approximated by measurements on histological slices of the contra-lateral muscle. There may be a small difference in cross-sectional area between the muscles on the left and right side of the vertical septum, and there may be an error on the measurements of histological cuts (incorrect dissection, slice deformation, incomplete slice unfolding, incorrect muscle area detection, ...).

The muscle forces are estimated based on assumed fibre stresses. It is currently not clear how well these estimates apply to the specific muscles of the seahorse tail. The specific prehensile function of the seahorse tail and the specific structure of the hypaxial myomere muscles suggest that the fibre stresses might be different

than those in other fish species.

5.4.2 Limitations of deformable models

Limitations because of the error on the geometry (that occurs during image segmentation, smoothing, and geometry generation based on a reference segment) are similar to those for the rigid bodies, although the models use this geometry without additional simplification (the skeletal element is not simplified to contain only the landmarks like the deformable bodies).

The uncertainty on the used material properties is rather high, since no data is available on the material behaviour of seahorse bone. It was assumed that this behaviour is similar that of to the acellular bone of the ribs of the great sculpin. Even so, the reported standard deviation of the Young's modulus for these ribs is almost 5%. Other reported Young's moduli of fish bone range from 45% less to 68% more than the used stiffness value. Consequently, the presumed Young's modulus can only be considered to be a rough estimation. The Young's modulus of the bone is an easily adaptable parameter in the model generation.

The mechanical behaviour of bone is usually much more complex than the linear elastic behaviour that was assumed. Rigorous material testing of a large set of bone sample in several directions would be required to develop a reliable material model for the bones in the seahorse tail. Given the small size and complex geometry of the bones in the seahorse tail this would be very challenging task. It is hereby possible that the behaviour of the vertebral bone proves to be significantly different than the behaviour of the bone of the dermal plates.

5.4.3 Conclusions and limitations on the compressive simulations

The simulations on the radial stiffness of the musculoskeletal structure of the seahorse tail seem to suggest that the main mechanical factors involved are:

- The vertebrae act as a supporting structure. The spines of the vertebrae (neural spine, hemal spine, and two lateral spines) stretch out to the dermal plates and connect to them, either directly or by means of connective tissue. The forces that act upon the dermal plates are transmitted for a large portion through these vertebral spines to the vertebra (as the gliding joints between the dermal plates will make the plates glide rather than transmit forces to the other plate).

- The ridges of the dermal plates will increase the bending stiffness of the plates. Forces with are roughly perpendicular to the longitudinal direction of the ridges will force the plates to bend. This bending is counteracted by the ridges that increase the the second moment of inertia. As compressive forces

are applied in the dorsoventral direction, the ridges on the lateral sides will accommodate the stresses. Likewise, lateral compressive forces will cause stresses in the ridges on the dorsal and ventral side.

The material model that was used has the same limitations as mentioned for the deformable bodies. The positioning of the compressive plates is another limitation: even though the starting position of these plates was determined meticulously, small changes in orientation of the plates can yield changes in the results.

The gliding joints were neglected in the compressive simulations. This undoubtedly has a significant effect on the results. Compressive simulations that included all joints were conducted as well, but currently show too much convergence issues to be included in the discussion (the large amount of contacting surfaces renders the simulations unstable).

Another limitation is that only one geometry was used. This geometry was based on the μCT-scan with the highest resolution, but this scan only had a limited field of view. Models of other regions of the tail could be created, but the detail of the geometry would be less due to the lower resolution.

6

Applications inspired by the seahorse tail

6.1 Introduction

In this chapter, engineering applications that could benefit from the insights gained from modelling the musculoskeletal structure of the seahorse tail will be discussed. From an engineering point of view, the interesting mechanical characteristics of the structure of the seahorse tail are the very high bending flexibility combined with the reasonably high compressive stiffness. In engineering designs, these are two mechanical characteristics that are typically challenging to combine. Achieving bending flexibility usually requires the use of as little material as possible, and preferably with a low Young's modulus. High radial stiffness, on the other hand, will typically require the use of a lot of material, which preferably has a high Young's modulus.

Not all discussed applications will require both high flexibility and compressive stiffness. The high flexibility of the seahorse tail structure can, for example, be inspiring for the design of flexible robotic arms. The efficient combination of both bending flexibility and compressive stiffness is, however, what sets the seahorse tail apart from other prehensile organs found in nature.

6.1.1 Engineering constraints versus biologic constraints

When using biological designs as a source of inspiration for industrial design, it is important to keep in mind that engineering constraints can be very different from biological constraints. Some constraints are common for both engineering and biology. As typical examples one can think of reliability, efficiency, fitness, and functionality. As typical examples of engineering constraints that do not apply to biology, one can think of cost (in the strict sense of the word), regulation, maintainability, and safety. And finally, some constraints found in biological designs but not in engineering designs are phylogenetic and genetic constraints (discussed in more detail in Chapter 2.2).

An important consequence of the differences in constraints is that nature's solution to a specific problem is not necessarily the best possible engineering solution to the problem. Moreover, because of the biological constraints that act on evolution, nature's solutions may not even be the best imaginable solutions. In mathematical terms one can think of solutions found in nature as being local maxima in fitness, while in engineering the focus should be on the absolute maxima.

The differences in constraints poses limitations on both how well a natural solution can be mimicked (e.g. because of differences in biological and engineering materials), and how appropriate the solution would be for engineering applications (e.g. because the design is too expensive or too difficult to control). These limitations should be kept in mind for the discussions on the applications inspired by the seahorse tail.

6.1.1.1 Mimicking the degrees of freedom of the seahorse tail

In most engineering applications, the engineer will typically try to minimize the amount of material that is consumed in the design (mainly because of the material cost constraint, but also e.g. to minimize weight and inertia, to make the structure aesthetically pleasing, to reduce recycling costs, etc.). To do so, the engineer will likely use materials with a high stiffness, like concrete and steel. Monolithic metal parts are not flexible, so in order to obtain flexibility in the designs, joint connections are usually added between the parts. Managing the movement of these joints will allow the engineer to manage the movement of the structure as a whole.

So in a first step towards creating an engineering structure that mimics the movement of the seahorse tail, we can design a structure consisting of metal parts that are connected by joints that mimic the skeletal joints in the seahorse tail. Figure 6.1 shows an illustrative example of such a structure design. This model was designed by Sam Robberecht as part of a master thesis at the Hogeschool Gent [117]. Much like the vertebral spines, the central parts have elongations in each of the six main directions, forming ball-and-socket joints at each end (in engineering these joints will usually be called ball joints). The gliding joints of

the seahorse tail are mimicked using cylindrical joints that contain longitudinal springs. Finally, in each of the four corners of the segments, an additional ball joint is placed to obtain full bending flexibility. The resulting structure has radial symmetry, indicating that a rotation of $90°$ around its longitudinal axis will yield the exact same structure.

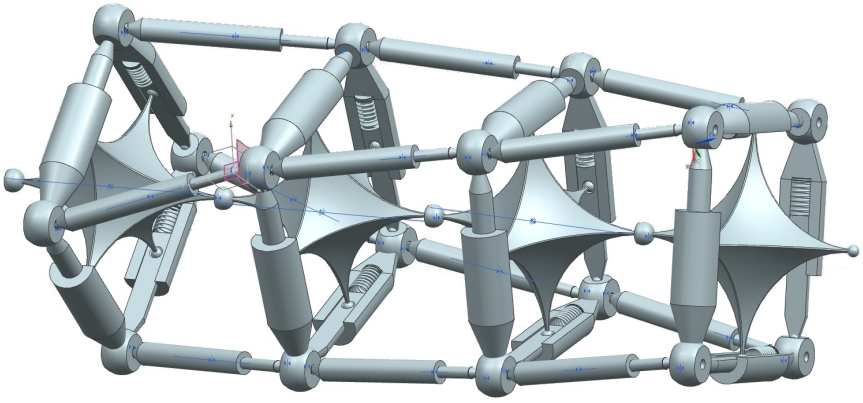

Figure 6.1: CAD of a possible model that mimics the degrees of freedom of the seahorse tail [117].

Even without any actuators, this structure is already relatively complex. The degrees of freedom quickly become very high when additional segments are added, which makes managing and constraining the movement of the structure cumbersome. Therefore, more feasible structural designs inspired by the seahorse tail should preferably have less components, less joints, and less degrees of freedom.

6.1.2 Comparable robotic designs in literature

The most evident applications resulting from studying the biomechanics of the seahorse tail are robotics that mimic the flexibility of the tail, either for prehension or for steerability. Some comparable robotic designs that have been published will be introduced in this section, while how these robotic designs can be interesting or inspiring for robotic designs based on the musculoskeletal system of the seahorse tail will be discussed later on in Chapter 6.3.1.

Prehensile robotics can mimic the behaviour of the tail when it grasps on to vegetation on the seabed. In this way, the robot can hold an object and change the position of this object. To achieve a good grip on the object, the robotic arm needs to fully wrap around it. To do so, the robot either requires continuous bending over a larger area (in case of a continuum style robot), or a large amount of articulating segments (in case of a robot that uses discrete articulators). This principle has previously been described in Chapter 2.5.

The main advantage of robots that mimic the grasping behaviour of prehensile organs, is that the requirements on the size, geometry, and position of the objects that need grasping are less strict than for example when the grasping is achieved through converging robotic 'fingers'. The contact area between the robot and the object is larger, allowing more variability in shape of the object, while the principle of moving the tentacle around the object and subsequently tightening the grip allows the object to be slightly out of position at the onset of prehension.

6.1.2.1 Robotic octopus arm

When looking purely at bio-inspired robotics in literature, the robotic octopus arm developed by Calisti et al. is most probably the closest related to what we try to do with the seahorse tail [61, 67]. Like the seahorse tail, the octopus arm is a prehensile organ (although the octopus uses its arms for locomotion as well). There is, however, an important difference in the way that the prehensile organ functions (and consequently in the way that robotics based on it function): the octopus arm has no bony skeleton. It relies on hydrostatic pressure to move the tentacle, rather than a supporting musculoskeletal structure.

The robotic arm inspired by the octopus arm contains no joints. Instead, the motion of the robotic arm is achieved by two cables: one steel cable on the axis of the tentacle, and one cable made from ultra high molecular weight polyethylene on the side of the tentacle (Figure 6.2). Pulling the cable on the central axis will shorten the robotic arm, whereas pulling the latter cable will introduce bending.

6.1.2.2 Snake-like robots and anguilliform fish robots

The introductions and discussions on snake-like and anguilliform fish robots are combined in this chapter, since the basic principle is the same in both cases: both are robotics consisting of a long chain of segments connected by actuators acting like hinge joints. This principle is demonstrated in Figure 6.3. The rotating joints need to generate lateral waves of the body that result in forward thrust. The main difference between both robotics lays in the interaction with the surroundings: the snake-like robots mostly use frictional anisotropy with the floor (so on the ventral side) [45, 54, 56, 58], whereas the anguilliform swimming robotics use the drag forces generated by the surrounding water (on the lateral sides) for forward propulsion [42, 46]. The frictional anisotropy in snake-like robots is in most cases achieved through passive wheels [58].

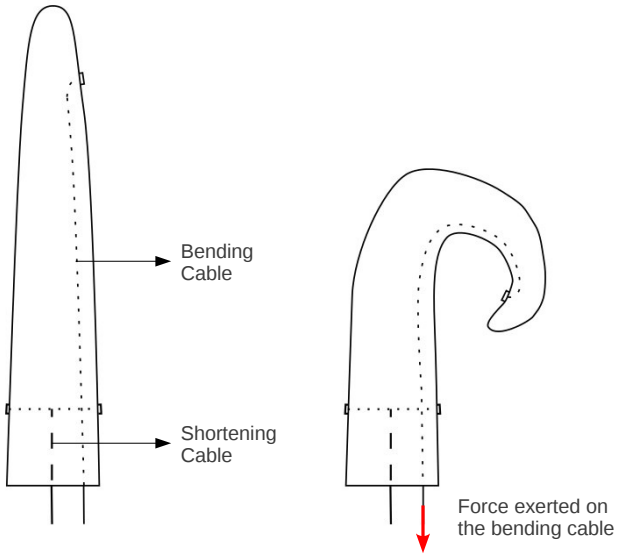

Figure 6.2: The bending of the robot inspired by the octopus arm is achieved through pulling a cable on the side of the tentacle [61].

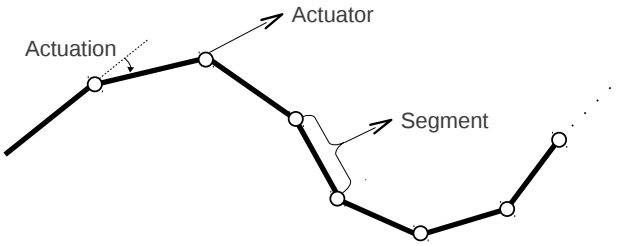

Figure 6.3: Principle of robotics based on snake-like or anguilliform locomotion.

6.2 Materials and methods

6.2.1 Biomimetic actuators

Introducing motion in bio-inspired robotics can be challenging. More in particular, it is often difficult to find actuators that realistically mimic the functionality of the muscles. In the past, several biomimetic actuators have been developed, examples of which include the use of shape memory alloys (SMAs), pneumatic artificial muscles (PAMs) like the McKibben pneumatic actuators, and electro-active polymers (EAP). These biomimetic actuators will be discussed below.

Shape memory alloy (SMA)

Shape memory alloys are commonly used in biomimetic actuators [118]. They refer to a group of metal alloys that can change shape under influence of temperature changes. This thermo-mechanical behaviour is called the shape memory effect (SME). When the temperature of the alloy crosses a certain phase transition temperature, the crystalline structure of the SMA switches between the martensite phase (at temperatures below the phase transition temperature) and the austenite phase (at temperatures above the phase transition temperature). This phase transition causes a change in internal stresses, which causes a change in shape or, if the SMA is fully constrained, a change in forces exerted on the environment.

Muscle contraction can be mimicked by wires made from SMAs. As the SMA wire is heated, and its crystalline structure goes into the high-temperature austenite phase, the wire hardens and contracts. Upon cooling, the structure reverts back to the low-temperature martensite phase, causing a relaxation of the wire. This behaviour mimics the contraction and relaxation of muscles. As an example, Figure 6.4 shows the design of a biomimetic finger that is powered by SMA wires [118].

Wires can only exert pulling forces (as pushing will buckle the wires), so in the majority of cases two wires are required to actuate one joint (unless passive actuators like springs are present): one for each direction of motion. This is not really a limitation, since skeletal muscles will also exert pulling forces on the tendons. In Figure 6.4, the wires required for bending and straightening the biomimetic finger are respectively indicated as flexor tendons and extensor tendons.

The design of the biomimetic finger can be inspiring for a robotic design inspired on the seahorse tail: SMA wires on the ventral and dorsal side of the segments can alternatively be heated and cooled to cause flexion (i.e. tail bending) and extension. By heating the ventral wires while cooling the dorsal wires, the robot can bend ventrally (prehension), and vice versa.

It should be noted that the typical strain recovery of SMAs during phase transition is limited to 8.5% [119]. As demonstrated elaborately in the previous chapter, these levels of strain are insufficient to bend a seahorse tail far enough to be used effectively as a prehensile organ. Consequently, robots that are inspired on the seahorse tail and use SMA wires to mimic the muscle function, need wires that are much longer than the muscles themselves, as the obtainable strains are much lower than observed in seahorse tail muscles. In practice this means that an actuator that bends a certain segment, needs to run over several segments to obtain sufficient displacement. This displacement then needs to be delivered to that specific segment only. A possible way of doing so, which will be discussed in chapter , is using Bowden cables, where the inner cable is made from SMA.

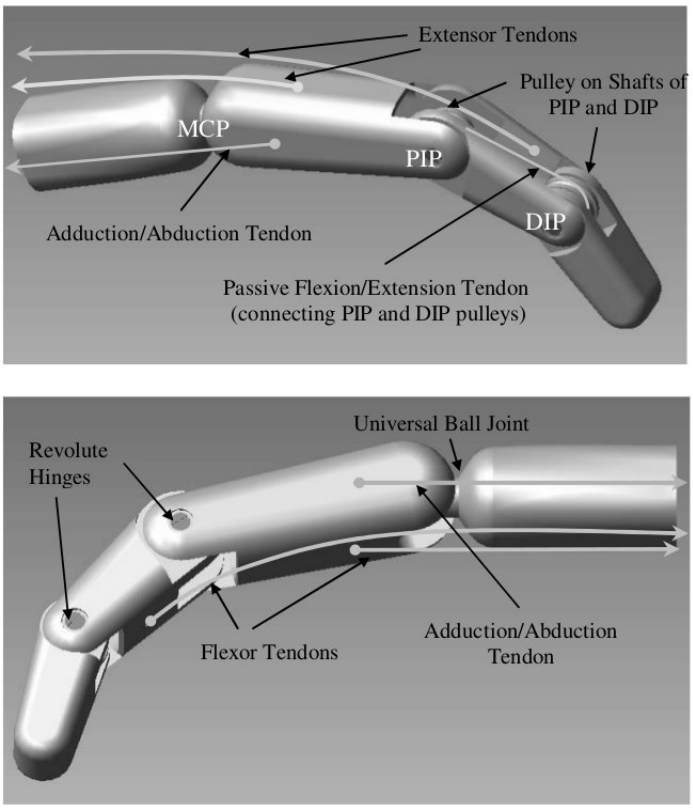

Figure 6.4: Conceptual drawing of a biomimetic finger that moves by contraction of SMA wires [118].

Pneumatic artificial muscle (PAM)

Pneumatic artificial muscles or PAMs consist of a volume enclosed by a reinforced membrane. Upon pressurizing the internal volume, the PAM expands radially and contracts axially (just like real muscles), thus generating uniaxial pulling forces.

The best known type of PAM is the so-called *McKibben muscle*. This type of PAM consists of an inner rubber tube surrounded by a braided sleeving. The rubber tube provides an airtight chamber that expands radially when being pressurized, while the braided sleeving transfers the tension to the attachments of the artificial muscle [120–122]. The working principle of the McKibben muscle is demonstrated in Figure 6.5. The high power to weight ratio of the McKibben muscle makes it a popular actuator in artificial limbs [123].

Depending on the type of PAM, contractions of more than 40% can be obtained. This implies that the McKibben actuators can simply be placed at the posi-

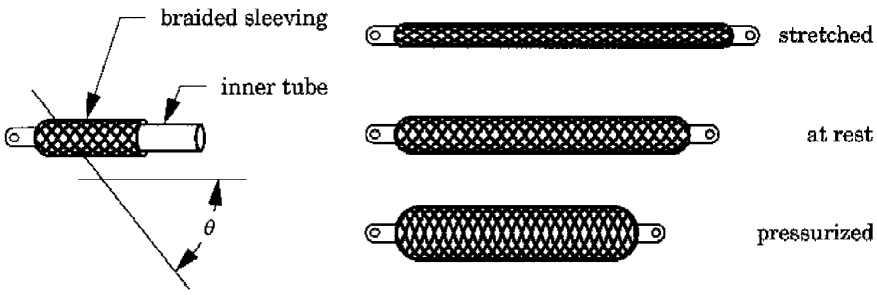

Figure 6.5: Working principle behind McKibben actuators [122].

tion of the bending muscles in the seahorse tail to actuate a seahorse tail mimicking robot, although large contractions on PAM will be accompanied by large radial expansion, placing geometric limitations on the robot. Another important limitation is that each artificial muscle must be connected with a tube that delivers the required pressure. As the amount of muscles in the seahorse tail is quite large, even for small amounts of segments, implementing these tubes without compromising bending performance is challenging, especially if the robot comprises parts that mimic the dermal plates of the tail. Moreover, if the bending between each of the segments is to be controlled, each of these tubes needs to have a separate steering mechanism, so that the pressurization of each individual muscle can be adapted. These control mechanisms can be rather complex, as the dynamic response of the PAMs is highly non-linear [123].

A final disadvantage of the McKibben muscle is the limited lifetime. The flexible membrane is connected to rigid fittings on both ends of the muscle, which introduces stress concentrations that can lead to rupture of the membrane [121].

Electro-active polymer (EAP)

A rather new yet very promising technique used for artificial muscles are actuators made from electro-active polymers (EAPs) [124–129]. Electro-active polymers are polymers that can change shape or size when subjected to electric fields. There are many sorts of EAPs, each with its own advantages and disadvantages. The forces generated by actuators made from EAPs are relatively low, but interestingly the strains can be very high, up to over 100% [124]. However, these particular strains bring the materials close to their ultimate tensile strength, and the required electric field is often so high that danger for discharge through air emerges. On the other hand, devices inspired by the seahorse tail could likely do with lower strains in the actuators. An example of an EAP actuators that can be used to mimic a muscle is shown in Figure 6.6.

The performance of many EAPs exceeds that of muscles in many respects, ren-

Figure 6.6: Muscle-mimicking actuator made from electro-active polymers [127].

dering them attractive for biomedical devices and biomimetic robots [126, 128]. Most EAPs are inexpensive to produce and have a high power to weight ratio. From a biomimetic point of view, the flexibility of the EAPs is particularly interesting. Like muscles, the electro-active polymer actuators can wrap around corners without losing their function. This is an interesting feature for a robot inspired on the seahorse tail: the HMM in the tail span several segments and thus need flexibility during high tail bending.

Other biomimetic actuators

A disadvantage of the commonly used McKibben artificial muscle is that during the full cycle of contraction, pressure needs to be provided. Moreover, if the reaction forces acting on the muscles are variable, a complex control mechanism is required to keep the muscle at a constant level of contraction. To avoid the use of such a continuous control mechanism in systems where contraction is required for prolonged periods of time (like prehensile robots), certain locking mechanisms are advised. For example, the braided sleeving of the McKibben muscle can be impregnated with a shape-memory polymer resin [130]. This resin can be cooled to below the glass transition temperature (T_g) of the resin when the McKibben muscle is fully contracted, thus allowing de-pressurization of the muscle while maintaining contraction. When the shape-memory polymer is heated above T_g, the artificial muscle again behaves like a regular PAM. Since the seahorse tail has been shown to be bended for prolonged periods of time, this type of artificial

muscle could be an interesting option for robots that mimic the prehension of the seahorse tail, as far as the grasping needs to be maintained with a fixed contraction for longer periods.

A more exotic biomimetic actuator is a silk wire. Upon lowering humidity, these wires have proven to contract in a reliable way [131]. The amount of strain is limited to 2.5%, necessitating the use of wires that are much longer than the muscles that they mimic. Moreover, changing humidity inside regions of a robot is not exactly an easy task, nor can it be done very fast.

6.3 Results and discussion

6.3.1 Robotic designs inspired by the seahorse tail

6.3.1.1 Robotic octopus arm

The robotic arm developed by Calisti et al. [61] uses one central cable to shorten the arm and one acentric cable to introduce bending (section 6.1.2). The seahorse tail cannot shorten by muscle contraction (or at least not significantly) due the vertebral spine, so the central cable is not very useful in designs based on the seahorse tail. The principle of having one single cable away from the central axis to induce bending, however, is an interesting simplification that could also be used in designs inspired by the seahorse tail. For example, one cable could run through the entire tail at roughly the position of the median ventral muscles. Pulling this cable would then generate bending in one direction (the ventral direction). When four cables are placed on each side of the robotic tail (ventral, dorsal, left, and right), bending in any direction can be achieved by pulling on one or two of the cables[1]. However, the drawback is that only a global bending can be specified, while local bendings cannot be induced.

Another disadvantage of using cables that run throughout the entire robotic arm is that the amount of local bending would be difficult to predict. The precise bending between two segments would not only depend on the force applied to the cables, but also on the local eccentricity of the cables, the friction of the cable in the local housing around it, and the precise properties of the intervertebral joint (or more specifically, its relative rotational stiffness and relative rotational friction).

The aforementioned issues could be solved by using more cables that only run through a portion of the robotic arm. Each cable could cause bending in a limited subset of segments, though complexity of the robotic system rises quickly with

[1] In fact, three cables would suffice to allow bending in all four directions. Yet the structure of the tail, with four spines emerging from the central vertebra, renders the implementation of four cables more practical. Moreover, the lever arm upon simultaneous pulling of two cables is larger when four cables are used.

each additional cable. Causing local shortening inside the robotic arm by pulling on a cable can be achieved using a so-called *Bowden cable*.

The Bowden cable is a flexible cable consisting of a hollow outer cable and an inner cable. By pulling on the inner cable, a change in distance between the ends of the inner and outer cable can be achieved. This principle is demonstrated in Figure 6.7. A common example of Bowden cables are the brake cables used on bicycles.

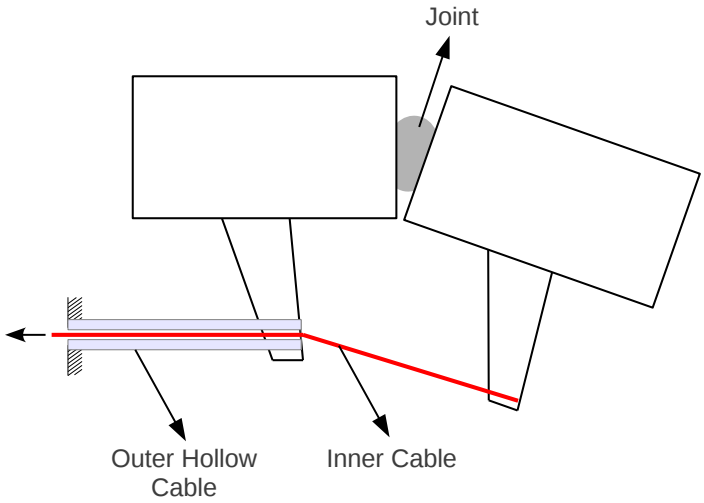

Figure 6.7: Using a Bowden cable located in the median ventral muscle position can induce local bending between two segments.

The required tension can be applied to the wires by winding them over pulleys connected to DC motors [132]. Implementing these pulleys and motors inside the robot can be challenging due to geometric and inertial constrictions, while routing the cables to an external pulley system can impractical if the robotic arm is bended [132]. The inner wire of the Bowden cable can therefore be made from MSA, so that the pulling forces on the wires can be introduced by heating them. The wires have to be relatively long to obtain sufficient bending, but they no longer have to be routed to an external driving system. Still, the wires would have to span several segments, resulting in more wires in the more proximal segments. These wires could affect the bending performance in these segments. If a large amount of segments is used, the required contraction per segment should become low enough to minimize this effect on the bending performance.

6.3.1.2 Snake-like robots and anguilliform fish robots

Contrary to snakes and anguilliform fish, the seahorse predominantly uses ventral instead of lateral bending. Moreover, the movement of the seahorse tail is not cyclic. Nevertheless, the design of the snake-like and anguilliform fish robots can still be a very good starting point for the design of seahorse tail-inspired robotics, as the basic movement of the joints is the same. The control mechanism on the other hand could be much simpler, since the undulatory locomotion of the anguilliform fish and snake-like robots doesn't need to be mimicked: the activation patterns used in locomotion are typically more complex and more sensitive to timing issues than the activation pattern during grasping.

The snake-like and anguilliform fish robotic designs can fairly easily be adapted to resemble the functionality of the seahorse tail. There is no fundamental difference in introducing lateral or ventral bending to the structure. The grasping structure will, however, usually require higher amounts of bending per segment, or a larger amount of segments, since it needs to wrap around the grasped object. Moreover, during the grasping a certain force will be required to hold on to the object while the position of the robotic arm (and thus the object) is altered. The actuators will need to be able to deliver this load reliably for several seconds. In short, the requirements for the actuators are more strict for the grasping robot, while the requirements for the control mechanisms are less strict.

6.3.2 Flexible tube design inspired by the seahorse tail

From an engineering point of view, one of the biggest disadvantages of the seahorse tail skeletal structure is the backbone that supports the dermal plates: this structure limits the free space within the structure itself. It was shown, however, that much of the compressive stiffness of the tail is created by the ridges on the dermal plates. If the intrasegmental gliding joints and the vertebrae are removed from the design of the seahorse tail skeleton, a structure of fairly high radial stiffness remains, with sufficient inner free space that can be used for examples to run cables or fluids through. Starting from this viewpoint, a conceptual design was developed, which is illustrated in Figure 6.8 and Figure 6.9.

The principle of augmenting the second moment of area of the cross-section by ridges is used in combination with the segmental layout of the seahorse tail to create a radially stiff structure with sufficient bending flexibility. The structure is simplified by applying radial symmetry. The design thus consists of a chain of segments, with each segment being a cylinder that is reinforced with three ridges to increase the radial stiffness. Between the segments there is a joint that can be considered as a longitudinal gliding joint (like the intersegmental gliding joint of the seahorse tail). The lose segments can be pushed together until the snap-fit joint between the segments joins both segments. This limits the materials that can

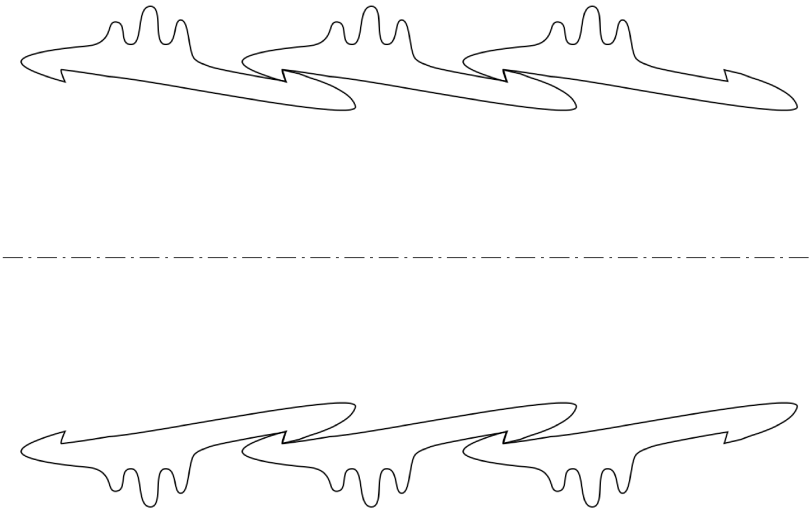

Figure 6.8: Conceptual drawing of a bio-inspired structure with high bending flexibility and high radial stiffness. The design has radial symmetry.

be used to reversibly deformable materials with a relatively low Young's modulus (such as most plastics, aluminium, rubber, etc.). From the position demonstrated in Figure 6.8, the gliding joint can locally be compressed, but not elongated. If the tube is bended, the gliding joint compresses on one side, while on the other side the snap-fit joint limits the extensibility.

Since there is no interior structure, the presented design can be used as a flexible tube. A common example of a flexible tube is the flexible hose of vacuum cleaners. One advantage of the presented design over regular flexible tubes is that the bending flexibility relies less on material deformation. Relatively stiffer materials could therefore be used, increasing the obtainable radial stiffness. Moreover, the wall thickness of the tube can be much larger, again increasing the obtainable radial stiffness without sacrificing the bending flexibility of the structure. Other advantages are for example that the length of the tube can be altered by adding segments, or, if the snap-fit joints are designed in a reversible way, removing segments.

The flexible tube has several possible practical applications, including:

- Flexible (electric) cable hoses. The segments need to be longitudinally compressed before the cables are introduced, since the stretched position would shorten upon bending, which would force the internal cables to compress.
- Flexible tubes for the transport of gasses (like exhausts, air intakes, ...). It should be noted that the gliding joints inhibits the structure of being fully air-tight, thus gasses can escape from the interior, especially if there is a

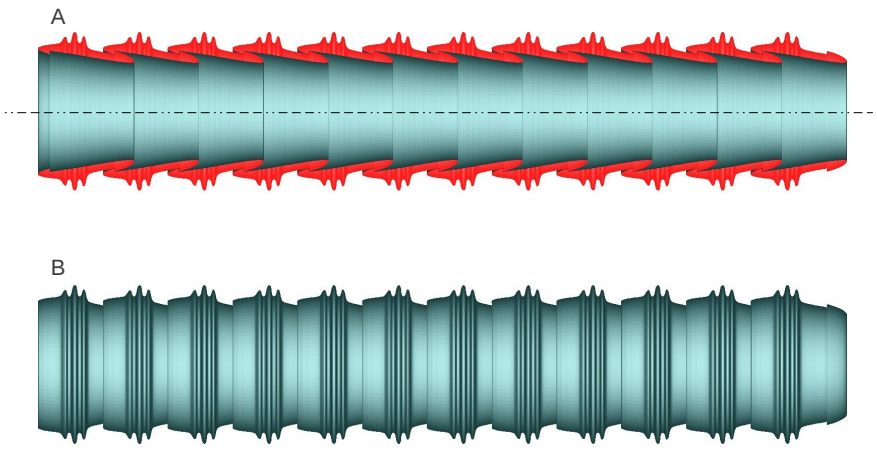

Figure 6.9: Three-dimensional reconstruction of the conceptual flexible hose design in cross-section (A) and from a lateral viewpoint (B), rendered in pyFormex.

pressure difference with the surroundings. The structure can be made in such a way that the segments compress the gliding joint in radial direction to limit this leakage.

6.3.3 Innovative steerable catheters

Besides prehension capability, another functionality of the seahorse tail that could be exploited in robotics is the steering capability. This means that the bending flexibility of the tail is used to guide the tip of a long object into a certain direction, so that the rest of the object can follow this direction. Robotics that use only this functionality do not necessarily have to contain many segments; a few segments can suffice for many applications. One such example, that will explored in this section, is a steerable catheter.

Catheters are medical devices consisting of a thin tube made from biomaterials. They are inserted in the body to perform surgical procedures or to treat diseases. A growing number of catheters can be bended (manually or by computer control systems) near the distal end during the procedure, usually by means of integrated pulling-wires [133]. These catheters are called steerable catheters. Their main advantage lies in the fact that surgeons can more easily manoeuvre the the catheter through the body.

Such a catheter could be the steerable catheter for stent delivery. In this case the steerability is used to avoid excessive damaging of the arterial wall while manoeuvring the stent into position through the arterial system of the patient. The tips of the catheter can more or less follow the curvature of the artery, as well as direct the catheter into side branches. Preserving the integrity of the arterial wall

is important, since these procedures are usually done in patients that are already prone to cardiovascular diseases, and damaged endothelial cells can be a cause of new cardiovascular problems (e.g. new formation of atherosclerosis) [134]. The steerability can also be used to manoeuvre a catheter into difficult positions like the side branch of a graft (demonstrated in Figure 6.10), within a kinked stent [133], or within the pericardium [65].

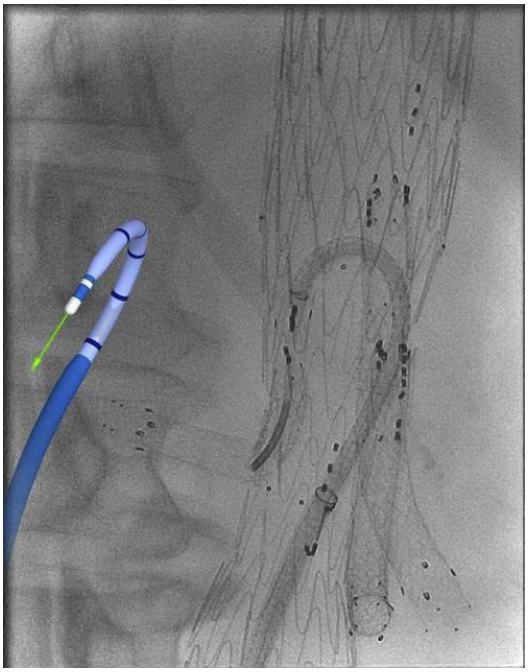

Figure 6.10: Using a steerable catheter to manoeuvre into a side branch of a graft [133].

The design of a steerable catheter could be inspired by the seahorse tail. The flexibility and bending performance of the tail can inspire efficient and robust bending of the steerable catheter. Actuation of the medical device could be obtained by pulling a wire at one side of the tube. It is possible to use multiple wires to better control the local bending, but such an increase in complexity is not advised, as a uniform bending at the distal tip of the catheter is sufficient for most applications.

Based on the flexible tube design of the previous section, and the actuation of the robotic arm inspired by the octopus arm (Chapter 6.1.2.1 and Chapter 6.3.1.1), a concept for a steerable catheter can be devised. The basic principle is drawn in Figure 6.11.

One cable located at the inner wall of the bendable tube is connected to the distal end of the tube. The cable can either be pulled by a pulling mechanism or be

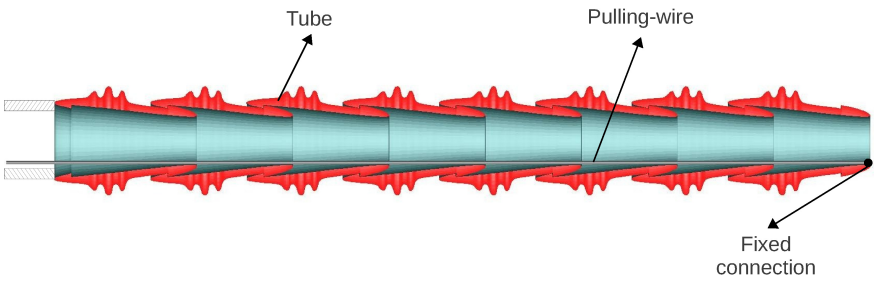

Figure 6.11: Conceptual drawing of the distal end of a steerable catheter.

contracted. The contraction can be established by temperature changes is case that SMA is used, or electric signals in case EAP is used (Chapter 6.2.1). If friction between the pulling-wire and the bendable tube is low, the bending of the distal end of the steerable catheter will be almost uniform.

The shape of the segments of the tube ensure that the radial stiffness is high enough to withstand external forces, while keeping sufficient space inside the tube to allow insertion of other tubes or wires. The gliding joints of the tube are a possible concern: tissues could become caught in the joints, or fluids could leak through the joints. The distal part of the catheter could be covered with an additional very flexible tubing to accommodate for these issues. The steerable catheter could potentially be used both as inner or outer guiding tube.

6.3.4 Other possible applications

Some other possible application areas will very briefly be discussed in this section. This is just meant as an indicator of other possibilities and is not meant to be elaborate, nor does it pretend to be complete.

Flexible stents

In the biomedical engineering field, a possible design topic that can benefit from the findings in this dissertation is the design of flexible stents. These stents are usually chosen for stenting arteries in the lower extremities, since these arteries are prone to rather harsh loading conditions. These loading conditions are created either by external forces (for superficial arteries) or by knee flexing (for arteries in the knee region). In both cases, the stent needs to be able to cope with rather large deformations (mostly bending), while still keeping a high radial stiffness, in order to keep the artery open for sufficient blood flow. Hence, the structure of the flexible stents needs to combine bending flexibility with radial stiffness, exactly the combination of mechanical properties that the seahorse tail achieves so efficiently. Designing a stent that is flexible enough is not so difficult. Designing

a stent that can cope with the many loading cycles is much more challenging, as can be evident from the fact that over one third of the femoral nitinol stents tend to fracture [135].

The flexible tube design from the previous section can be a starting point for the design of such a flexible stent. However, the joints in this design are not applicable to stents (since longitudinal displacements of parts of the stent can damage the arterial wall). These joints could be replaced by other, non-articulating sections that allow longitudinal displacement.

Protective clothing for extreme sports and stuntmen

As extreme sports become more popular, the need for protective clothing that limits the movement as little as possible increases. Also for stuntmen protective clothing is of the utmost importance. In case of stunts in the film industry, the protective armour needs to be as thin as possible, so it can be worn beneath regular clothes without being visible. The geometry of the dermal plates of the seahorse tail and the way that they articulate (without sacrificing the bending flexibility of the structure) can be inspiring in developing such high-tech clothing. Similar research has been done based on the scale armour of the fish *Polypterus senegalus* [136].

6.4 Conclusions

Several applications that can benefit from studying the design of the musculoskeletal structure of the seahorse tail have been discussed in this chapter. A preliminary analysis was conducted on designing prehensile robots inspired on the seahorse tail. Existing robotics inspired on other animals can be a starting point for the development of such a robotic arm. Most closely related are the robotics inspired by snake locomotion and anguilliform swimming, as well as robotic arm inspired by the octopus arm.

Bowden cables at the position of the median ventral muscles of the seahorse tail can be used to bend a robot that mimics the skeletal structure of the seahorse tail. In this way, both localised bending between specific segments and distributed bending over several segments can be obtained. The muscle function in the seahorse tail can be mimicked by biomimetic actuators, like pneumatic artificial muscles are actuators constructed from shape memory alloys or electro-active polymers.

A basic concept for a flexible tube inspired by the dermal plates of the seahorse tail was presented. This design demonstrates how the supporting structure of the backbone (that keeps the structure form being hollow) can fully be taken over by providing sufficient radial stiffness to the outer hull by means of ridges that resemble the ridges on the dermal plates of the seahorse tail. Such flexible yet radially stiff hoses could for example be used to protect (bundles of) electric cables.

The same principle can be applied to the design of innovative steering catheters, where the flexible tube is actuated by a pulling-wire attached to the distal end.

Other applications that can benefit from the biomechanics of the seahorse tail are flexible stents for the lower extremities and protective clothing for extreme sports and stuntmen.

7 Conclusions and perspectives

In this dissertation, advanced multibody and finite element analyses were performed on the specialized musculoskeletal structure of the seahorse tail. These analyses were needed to provide clear insights in the mechanics involved in the tail structure that allows the efficient combination of bending flexibility and compressive stiffness. Such insights can be inspiring for engineering designs that need to include one or both of these mechanical characteristics. In this chapter, the conclusions drawn in this dissertation are summarized, and suggestions for future research that builds on this dissertation are provided.

7.1 General conclusions

More and more engineers turn to nature for design inspiration, as nature provides field-tested, efficient, and robust solution to many real-world problems. The seahorse tail is a particularly interesting design in nature, as it combines bending flexibility (to act as a prehensile organ) with radial stiffness (to better protect the tail from external forces), a combination of mechanical properties that is valued in many engineering applications. To analyse how the seahorse tail manages to efficiently combine two usually conflicting design parameters, the musculoskeletal structure of the tail was studied through versatile biomechanical models generated based on surface models obtained by segmenting μCT-scans.

Looking for design inspiration in nature is often called biomimicry or biomimetics, while the resulting designs are called bio-inspired designs. Some examples

of popular bio-inspired designs were discussed in Chapter 2. Specific attention was given to designs that show some relevance to designs inspired by the seahorse tail. In particular, designs that mimic the motion of fish were discussed (since the muscles that generate the motion of the seahorse tail are essentially the same). The most important designs in this aspect are fish robots that mimic the anguilliform swimming mode, since these robotics show chains of segments connected by rotating actuators, a basic design approach that can also be used when designing robotics that mimic the seahorse tail. However, the seahorse tail plays no role in locomotion, but in prehension. Several robotics that are inspired by prehensile organs were therefore discussed. There is a fundamental difference between prehensile organs that have no skeleton and therefore use internal hydrostatic pressures, and prehensile organs that use articulation of skeletal elements. This difference can sometimes also be found in the robotics derived from the prehensile organ. Both of these approaches have some relevance to this dissertation, but this is discussed in Chapter 6.

Some important principles of the seahorse tail anatomy were discussed in Chapter 3. The tail consists of a chain of uniformly shaped segments. The changes in size and inclination of these segments were quantified for a *Hippocampus reidi* specimen, in order to be included in the biomechanical models. The muscle structure was studied based on high resolution synchrotron scans. The seahorse tail muscles can be divided into hypaxial myomere muscles, epaxial myomere muscles, and median ventral muscles. The cross-sectional area of the muscles throughout the tail was approximated, and estimations about muscle performance were thereafter derived. Relative to the local cross-sectional area of the tail, the cross-sectional area of the myomere muscles remains approximately the same, whereas the cross-sectional area of the median ventral muscles increases. For the passive muscles, the passive response was measured on a single *Hippocampus reidi* specimen and showed that the hypaxial myomere muscles have almost ten times the stiffness of the epaxial myomere muscles. The results give an indication of the passive forces that can be expected for these muscles. Yet, the limited sample size does not allow general conclusions on the passive muscle response for all seahorses of the aforementioned species. Some reservations also remain about possible damaging of the tested tissues, and the lack of a generally accepted testing procedure.

Details on the parametric model generation were supplied in Chapter 4. The model generation was automated using pyFormex scripts. The large amount of skeletal elements, joints, and muscles makes a manual approach cumbersome. Using an automated approach allows easy generation of models with different parameters and integration of other seahorse species. The detection of the different landmarks (locations of the joints and muscle attachments) was based largely on the shape factor of the 3D surface models of the skeletal elements.

The results of the multibody dynamics and finite element models were discussed in Chapter 5. Simulations with deformable skeletal elements showed, in the absence of external forces, negligible deformation during moderate amounts of bending. Consequently, simulations on the tail motion consisted of rigid bodies. The multibody dynamics model of the tail can mimic tail motion by either providing length changes of the muscles, or by providing contraction forces for the muscles. By activating bilateral or unilateral hypaxial myomere muscle contraction, the tail model can bend in respectively ventral or ventral-lateral direction, while tracking the motion of the skeletal elements and joints, muscle forces, and joint forces. Myomere muscle strains that are typically found in fish that use undulatory locomotion are insufficient to allow the seahorse tail to function as a prehensile organ, so other muscle contractions were studied. During unilateral muscle contraction, elaborate torsion can be found throughout the tail, which may be needed to allow the seahorse to orient itself while being attached to an object.

The compressive stiffness of the tail was discussed based on finite element simulations on the tail skeleton. The deformable skeleton was compressed by converging plates, showing relatively high stresses on the ridges of the dermal plates that are located on the side that was not compressed. The ridges increase the bending stiffness of the flat sides of the dermal plates, which likely is important for the relatively high compressive stiffness of the tail.

Several applications that can benefit from studying the design of the musculoskeletal structure of the seahorse tail were discussed in Chapter 6. A preliminary analysis was conducted on designing prehensile robots inspired on the seahorse tail. Existing robotics inspired on other animals can be a starting point for the development of such a robotic arm. Most closely related are the robotics inspired by snake locomotion and anguilliform swimming, as well as a robotic arm inspired by the octopus arm.

In such robotics inspired by the biomechanics of the seahorse tail, several biomimetic actuators can be used to mimic the muscle function in the seahorse tail. When the biomimetic actuators are wires that can contract, it can be interesting to use Bowden cables to make sure that the contraction affects the bending between just two segments, as it is difficult to find wires that can (reliably) obtain strains that come close to the strains observed in the muscles of the seahorse tail.

As another example of an application, a basic concept for a flexible yet radially stiff tube inspired by the dermal plates of the seahorse tail was presented as well. Such flexible hoses could for example be used to protect cables, and could be the starting point for development of flexible stents. Building on this design, the basic layout for a steerable catheter was presented. A wire on one side of the tube, attached to the distal end, could be used as actuator. This wire could be a regular cable, or one of the discussed biomimetic actuators.

Other applications that can benefit from the biomechanics of the seahorse tail

are flexible stents for the lower extremities and protective clothing for extreme sports and stuntmen.

7.2 Future work

The current model leaves room for improvement. More in particular, some parameters of the model need to be experimentally verified. The model has been prepared for this by including these values as adaptable parameters. Some values that could be checked are the Young's modulus of the bone and the stiffness of the different joints of the tail. The passive extensibility of the muscles is currently based on one measurement for each muscle type. The high difference in muscle extensibility between the hypaxial and epaxial side may suggest that the muscle tissue was damaged during the mechanical testing. Some more muscle samples should be tested to confirm the passive extensibility of the myomere muscles.

Since the microhardness of the dermal plates differs at different positions on the dermal plates [10], it is likely that the Young's modulus also differs throughout these dermal plates. To get a more accurate distribution of elasticity throughout the bones, the local grey-values (Hounsfield values) on the μCT-scans could be used to calculate the local mechanical properties. This technique is commonly used for modelling human trabecular bone [137–139]. Incorporating a non-uniform elasticity model for the bone based on the grey values in the scans should yield more reliable results for those simulations that include deformable bodies.

The multibody dynamics model is constructed from μCT-scans of one single individual. It could be interesting to verify whether scans of other specimens yield similar results. Moreover, in this dissertation we specifically focused on the tail of the *Hippocampus reidi*. At first sight, the mechanics of the musculoskeletal system of other seahorse species does not seem to be significantly different, but it would be better to confirm this by following the presented procedures, but starting from scans of the tails of some other seahorse species. During the development of the scripts that generate the parametric models, care was given to allow easy integration of other seahorse species. However, we did not test the procedure on any species except for the *Hippocampus reidi*. Most likely some fine-tuning would be required to account for certain unexpected differences between the tail structure of the different species.

The framework that was developed in this dissertation lends itself nicely to do more elaborate studies on certain features of the seahorse tail. The biomechanical model of the seahorse tail could be used to test certain hypotheses on the functional morphology and behaviour of the seahorse. The added advantage here is that many of these tests cannot (easily) be done in-vivo. For example, several other activation patterns can be applied to the muscles and the effect on the motion of the tail can be quantified. This dissertation was written from an engineering point of view, so

the testing of biological hypotheses using the developed framework was relatively limited. Future work could therefore focus on formulating and testing biological hypotheses with respect to the functional morphology of the seahorse tail.

Continuing on this path, the bio-inspired robotics that could be developed may be used to further study the functional morphology of the seahorse tail on a physical setup. The basis for this has been developed in two master theses at the Hogeschool Gent using rapid prototyping of the skeletal elements [117, 132]. Combined with some of the biomimetic actuators discussed in this dissertation, a robotic seahorse tail can be devised. By applying certain activation patterns to these actuators biologically valuable information on the tail motion could be obtained. Having immediate visual feedback on the motion by using such a physical setup can be of great value. In this way it could also be easier and faster to find approximate muscle activation patterns that at the source of certain observed seahorse tail motions.

The high bending flexibility of the seahorse tail is a rare characteristic among fish, but it is not unique. Some closely related pipehorses share the extensive tail bending capability of the seahorse [11, 68]. Studying the differences in mechanics between the seahorse tail and the pipehorse tail could be interesting, especially from a evolutionary point of view. In this respect, it would be interesting to include the tail mechanics of some pipefish as well, since their tail represents the ancestral condition of the seahorse and pipehorse tail (although the pipefish tail is insufficiently flexible to act as a prehensile organ) [68]. The musculoskeletal tail structure of both the pipehorses and the pipefish is different than that of the seahorse tail. Consequently, generating biomechanical models of the tails of these genera would require more extensive adaptations of the scripts used in this dissertation.

The possible applications inspired on the seahorse tail have been discussed rather briefly, and and this point no specific designs have been worked out to a working prototype. Currently, the most promising applications are the design of a flexible tube, the design of a steerable catheter, and the design of a robotic arm that mimics the seahorse tail prehension. Each of these could be the focus of future research.

A

Publications

Publications in international journals

First author

- T. Praet, D. Adriaens, S. Van Cauter, B. Masschaele, M. De Beule, B. Verhegghe. Inspiration from nature: dynamic modelling of the musculoskeletal structure of the seahorse tail, *International Journal for Numerical Methods in Biomedical Engineering*, 28(10):1028-1042, 2012.

- T. Praet, A. Maia, C. Neutens, D. Adriaens, M. De Beule, B. Verhegghe. Combined flexibility and stiffness of the seahorse tail: a modelling approach, *Journal of Experimental Biology*, submitted.

Co-author

- S. Daggumati, W. Van Paepegem, J. Degrieck, T. Praet, B. Verhegghe, J. Xu, S. Lomov, and I. Verpoest. Local strain in a 5-harness satin weave composite under static tension : part ii : Meso-fe analysis. *Composites Science and Technology*, 71(9):1217-1124, 2011.

Book chapters

- D. Adriaens, T. Praet, A. Genbrugge, H. Leysen, J. Soons, D. Van Loo, S. Van Cauter, M. Dierick, R. Boistel, M. De Beule, A. Herrel, B. Verhegghe, J. Dirckx, and L. Van Hoorebeke. Micro-ct-scanning as a valuable source of data for musculoskeletal studies in biology. In *J. Van Acker, L. Van Hoorebeke, P. Jacobs, V. Cnudde, and J. Van den Bulcke, editors, X-ray tomography as a multidisciplinary research tool : exploring new frontiers*, page 59. Ghent University. Centre for X-ray Tomography (UGCT), 2010.

List of Figures

List of Tables

References

[1] Sam Van Wassenbergh, Gert Roos, and Lara Ferry. *An adaptive explanation for the horse-like shape of seahorses*. Nature Communications, 2(164), 2011.

[2] Emilano Bruner and Valerio Bartolino. *Morphological Variation in the seahorse vertebral system*. International Journal of Morphology, 26(2):247–262, 2008.

[3] Alan J. Kendrick and Glenn A. Hyndes. *Variations in the dietary compositions of morphologically diverse syngnathid fishes*. Environmental Biology of Fishes, 72:415–427, 2005.

[4] N C Perante, M G Pajaro, J J Meeuwig, and A C J Vincent. *Biology of a seahorse species, Hippocampus comes in the central Philippines*. Journal of Fish Biology, 60:821–837, 2002.

[5] Hans M Peters. *Beiträge zur Ökologischen Physiologie des Seepferdes (Hippocampus Brevirostris)*. Zeitschrift für vergleichende Physiologie, 33:207–265, 1951.

[6] H. Weber. *Beiträge zur Bewegungsphysiologie der Hippocampus-Arten.* Zeitschrift für vergleichende Physiologie, 5(1):1–36, 1927.

[7] *http://en.wikipedia.org/wiki/Salmon*. Visited on December 3, 2012.

[8] Peter R Teske, Michael I Cherry, and Conrad A Matthee. *The evolutionary history of seahorses (Syngnathidae: Hippocampus): molecular data suggest a West Pacific origin and two invasions of the Atlantic Ocean*. Molecular Phylogenetics and Evolution, 30:273–286, 2004.

[9] Peter R Teske and Luciano B Beheregaray. *Evolution of seahorses' upright posture was linked to Oligocene expansion of seagrass habitats*. Biology Letters, 5:521–523, 2009.

[10] Michael M. Porter, Ekaterina Novitskaya, Ana Bertha Castro-Cesena, Marc A. Meyers, and Joanna McKittrick. *Highly deformable bones: un-*

usual deformation mechanisms of seahorse armor. Acta Biomaterialia, 2013.

[11] Melina E Hale. *Functional morphology of ventral tail bending and prehensile abilities of the seahorse, Hippocampus kuda*. Journal of Morphology, 227:51–65, 1996.

[12] Rudie Herman Kuiter. *Seahorses, pipefishes and their relatives: a comprehensive guide to Syngnathiformes*. TMC, 2000.

[13] *http://australianmuseum.net.au/image/Sydneys-Pygmy-Pipehorse/*. Visited on November 19, 2012.

[14] *http://www.ifg.bioteck.org/Fish%20species/Histiogamphelus%20briggsi.htm*. Visited on July 5, 2012.

[15] *http://www.marlin.ac.uk/speciesfullreview.php?speciesID=4801*. Visited on July 5, 2012.

[16] *http://www.divegallery.com/Leafy_Sea_Dragon_9.htm*. Visited on July 5, 2012.

[17] Miquel Planas, Alexandro Chamorro, Particia Quintas, and Antonio Vilar. *Establishment and maintenance of threatened long-snouted seahorse, Hippocampus guttulatus, broodstock in captivity*. Aquaculture, 283:19–28, 2008.

[18] J. M. R. Curtis. *A case of mistaken identity: skin filaments are unreliable for identifying Hippocampus guttulatus and Hippocampus hippocampus*. Journal of Fish Biology, 69:1855–1859, 2006.

[19] Amanda C. J. Vincent, S. J. Foster, and H. J. Koldewey. *Conservation and management of seahorses and other Syngnathidae*. Journal of Fish Biology, 78:1681–1724, 2011.

[20] *IUCN 2012. IUCN Red List of Threatened Species. Version 2012.1. ¡www.iucnredlist.org¿*. Downloaded on 05 July 2012.

[21] Anthony B. Wilson, Ingrid Ahnesjo, Amanda C. J. Vincent, and Axel Meyer. *The dynamics of male brooding, mating patterns, and sex roles in pipefishes and seahorses (family syngnathidae)*. Evolution, 57(6):1374–1386, 2003.

[22] H. Hatze. *The meaning of the term 'Biomechanics'*. Journal of Biomechanics, 7(2):189–190, 1974.

[23] Michael Helms, Swaroop S. Vattam, and Ashok K. Goel. *Biologically inspired design: process and products*. Design Studies, 30(5):606–622, 2009.

[24] Mary C. McKitrick. *Phylogenetic constraint in evolutionary theory: has it any explanatory power?* Annual Review of Ecology and Systematics, 24:307–330, 1993.

[25] *http://www.peterpaulrubens.org*. Visited on July 2, 2012.

[26] Sonya Quinn and William Gaughran. *Bionics - An inspiration for intelligent manufacturing and engineering*. Robotics and Computer-Integrated Manufacturing, 26(6):616–621, 2010.

[27] *http://domestic-science.blogspot.be/2011/03/velcro-under-microscope.html*. Visited on July 2, 2012.

[28] *http://inhabitat.com/building-modelled-on-termites-eastgate-centre-in-zimbabwe*. Visited on July 2, 2012.

[29] Karsten Peters, Anders Johansson, Audrey Dussutour, and Dirk Helbing. *Analytical and numerical investigation of ant behavior under crowded conditions*. Advances in Complex Systems, 9:337–352, 2006.

[30] Frank E. Fish, Laurens E. Howle, and Mark M. Murray. *Hydrodynamic flow control in marine mammals*. Integrative and Comparative Biology, 48(6):788–800, 2008.

[31] *http://upload.wikimedia.org/wikipedia/commons/9/9e/Humpback_ stellwagen_edit.jpg*. Visited on Novemner 20, 2012.

[32] *http://inventorspot.com/articles/humpback_whale_inspires_energy_saving_whalepower_tubercle_techno_30079*. Visited on November 20, 2012.

[33] Alborz Mahdavi, Lino Ferreira, Cathryn Sundback, Jason W. Nichol, Edwi P. Chan, and David J. D. Carter. *A biodegradable and biocompatible gecko-inspired tissue adhesive*. Proceedings of the National Academy of Sciences of the USA, 105(7):2307–2312, 2008.

[34] Laura Raibeck, John Reap, and Bert Bras. *Investigating environmental burdens and benefits of biologically inspired self-cleaning surfaces*. CIRP Journal of Manufacturing Science and Technology, 1:230–236, 2009.

[35] *http://www.treehugger.com/slideshows/clean-technology/nature-inspired-innovation-9-examples-of-biomimicry-in-action*. Visited on July 4, 2012.

[36] J P Whitney and J R Wood. *Conceptual design of flapping-wing micro air vehicles*. Bioinspiration & Biomimetics, 7(3):1–10, 2012.

[37] Pranay Seshadri, Moble Benedict, and Inderjit Chopra. *A novel mechanism for emulating insect wing kinematics*. Bioinspiration & Biomimetics, 7(3), 2012.

[38] Hyungmin Park and Haecheon Choi. *Kinematic control of aerodynamic forces on an inclined flapping wing with asymmetric strokes*. Bioinspiration & Biomimetics, 7(1), 2012.

[39] Leandro dos Santos Coelho and Viviana Cocco Mariani. *Use of chaotic sequences in a biologically inspired algorithm for engineering design optimization*. Expert Systems with Applications, 34(3):1905–1913, 2008.

[40] Harold H. Kung and Mayfair C. Kung. *Nature-inspired design and synthesis of heterogeneous and macromolecular catalysts*. Catalysis Today, 148(1-2):2–5, 2009.

[41] Junzhi Yu, Min Tan, Shuo Wang, and Erkui Chen. *Development of a biomimetic robotic fish and its control algorithm*. IEEE Transactions on Systems, Man, and Cybernetics - Part B: Cybernetics, 34(4):1798–1810, 2004.

[42] H. Yamada, S. Chigisaki, M. Mori, K. Takita, K. Ogami, and S. Hirose. *Development of amphibious snake-like robot ACM-R5*. Proceedings of the 36th International Symposium on Robotics, 2005.

[43] Chao Zhou, Min Tan, Zhiqiang Cao, Shuo Wang, Douglas Creighton, Nong Gu, and Saeid Nahavandi. *Kinematic modeling of a bio-inspired robotic fish*. 2008 IEEE International Conference on Robotics and Automation, pages 695–699, 2008.

[44] P. Krishnamurthy, F. Khorrami, J. de Leeuw, M. E. Porter, K. Livingston, and J. H. Jr. Long. *A Multi-Body Approach for 6DOF Modeling of Biomimetic Autonomous Underwater Vehicles with Simulation and Experimental Results*. Control Applications & Intelligent Control, pages 1282–1287, 2009.

[45] Alessandro Crespi, Andre Badertscher, Andre Guignard, and Auke Jan Ijspeert. *Amphibot I: an amphibious snake-like robot*. Robotics and Autonomous Systems, 50:163–175, 2005.

[46] Alessandro Crespi, Auke Jan Ijspeert, and Ecole Polytechnique F. *AmphiBot II : An Amphibious Snake Robot that Crawls and Swims using a Central Pattern Generator*. Proceedings of the 9th International Conference on Climbing and Walking Robots, (September):19–27, 2006.

[47] Zheng Chen, Stephan Shatara, and Xiaobo Tan. *Modeling of biomimetic robotic fish propelled by an ionic polymermetal composite caudal fin*. IEEE/ASME Transactions on Mechatronics, 15(3):448–459, 2010.

[48] Jindong Liu and Huosheng Hu. *Biological Inspiration: from carangiform fish to multi-joint robotic fish*. Journal of Bionic Engineering, 7:35–48, 2010.

[49] Mohsen Siahmansouri, Ahmad Ghanbari, and Mir Masoud Seyyed Fakhrabadi. *Design, implementation and control of a fish robot with undulating fins*. International Journal of Advanced Robotic Systems, 8(5):61–69, 2011.

[50] Sung Hoon Kim, Kyoosik Shin, Shuichiro Hashi, and Kazushi Ishiyama. *Magnetic fish-robot based on multi-motion control of a flexible magnetic actuator*. Bioinspiration & Biomimetics, 7, 2012.

[51] L Wen, T M Wang, G H Wu, and J H Liang. *Hydrodynamic investigation of a self-propelled robotic fish based on a force-feedback control method*. Bioinspiration & Biomimetics, 7, 2012.

[52] Chunlin Zhou and K. H. Low. *Design and Locomotion Control of a Biomimetic Underwater Vehicle with Fin Propulsion*. IEEE/ASME Transactions on Mechatronics, 17(1):25–35, 2012.

[53] Zeki Y Bayraktaroglu, Atilla Klçarslan, Ahmet Kuzucu, Vincent Hugel, Pierre Blazevic, and A Wheel-less Snake-like Mechanism. *Design and Control of Biologically Inspired Wheel-less Snake Robot*. Biomedical Robotics and Biomechatronics, 2006.

[54] Saori Sugita, Kazunori Ogami, Guarnieri Michele, Shigeo Hirose, and Kensuke Takita. *A study on the mechanism and locomotion strategy for new snake-like robot active cord mechanism - slime model 1 ACM-s1*. Journal of Robotics and Mechatronics, 20(2):302–303, 2008.

[55] Z Y Bayraktaroglu. *Snake-like locomotion: Experimentations with a biologically inspired wheel-less snake robot*. Mechanism and Machine Theory, 44:591–602, 2009.

[56] Xiaodong Wu and Shugen Ma. *CPG-based control of serpentine locomotion of a snake-like robot*. Mechatronics, 20:326–334, 2010.

[57] Pal Liljeback, Kristin Y Pettersen, Ø yvind Stavdahl, and Jan Tommy Gravdahl. *Snake Robot Locomotion in Environments With Obstacles*. IEEE/ASME Transactions on Mechatronics, 17(6):1158–1169, 2012.

[58] David L. Hu, Jasmine Nirody, Terry Scott, and Michael J. Shelley. *The mechanics of slithering locomotion*. Proceedings of the National Academy of Sciences of the USA, 106(25):10081–10085, 2009.

[59] Ali Shaukat. *Newton-Euler approach for bio-robotics locomotion dynamics: from discrete to continuous systems*. PhD thesis, Université Nantes, 2011.

[60] William M. Kier and Kathleen K. Smith. *Tongues, tentacles and trunks: the biomechanics of movement in muscular-hydrostats*. Zoological Journal of the Linnean Society, 83:307–324, 1985.

[61] M. Calisti, M. Giorelli, G. Levy, B. Mazzolai, B. Hochner, C. Laschi, and P. Dario. *An octopus-bioinspired solution to movement and manipulation for soft robots*. Bioinspiration & Biomimetics, 6, 2011.

[62] *http://www.linuxfordevices.com/c/a/News/Robotic-arm-runs-Linux/*. Visited on November 12, 2012.

[63] Michael W Hannan and Ian D Walker. *Kinematics and the Implementation of an Elephant's Trunk Manipulator and Other Continuum Style Robots*. Journal of Robotic Systems, 20(2):45–63, 2003.

[64] *http://www.festo.com/cms/en_corp/9655_10219.htm*. Visited on July 3, 2012.

[65] Takeyoshi Ota, Amir Degani, David Schwartzman, Brett Zubiate, Jeremy McGarvey, Howie Choset, and Marco A. Zenati. *A Highly Articulated Robotic Surgical System for Minimally Invasive Surgery*. The Annals of Thoracic Surgery, 87:1253–1256, 2009.

[66] Kai Xu, Roger E. Goldman, Jienan Ding, Peter K. Allen, Dennis L. Fowler, and Nabil Simaan. *System Design of an Insertable Robotic Effector Platform for Single Port Acces (SPA) Surgery*. The 2009 IEEE/RSJ International Conference on Intelligent Robots and Systems, pages 5546–5552, 2009.

[67] C. Laschi, B. Mazzolai, V. Mattoli, M. Cianchetti, and P. Dario. *Design of a biomimetic robotic octopus arm*. Bioinspiration & Biomimetics, 4, 2009.

[68] Céline Neutens. *Evolutionary morphology of the prehensile tail in seahorses (Sygnatidae, Hippocampus): a microscopical-anatomical 3D study*. Master thesis, Ghent University, 2011.

[69] Steven Vogel. *Comparative Biomechanics, Life's Physical World*. Princeton University Press, 2003.

[70] *http://www.biology-resources.com/drawing-fish-swimming.html*. Visited on July 6, 2012.

[71] John H. Long, Bruce Adcock, and Robert G. Root. *Force transmission via axial tendons in undulating fish: a dynamic analysis*. Comparative Biochemistry and Physiology Part A, 133:911 – 929, 2002.

[72] P W Webb. *Body form, locomotion and foraging in aquatic vertebrates*. American Zoologist, 24(2):107–120, 1984.

[73] C. C. Lindsey. *Form, Function, and Locomotory Habits in Fish*. In Fish Physiology, chapter 1, pages 8–10. Volume 7 edition, 1978.

[74] C M Breder and H E Edgerton. *An analysis of the locomotion of the seahorse, Hippocampus, by means of high speed cinematography*. Annals of the New York Academy of Sciences, XLIII(4):145–172, 1942.

[75] T R Consi, P A Seifert, M S Triantafyllou, and E R Edelman. *The dorsal fin engine of the seahorse (Hippocampus sp.)*. Journal of Morphology, 248:80–97, 2001.

[76] K. Kumaravel, E. Rethina Priya, S. Ravichandran, and T. Balasubramanian. *Morphological Perspectives of the Seahorse Hippocampus kuda (Bleeler) Vertebral System*. International Scientific Research Journal, 2(1):63–69, 2010.

[77] Lisa J. Rosenberger. *Pectoral Fin Locomotion in Batoid Fishes: Undlation versus Oscillation*. The Journal of Experimental Biology, 204:379–394, 2001.

[78] Sven Gemballa and Felix Vogel. *Spatial arrangement of white muscle fibres and myoseptal tendons in fishes*. Comparative Biochemistry and Physiology Part A, 133:1013 – 1037, 2002.

[79] Johan L. Van Leeuwen. *A mechanical analysis of myomere shape in fish*. The Journal of Experimental Biology, 202:3405 – 3414, 1999.

[80] Mark W. Westneat, Melina E Hale, Matthew J. McHenry, and John H. Long. *Mechanics of the fast-start: muscle function and the role of intramuscular pressure in the escape behavior of Amia Calva and Polypterus Palmas*. The Journal of Experimental Biology, 201:3041–3055, 1998.

[81] Felix Vogel and Sven Gemballa. *Locomotory design of 'cyclostome' fishes: spatial arrangement and architecture of myosepta and lamellae*. Acta Zoologica, 81:267 – 283, 2000.

[82] Sven Gemballa and Kerstin Treiber. *Cruising specialists and accelerators Are different types of fish locomotion driven by differently structured myosepta?* Zoology, 106:203–222, 2003.

[83] Mark W. Westneat, William Hoese, Charles A. Pell, and Stephen A. Wainwright. *The horizontal septum: mechanisms of force transfer in locomotion of scombrid fishes (Scombridae, Perciformes)*. Journal of Morphology, 217:183–204, 1993.

[84] John H. Long and Karen S. Nipper. *The importance of body stiffness in undulatory propulsion*. American Zoology, 36:678–694, 1996.

[85] Robert E. Shadwick and Sven Gemballa. *Structure, Kinematics, And Muscle Dynamics In Undulatory Swimming*. Fish Physiology, 23:241–280, 2005.

[86] James M. Wakeling and Ian A. Johnston. *Muscle power output limits fast-start performance in fish*. The Journal of Experimental Biology, 201:1505–1526, 1998.

[87] Lawrence Yoo, Hansang Kim, Vijay Gupta, and Joseph L. Demer. *Quasi-linear Viscoelastic Behavior of Bovine Extraocular Muscle Tissue*. Investigative Ophtalmology & Visual Science, 50(8):3721–3728, 2009.

[88] John D. Altringham and Ian A. Johnston. *Modelling muscle power output in a swimming fish*. Journal of Experimental Biology, 148:395–402, 1990.

[89] Neil Curtis, Marc E. H. Jones, Susan E. Evans, Paul O'Higgins, and Michael J. Fagan. *Feedback control from the jaw joints during biting: An investigation of the reptile Sphenodon using multibody modelling*. Journal of Biomechanics, 43:3132–3137, 2010.

[90] Richard L. Gajdosik. *Passive extensibility of skeletal muscle: review of the literature with clinical implications*. Clinical Biomechanics, 16:87–101, 2001.

[91] Robert J. Beichner. *Physics for Scientists and Engineers*. Brooks/Cole Publishing Company, 2000.

[92] Robert M. Biltz and Edmund D. Pellegrino. *The chemical anatomy of bone: I. A comparitive study of bone composition in sixteen vertebrates*. The journal of bone and joint surgery, 51(3):456–466, 1969.

[93] Anthony Herrel, Hon-Fai Choi, Natalie De Schepper, Peter Aerts, and Dominique Adriaens. *Kinematics of swimming in two burrowing anguilliform fishes*. Zoology, 14:78–84, 2011.

[94] Ahmed A. Shabana. *Dynamics of Multibody Systems*. Cambridge University Press, 2005.

[95] Sarah R. Sullivan, Noshir A. Langrana, and Sue Ann Sisto. *Multibody computational biomechanical model of the upper body*. Proceedings of IDETC/-CIE, 2005.

[96] Neil Curtis. *Craniofacial biomechanics: an overview of recent multibody studies*. Journal of Anatomy, 218:16–25, 2011.

[97] E. Otten. *Inverse and forward dynamics: models of multi-body systems*. Philosophical Transactions of the Royal Society B: Biological Sciences, 358:1493 – 1500, 2003.

[98] L. R. Iwasaki, P. E. Petsche, W. D. McCall Jr., D. Marx, and J. C. Nickel. *Neuromuscular objectives of the human masticatory apparatus during static biting*. Archives of Oral Biology, 48:767–777, 2003.

[99] Neil Curtis, Marc E. H. Jones, A. K. Lappin, Paul O'Higgins, Susan E. Evans, and Michael J. Fagan. *Comparison between in vivo and theoretical bite performance: Using multi-body modelling to predict muscle and bite forces in a reptile skull*. Journal of Biomechanics, 43:2804–2809, 2010.

[100] Neil Curtis, Marc E. H. Jones, Susan E. Evans, JunFen Shi, Paul O'Higgins, and Michael J. Fagan. *Predicting muscle activation patterns from motion and anatomy: modelling the skull of Sphenodon (Diapsida: Rhynchocephalia)*. Journal of The Royal Society Interface, 7:153–160, 2010.

[101] Mehran Moazen, Neil Curtis, Susan E. Evans, Paul O'Higgins, and Michael J. Fagan. *Rigid-body analysis of a lizard skull: Modelling the skull of Uromastyx hardwickii*. Journal of Biomechanics, 41:1274–1280, 2008.

[102] Neil Curtis, Kornelius Kupczik, Paul O'Higgins, Mehran Moazen, and Michael Fagan. *Predicting skull loading: applying multibody dynamics analysis to a Macaque skull*. The Anatomical Record, 291:491–501, 2008.

[103] K T Bates and P L Falkingham. *Estimating maximum bite performance in Tyrannosaurus rex using multi-body dynamics.* Biology letters, (February), February 2012.

[104] Sofie Van Cauter. *Automatic Localisation of Landmarks on Virtual Bone Models*. Phd dissertation, Ghent University, 2012.

[105] Jan J Koenderink and Andrea J Van Doorn. *Surface shape and curvature scales*. Image and vision computing, 10(8):557–564, 1992.

[106] Wim j M Van Damme, Ferry H Oosterhoff, and Wim A Van De Grind. *Discrimination of 3-D shape and 3-D curvature from motion in active vision*. Perception & Psychophysics, 55(3):340–349, 1994.

[107] J Vollmer, R Mencl, and H Muller. *Improved Laplacian Smoothing of Noisy Surface Meshes*. Computer Graphics Forum, 18(3):131–138, 1999.

[108] Liat Cohen, Mason Dean, Anna Shipov, Ayelet Atkins, Efrat Monsonego-Ornan, and Ron Shahar. *Comparison of structural, architectural and mechanical aspects of cellular and acellular bone in two teleost fish*. The Journal of Experimental Biology, 215:1983–1993, 2012.

[109] Jaquan M. Horton and Adam P. Summers. *The material properties of acellular bone in a teleost fish*. The Journal of Experimental Biology, 212:1413 – 1420, 2009.

[110] Sander Kranenbarg, Tim Van Cleynenbreugel, Henk Schipper, and Johan Van Leeuwen. *Adaptive bone formation in acellular vertebra of sea bass (Dicentrarchus labrax L.)*. The Journal of Experimental Biology, 208:3493–3502, 2005.

[111] Geir K Totland, Per Gunnar Fjelldal, Harald Kryvi, Guro Lokka, Anna Wargelius, Anita Sagstad, Tom Hansen, and Sindre Grotmol. *Sustained swimming increases the mineral content and osteocyte density of salmon vertebral bone*. Journal of Anatomy, 219:490–501, 2011.

[112] J. D. Currey. *Mechanical properties and adaptations of some lessfamiliar bony tissues*. Journal of the Mechanical behavior of Biomedical Materials, 3:357–372, 2010.

[113] N. K. Sharma, D. K. Sehgal, R. K. Pandey, and Ruchita Pal. *Finite element simulation of cortical bone under different loading and anisotropic yielding situations*. Proceedings of the World Congress on Engineering and Computer Science, II, 2012.

[114] J. Y. Rho, S. R. Mishra, K. Chung, J. Bai, and G. M. Pharr. *Relationship between ultrastructure and the nanoindentation properties of intramuscular herring bones*. Annals of Biomedical Engineering, 29:1082–1088, 2001.

[115] Margareta Nordin and Victor H. Frankel. *Biomechanics of tissues and structures of the musculoskeletal system*. In Basic Biomechanics of the Musculoskeletal System, pages 33–36. Lippincott Williams & Wilkins, third edition, 2001.

[116] Christoph Baumgarten and Gerald Farin. *Approximation of logarithmic spirals*. Computer Aided Geometric Design, 14:515–432, 1997.

[117] Sam Robberecht. *Construeren van een fysisch model van de staart van een zeepaardje via rapid prototyping*. Master thesis, Hogeschool Gent, 2011.

[118] Vishalini Bundhoo and Edward J. Park. *Design of an artificial actuated finger towards biomimetic prosthetic hands*. Proceedings of the 12th International Conference on Advanced Robotics, pages 368–375, 2005.

[119] Darel E. Hodgon and Robert J. Biermann. *Shape Memory Alloys*. In ASM Handbook, Volume 2: Properties and Selection: Nonferrous Alloys and Special-Purpose Materials, pages 897–902. 1990.

[120] B. Tondu. *Modeling and control of McKibben artificial muscle robot actuators*. Control Systems, IEEE, 20(2):15–38, 2000.

[121] Frank Daerden and Dirk Lefeber. *Pneumatic artificial muscles: actuators for robotics and automation*. European Journal of Mechanical and Environmental Engineering, 47(1):10–21, 2002.

[122] Bjorn Verrelst, Ronald Van Ham, Bram Vanderborcht, Dirk Lefeber, Frank Daerden, and Michael Van Damme. *Second generation pleated pneumatic artificial muscle and its robotic applications*. Advanced Robotics, 20(7):783–805, 2006.

[123] Kexin Xing, Yongji Wang, Quanmin Zhu, and Hanying Zhou. *Modeling and control of McKibben artificial muscle enhanced with echo state networks*. Control Engineering Practice, 20:477–488, 2012.

[124] Yoseph Bar-Cohen. *Electroactive Polymers as Artificial Muscles Reality and Challenges*. Proceedings of the 42nd AIAA Structures, Structural Dynamics, and Materials Conference (SDM), 2001.

[125] S. Naomi Davidson. *Development of Conducting Polymer Based Biomimetic Muscles and Fabrication Techniques for an Artificial Pectoral Fish Fin*. Master thesis, Massachusetts Institute of Technology, 2002.

[126] Tissaphern Mirfakhrai, John D.W. Madden, and Ray H. Baughman. *Polymer artificial muscles*. Materials Today, 10(4):30–38, 2007.

[127] G. Kovacs, L. During, S. Michel, and G. Terrasi. *Stacked dielectric elastomer actuator for tensile force transmission*. Sensors and Actuators A, 155:299–307, 2009.

[128] Xuan-Lun Wang, Il-Kwon Oh, and Sunwoo Lee. *Electroactive artificial muscle based on crosslinked PVA/SPTES*. Sensors and Actuators B, 150:57–64, 2010.

[129] Iain A. Anderson, Todd A. Gisby, Thomas G. McKay, Benjamin M. O'Brien, and Emilio P. Calius. *Multi-functional dielectric elastomer artificial muscles for soft and smart machines*. Journal of Applied Physics, 112(041101), 2012.

[130] Kazuto Takashima, Jonathan Rossiter, and Toshiharu Mukai. *McKibben artificial muscle using shape-memory polymer*. Sensors and Actuators A, 164:116–124, 2010.

[131] Ingi Agnarsson, Ali Dhinojwala, Vasav Sahni, and Todd A. Blackledge. *Spider silk as a novel high performance biomimetic muscle driven by humidity*. The Journal of Experimental Biology, 212:1990–1994, 2009.

[132] Piet Vandevyver. *Constructie van een elektromechanisch model van een zeepaardenstaart*. Master thesis, Hogeschool Gent, 2012.

[133] Tom Carrell, Neville Dastur, Richard Salter, and Peter Taylor. *Use of a remotely steerable robotic catheter in a branched endovascular aortic graft*. Journal of Vascular Surgery, 55(1):223–225, 2012.

[134] Bernhard Hennig and Ching K. Chow. *Lipid peroxidation and endothelial cell injury: implications in atherosclerosis*. Free radical biology and medicine, 4:99–106, 1988.

[135] Dierk Scheinert, Susanne Scheinert, Jacqueline Sax, Christopher Piorkowski, Sven Braunlich, Matthias Ulrich, Giancarlo Biamino, and Andrej Schmidt. *Prevalence and Clinical Impact of Stent Fractures after Femoropopliteal Stenting*. Journal of the American College of Cardiology, 45(2):312–315, 2005.

[136] Juha Song, Christine Ortiz, and Mary C. Boyce. *Thread-protection mechanics of an armored fish*. Journal of the Mechanical behavior of Biomedical Materials, 4:699–712, 2011.

[137] MJ. Ciarelli, SA. Goldstein, JL. Kuhn, DD. Cody, and MB. Brown. *Evaluation of orthogonal mechanical properties and density of human trabecular bone from the major metaphyseal regions with materials testing and computed tomography*. Journal of Orthopaedic Research, 9(5):674–682, 1991.

[138] J. Y. Rho, M. C. Hobatho, and R. B. Ashman. *Relations of mechanical properties to density and CT numbers in human bone*. Medical Engineering and Physics, 17(5):347–355, 1995.

[139] Sarah L. Lancianese, Edmund Kwok, Christopher A. Beck, and Amy L. Lerner. *Predicting regional variations in trabecular bone mechanical properties within the human proximal tibia using MR imaging*. Bone, 43:1039–1046, 2008.